KOMUNIKÁCIE
C O M M U N I C A T I O N S

kamuNikácie
C O M M U N I C A T I O N S

Dear Readers,

It is just 20 years from the first volume of the Communications - Scientific Letters of the University of Zilina was published. During twenty years the letters offer a range of ideas and focus on new knowledge and creativity, offer the possibilities sharing knowledge, the results of some projects and research teams. Over the last two decades, the scientific letters have been managed by three chief editors.

Each of them was able to move the Communications gradually up to a higher and more professional level. Professor Polednak started the magazine and set a challenging pace, and professor Bokuvka succeeded not only in this pace but managed to redefine the quality, and associate professor Mozer moves the border again. It belongs to them for their efforts, the dedication and the courage to come up with new solutions recognition.

University of Zilina is the higher education institution with one of the longest tradition in the Slovak Republic. It was founded 65 years ago in Prague as the College of Railways and after various changes as well as the technology development and enlargement of educational and research areas it become a fully university in character, named since November 1996 University of Zilina. Today the University of Zilina has approximately 1500 employees including 700 teachers and 200 researchers and 7800 students.

Although 20 years ago it seemed like a utopia to publish a scientific journal on communication and to involve not only our academic community, but the wider professional public within Europe, we can now say that we have reached a good level long ago. The differences remain, for the world is not standing and waiting, but we still keep pace and we seem to be able to do even more. The public and scientific response to the content of scientific letters has been positive.

Success in the current world means being able to do things that go beyond current needs and requirements. A few years might be too late. To deal with new themes, tasks and talents and to develop them, requires courage, patience, clear vision and trust. It may be difficult, but the university that wants to be prepared to address the challenges of the future, or to actively challenge them, has no other choice.

Pleasant reading.

Tatiana Corejova

kоmunikácie
COMMUNICATIONS

Branislav Dobrucky - Slavomir Kascak - Michal Prazenica - Pavel Pavlasek*

DIRECT AC-AC PROPULSION SYSTEM USING MATRIX CONVERTER AND 5Φ TRACTION MOTOR FOR HEV VEHICLE

The paper deals with direct AC-AC propulsion system using [n×5] matrix converter and five-phase traction induction motor (IM) for hybrid electric vehicle (HEV) including electronic differential. Using the direct AC-AC system, in comparison to classical rectifier-inverter with DC link, features smaller on-state semiconductor switches losses and consequently higher efficiency of power train of the vehicle. The major advantage of using a five-phase machine instead of three-phase one is in smaller torque pulsation and better fault tolerance under one phase of supply. There are presented comparative analyses of [3×5], [5×5], [2×5], [1×5], [0×5] matrix converter feeding five-phase induction motor for HEV vehicle. Modeling and simulation are done using Matlab-Simulink environment, and simulation experimental results are given in the paper.

Keywords: *AC/AC power train, matrix converter, five-phase induction motor, electric drive, bidirectional switch, modeling and simulation*

1. Introduction

Automobile propulsion system needs to develop maximum torque at zero speed. This cannot be achieved with conventional internal combustion engines (ICE). For ICE vehicles efficiency is rather small at low speeds and has a maximum value near rated speed. The usual arrangement of the electrical as well as non-electrical vehicles involves only one traction engine driving two wheels using a differential gear. In contrast, HEV and EV vehicle with multiple motor-wheels may represent benefits such as improving vehicle performance with better weight distribution and no power failure in the differential and the possibility to control the acceleration of each wheel separately for better stability in difficult or dangerous situations. Concept of HEV with ICE-electric motor aims to overcome the disadvantages of the pure electric vehicles, whose engines are powered by electric batteries: the limited duration of use (low autonomy) and time needed to recharge the batteries.

The possible operating modes of hybrid electric drive trains are [1]: pure electric: ICE is stopped and the vehicle is propelled only by batteries energy, pure engine mode: the vehicle is powered with energy provided by electric generator driven by engine. The batteries do not provide and do not take energy from the drive train. Hybrid mode: The traction power is drawn from both the engine-generator and the batteries. Engine traction and battery charging mode: The ICE-generator provides the energy needed

for the batteries charging and the propulsion vehicle. Regenerative braking mode: the engine is turned off and the traction motor is operated as generator and the energy provided is used to charge the batteries. Batteries charging mode: The engine – generator charges the batteries and the traction motor is not supplied. Hybrid batteries charging mode: both the engine-generator and the traction motor operate as generator to charge the batteries.

Traction drive used in electric vehicles can be divided into two categories: (a) single-drive system and (b) multi-drive system. With multi-drive systems, the motor controllers must additionally be configured to provide an electronic differential effect i.e. they must also perform a similar function as their mechanical differential counterpart. Thus, the electronic differential must take into account the speed difference between the two wheels when cornering.

Configuration with motor-wheels allows flexibility of the car; removes the central drive motor and associated transmission parts of the propulsion system of the vehicle. The main advantage of the electric motor in the wheel is adjustable traction and individual braking torque with high precision without ingestion gearbox, drive shaft, differential gear and other complex and heavy parts of power transmission [2, 3]. One of such a traction system is shown in Figure 1.

* **Branislav Dobrucky, Slavomir Kascak, Michal Prazenica, Pavel Pavlasek**
  Department of Mechatronics and Electronics, Faculty of Electrical Engineering, University of Zilina, Slovakia
  E-mail: branislav.dobrucky@fel.uniza.sk
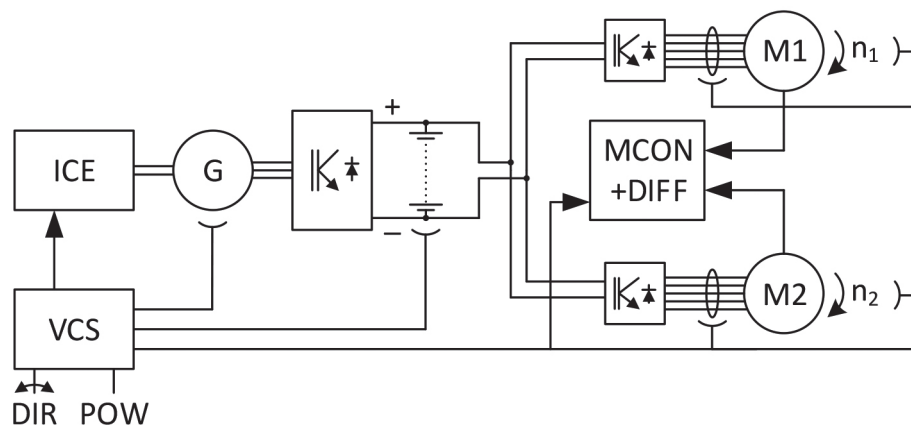
Figure 1 Series HEV with two VSI converters two motor wheels and electronic differential

a)   *b)*
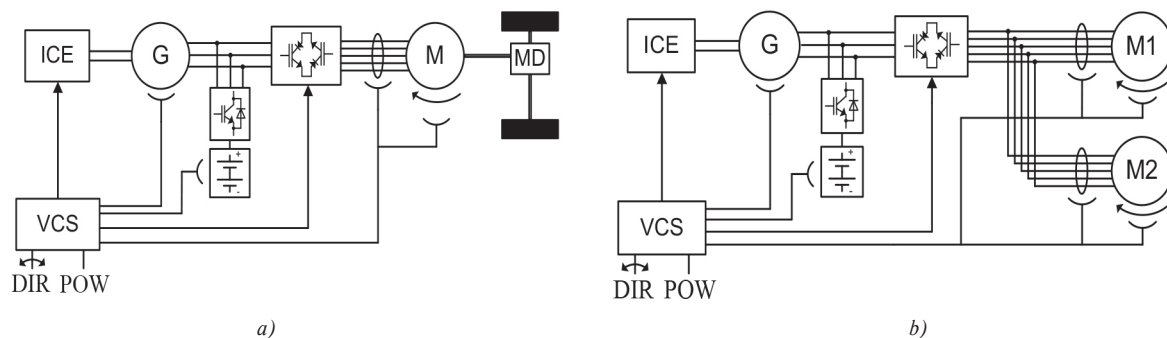
Figure 2 Direct AC-AC propulsion system with one [3x5] matrix converter and mechanical differential (a) or parallel connected two 5ΦIM (b)
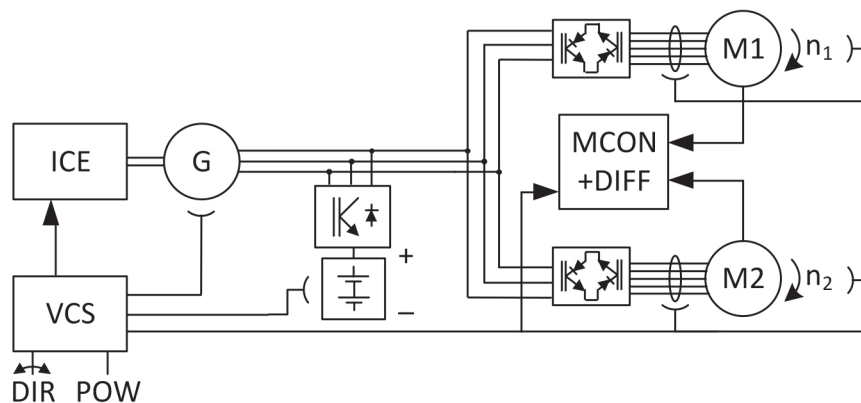
Figure 3 Direct AC-AC propulsion system with two [3x5] matrix converter and two 5ΦIM traction motor wheels

Another approach with high frequency AC interlink [1x3] MxC is presented in [4, 5].

2. New AC/AC traction propulsion system

When omitting systems with mechanical differential used for propelling the two back-driving wheels of the vehicle Figure 2a, there still remain two different configurations of the direct AC/AC traction systems. One of them, called independent control

of machines fed by one [3x5] matrix converter, Figure 2b. But, the papers [6, 7] explain that, although parallel multi-phase multi-motor drives and series connected multi-phase multi-motor drive systems are feasible and in principle offer good quality of dynamic performance as well, they do not hold a real prospect for industrial applications so far.

So, proposed propulsion system is presented in Figure 3 and comprises of two machines (PMSM, IM, SRM,..) that ensure the drive, including an electronic differential.

a)

b)
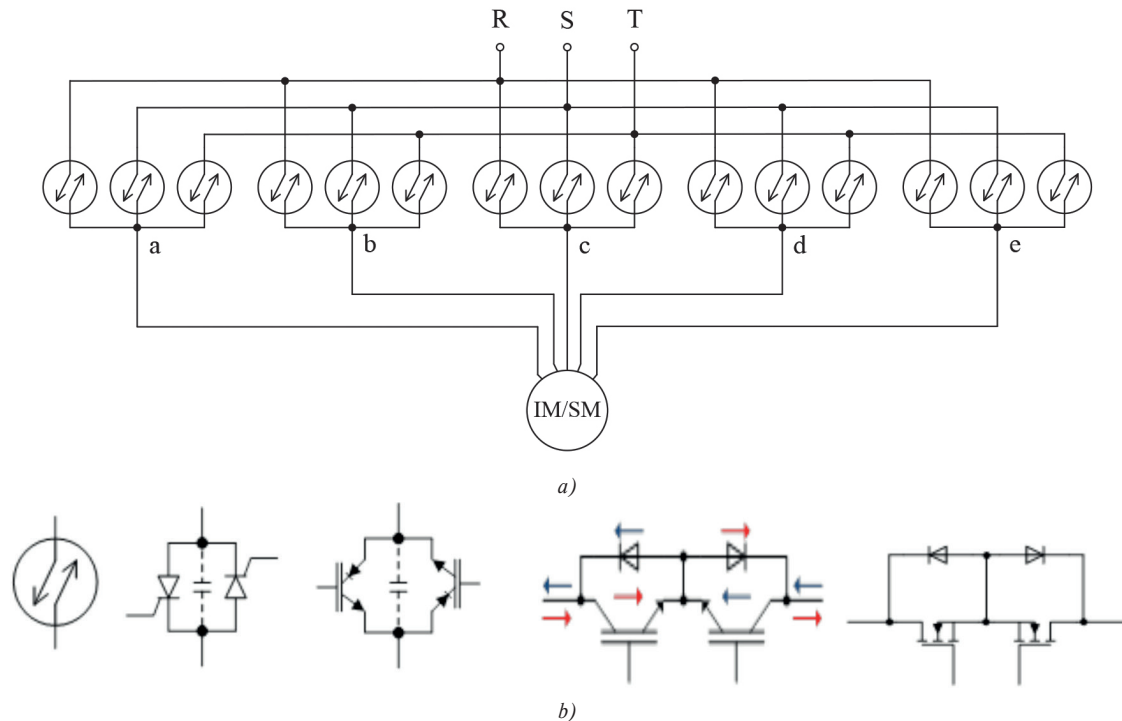
Figure 4 *Principle scheme of 3x5 matrix converter (a) with antiparallel or inversely connected BDS switches (b)*

The proposed traction system consists of two [3x5] matrix converters and two five-phase machines (IM) that ensure the drive of two back-driving wheels. The control of them is provided by an electronic differential offering good quality of a dynamic performance of the HEV vehicle. Propulsion system can be operated from both ICE engine and/or traction accu-battery.

The main difference between series HEV propulsion system AC/DC/AC (Figure 1) and direct AC/AC is that the second one does not comprise DC interlink between rectifier a VSI inverter. Thus, instead of voltage drops on rectifier- and inverter switches are substituted by a voltage drop on bidirectional switches of MxC only. If we consider just simple antiparallel connection of switches, then the total resulting voltage drop will be twice lesser. On the other hand, the operation from the accu-battery should be provided by additional converter.

Principle schematics of [3x5] matrix converter is shown in Figure 4a. It comprises 15 bidirectional switches (BDS) consisting of two semiconductor devices: turn-off GTO thyristors or reverse blocking RB IGBT transistors, Figure 4b.

The main problem of such bidirectional connection of BDS is withdrawing the energy of switched-off MxC circuit. Therefore, during inter-commutation of switches active snubbers should be used. There is necessary five snubber group– each for single phase a), b), c), d), e) of the motor. The basic scheme of this connection [8-10] is presented in Figure 5.

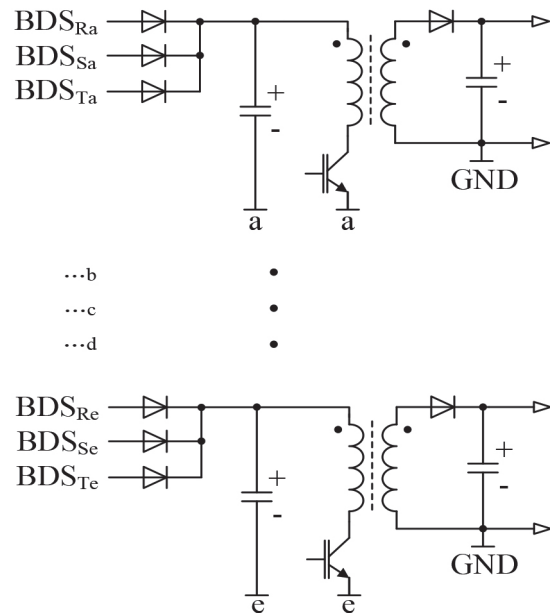**Figure 5** *Basic connection of snubber groups with active transfer of commutation energy*

3. Modelling and analysis of [3x5] matrix converter

The MxC can be studied based on two separated virtual stages reflecting the two stages of the conventional converter (rectifier-inverter) [11-13], Figure 6. Since at any given time at least one phase of the power supply voltage is positive and at least
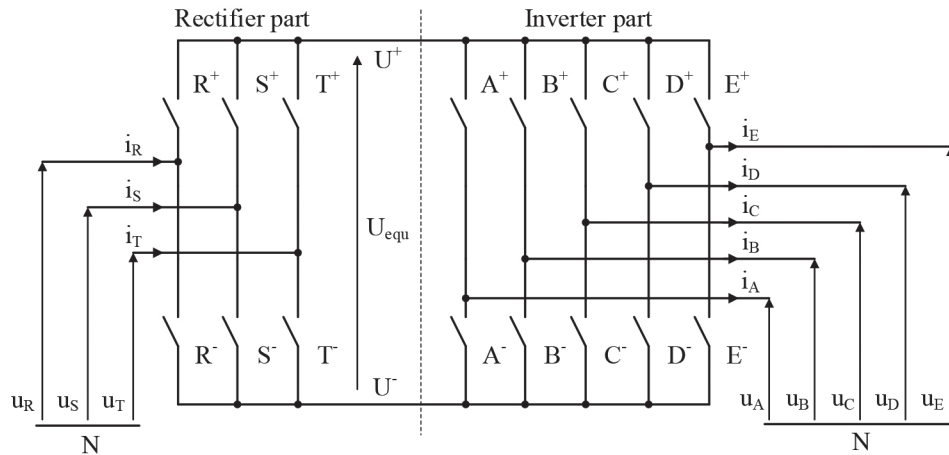
Figure 6 *Virtual model of indirect MxC with fictitious DC link*

a)

b)
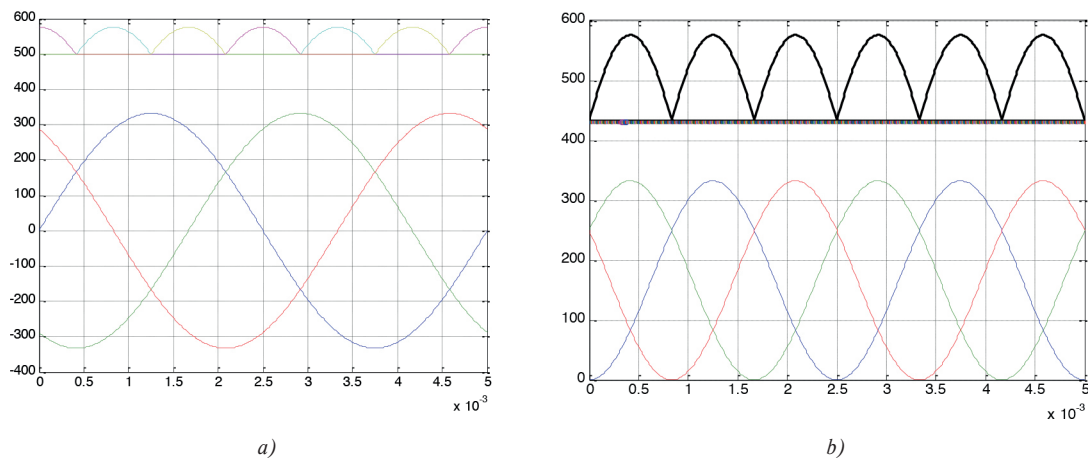
Figure 7 *Time waveforms of fictitious DC link voltage (a) and voltage square function (b)*
x: time, y: u_A, u_B, u_C, u_A, and u_{equ} voltages

another phase is negative, the fictitious DC link voltage is given by difference between U^+ and U^- potentials.

Then, MxC output voltage can be calculated by these Equations (1)

$$\begin{bmatrix} u_a \\ u_b \\ u_c \\ u_d \\ u_e \end{bmatrix} = \begin{bmatrix} u_{m1} & 1-u_{m1} \\ u_{m2} & 1-u_{m2} \\ u_{m3} & 1-u_{m3} \\ u_{m4} & 1-u_{m4} \\ u_{m5} & 1-u_{m5} \end{bmatrix} \begin{bmatrix} R^+ & S^+ & T^+ \\ R^- & S^- & T^- \end{bmatrix} \begin{bmatrix} u_R \\ u_S \\ u_T \end{bmatrix} \tag{1}$$

where $u_{mk} = r\cos(\varphi)\sin\left(\omega_0 t - \dfrac{2\pi}{5}(k-1)\right) + 1/2$ for k=1...5

$r = \dfrac{\cos(\varphi - \pi/3)}{\cos(\varphi)}$ and $\varphi = \omega t\big|_{\text{mod}(\frac{\pi}{3})} - \pi/6$

$R^+...T^-$ are logical variables for the *max* and *min* input phase voltage.

Average values of the fictitious DC interlink can be calculated. Derivation based on definition Equations (2), (3) is given in Appendix for 3-, 5-, and 2-phase systems. Average values of the fictitious DC interlink voltage for 3-phase system

$$U_{DCav} = \frac{6}{\pi} U_m \int_{\pi/3}^{\pi/2} \sin(\omega t)\, dt \tag{2}$$

Since the power of interlink and also torque of IM are dependent on voltage square function $(P_{av} \sim U_{rms}^2 / |Z| \to T_{mech} \sim P_{av}/\omega_{mech})$ the average values of the fictitious DC interlink voltage square function for 3-phase system can be expressed for 3-phase system as

$$U^{(2)}_{DCav} = \frac{6}{\pi} U_m \int_{\pi/3}^{\pi/2} \sin^2(\omega t)\, dt \tag{3}$$

The fictitious DC link voltage and voltage square function are presented in Figure 7a,b.

Table 1 Average values of the fictitious DC interlink

Supply system	U_{DCav} x U_m	$U^{(2)}_{DCav}$ x U_m
3-phase system	0.955 U_m	0.913 U_m
5-phase system	0.984 U_m	0.968 U_m
2-phase system	0.900 U_m	0.818 U_m

Table 2 Ratios of both parameters $\dfrac{U_m}{U_{DCav}}$ and $\dfrac{U_m}{U^{(2)}_{DCav}}$

Supply system	$\dfrac{U_m}{U_{DCav}}$	$\dfrac{U_m}{U^{(2)}_{DCav}}$	Oversizing [per cent]
3-phase system	1.047	1.095	9.5 %
5-phase system	1.017	1.033	3.3 %
2-phase system	1.111	1.222	22.2 %

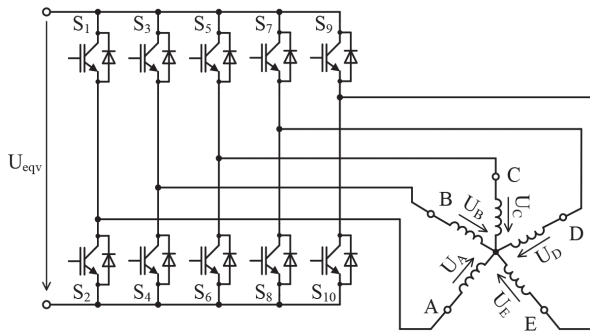Figure 8 Equivalent circuit scheme of inverter stage of indirect MxC with fictitious DC interlink and five-phase IM motor
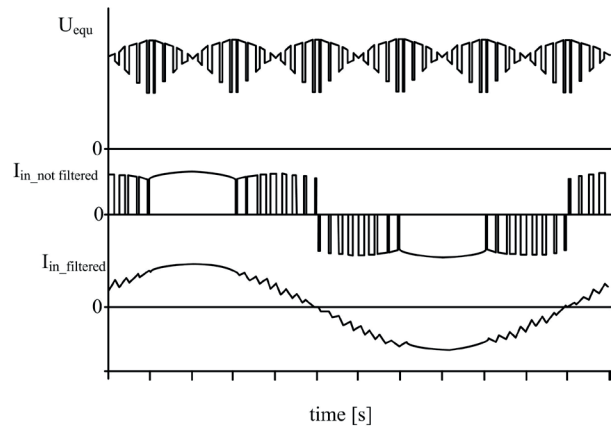
Figure 9 Principle of PWM modulation of [3x3] MxC under fictitious DC interlink

Results of both voltage average value parameters for all three systems are shown in the Table 1.

Based on these values the important parameters as ratios $\dfrac{U_m}{U_{DCav}}$ and $\dfrac{U_m}{U^{(2)}_{DCav}}$ can be calculated. Values of the ratios of both parameters are shown in the Table 2.

It can be deduced from Table 2 that by given power, also torque, the 3-phase machine should be oversized against 5-phase one by ~ 6 %. By other words, the maximum power and torque of 3-phase and 2-phase machines will be greater against 5-phase one by ~ 6 % and/or ~ 19 %, respectively. So, the compromise between these three propulsion systems is three-phase supply with 3ΦSG generator, [3x5] matrix converter five-phase traction motor 5ΦIM.

4. Modeling of drive with 5ΦIM traction motor fed by fictitious DC link ten-pulse frequency converter

Based on above, the derivations of the equivalent schematics for modelling and simulation can be introduced, Figure 8.

Then, stator voltage of 5ΦIM motor in vector form is [14, 15]

$$u_s = \mathrm{Re}\left(u_s\right) + j\,\mathrm{Im}\left(u_s\right) =$$
$$= \frac{2}{5}\left(u_a + u_b e^{j\frac{2\pi}{5}} + u_c e^{j\frac{4\pi}{5}} + u_d e^{j\frac{6\pi}{5}} + u_e e^{j\frac{8\pi}{5}}\right) \tag{4}$$

and possible scalar form:

$u_s = \mathrm{Re}\left(u_s\right) + j\,\mathrm{Im}\left(u_s\right) = u_\alpha + j u_\beta$. Similarly, the current vector can be expressed as $i_s = i_\alpha + j i_\beta$.

Consequently, the model of 5ΦIM motor can be expressed by Equations (5), (6).

$$\frac{d}{dt}\begin{pmatrix} i_s \\ i_r \\ \omega_m \end{pmatrix} = A\begin{pmatrix} i_s \\ i_r \\ \omega_m \end{pmatrix} + B\begin{pmatrix} u_s \\ u_r \\ 0 \end{pmatrix} \tag{5}$$

where A, B are matrices of system parameters

$$A = \begin{pmatrix} -\dfrac{R_r}{L_r} & \omega_r & M\dfrac{R_r}{L_r} & 0 \\ -\omega_r & -\dfrac{R_r}{L_r} & 0 & M\dfrac{R_r}{L_r} \\ \dfrac{MR_r}{\sigma L_s L_r^2} & \dfrac{M}{\sigma L_s L_r}(\omega_s - \omega_r) & -\dfrac{R_s}{\sigma L_s} & \omega_s \\ \dfrac{M}{\sigma L_s L_r}(\omega_s - \omega_r) & \dfrac{MR_r}{\sigma L_s L_r^2} & -\omega_s & -\dfrac{R_s}{\sigma L_s} \end{pmatrix};$$

$$B = \begin{pmatrix} 1 & 0 & 0 & 0 \\ 0 & 1 & 0 & 0 \\ -\dfrac{M}{\sigma L_s L_r} & 0 & \dfrac{1}{\sigma L_s} & 0 \\ 0 & -\dfrac{M}{\sigma L_s L_r} & 0 & \dfrac{1}{\sigma L_s} \end{pmatrix}$$

and ω_m is calculated as

$$\frac{d}{dt}\omega_m = \frac{T_{elmg} - T_{load}}{J_m}. \tag{6}$$

From the point of view of control strategies (PWM, SVC,) these are not particularly investigated in the paper. Nor special strategies during loss of one phase of the feeding source. Anyway, such strategies are commonly used, e.g. in the works [9-12], [14-16].

Figure 10 *Start-up of 5ΦIM fed by [3x5] matrix converter for speed and torque (a), detailed waveforms of phase voltage and current at steady-state (b)*

Figure 11 *Start-up of 5ΦIM fed by [5x5] matrix converter for speed and torque (a), detailed waveforms of phase voltage and current at steady-state (b)*

Possible PWM modulation for [3x3] matrix converter is shown in Figure 9.

5. Simulation experiment results

There are results of simulation experiments of five-phase induction motor 5ΦIM with different supplies shown in Figures 10-14:
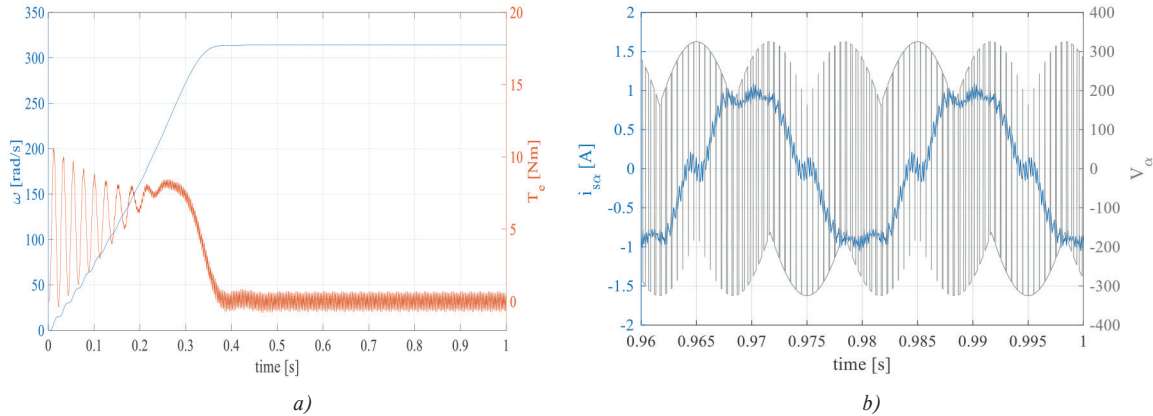
- 5ΦIM fed by [3x5] matrix converter
- 5ΦIM fed by [5x5] matrix converter
- 5ΦIM fed by [2x5] matrix converter
- 5ΦIM fed by [1x5] matrix converter
- 5ΦIM fed by [0x5] matrix converter, where [0x5] means matrix converter with pure DC supply.

Simulations were done using fictitious voltage by Figure 7 and Figure 8 in Matlab Simulink environment.

It is clear that obtained results show that voltage is periodic and current follows the desired amplitude and frequency.

6. Conclusions

There have been investigated different supply systems: [3x5], [5x5], [2x5], [0x5], [0x5] matrix converter fed five-phase induction motor for HEV vehicle in the paper. 5ΦIM traction motor has been chosen because five-phase motor drive with series or parallel connected motors is feasible and in principle offer good quality of dynamic performance. This is not possible with three-phase motors.

From the point of view of supply systems, the [3x5] MxC with 5ΦIM system is good compromise from economic and industrial applications. The obtained results show that, the [5x5] MxC with 5ΦIM propulsion system reaches approximately results as the system supplied from DC source i.e. accu-battery. Besides, it is known that five-phase application has the following advantages in comparison to the three-phase supply application [12], [17]: The speed curve response time dynamics is faster, the torque curve has lower ripple rate, the value of the output voltage of the converter is higher. Furthermore, the amplitude of the output current in five
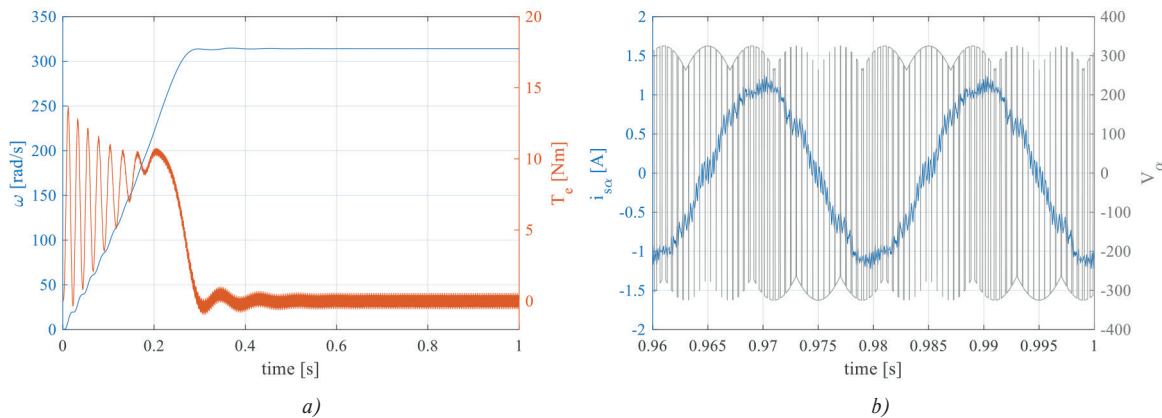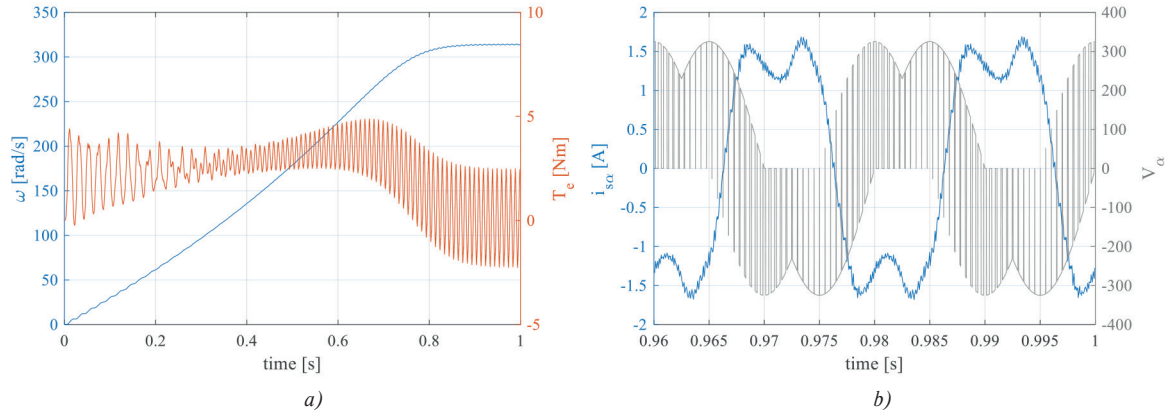
Figure 12 Start-up of 5ΦIM fed by [2x5] matrix converter for speed and torque (a), detailed waveforms of phase voltage and current at steady-state (b)
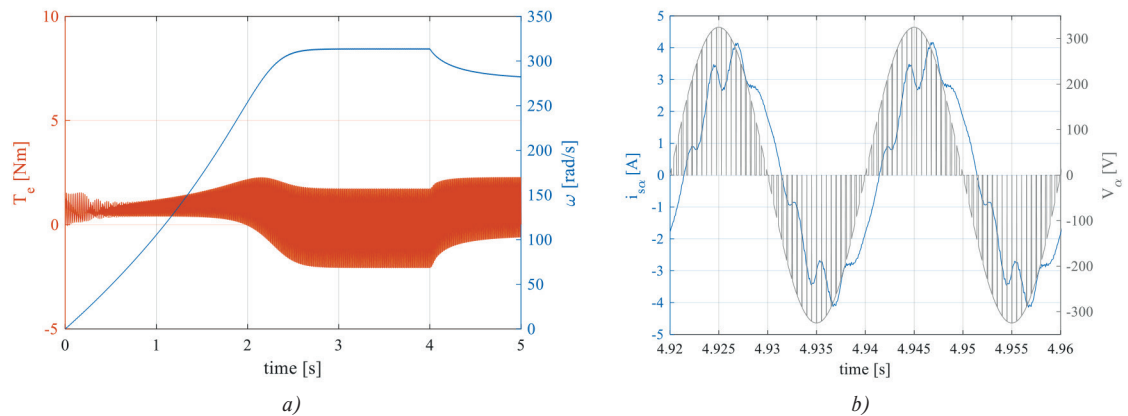
Figure 13 Start-up of 5ΦIM fed by [1x5] matrix converter for speed and torque (a), detailed waveforms of phase voltage and current at steady-state (b)
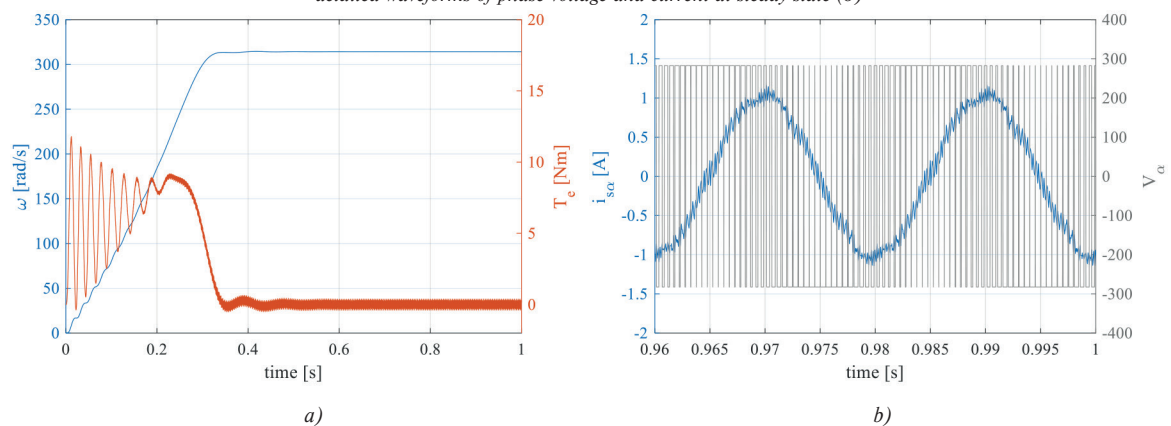
Figure 14 Start-up of 5ΦIM fed by [0x5] matrix converter for speed and torque (a), detailed waveforms of phase voltage and current at steady-state (b)

phase motors is reduced compared to the three-phase one which can prevent deterioration of the windings; it uses smaller gauge switches (reduces the cost of purchase and maintenance).

The present approach can be generalized for more than five-phase output and has some inherent advantages that make

this application a very promising solution, especially when it is connected to a multiphase machine to profit mainly from all its benefits in industrial plant applications.

Appendix

Average value of fictitious DC link since 3-phase supply

$$U_{DCav} = \frac{6}{\pi} U_m \int_{\pi/3}^{\pi/2} \sin(\omega t) dt = \frac{6}{\pi} U_m \cos\left(\frac{\pi}{3}\right) = \frac{3}{\pi} U_m \doteq$$
$$\doteq 0.955 \, U_m$$

thus ratio of $\dfrac{U_m}{U_{DCav}} \doteq 1.047$.

Average value of fictitious DC link since 5-phase supply

$$U_{DCav} = \frac{10}{\pi} U_m \int_{2\pi/5}^{\pi/2} \sin(\omega t) dt = \frac{10}{\pi} U_m \cos\left(\frac{2\pi}{5}\right) \doteq 0.984 \, U_m$$

thus ratio of $\dfrac{U_m}{U_{DCav}} \doteq 1.017$.

Average value of fictitious DC link since 2-phase supply

$$U_{DCav} = \frac{4}{\pi} U_m \int_{\pi/4}^{\pi/2} \sin(\omega t) dt = \frac{4}{\pi} U_m \cos\left(\frac{\pi}{4}\right) = \frac{2\sqrt{2}}{\pi} U_m \doteq$$
$$\doteq 0.900 \, U_m$$

thus the ratio of $\dfrac{U_m}{U_{DCav}} \doteq 1.111$.

Average value of fictitious DC link voltage square function for 3-phase supply

$$U^{(2)}_{DCav} = \frac{6}{\pi} U_m \int_{\pi/3}^{\pi/2} \sin^2(\omega t) dt =$$
$$= \frac{6}{\pi} U_m \left\{ \frac{1}{2}\left[\left(\frac{\pi}{2} - \frac{\pi}{3}\right) - \frac{1}{2}\left(\sin 2\frac{\pi}{2} - \sin 2\frac{\pi}{3}\right)\right]\right\} \doteq$$
$$\doteq 0.913 \, U_m$$

where $\sin^2(\omega t) = \frac{1}{2}[1 - \cos(2\omega t)]$ and ratio $\dfrac{U_m}{U^{(2)}_{DCav}} \doteq 1.095$.

Average value of fictitious DC link voltage square function for e 5-phase supply

$$U^{(2)}_{DCav} = \frac{10}{\pi} U_m \int_{2\pi/5}^{\pi/2} \sin^2(\omega t) dt =$$
$$= \frac{10}{\pi} U_m \left\{ \frac{1}{2}\left[\left(\frac{\pi}{2} - \frac{2\pi}{5}\right) - \frac{1}{2}\left(\sin 2\frac{\pi}{2} - \sin 2\frac{\pi}{5}\right)\right]\right\} \doteq$$
$$\doteq 0.968 \, U_m$$

So, the ratio $\dfrac{U_m}{U^{(2)}_{DCav}} \doteq 1.033$.

Average value of fictitious DC link voltage square function for 2-phase supply

$$U^{(2)}_{DCav} = \frac{4}{\pi} U_m \int_{2\pi/5}^{\pi/2} \sin^2(\omega t) dt =$$
$$= \frac{4}{\pi} U_m \left\{ \frac{1}{2}\left[\left(\frac{\pi}{2} - \frac{2\pi}{5}\right) - \frac{1}{2}\left(\sin 2\frac{\pi}{2} - \sin 2\frac{\pi}{5}\right)\right]\right\} \doteq$$
$$\doteq 0.818 \, U_m$$

and ratio $\dfrac{U_m}{U^{(2)}_{DCav}} \doteq 1.222$.

References

[1] EHSANI, M., GAO, Y., EMADI, A.: Modern Electric, Hybrid-and Fuel Cell Vehicles. CRC Press, Boca Raton, USA, 2010.

[2] HARTANI, K., BOURAHLA, M., MILOUD, Y., SEKOUR, M.: Electronic Differential with Direct Torque Fuzzy Control for Vehicle Propulsion System. Turkish Journal Of Electrical Engineering Computer Sciences, 17(1), 21-38, 2009.

[3] DOBRUCKY, B., ZASKALICKY, P., PAVLASEK, P.: Control of Hybrid-and Electrical Vehicle with Five-Phase IM Motor. Autobusy-Efficiency of Transport, 18(6), 1191-1195, 2017.

[4] GONTHIER, L., BERNOT, F., BOCUS, S. D., ELBAROUDI, S., BERTHON, A.: High-Efficiency Soft-Commutated DC-AC-AC Converter for Electric Vehicles. ElectroMotion, 5(2), 54-64, 1998.

[5] DOBRUCKY, B., HAVRILA, R., DUBOVSKY, J.: A Single-Phase Supplied Matrix Converter with Unity Power Factor. PEMC, Prague, 1998.

[6] SEMAIL, E., LEVI, E., BOUSCAYROL, A., KESTELYN, X.: Multi-Machine Modeling of Two Connected Series 5-Phase Synchronous Machines: Effect of Harmonics on Control. Proceedings of IEEE European Conference on Power Electronics and Applications, Germany, 10, 2005.

[7] JONES, M., LEVI, E., VUKOSAVIC, S. N.: Independent Control of Two Five-Phase Induction Machines Connected in Parallel to a Single Inverter Supply. Proceedings of IEEE Industrial Electronics Society Annual Meeting (IECON'06), France, 1257-1262, 2006.

[8] FRIVALDSKY, M., DOBRUCKY, B., SCELBA, G., SPANIK, P., DRGONA, P.: Bidirectional Step-Up/Step-Down DC/DC Converter with Magnetically Coupled Coils. Communications - Scientific Letters of the University of Zilina, 15(3), 21-25, 2013.

[9]   NEFT, CH. L., SCHAUDER, C. D.: Theory and Design of a 30-hp Matrix Converter. IEEE Transactions on Industry Applications, 28(3), 546-551, 1992.

[10] SCHAUDER, C. D.: Hidden DC-Link AC/AC Converter Using Bilateral Power Switches. United States Patent 4,642,751.

[11] JUSSILA, M., TUUSA, H.: Comparison of Direct and Indirect Matrix Converters in Induction Motor Drive. Proceedings of IEEE Industrial Electronics.Conference, (IECON'06), France, 1621-1626, 2006.

[12] REZAOUI, M. M., KOUZOU, A., MAHMOUDI, M. O., NEZLI, L.: Comparison Performances between Two Matrix Converters [3x3] and [3x5] Supplying a Multi-Phases Induction Machine. Journal of Electrical Engineering, 16(1), 217-227, 2016.

[13] CHLEBIS, P., SIMONIK, P., KABASTA, M.: The Comparison of Direct and Indirect Matrix Converters. Proceedings of Progress in Electromagnetics Research Symposium (PIERS 2010), USA, 310-313, 2010.

[14] SCHREIER, L., BENDL, J., CHOMAT, M.: Five-Phase Induction Machine Fed from Ten-Pulse Frequency Converter. Proceedings of 18th International Conference on Electrical Drives and Power Electronics (EDPE), Slovakia, 2011, on CD ROM.

[15] ZASKALICKY, P.: Mathematical Model of a Five-Phase Voltage-Source PWM Controlled Inverter. Electrical Engineering – Archiv für Elektrotechnik, Springer-Verlag GmbH, Germany, 2017. Published on-line 12-09-2017.

[16] FANG, Y., TAN, G., LIU, H.: Space Vector Modulated Three-Phase to Two-Phase Matrix Converter. Proceedings of International Conference on Electrical Engineering, 2009.

[17] SCHREIER, L., BENDL, J., CHOMAT, M.: Operation of Five-Phase Induction Motor after Loss of One Phase of Feeding Source. Electrical Engineering, 99(1), 9-18, 2017.

Simon Zossak - Marek Stulrajter - Pavol Makys*

SELF-SENSING CONTROL OF PMSM AT ZERO AND LOW SPEED

The paper deals with control of Permanent Magnet Synchronous Motor (PMSM) without a rotor position sensor. In the low and zero speed region, the rotor saliencies are utilized to obtain the information about the rotor position. Self-sensing control techniques employ high frequency (hf) signal injection to excite the saliencies. The proposed algorithm enables tracking the saliency and allows PMSM control at zero and low speed. The theoretical assumptions were experimentally verified including the initial rotor position detection.

***Keywords:** PMSM, self-sensing, low speed, position estimation, hf signal injection*

1. Introduction

Vector control of AC machines like FOC (Field Oriented Control) or DTC (Direct torque control) provides a very good dynamic performance and full start-up torque. This technique enables separate control of electromagnetic torque and magnetizing flux of the motor. On the other hand, these structures require information about the rotor position. This can be obtained by mechanical sensors such as Hall Effect sensors, encoders or resolvers. A control without these mechanical sensors is known as self-sensing, auto-sensing or eigen-sensing since the position information is an inherent part of the machine thanks to magnetic and construction asymmetry ('the machine is the sensor') [1-3]. It brings benefits such as lower cost of the drive (which is an important factor in automotive industry), capability of high speed operation (where sensor is mechanical restriction) and can be used as redundant solution in case of sensor failure. There are two categories of these algorithms: model based methods and methods utilizing the machine anisotropy that is a function of the rotor position. As an example of model based method, a back-EMF observer can be mentioned. However, this observer can be used only for medium to high speed operating range because the amplitude of back-EMF voltage is proportional to the angular velocity and is very small for precise position estimation at low speed.

The significant saliency can be observed in interior PM synchronous machine, which yields to different inductance in d and q-axis. This paper describes a saliency tracking method to estimate the rotor position. The magnetic saliency is excited with the high frequency (hf) voltage signal. Proposed algorithm has

been designed to work at zero and low speed region, including detection of initial rotor position. This algorithm together with a model based observer [4, 5] offers a solution for PMSM control without a position sensor within the entire speed range.

2. PMSM mathematical model

To simplify mathematical model of 3-phase machine, 2-phase rotational (*dq*) frame can be used, which is aligned and rotates synchronously with the rotor. After transformation of voltage and torque equations and some mathematical corrections, motor model can be written as follows:

$$\begin{bmatrix} u_d \\ u_q \end{bmatrix} = R_s \begin{bmatrix} i_d \\ i_q \end{bmatrix} + \begin{bmatrix} L_d & 0 \\ 0 & L_q \end{bmatrix} \frac{d}{dt} \begin{bmatrix} i_d \\ i_q \end{bmatrix} + \omega_e \begin{bmatrix} -L_q \\ L_d \end{bmatrix} \begin{bmatrix} i_d \\ i_q \end{bmatrix} + \omega_e \psi_{pm} \begin{bmatrix} 0 \\ 1 \end{bmatrix} \quad (1)$$

where R_s is stator resistance, L_d and L_q are d and q axis synchronous inductances, ω_e is electric angular speed and ψ_{pm} is flux of permanent magnets.

$$m_e = \frac{3}{2} \cdot p \cdot \left(\psi_{pm} \cdot i_q + (L_d - L_q) \cdot i_d \cdot i_q \right) \quad (2)$$

In Equation (2), the first synchronous electromagnetic torque term is independent of i_d current, but it is directly proportional to the stator current component i_q. In contrast, the second reluctance torque term is proportional to the $i_d i_q$ current component product and to the difference of the inductance values

---

* ¹Simon Zossak, ²Marek Stulrajter, ¹Pavol Makys
¹Department of Power Electrical Systems, Faculty of Electrical Engineering, University of Zilina, Slovakia
²NXP Semiconductors, Roznov pod Radhostem, Czech Republic
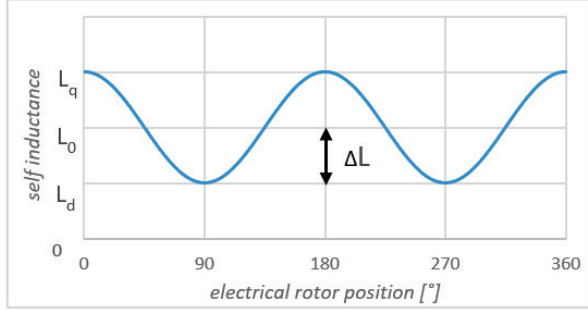E-mail: simon.zossak@fel.uniza.sk

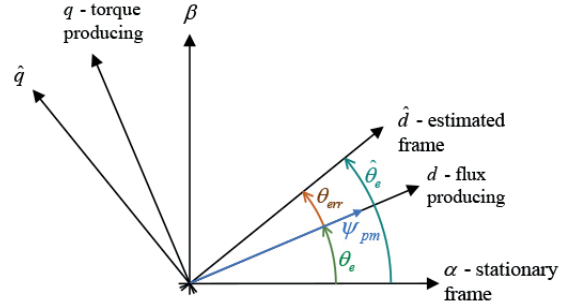**Figure 1** *Stator phase self-inductance as a function of rotor position*

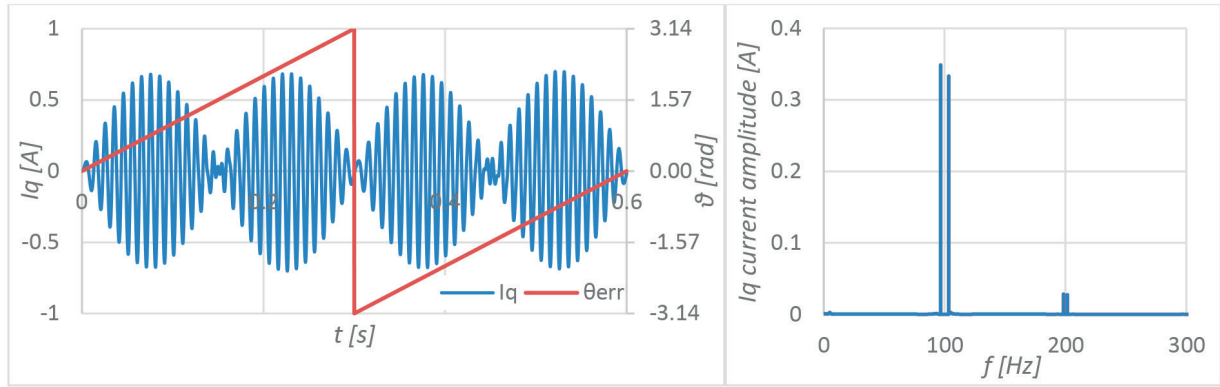**Figure 2** *Estimated and real reference frame*

Figure 3 *Dependence of current amplitude on estimation error θ_{err} and frequency spectrum of $\hat{i}_q$*

$(L_d - L_q)$. The angular speed is proportional to the difference between electromagnetic and load torque [6-8]:

$$\frac{d\omega_e}{dt} = \frac{p}{J}(m_e - m_{zt}) \tag{3}$$

The inductance variation in salient-pole machines arises because the permanent magnets are either inset or buried in the rotor. Since the permeability of the permanent magnets is low $\mu_{rM} \approx \mu_0$, the effective air-gap length is larger in the direction of the magnets flux than it is in perpendicular direction. Magnetic reluctance in d-axis is therefore high and inductance low. On the contrary, magnetic reluctance in q-axis is low and inductance high. So, the inequality $L_d > L_q$ applies.

This type of the motor saliency is directly linked to the rotor position. The stator phase inductance as function of the rotor position is shown in Figure 1.

To track this saliency and thus extract the rotor position information, an additional signal needs to be added to the supply voltage. There is a plenty of methods using different approach to excite the motor. The most common are injection of high frequency sinusoidal voltage signal or discrete voltage test pulses (e.g. INFORM method). Such signal excites the magnetic saliency and enables its extraction. The high frequency voltage signal injection is used in this paper, due to the easier implementation with voltage source inverter [6, 9].

To analyze the motor behavior in high frequency spectra, the mathematical model of PMSM described in Equation (1) is transformed to frequency domain:

$$\begin{bmatrix} u_d(j\omega_c) \\ u_q(j\omega_c) \end{bmatrix} = \begin{bmatrix} R_s + j\omega_c L_d & -\omega_e L_q \\ \omega_e L_q & R_s + j\omega_c L_d \end{bmatrix}\begin{bmatrix} i_d(j\omega_c) \\ i_q(j\omega_c) \end{bmatrix} + \\ + \omega_e \begin{bmatrix} 0 \\ \psi_{pm} \end{bmatrix} \tag{4}$$

where ω_c is frequency of injected signal, that is much higher than fundamental frequency of the motor ω_e ($\omega_c \gg \omega_e$).

Assuming the *hf* voltage signal is injected only in estimated d-axis, then $\hat{u}_d = U_m \sin(\omega_c t)$ and $\hat{u}_q = 0$, and current components can be expressed as follows [4]:

$$\begin{bmatrix} \hat{i}_d \\ \hat{i}_q \end{bmatrix} = -\frac{\hat{U}_m}{\omega_c L_d L_q}\cos(\omega_c t)\begin{bmatrix} L_0 - \Delta L \cos(2\theta_{err}) \\ \Delta L \sin(2\theta_{err}) \end{bmatrix} \tag{5}$$

where angle θ_{err} is angle between estimated and real reference frame:

$$\theta_{err} = \hat{\theta}_e - \theta_e \tag{6}$$

The position of real reference frame is given by the position of permanent magnet flux and the position of estimated reference frame is given by the estimated position of rotor flux as shown in Figure 2.
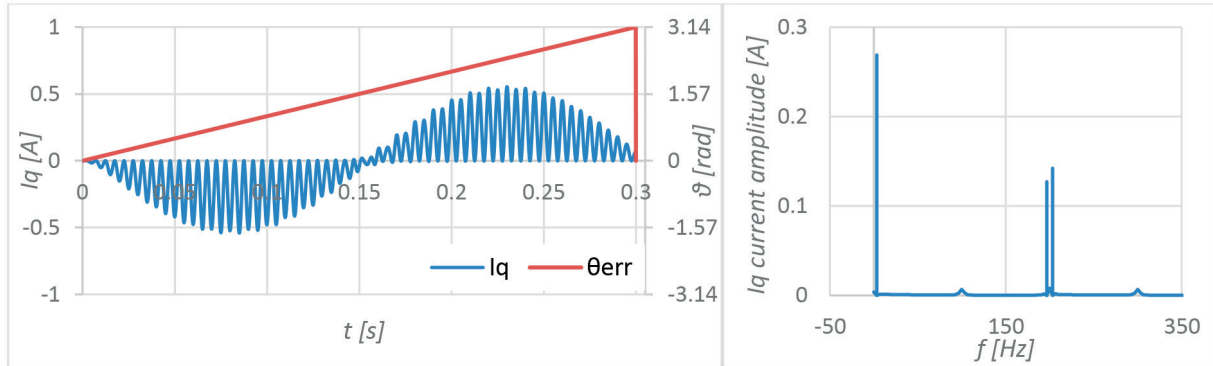
Figure 4 *Demodulated current* $\hat{i}_{q\_dmd}$ *and its frequency spectrum*
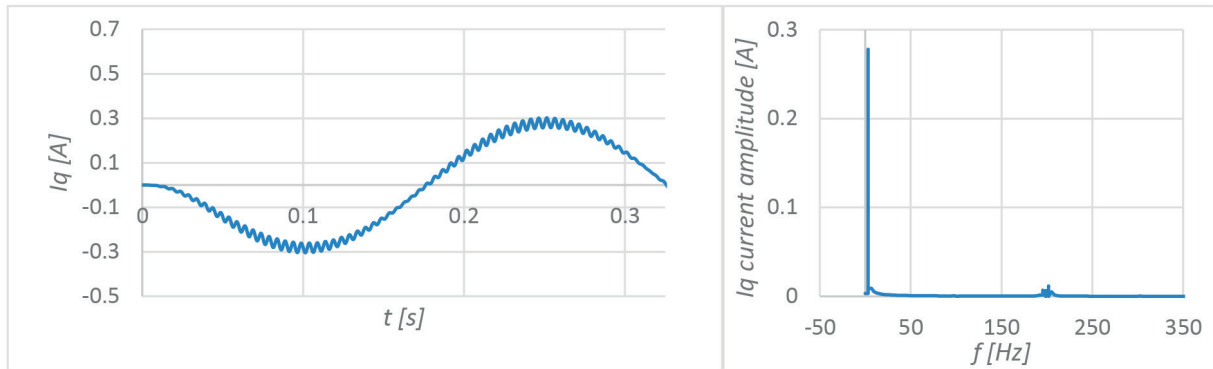

Figure 5 *Filtered current* $\hat{i}_{q\_LPF}$ *and its frequency spectrum*

3. Saliency observer

The position of permanent magnet flux (d-axis) needs to be known for maximal efficiency of FOC. The angle θ_{err} can be extracted from the Equation (5) for current $\hat{i}_q$. The waveform of this current during one electrical revolution of the rotor is shown in Figure 3. The current has zero amplitude if the angle θ_{err} is equal to any integer multiple of $\dfrac{\pi}{2}$.

The high and low frequency components are separated by heterodyning demodulation. Demodulation is based on multiplication of the current $\hat{i}_q$ from Equation (5) by an auxiliary signal $\cos(\omega_c t)$ with identical frequency and phase as modulated signal [4]:

$$\hat{i}_q = -\frac{\hat{U}_m \Delta L}{\omega_c L_d L_q}\cos(\omega_c t)\sin(2\theta_{err}) \quad / \cdot \cos(\omega_c t) \tag{7}$$

By applying the mathematical rules, the Equation (7) will be transformed into the following form:

$$\hat{i}_{q\_dmd} = -\frac{I_1}{2}\sin(2\theta_{err}) - \frac{I_1}{2}\sin(2\theta_{err})\cos(2\omega_c t) \tag{8}$$

where the magnitude of the original and modulated current is expressed as:

$$I_1 = -\frac{\hat{U}_m \Delta L}{\omega_c L_d L_q} \tag{9}$$

The low and high frequency component are clearly visible in spectrum of demodulated current in Figure 4.

High frequency component in Equation (8) can be afterwards attenuated with a Low Pass Filter:

$$\hat{i}_{q\_LPF} = -\frac{I_1}{2}\sin(2\theta_{err}) \tag{10}$$

The current waveform after filtering the high frequency component can be seen in Figure 5.

The angle θ_{err} can then be calculated as follows:

$$\theta_{err} = -\frac{1}{2}\arcsin\left(\frac{-2 \cdot \hat{i}_{q\_LPF}}{I_1}\right) \tag{11}$$

Saliency observer [4] is in fact a closed-loop system which forces the filtered component of the current $\hat{i}_q$ to be zero, and therefore setting θ_{err} to zero. Thus the estimated *dq* frame match the real *dq* frame, and estimated rotor position reflex the rotor flux position.

The control structure of saliency observer is shown in Figure 6. The abc currents are transformed to the estimated rotational frame $\hat{d}\hat{q}$ using the estimated rotor position.
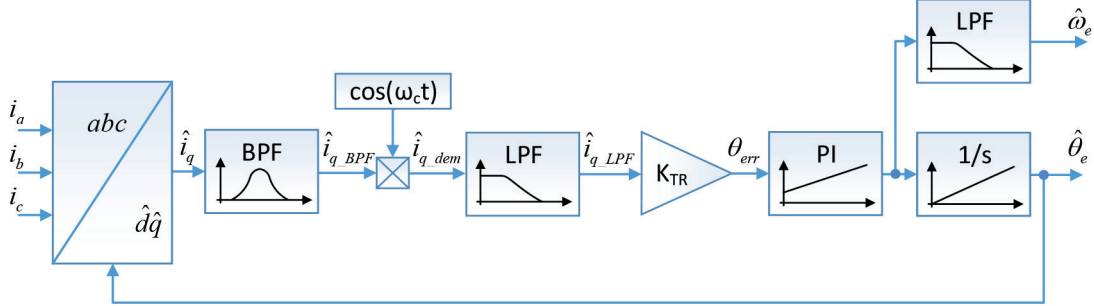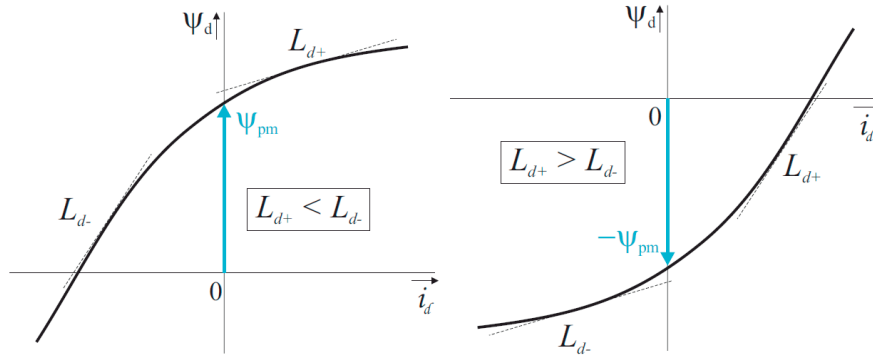
Figure 6 *Block diagram of Saliency observer*

Figure 7 *Magnetic flux in d-axis as function of i_d current, corresponding to north (on the left) and south (on the right) pole*

The current $\hat{i}_q$ is used for demodulation by heterodyning and set of filters, to extract the information about the error angle between the real *dq* frame and estimated *dq* frame. The estimation error θ_{err} is then processed by a PLL to generate the estimated rotor position by minimizing the estimation error.

4. PM polarity detection

As can be seen in Equation (10), the term of current $\hat{i}_{q\_LPF}$ can be zero if the estimation error is $\theta_{err} = k \cdot 2\pi$, but also if it is $\theta_{err} = \pi + k \cdot 2\pi$, where $k = 0, \pm1. \pm2,....$ The π offset in the position error indicates a displacement 180° between the north and south pole of the magnet. To eliminate this phenomenon, an initial position detection approach including the PM polarity detection has to be adopted. The PM polarity detection is based on stator core saturation phenomenon. Assuming the magnetic operating point is placed on the knee of the hysteresis curve, making the saturation effect visible even with small variation in d-axis current $\hat{i}_d$ as shown in Figure 7.

This theoretical relationship can be approximated using Taylor series expansion as follows [4]:

$$i_{d\_north} \approx \frac{1}{L_d}(\psi_d - \psi_{pm}) - \frac{1}{2}\frac{d^2 i_d}{d\psi_d^2}(\psi_d - \psi_{pm})^2 \qquad (12)$$

$$i_{d\_south} \approx \frac{1}{L_d}(\psi_d - \psi_{pm}) + \frac{1}{2}\frac{d^2 i_d}{d\psi_d^2}(\psi_d - \psi_{pm})^2 \qquad (13)$$

Where injected signal is sinusoidal with given amplitude and frequency, so magnetic flux is given as:

$$\psi_d = \int u_d dt = \int U_m \sin(\omega_c t) dt = -\frac{U_m}{\omega_c}\cos(\omega_c t) \qquad (14)$$

After substituting (14) into (13), current i_d can be written as:

$$i_d = I_{d\_DC} + I_{d\_c}\cos(\omega_c t) + I_{d\_2c}\cos(2\omega_c t) \qquad (15)$$

Where:

$$R_d = \frac{1}{L_d} \ ; \ R_d' = \frac{1}{2}\frac{d^2 i_d}{d\psi_d^2} \qquad (16)$$

$$I_{d\_DC} = \frac{1}{2}\frac{U_m^2 R_d' + \psi_{pm}^2 R_d' \omega_c^2 - \psi_{pm} R_d}{\omega_c^2} \qquad (17)$$

$$I_{d\_c} = \frac{U_m(2R_d'\psi_{pm} - R_d)}{\omega_c} \ ; \ I_{d\_2c} = \frac{1}{2}\frac{U_m^2 R_d'}{\omega_c^2} \qquad (18)$$

The block diagram of PM polarity detection method is shown in Figure 8. The d-axis current signal is processed similarly as q-axis current in case of initial position detection. Amplitude polarity of 2nd harmonic of the injected signal I_{d_2c} identifies the polarity of PM. If $I_{d\_2c} > 0$, determined position is correct, but
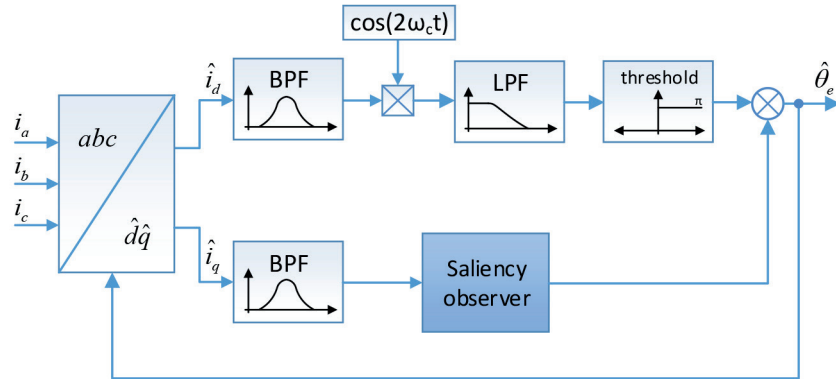
Figure 8 *Block diagram of Saliency observer with PM polarity detection algorithm*
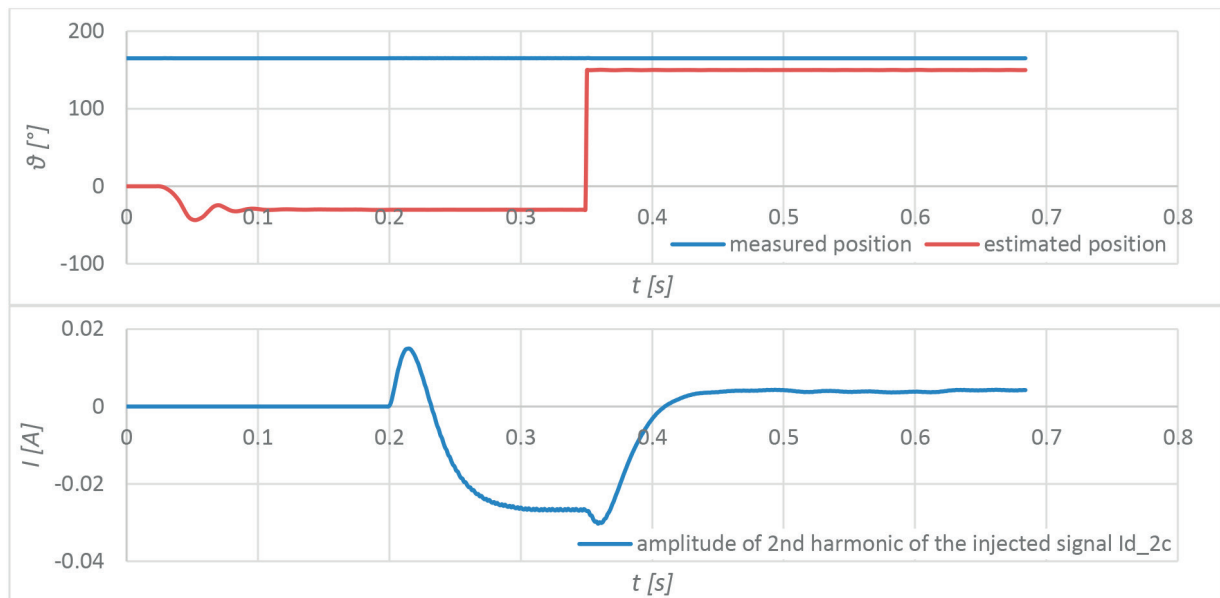
Figure 9 *Initial position detection respecting PM polarity*

if $I_{d\_2c} < 0$, the angle offset π has to be added to the estimated position.

Then both algorithms result into one solution for initial position detection respecting the PM polarity and estimation the rotor flux position for zero and small speed. The fusion of both algorithms can be seen in Figure 9.

5. Experimental Results

The described self-sensing technique was verified on real PMSM motor. The NXP MPC5643L MCU for automotive and industrial applications was used as control device. The estimated position was compared with position measured by encoder.

Initial position detection including the PM polarity correction can be seen in Figure 9. At the beginning of the test, the south pole of PM is detected. As soon as the negative steady state of the

I_{d_2c} component is evaluated, the estimated position is corrected by 180°.

In Figure 10 is the PMSM rotating at 300 rpm in negative direction. At 0.28 s, the same speed in positive direction is required. The measured rotor flux position is compared with estimated position in middle graph. Position estimation error in electrical degrees is plotted below. The speed ripple is caused mainly by cogging torque, most visible at low speeds. This issue can be subject of the following research.

6. Conclusion

In this paper, the self-sensing control of PMSM at zero and low speed was presented. The high frequency voltage signal was used to excite the motor saliency which is a function of the rotor position. The saliency observer as well as the magnet polarity
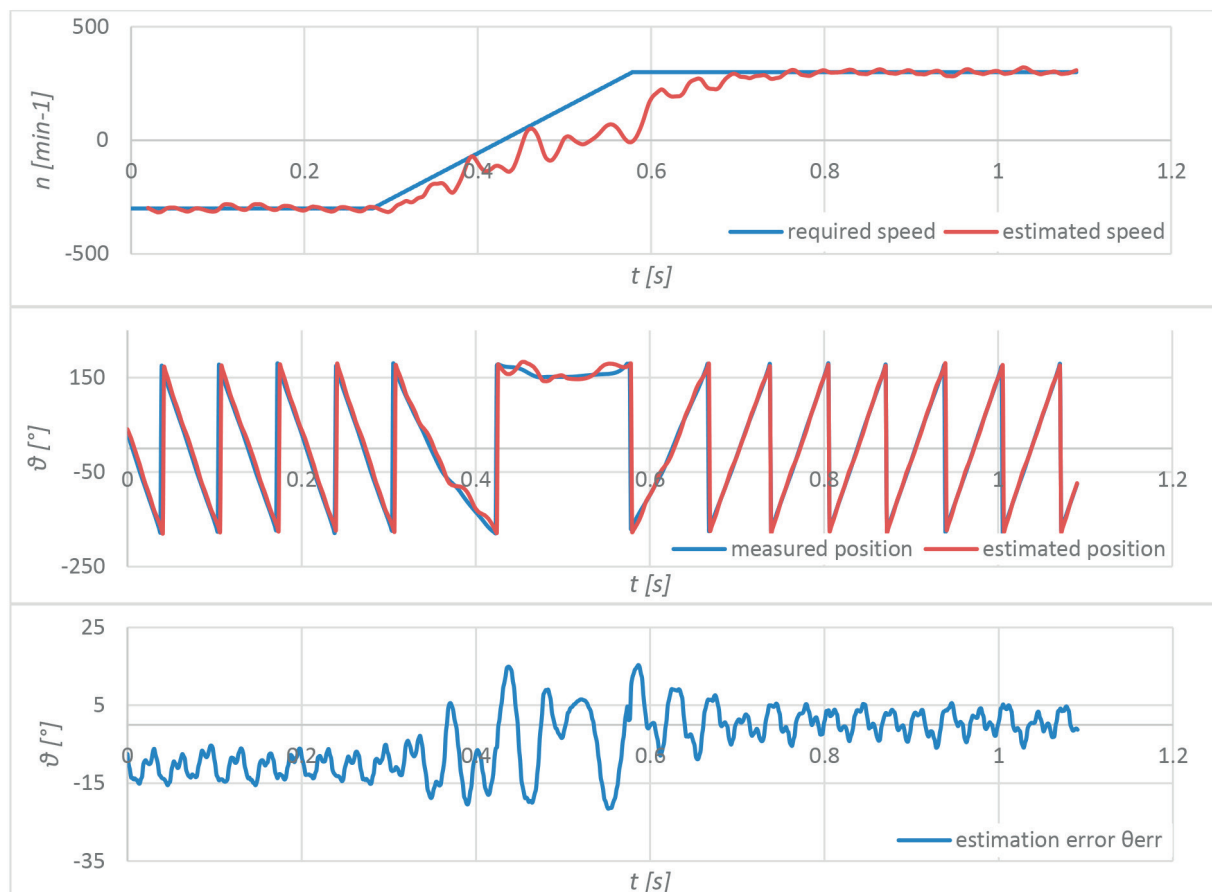
Figure 10 Reversing polarity of required speed

detection method was derived from the motor model considering high frequency signals. Tracking this saliency leads to the rotor flux position which is considered as a rotor position. Proposed algorithms return a correct initial position which enables full start-up torque generation. Both methods were implemented and verified on a real experimental rig with PMSM motor. Achieved results have confirmed the theoretical assumptions and shown that the methods based on the motor anisotropy can be successfully used in self-sensing control.

An additional optimization of the algorithm, accuracy improvement or torque ripple reduction will be a subject of further work.

Acknowledgement

References

[1] Proceedings of International Conference Symposium on Sensorless Control for Electrical Drives. (SLED 2017), Italy, 2017.
[2] CONSOLI, A., SCARCELLA, G., SCELBA, G., TESTA, A., TRIOLO, D. A.: Sensorless Rotor Position Estimation in Synchronous Reluctance Motors Exploiting a Flux Deviation Approach. IEEE Transactions on Industry Applications 43(5), 1266-1273, 2007.
[3] SCARLETTA, G., SCELBA, G., TESTA, A.: High Performance Sensorless Controls Based on HF Excitation: A viable Solution for Future AC Motor Drives? In IEEE Workshop on Electrical Machines Design, Control and Diagnosis (WEMDCD), Turkey, 2015.
[4] FILKA, R., BALAZOVIC, P., DOBRUCKY, B.: Transducerless Speed Control with Initial Position Detection for Low Cost PMSM Drives. Proceedings of 13th International Power Electronics and Motion Control Conference (EPE/PEMC 2008), Poland, 2008.

[5] BOJOI, R., PASTORELLI, J., BOTTOMLEY, J., GIANGRANDE, P., GERADA, C.: Sensorless Control of PM Motor Drives - A Technology Status Review. Proceedings of the IEEE 1st Workshop on Electrical Machines Design Control and Diagnosis (WEMDCD ‹13), France, 168–182, 2013.

[6] CONSOLI, A., SCARCELLA, G., TESTA, A.: Industry Application of Zero-Speed Sensorless control Techniques for PM Synchronous Motors. IEEE Transactions on Industry Applications, 37(2), 513 – 521, 2001.

[7] STULRAJTER, M., HRABOVCOVA, V., FRANKO, M.: Permanent Magnets Synchronous Motor Control Theory. Journal of Electrical Engineering, 58(2), 79 – 84, 2007.

[8] HRABOVCOVA, V., RAFAJDUS, P., FRANKO, M., HUDAK, P.: Measurements and Modeling of Electrical Machines. EDIS – Publishing house of University of Zilina, Zilina, 2004.

[9] RIBEIRO, L., DEGNER, W., BRITZ, F., LORENZ, R.: Comparison of Carrier Signal Voltage and Current Injection for Estimation of Flux Angle or Rotor Position. Proceedings of IEEE Industry Applications Conference, USA, 1998.

kOMUNikacie
COMMUNICATIONS

Roman Konarik - Michal Prazenica - Slavomir Kascak*

ENHANCED DIRECT CONVERTER WITH MINIMUM SWITCHING DEVICES AND VARIABLE CAPACITOR

The paper deals with a single-leg direct (matrix) converter with minimum switching devices and enhancements for improving current THD and phase advancing with the use of variable (switched) capacitors. This converter supplies single-phase induction motor (SPIM). Due to strongly non-harmonic phase voltages, an additional circuit should be used, so that phase-currents can be nearly harmonic. Simulations are done under both resistive-inductive load and motoric load. Speed control was realized using vector control with current controlled pulse-width-modulation (hysteresis regulator). Verification of such a drive system was done using dSpace environment. Preliminary results are given in the paper.

Keywords: one-leg matrix converter, bi-directional switch, single-phase induction motor - SPIM, speed control, pulse width modulation, switched capacitor

1. Introduction

The Single-phase induction motor - SPIM is widely used in a range of applications such as residential blowers, pumps, and compressors operated under fixed frequency. Using variable speed operation, this drive brings possible energy and money saving for consumers [1-3]. The motor can be supplied either from two single-phase or one three-phase VSI inverter [2, 4]. The matrix converter (MxC) topology has become well known after substitution of thyristor-devices in cyclo-converters by switched-off elements acting in the high-frequency range, in 70-80-years [5-7]. The MxC replaces two energy conversion by one energy conversion only because within the converter there is not an energy storage element. Since classical electric conversion uses DC-link converters with somewhat large smoothing capacitors, direct MxC operates without a DC-link circuit. One of the main advantages of that is unity power factor on its input side. Another advantage is that this converter generally offers sinusoidal input and output, harmonics quantity and bi-directional energy flow. To save some amount of power switching elements, it is possible to use the one-leg connection of the converters. The basic configuration of single-leg MxC was derived from single-leg voltage source inverter [1], [4], and for the first time was published in 2015, [5] with analysis and modeling [8]. Preliminary comparison of a SPIM Drive Fed by VSI and MxC with Option of Speed Reduction has been made in [9]. The proposed system, in relation to the conventional system currently used, reduces the number of power switching elements of the converter.

2. Single leg matrix converter

There are basically two different topologies of single-leg matrix converter derived from topologies of single-leg voltage source inverter [5], [9], Figure 1 and Figure 3. Similarly to single-leg voltage source inverter, single-leg matrix converter also works with two operation modes.

2.1 Topology of a single leg MxC fed single phase induction motor for full speed operation

Basic connection is given in Figure 1. Denotes R1, L1 and R2, L2 represent the phase windings of the motor.

In full speed regime of operation, the main phase of IM is supplied by one half of the main voltage directly; therefore, the motor should be designed for that voltage. The auxiliary phase is supplied by one-leg matrix converter creating voltage with phase shift by 90 degrees against voltage of the main phase.

The first operation mode can be called "Full speed operation." The main phase is fed by voltage source $U_{AC}/2$ and auxiliary phase is fed by a single leg MxC. As in the single leg, VSI using MxC is also necessary to sense phase of AC voltage source and ensure 90° phase shift for auxiliary phase.

It is necessary to be aware of that supply voltage for the auxiliary phase is strongly non-harmonic, Figure 2.

* **Roman Konarik, Michal Prazenica, Slavomir Kascak**
   Department of Mechatronics and Electronics, University of Zilina, Zilina, Slovakia
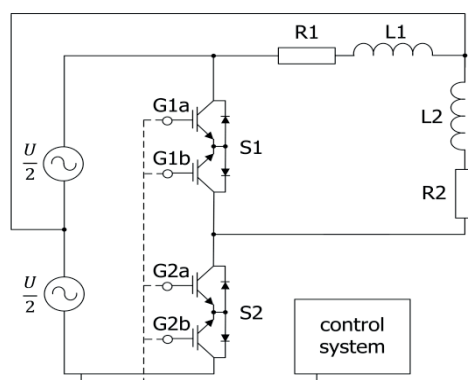   E-mail: roman.konarik@fel.uniza.sk

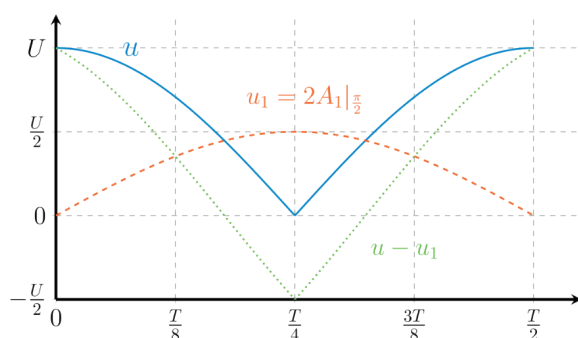Figure 1 *Single leg matrix converter topology for full speed operation*

Figure 2 *Supply voltage for auxiliary phase and its fundamental harmonic [8]*

Figure 3 *Single leg matrix converter topology for reduced operation*
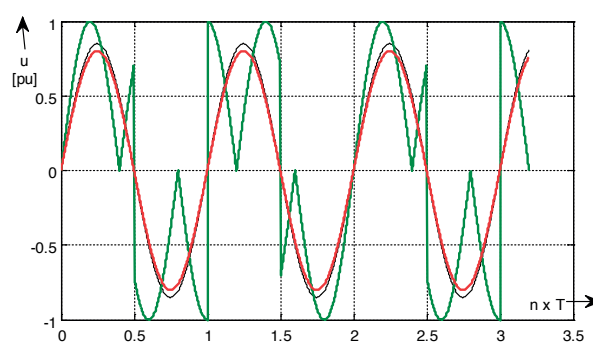
Figure 4 *Supply voltage of both phases with its fundamental harmonics in reduced speed regime at 33.33 Hz*

As the magnitude of fundamental harmonic is equal to one half of the network magnitude, the induction motor should be designed to that value of supply network voltage.

Besides, it is also important, that total harmonic distortion of the auxiliary phase voltage reaches up to 86 %, so the torque of the sum of higher harmonics will permanently brake, and start-up of the motor is practically impossible. Using some control method (e.g., hysteresis CC_PWM) the current shape will be good, but anyway, the value of the auxiliary phase voltage will be always smaller as the nominal one.

2.2 Topology of a single leg MXC fed single phase induction motor to reduce the speed operation

The second operation mode is also called "Reduced speed operation." Main and auxiliary phase is fed by single leg MxC, Figure 3. The speed of induction machine is given by the frequency of voltage. The phase shift is ensured by a capacitor connected in series with the auxiliary phase.

Similarly, as in the previous case, waveforms of supply voltages are still strongly non-harmonic ones, Figure 4.

So, it is necessary to accept some measures for improving the voltage and current, respectively, waveforms.

2.3 Using LC filters and switched capacitors for improvement of converter waveforms

Using resonant $L_{res}C_{res}$ filter in main and/or auxiliary phase and designed, e.g., by [10] the current waveform will be acceptable Figure 5 and Figure 6. The problem, maybe, could be regarding a higher voltage of the resonant capacitor and/or bigger dimensions of the filter element due to relatively smaller resonant frequency.

Another possibility is to use the non-resonant low-pass filter on the output of the converter. Results, as regarding to phase currents, are similar to those of resonant filter, Figure 7 and Figure 8.

Another problem is that under variable frequency the value of both capacitors, for phase shift and for resonance, should also be variable one. One of the solutions, how to provide this problem, is to use switching capacitors [11, 12]. Anyway, the number of electronic switches will be higher. There is shown acting of switching capacitance for controlled phase shift 90 deg., in Figure 9 and Figure 10.
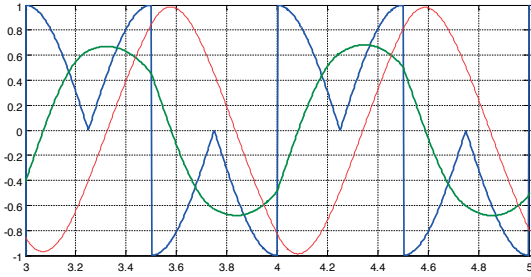
Figure 5 *Supply voltage (blue) and current (green) of auxiliary phase, and capacitor voltage (red) at nominal speed, 50 Hz – without PWM*
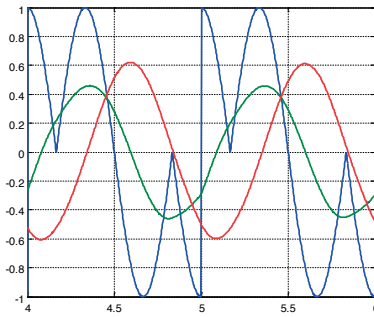
Figure 6 *Supply voltage (blue) and current (green) of main and auxiliary phases, and capacitor voltage (red) at reduced speed, 33.33 Hz – without PWM*
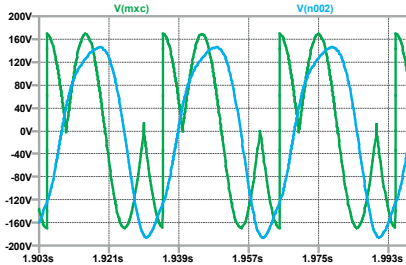
Figure 7 *Supply voltage (green) and voltage (blue) of main and auxiliary phases at reduced speed, 33.33 Hz – without PWM*
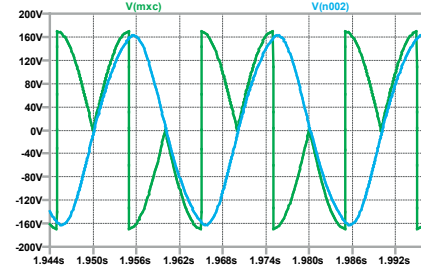
Figure 8 *Supply voltage (green) and voltage (blue) of main and auxiliary phases at full speed, 50 Hz – without PWM*
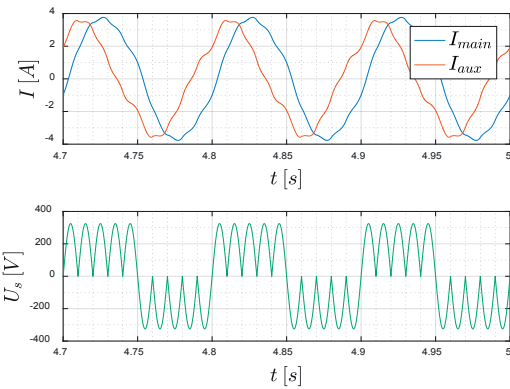
Figure 9 *Quadrature currents of single-phase induction motor at 10 Hz*
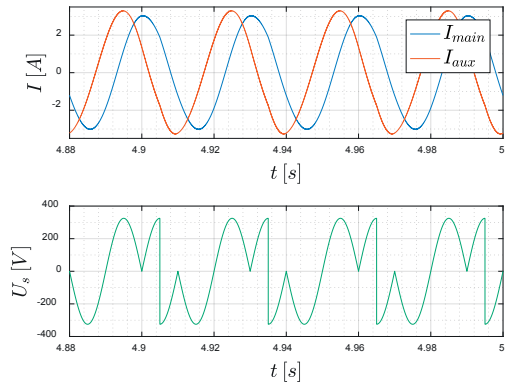
Figure 10 *Quadrature currents of single-phase induction motor at 33.33 Hz*

3. Single phase induction machine

3.1 Model of single phase induction motor

Model of such a motor is well known [1-4], [11]. So, the electric machine being considered may be described by the following set of ordinary differential equations in the stator reference coordinate frame under the commonly used simplifying assumptions:

$$u_{s\alpha} = R_{s\alpha} \cdot i_{s\alpha} + L_{s\alpha} \cdot \frac{di_{s\alpha}}{dt} + L_{M\alpha} \cdot \frac{di_{r\alpha}}{dt} \qquad (1)$$

$$u_{s\beta} = R_{s\beta} \cdot i_{s\beta} + L_{s\beta} \cdot \frac{di_{s\beta}}{dt} + L_{M\beta} \cdot \frac{di_{r\beta}}{dt} \qquad (2)$$

$$0 = R_{r\alpha} \cdot i_{r\alpha} + L_{s\alpha} \cdot \frac{di_{r\alpha}}{dt} + L_{M\alpha} \cdot \frac{di_{M\alpha}}{dt} + $$
$$+ \frac{1}{N} \cdot \omega_m \cdot (L_{r\beta} \cdot i_{r\beta} + L_{M\beta} \cdot i_{s\beta}) \qquad (3)$$

$$0 = R_{r\beta} \cdot i_{r\beta} + L_{r\beta} \cdot \frac{di_{r\beta}}{dt} + L_{M\beta} \cdot \frac{di_{s\beta}}{dt} - $$
$$- N \cdot \omega_m \cdot (L_{r\alpha} \cdot i_{r\alpha} + L_{M\alpha} \cdot i_{s\alpha}) \qquad (4)$$

$$T_e = pp \cdot [N \cdot (L_{r\alpha} \cdot i_{r\alpha} + L_{M\alpha} \cdot i_{s\alpha}) \cdot i_{r\beta} - $$
$$- \frac{1}{N} \cdot (L_{r\beta} \cdot i_{r\beta} + L_{M\beta} \cdot i_{s\beta}) \cdot i_{r\alpha}] \qquad (5)$$

$$T_e = T_{load} + J \cdot \frac{d\omega_m}{dt} \qquad (6)$$

where N is the ratio between the effective numbers of turns in the auxiliary and the main stator windings; ω_m - mechanical angular speed, and pp - is the number of pole pairs.
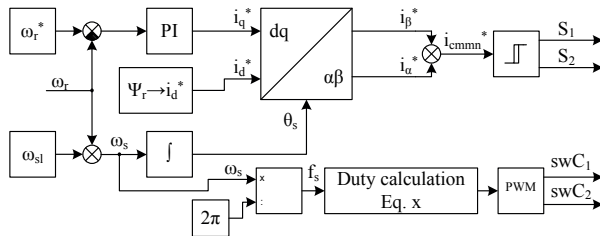
Figure 11 Block scheme of speed control of the drive with single-phase
induction motor and single-leg matrix converter

Figure 13 Quadrature currents of main and auxiliary phases main
(blue) and auxiliary (red) at reduced speed, 33.33 Hz – with PWM

a)
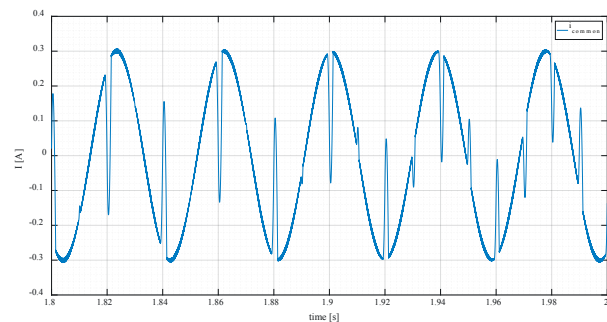
Figure 14 The current of both phases-common phase at reduced speed,
33.33 Hz – with PWM

b)

Figure 12 Block scheme: a) CC_PWM (hysteresis) control of the drive,
b) switched capacitor circuit

3.2 Speed control of a single-phase induction motor fed by single leg MXC

The basic control schematic is shown in Figure 11.

It deals with common vector control. Moreover, phase-shift of auxiliary phase is controlled by computation of duty cycle for the needed value of the running capacitor.

Current of common phase is controlled by CC_PWM (hysteresis) controller [13, 14], Figure 12.

4. Modeling and simulations

All simulations were calculated using the Matlab-Simulink package for source voltage 230 V_{RMS}, 50 Hz at full speed operation, a calculation step of 1e^{-5} sec.

Parameters of the single-phase motor:

Stator voltage 230 V

Stator resistance $R_{s\alpha}$ = 58.85 Ω; $R_{s\beta}$ = 66.1 Ω; R_r = 80 Ω

Stator inductance L_{sd} = 1.835 H; L_{sq} = 1.64 H

Mutual inductance between rotor and stator

M_{srd} = 1.74 H; M_{srq} = 1.52 H

Moment of inertia J = 0.0000488 kg.m2

Number of pole pairs pp = 1;

The capacitance of the capacitor in auxiliary phase C = 14.6 µF.

4.1 Simulations of a single-phase induction motor fed by single leg MxC with PWM only

Single-phase induction motor was fed by voltage waveform depicted in Figure 5 or Figure 6, respectively. Simulation result of phase currents waveforms are shown in Figure 13.

The current of common phase, i.e., current taking from the network is given in Figure 14.

4.2 Simulations of a single-phase induction motor fed by single leg MxC with PWM and resonant LC filter

Single-phase induction motor was fed by voltage as above, and the simulation result of both phase currents and common phase current are depicted in Figure 15 and Figure 16 are nearly harmonic ones.
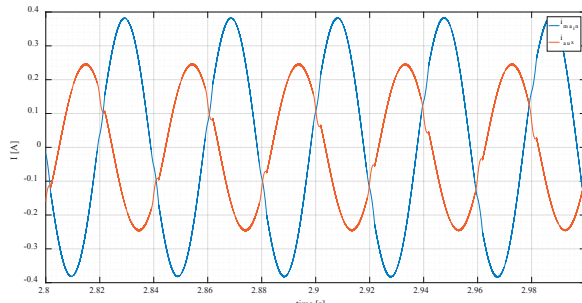
Figure 15 The current of both phases-common phase at reduced speed, 33.33 Hz – with PWM and resonant LC filter
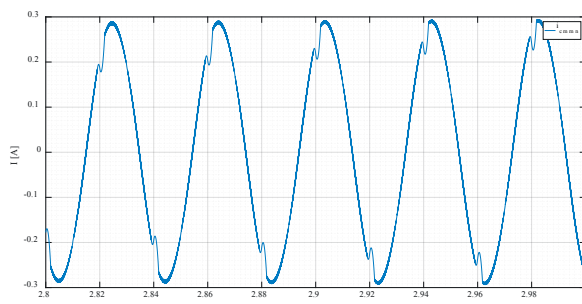
Figure 16 The common current of both phases reduced speed, 33.33 Hz – with PWM and resonant LC filter

Figure 17 Quadrature currents of main and auxiliary phases main (blue) and auxiliary (red) at full speed, 50 Hz – without PWM
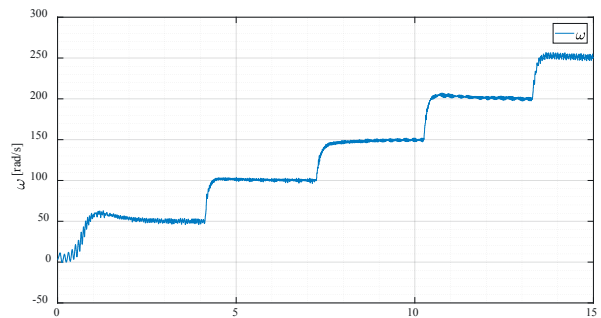
Figure 18 Step changes of angular speed

4.3 Simulations of a single-phase induction motor fed by single leg MxC at full speed without PWM

Single-phase induction motor was fed by the voltage from the network, therefore, waveforms of both voltage and currents depicted in Figure 17 are harmonic ones.

5. Verification using two-phase induction motor and controlled using dSpace

Single-phase induction motor, with parameters given in Chap. 4, was controlled through dSpace control system.
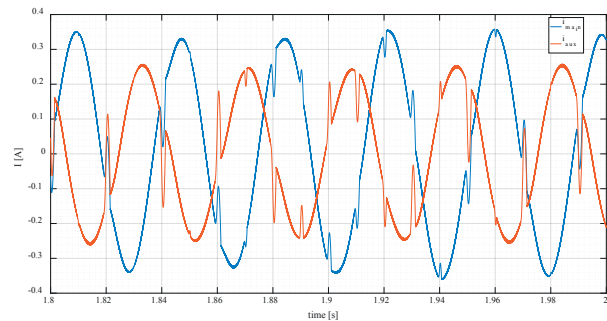
Speed control of single-phase induction motor fed by single leg MxC, including start-up, was realized by the setting of requested angular speed to 50 rad/sec, consequently after start-up 100 rad/sec, and then 150, 200 and 250 rad/sec, respectively. Time dependence of measured angular speed is shown in Figure 18. Corresponding currents of main and auxiliary phases are given in Figure 19.

The detailed corresponding common current of both phases of the single-phase induction motor is depicted in Figure 19. The voltage waveforms of switched capacitors switching frequency

(5kHz) are depicted in Figure 20 and the value of the voltage for each capacitor depends on the duty cycle.

In Figure 21 are depicted details of phase current of single phase induction machine. It can be seen in the figures that the currents are almost harmonic.

6. Conclusion

The paper brings simulation and experimental result of single-phase motor drive that consists of single-phase induction motor fed by enhanced single leg MxC with switched capacitors.

Simulations were done with both resistive-inductive load and motoric load. Due to strongly non- harmonic phase voltages the additional circuits were implemented and investigated: resonant LC filter and/or low-pass filter, respectively. Accepting mentioned measures, the phase-currents are nearly harmonic. It is very important from the point of view of the influence of the supply network.

As can be seen in the Figure 14 and Figure 16 respectively, the common phase current taken from the network is nearly sinusoidal with the harmonic time waveform. This is one of the advantages of the described drive system. Another advantage is minimum active switching devices, because the single-leg
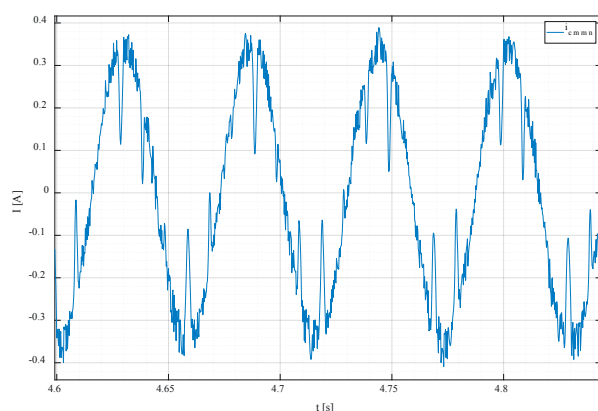
Figure 19 Detail of the common current of main and auxiliary phases
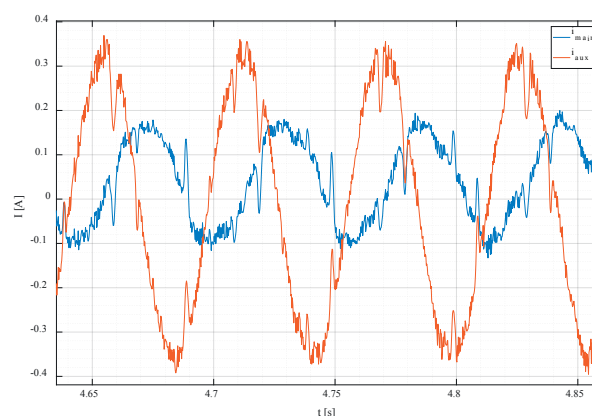
Figure 21 Detail of the currents of main and auxiliary phases main (blue) and auxiliary (red)
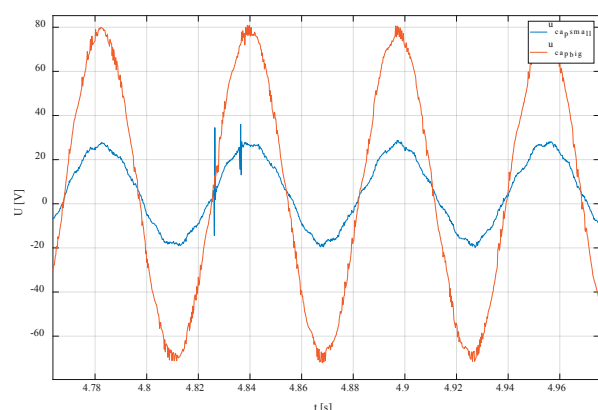
Figure 20 Detail of capacitor voltages: a small capacitor (blue) and a large capacitor (red) at capacitor switching frequency of 5kHz

matrix converter in basic connection topology needs just two bidirectional switches. But for the demanded vector control it is necessary to use a switched capacitor to maintenance 90 deg phase-shift in whole speed range under a no-load and nominal load of the motor. Application of the switched capacitors brings the possibility of a wider range of angular speed and improvement of the electromagnetic torque. The switching frequency of the capacitors direct impacts the voltage ripple on the capacitors.

The novelty of the paper is also in speed control that was realized using adapted vector control with current controlled pulse width modulation (hysteresis regulator). Verification of such a drive system was done using dSpace environment. The results showed the good behavior of the motor. Experimental verification was realized without additional LC circuit, so far. Future work can be focused on selecting the proper type of the filter, its optimal design. Also, selecting the right value of capacitor for the auxiliary phase is important. Modern control method, torque and angular speed ripple reduction, and so on, can be used.

References

[1] CHOMAT, M., LIPO, T. A.: Adjustable-Speed Single-Phase IM Drive with Reduced Number of Switches. IEEE Transactions on Industry Applications, 39(3), 819-825, 2003.

[2] BENEDICT, E. R., LIPO, T. A.: Improved PWM Modulation for a Permanent-Split Capacitor Motor. Conference Record of International IEEE-IAS Annual Meeting, Italy, 2004-2010, 2000.

[3] WU, M., LU, D. D-CH.: Active Stabilization Methods of Electric Power Systems with Constant Power Loads. A Review. Journal of Modern Power Systems and Clean Energy, 2(3), 233-243, 2014.

[4] VODOVOZOV, V., LILLO, N., RAUD, Z.: Single-Phase Electric Drive for Automotive Applications. Proceedings of International Symposium on Power Electronics. Electrical Drives, Automation and Motion (SPEEDAM'14), Italy, 2014.

[5] DOBRUCKY, B., LASKODY, T., PRAZENICA, M.: A Novel Supply System for Two- Phase Induction Motor by Single Leg Matrix Converter. Elektronika ir elektrotechnika, 21(4), 13-16, 2015.

[6] ZUCKERBERGER, A., WEINSTOCK, D. ALEXANDROVITZ, A.: Single-Phase Matrix Converter. IEE Proceedings - Electric Power Applications, 144(4), 235-240, 1997.

[7] JEEVANANTHAN, S., DANANJAYAN, P., MADHAVAN, R.: Novel Single-Phase to Single-Phase Cyclo-Conversion Strategies. Mathematical and Simulations Studies. International Journal of Power and Energy Systems, 27(4), 414-423, 2004.

[8] STEFANEC, P., DOBRUCKY, B.: One Leg MxC Analysis and Modelling. Proceedings of International Conference on Electrical Drives and Power Electronics (EDPE), Slovakia, 2015.

[9] LASKODY, T., DOBRUCKY, B., STEFANEC, P., PRAZENICA, M.: Comparison of a Single-Phase Induction Motor Drive Fed by VSI and MxC with Option of Speed Reduction. Proceedings of International Conference on Electrical Drives and Power Electronics (EDPE), Slovakia, 2015.

[10] KONARIK, R., DOBRUCKY, B., STEFANEC, P.: Improved Two-Phase One-Leg Matrix Converter Using L-C Filter. Proceedings of International Conference on Mechatronics, Control and Automation Engineering (ICAMM 2016), Thailand, 2016.

[11] LETTENMAINER, A., NOVOTNY, D., LIPO, T. A.: Single-Phase Induction Motor with an Electronically Controlled Capacitor. IEEE Transactions on Industry Applications, 27(1), 38-43, 1988.

[12] DANILA, A., MARGINEANU, I., CAMPEANU, R., SUCIU, C., BOIAN, I.: The Optimization of the Single/Two Phase Induction Motor Start-Up with Electronically Switched Capacitor. Proceedings of IEEE International Conference on Automation, Quality and Testing, Robotics (AQTR'08), Romania, 450 – 453, 2008.

[13] GONG, W., HU, S., SHAN, M., XU, H.: Robust Current Control Design of a Three-Phase Voltage Source Converter. Journal of Modern Power Systems and Clean Energy, 2(1), 16-22, 2014.

[14] KASCAK, S., LASKODY, T., PRAZENICA, M., KONARIK, R.: Current Control Contribution to a Single-Phase Induction Motor Fed by Single-Leg VSI Inverter. Proceedings of International Conference ELEKTRO 2016, Slovakia, 172-172, 2016.

Matus Danko - Michal Taraba - Juraj Adamec - Peter Drgona*

VISUALIZATION OF SKODA INSTRUMENT CLUSTER

Most signals in modern vehicles which are transmitted from sensors to control units or actuators are transmitted via bus. The most common automotive data bus is Controller Area Network(CAN). Some of transmitted signals are speed of the vehicle, engine speed and coolant temperature which are used for visualization of Skoda Octavia instrumental cluster. For this visualization, CAN BUS communication is filtered and processed, to obtain three message objects to observe required data. For data acquisition from bus is used modular system CompactRio with module for CAN BUS from National Instruments. The whole application is created in visual programming language LabVIEW using FPGA module.

***Keywords:** CAN, CAN BUS, Skoda instrument cluster, CompactRIO*

1. Introduction

At the end of 80´s German company Robert Bosh GmbH proposed data communication network called CAN (Controller Area Network). The original intention was transmission of information between sensors, control units and power components of the car and saving cabling. With development of electronics in vehicles arise requirement to divide systems of car to specific section by reliability and usefulness. Communication between these systems is necessary to monitor their function, setting of parameters, calibration and in first place, distribution of data which are no longer only simple binary or analog values.

2. CAN BUS

2.1 Layered structure

The object layer of CAN BUS is concerned with message filtering as well as status and message handling [1].

The transfer layer represents the kernel of the CAN protocol. It represents messages received to the object layer and accepts messages to be transmitted by the object layer. The transfer layer is responsible for bit timing and synchronization, message framing, arbitration, acknowledgement, error detection and signaling, and fault confinement [1].

The physical layer defines how signals are transmitted. The physical layer is not defined here, as it will vary according to the requirements of individual applications (for example, transmission medium and signal level implementations) [1].

2.2 Message routing

The content of a message is described by an identifier. The Identifier does not indicate the destination of the message, but describes the meaning of the data, so that all nodes in the network are able to decide by message filtering whether the data is to be acted upon by them or not. Within a CAN network, it is guaranteed that a message is accepted simultaneously either by all nodes or by no node. Thus, data consistency is a property of the system achieved by the concepts of multicast and by error handling [1].

2.3 Arbitration

Whenever the bus is free, any node may start to transmit a message. If two or more nodes start transmitting messages at the same time, the bus access conflict is resolved by bit-wise arbitration using the Identifier. The mechanism of arbitration guarantees that neither information nor time is lost. If a Data frame and a Remote frame with the same Identifier are initiated at the same time, the Data frame prevails over the Remote frame. During arbitration (Figure 1), every transmitter compares the level of the bit transmitted with the level that is monitored on

* **Matus Danko, Michal Taraba, Juraj Adamec, Peter Drgona**
  Department of Mechatronics and Electronics, Faculty of Electrical Engineering, University of Zilina, Slovakia
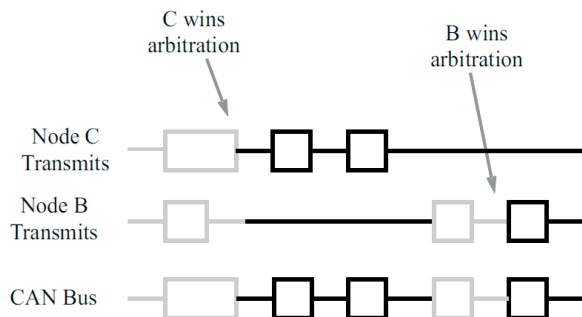 E-mail: matus.danko@fel.uniza.sk

Figure 1 *Arbitration on a CAN Bus [2]*

Figure 2 *Standard data frame [2]*
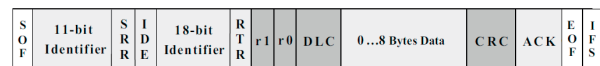
Figure 3 *Extended data frame [2]*

the bus. If these levels are equal the node may continue to send. When a recessive level is sent, but a dominant level is monitored, the node has lost arbitration and must withdraw without sending any further bits [1].

3. Frame types of CAN BUS

Message transfer is manifested and controlled by four different frame types:

- A Data frame carries data from a transmitter to the receivers.
- A Remote frame is transmitted by a bus node to request the transmission of the Data frame with the same Identifier.
- An Error frame is transmitted by any node on detecting a bus error.
- An Overload frame is used to provide for an extra delay between the preceding and the succeeding Data or Remote frames [2].

3.1 Data frame

A Data frame is composed of seven different bit fields: Start of the frame, Arbitration field, Control field, Data field, CRC field, ACK field, End of the frame. The Data field can be of length zero [1].

The meanings of the bit fields of Figure 2 are:
- SOF - The single dominant start of frame (SOF) bit marks the start of a message, and is used to synchronize the nodes on a bus after being idle.
- Identifier-The Standard CAN 11-bit identifier establishes the priority of the message. The lower the binary value, the higher its priority.
- RTR - The single remote transmission request (RTR) bit is dominant when information is required from another node. All nodes receive the request, but the identifier determines the specified node. The responding data is also received by all nodes and used by any node interested. In this way, all data being used in a system is uniform.

- IDE - A dominant single identifier extension (IDE) bit means that a standard CAN identifier with no extension is being transmitted.
- r0 - Reserved bit (for possible use by future standard amendment).
- DLC - The 4-bit data length code (DLC) contains the number of bytes of data being transmitted.
- Data - Up to 64 bits of application data may be transmitted.
- CRC - The 16-bit (15 bits plus delimiter) cyclic redundancy check (CRC) contains the checksum (number of bits transmitted) of the preceding application data for error detection.
- ACK - Every node receiving an accurate message overwrites this recessive bit in the original message with a dominate bit, indicating an error-free message has been sent. Should a receiving node detect an error and leave this bit recessive, it discards the message and the sending node repeats the message after rearbitration. In this way, each node acknowledges (ACK) the integrity of its data. ACK is 2 bits, one is the acknowledgment bit and the second one is a delimiter.
- EOF - This end-of-frame (EOF), 7-bit field marks the end of a CAN frame (message) and disables bit-stuffing, indicating a stuffing error when dominant. When 5 bits of the same logic level occur in succession during normal operation, a bit of the opposite logic level is stuffed into the data.
- IFS - This 7-bit interframe space (IFS) contains the time required by the controller to move a correctly received frame to its proper position in a message buffer area [2].

As shown in Figure 3, the Extended CAN message is the same as the Standard message with the addition of:
- SRR - The substitute remote request (SRR) bit replaces the RTR bit in the standard message location as a placeholder in the extended format.
- IDE - A recessive bit in the identifier extension (IDE) indicates that more identifier bits follow. The 18-bit extension follows IDE.
- r1 - Following the RTR and r0 bits, an additional reserve bit has been included ahead of the DLC bit [2].
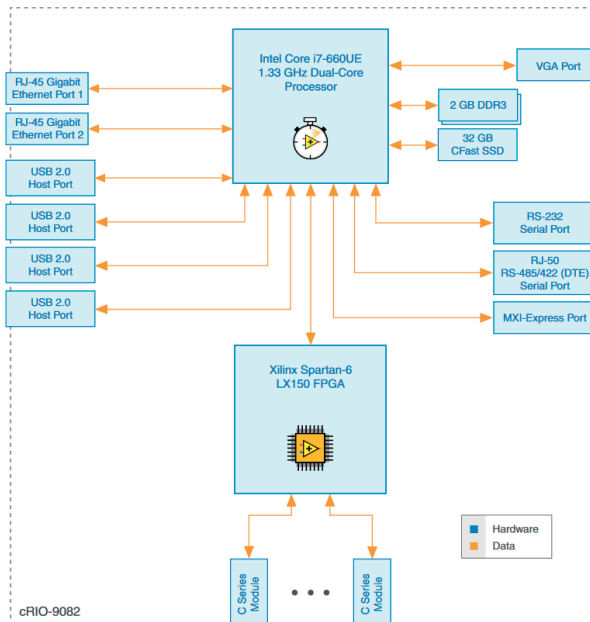
Figure 4 *NI cRIO 9082 Hardware overview*

Figure 5 *NI 9853 Hardware overview[5]*

3.2 Remote frame

The intended purpose of the remote frame is to solicit the transmission of data from another node. The remote frame is similar to the data frame, with two important differences. First, this type of message is explicitly marked as a remote frame by a recessive RTR bit in the arbitration field, and secondly, there is no data [2].

3.3 Error frame

The error frame is a special message that violates the formatting rules of a CAN message. It is transmitted when a node detects an error in a message and causes all other nodes in the network to send an error frame as well. The original transmitter then automatically retransmits the message. An elaborate system of error counters in the CAN controller ensures that a node cannot tie up a bus by repeatedly transmitting error frames [2].

3.4 Overload frame

The overload frame is mentioned for completeness. It is similar to the error frame with regard to the format, and it is transmitted by a node that becomes too busy. It is primarily used to provide an extra delay between messages [2].

4. Used hardware

4.1 NI cRio 9082

The high-performance multicore NI cRIO-9082, block schematic shown on Figure 4, provides advanced Intel Core i7 dual-core processing, built-in VGA display output for an integrated user interface, and the option to use a Microsoft Windows Embedded Standard 7 (WES7) or LabVIEW Real-Time OS. The increased processing power of the cRIO-9082 makes it well suited to perform the advanced processing tasks required by complex applications such as machine vision and rapid control prototyping. Choose LabVIEW Real-Time to take advantage of deterministic execution and the highest degree of reliability in continuous operation environments. The high-performance multicore cRIO-9082 also offers the widest array of connectivity and expansion options available in the CompactRIO platform, including the high-bandwidth and low-latency MXI-Express bus for expansion using the 14-slot MXI-Express RIO chassis [3, 4].

4.2 NI 9853

The NI 9853 has two 9-pin male D-Sub connectors that provide connections to a CAN bus. Each port on the NI 9853 has pins for CAN_H and CAN_L, to which you connect the CAN bus signals. Each port has two common pins (COM) that are internally connected to the module's isolated reference and serve as the reference ground for CAN_H and CAN_L. You can connect the CAN bus reference ground (sometimes referred to as CAN_V-) to one or both COM pins. The port also has an

Table 1 Meaning of LED

LED	SD Card Slot	Description
Present (Card 0), Green	SD Card Slot 0	This LED is lit when an SD Card is in Slot 0 and the SD Card slot door is closed.
Busy (Card 0), Yellow	SD Card Slot 0	This LED is lit when the card in Slot 0 is active. This LED is flashing when the NI 9802 is performing I/O on the card in Slot 0. Do not remove the SD Card while this LED is lit or flashing.
Present (Card 1), Green	SD Card Slot 1	This LED is lit when an SD Card is in Slot 1 and the SD Card slot door is closed.
Busy (Card 1), Yellow	SD Card Slot 1	This LED is lit when the card in Slot 1 is active. This LED is flashing when the NI 9802 is performing I/O on the card in Slot 1. Do not remove the SD Card while this LED is lit or flashing.
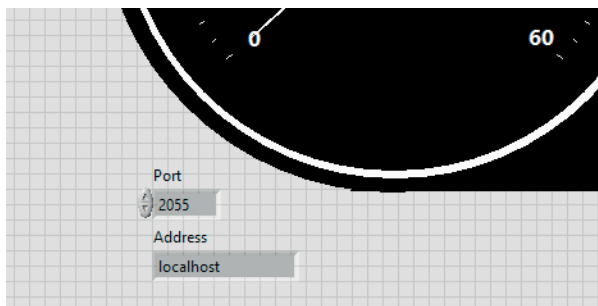
Figure 6 Visualization of the cluster by TCP with extra control
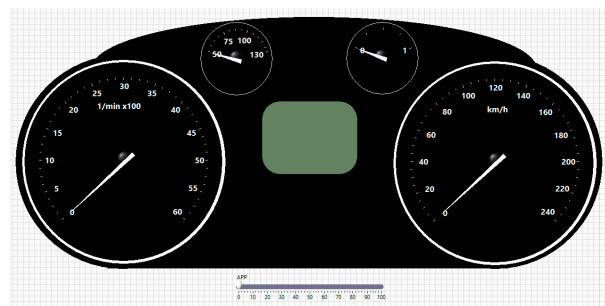
Figure 7 Visualization of Skoda instrument cluster

optional shield pin, SHLD, that you can connect to a shielded CAN cable. Connecting SHLD may improve signal integrity and EMC performance in a noisy environment [5].

CAN0 of the NI 9853 is internally powered (Figure 5), and therefore requires no external power supply. CAN1 requires an external power supply of +8 to +25 V to operate. Supply power to the V_{SUP} pin of CAN1 from the CAN bus [5].

4.3 NI 9802

The NI 9802 is an SD Card storage module that can read from and write to SD Cards. The NI 9802 has two SD Card slots into which you can insert NI-approved SD Cards. The card slots each have a door to protect the SD Cards while in the module. Each door is connected to a switch that indicates to the NI 9802 software when it is safe to read from or write to the SD Card. The NI 9802 has four LEDs that indicate which slots contain an SD Card and if the SD Card is active. Refer to Table 1 for descriptions of each of the LEDs on the NI 9802 and when it is safe to remove SD Cards from the NI 9802 [6].

5. CAN BUS analysis

The whole application is created in visual programming language LabVIEW using FPGA module. The project has four programs, first is for data acquisition from CAN BUS. At start of the program, it is necessary to set up delay for transmitter and receiver initialization and CAN BUS speed for each port. CAN BUS speed can be set in two different ways. The first way is by setting the speed in the configuration of NI 9853. The second way is by setting of the speed through constant for bit timing register. In the second program, received data from CAN BUS are saved as local variables for next processing. The last two programs processing local variables for visualization and transferring data by TCP protocol on other devices such as touch panel. Visualization on other devices through TCP/IP has two extra controls (Figure 6), IP address of the source and port [7-9].

For visualization of instrument cluster from Skoda vehicle (Figure 7) three messages of CAN communication are filtered, which are further processed. Compared to the physical cluster our visualization of the cluster does not display mileage and fuel gauge because these signals are not sent by CAN BUS.

The first CAN message contains data for speedometer and accelerator pedal position. As mentioned above, CAN BUS can transmit only eight-bit number, this means 255. If there is needed a value greater than this number, it is necessary to use more than one eight-bit number. For RPM, the second byte is used as lower eight bits and the third byte as upper eight bits. Real RPM is the result of division by four after joined of these upper and lower eight bits. The seventh byte is used for displaying accelerator position in percent.
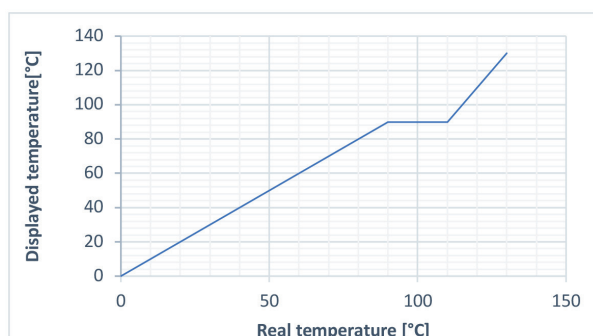
Figure 8 The non-linearized curve of the temperature gauge

Third CAN message is needed to get the speed of the vehicle. For data of RPM, two bytes, second and third are used. After joining, the result is divided by 100.

The first bit of the second CAN message contains information about the temperature of the coolant. To get the right range of temperature, division by ¾ and subtraction 48 is necessary, due to the fact, that the temperature of coolant can be below zero. Next step in data processing is nonlinearization of temperature gauge as a physical gauge so we can't see hysteresis of the thermostat.

Temperature displayed on gauge up to 90 °C is real, range from 90 °C to 110 °C, which is operating temperature of the engine is displayed as 90 °C, from 110 °C is temperature curve nonlinearized as shown in Figure 8.

6. Conclusion

The main purpose of this paper was to design highly sophisticated CAN BUS analyzer using powerful CompactRIO with dual-core processor and FPGA, a module for CAN BUS and module for SD Cards for data logging. Data from CAN BUS are acquired every 10 or 20ms and processed for visualization of Skoda Octavia II instrument cluster. RPM, the speed of the vehicle, coolant temperature and positions of accelerator pedal are processed data, yet. Data processing for other indicators are possible except fuel gauge because the signal of fuel level is transferred analog.

Acknowledgment

References

[1] Freescale Semiconductor, Inc., Bosch Controller Area Network (CAN) Version 2.0.

[2] Texas isntrument, Introduction to the Controller Area Network (CAN), 2008.

[3] National instruments, Getting started guide NI cRIO-9082, 2016.

[4] National instruments, User manual NI cRIO-9082, 2016.

[5] National instruments, Getting started guide NI 9853, 2015.

[6] National instruments, Operating instruction and specification NI 9802, 2009.

[7] KONIAR, D., HARGAS, L., SIMONOVA, A., HRIANKA, M., LONCOVA, Z.: Virtual Instrumentation for Visual Inspection in Mechatronic Applications, Procedia Engineering (Modelling of Mechanical and Mechatronic Systems), 96, 227 – 234, 2014.

[8] SPANIK, P., HARGAS, L., HRIANKA, M., KOZEHUBA, I.: Application of Virtual Instrumentation LabVIEW for Power Electronic System Analysis. Proceedings of the 12th International Power Electronics and Motion Control Conference (EPE-PEMC 2006), Slovenia, 1699-1702, 2006.

[9] HARGAS, L., KONIAR, D., STOFAN, S.: Sophisticated Biomedical Tissue Measurement Using Image Analysis and Virtual Instrumentation, LabVIEW Practical Applications and Solutions. Chapt. 8. Ed: FOLEA, S. InTech, Rijeka, p. 155-180, 2011.

kOMUNIKáCIE
COMMUNICATIONS

Milan Sebok - Miroslav Gutten - Juraj Adamec - Adam Glowacz - Jerzy Roj*

ANALYSIS OF THE ELECTRONIC FUEL INJECTOR OPERATION

The paper deals with research results of electronic fuel system injection (FSI) and its possible measurement for diagnostic analysis. In the parts of the paper the design and operation of a typical fuel injection system is described and its electronic part is analysed. The procedure for the detection of the injector malfunction based on the analysis of differential current characteristic has also been proposed. In the end the differences in the electrical parameters of the individual fuel injectors on the based comparison of reference and failure current are shown.

Keywords: electronic fuel injector, diagnostics, measurement, current characteristic analysis

1. Introduction

Electronic fuel injector is an important part of the engine gasoline fuel system. The fuel injector is a solenoid valve. Forces which act on the active injector core are caused by friction, spring tension and fuel pressure. Rising current curve is partially different from the curve of an ideal inductor current [1].

The effect which causes a change of permeability is caused by the movement of the needle valve. Injector opening time is visible on the current characteristics and the closing time – on the voltage characteristics. Stopping the movable element of the injector is seen as disturbance on the measured characteristics [2].

2. Principle of the electronic fuel injector operation

Electronic fuel injector is an electromagnetic valve. Its internal structure is shown in the Figure 1. The basic part of the valve is armature, needle valve, iron core, electromagnetic coil and returning spring. Before injection, the needle valve is compressed tightly on the fuel needle valve pedestal by spring and fuel. Electromagnetic force provided by injection coil is greater than spring force fuel pressure and friction force. When the current flows through the coil, then the needle valve opens upward, the electronic fuel injector sprays once. When in the injector coil power is turned off, under spring force effect, the needle valve

electromagnetic force decreases rapidly. The needle valve starts closing, then an injection process will be finished [3, 4].

3. Measuring system for determining the current and voltage characteristics of the fuel injectors

Figure 2 shows block diagram of the measuring system for gasoline injectors. The main component of the electronic control device is a programmable controller, which is designed to open and close the transistors. Injectors are connected to the collectors of these transistors. Five buttons keypad allows setting the transistors opening time. LCD display shows the current mode.

To test the operation of the injection system and track the required signals, we have designed a test device to control the injector intake valves of the spark-ignition engine. The control of the electronics is analogous to the signal generator.

The pressure vessel makes it possible to create a liquid pressure (replacing the fuel pump) in the range of 0 to 300 kPa (Figure 3), which corresponds to the fuel pressure in the automobile. From a pressure vessel, the liquid is brought to a common pipe to which all the injectors are attached.

Vessel flow measuring vessels are placed under individual injectors. They allow to determine differences in the amount of injected fuel by individual injectors and injector flow.

The measured current and voltage characteristics show the deviations from the ideal state. Movement of the core, which

* ¹**Milan Sebok,** ¹**Miroslav Gutten,** ²**Juraj Adamec,** ³**Adam Glowacz,** ⁴**Jerzy Roj**
  ¹Department of Measurements and Applied Electrical Engineering, Faculty of Electrical Engineering, University of Zilina, Slovakia
  ²Department of Mechatronics and Electronics, Faculty of Electrical Engineering, University of Zilina, Slovakia
  ³Computer Science and Biomedical Engineering, Faculty of Electrical Engineering, Automatics, AGH University of Science and Technology, Krakow, Poland
  ⁴Faculty of Electrical Engineering, Silesian University of Technology, Gliwice, Poland
  E-mail: gutten@fel.uniza.sk
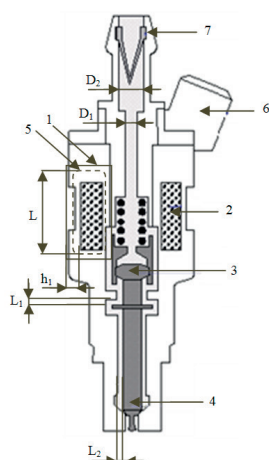
Figure 1 *Construction of an electronic fuel injector [5]: 1-iron core, 2-electromagnetic coil, 3-armature, 4-needle valve, 5-yoke of magnet, 6- electrical connection, 7-filter*
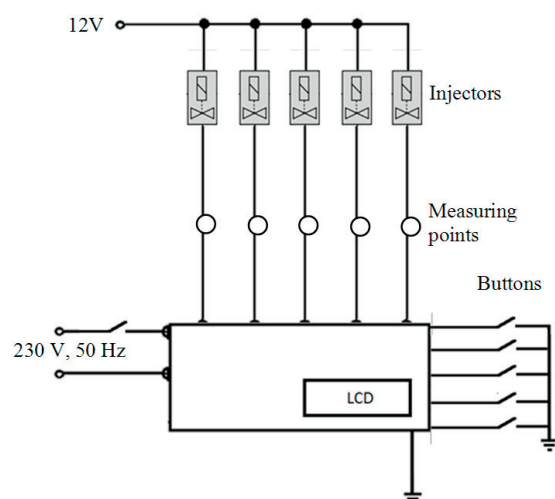
Figure 2 *Block diagram of the measuring system*

Figure 3 *Testing device*

Figure 4 *Fuel injector voltage and current characteristics*

causes the inductance change, affects the current and voltage characteristics.

The measurement results shown in Figure 4 were divided into a few intervals. The interval A is the injector inaction, B refers to moving the injector core, C is the injection action with the current increasing, D is the injector in operation, E refers to the overvoltage caused by the inductance of the injector (moving core injector to the initial position), F is the fading overvoltage and G is the injector inaction [6].

The time required to open the 12-16 ohm injector is about 1.5 ms. This time is depending on the fuel pressure, injector spring force, inertial core properties, electromagnetic coil, core and injector material. The time required to close the injector is only half of the opening time. Closing of the injector is executed by spring and fuel pressure only.

4. Current characteristic analysis

In Figure 5a are shown the measured characteristics of the reference current and failure current. The reference current time behaviour is composed of five measurements with the fluid under pressure at 2.5 bar.

Sampling value on oscilloscope has been set to 100 kS/s (time between the samples is 10 μs). The injection time has been set to 5 ms. Characteristic of the failure current was obtained by stopping the needle valve in the open position.

The difference between the reference and fault currents is shown in Figure 5b. On this characteristic can be seen two extremes. One is in 650 μs (for current: 64 mA) and the second is in 1460 μs (for current: -180 mA).

Figure 6 shows the current characteristics for another, often occurring movement problem of the injector valve needle. In this case the needle valve solely moves in the top portions of its
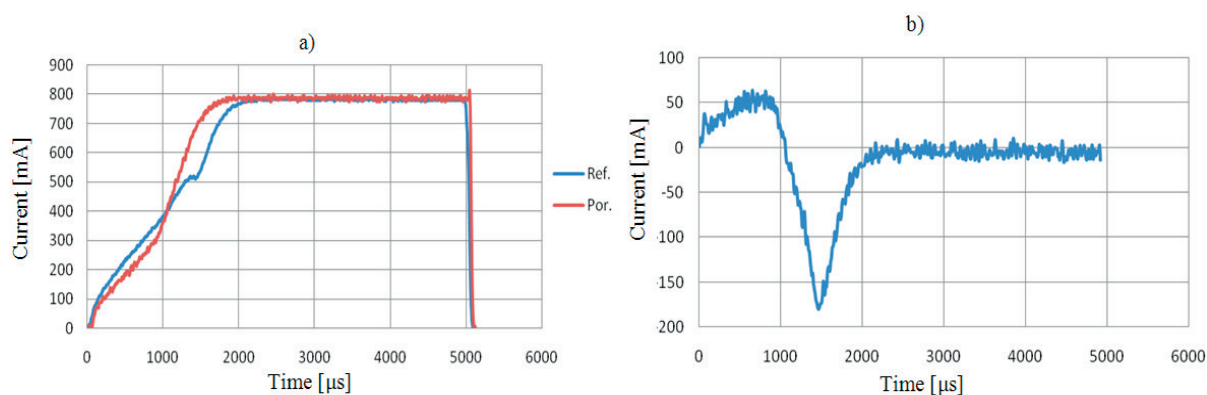
Figure 5 Reference injector current and the current at standstill needle valve in the open position: a) referent and failure currents, b) their difference
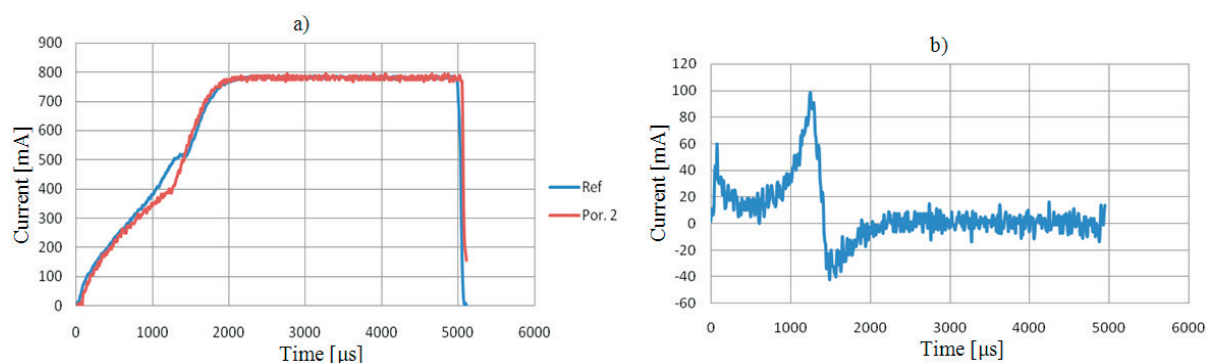
Figure 6 Reference injector current and the partial movement current of the needle valve: a) referent and failure currents, b) their difference
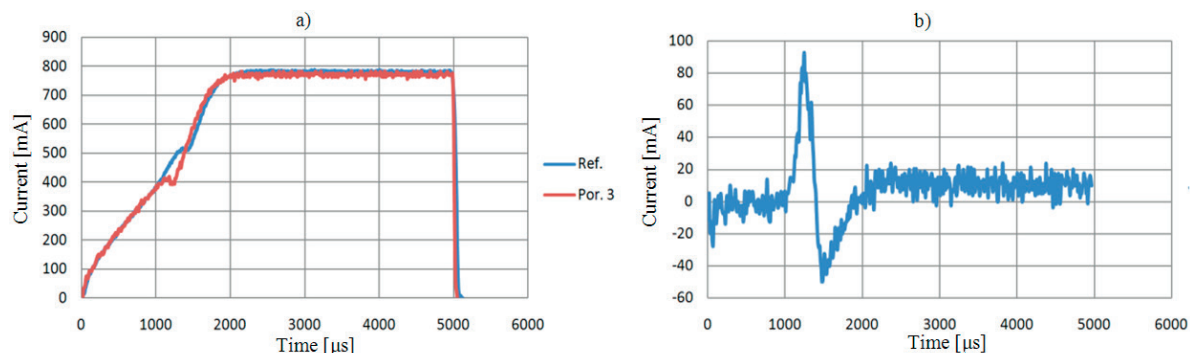
Figure 7 Reference injector current and current at a fuel zero pressure: a) referent and failure currents, b) their difference

moveable sector. The difference between the reference and failure currents again shows the extremes. The first one is marginal for diagnostics of fuel injector. Two others are in 1250 µs (for current: 100 mA) and in 1490 µs (-43 mA).

Reduction of the fluid pressure shortens the time necessary to open the fuel injector. This is illustrated by the measurement results shown in Figure 7. On the differential characteristic, again could be seen two extremes, in 1250 µs (for current: 92.5 mA) and in 1480 µs (-50 mA).

There are many types of fuel injectors. The difference is mostly in arrays of injection quantity and in a way of injection (e.g. Figure 8). There are differences by the fuel injector of the same type too. We obtain differences in the characteristics of four fuel injectors from the same car. Measurement results are visible in Figure 9 [7].

5. Discussion

In the Figure 10a is visible the influence of the fuel pressure changes on current characteristics. The pressure was increased from 0 to 2.6 bar (260 kPa).
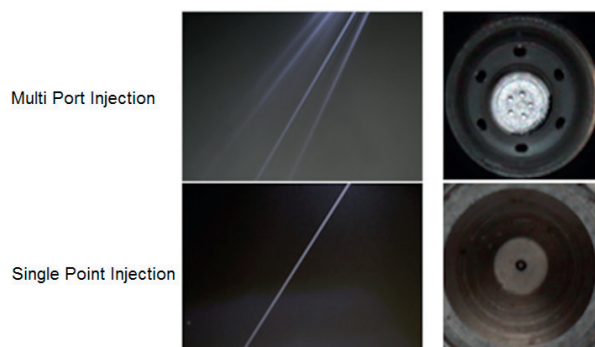
Figure 8 *Differences in the injection for different types of injectors*
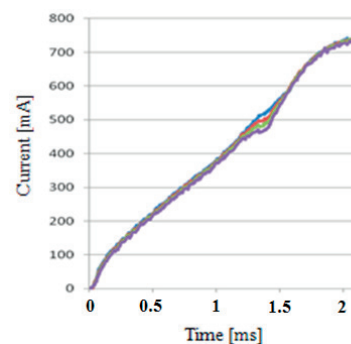
Figure 9 *Differences in current characteristics for the same type of the injectors*
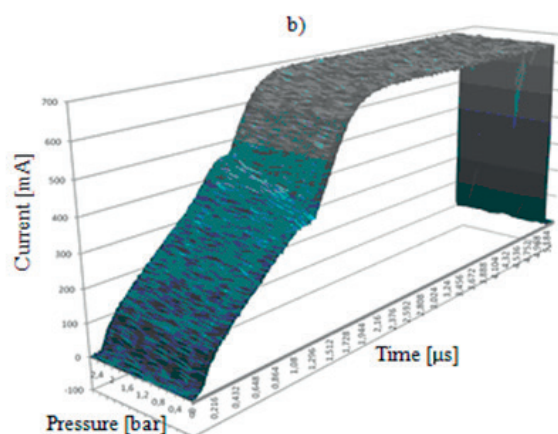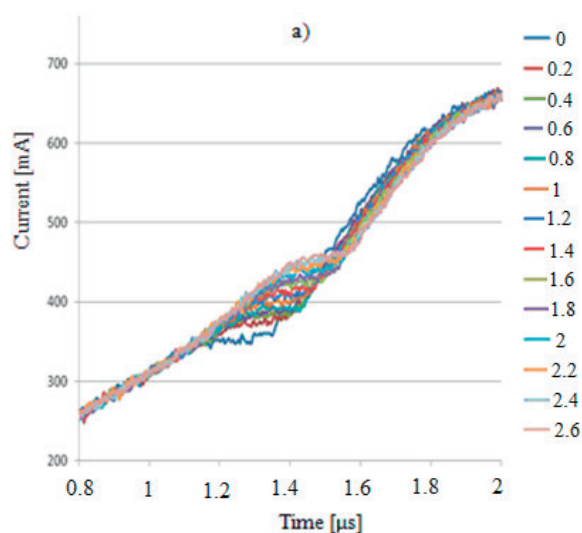
Figure 10 *Effect of fuel pressure changes on the current characteristics: a) 2d chart, b) 3d chart*
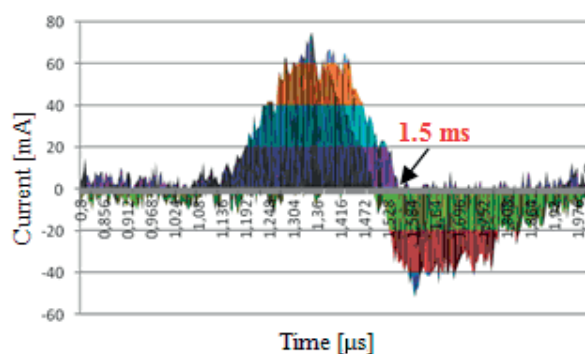
Figure 11 *Current waveform during the fuel pressure drop*
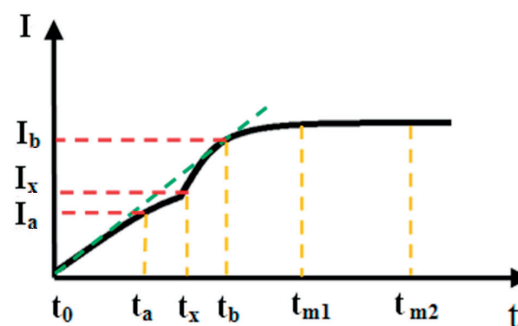
Figure 12 *Current characteristic with marked moments of time in which the current measurement allows to determine the state of the injector system*

Subtracting the reference signal from the chart shown in Figure 10b allows obtaining a differential signal, which may be treated as a fault signal or a fault decomposition.

The exemplary fault decomposition is illustrated in Figure 11. As the cause of failure is assumed the fuel pressure drop caused by, for example, inactive hot pump, choked fuel filters, damaged tubes and eventually corrupted regulator pressure. The time to open the fuel injector is approximately 1.5 ms.

6. Conclusion

Figure 12 shows the idealized timing chart of the current during the fuel injector operation. Some characteristic moments of time and the corresponding current values have been marked on it which can be useful for determining the state of the injection system. It is possible to determine the opening time of the fuel injector by monitoring the t_x time. This time had influence on the pressure ratios of fuel jet and assembled the solution of the injector. It is possible to determine the fault fuel pressure by evaluating these times or determining the damage of reversible springs of the fuel injector. Implementing measurement in the times t_{m1} and t_{m2}, allows to obtain the maximum current.

The fuel injectors have many differences resulting from the production technology. It causes difference in the injector voltage and current characteristic. In order to detect the fault state, it is needed to use self-learning process, by the use of an appropriate self-learning algorithm. Such issues will be described in the next paper.

Acknowledgments

References

[1] TRAISTARU A., SORA, I.: Real Time Estimation of Li-Ion Battery Resistance Used in the Automotive Industry. Journal of Electrical Engineering, 10(4), 10-15, 2010.

[2] LONGFA X., ZHENDONG Z., Hui G., etc: Research on the Opening and Closing Times of an Electromagnetic Injector. Journal of University of Shanghai for Science and Technology. 32, 297-301, 2010.

[3] ZHONGYI M., YAOYI Q., XIUMIN Y., etc.: Mathematical Model for the Injection Process of the Electronic Controlled Injectors. Transactions of CSICE, 15(2), 231-236, 1997.

[4] CONGBO Y., ZHENDONG Z., ZHIYUAN L.: Experimental Research and Design for Electronic Control Injector Test about Flow Characteristic. Journal of Agricultural Mechanization Research, 12, 194-196, 2007.

[5] CHEN L., ZHANG Z.: Study on the Measurement of Dynamic Characteristics for Automotive Electronic Fuel Injector. International Conference on Transportation, Mechanical, and Electrical Engineering (TMEE 2011), China, 511-514, 2011.

[6] SIMKO M., CHUPAC, M.: Non-Destructive Method of Measurement of Radio Transmitters Antenna Systems. Elektronika ir Elektrotechnika/Electronics and Electrical Engineering, 107(1), 33-36, 2011.

[7] DELLI COLLI, V., MARINETTI, F.: Traction Control for a PM Axial-Flux In-Wheel Motor. Journal of Electrical Engineering, 7(4), 2007.

KOMUNIKáCIE
C O M M U N I C A T I O N S

Daniel Korenciak - Miroslav Gutten - Juraj Adamec - Adam Glowacz - Adam Cichy*

ANALYSIS OF ENGINE KNOCK SENSOR

The paper deals with design of a simple device for the detection of this disorder. In the beginning of the paper the effect of the undesirable detonation combustion in internal combustion engines is described. An engine control unit monitors these detonations using piezoelectric knock sensors. With the control of these sensors the detonations can be objectively measured just outside the car on the test panels. If this component provides small amplitude of the output voltage it could happen that it would have been in the areas of the engine ignition combustion.

Keywords: *knock sensor, diagnostic, testing device*

1. Introduction

A knock sensor allows the engine to run with the ignition timing as far advanced as possible. The computer will continue to advance the timing until the knock sensor detects pinging. At that point the computer retards the ignition timing just enough for stopping the pinging.

The knock sensor responds to the spark knock caused by pre-detonation of the air/fuel mixture. As the flame moves to the front out of the spark plug ignition point, pressure waves in the chamber crash into the piston or cylinder walls resulting in a sound known as a knock or ping. This is caused by using a fuel with a low octane rating, overheating, or over advanced timing. It can sometimes be caused by hot carbon deposits on the piston or cylinder head that raise compression. A knock sensor is comprised of piezoelectric materials; crystals that when impacted, generate a voltage (same idea as a BBQ ignitor). This voltage is monitored by the computer, and when an irregularity is detected, the computer corrects timing in variable valve timing engines, or triggers Diagnostic Trouble Code in older vehicles [1-3].

2. Engine knocking

Detonation can be prevented by any or all of the following techniques:

- The use of a fuel with high octane rating, which increases the combustion temperature of the fuel and reduces the proclivity to detonate;
- enriching the air-fuel ratio which alters the chemical reactions during combustion, reduces the combustion temperature and increases the margin above detonation;
- reducing peak cylinder pressure by decreasing the engine revolutions (e.g., shifting to a higher gear, there is also evidence that knock occurs more easily at high rpm than low regardless of other factors);
- decreasing the manifold pressure by reducing the throttle opening, boost pressure or
- reducing the load on the engine.

At detonation combustion occurs to rapid changes in pressure (Figure 1). These fast pressure changes; generated by sound waves, which are in modern automobiles captured by the knock sensor [4].

3. Adaptive knock control

At dynamic engine transients, mismatches of the ignition angle occur resulting in increased knock occurrence rates. The response time of knock control can be reduced by a feed-forward control angle $\alpha_i(n)$ stored in an adaptive ignition angle map. Contrary to lambda control, a successful global error model has not yet been found. The values of the ignition angle map must

* ¹Daniel Korenciak, ¹Miroslav Gutten, ²Juraj Adamec, ³Adam Glowacz, ⁴Adam Cichy
¹Department of Measurements and Applied Electrical Engineering, Faculty of Electrical Engineering, University of Zilina, Slovakia
²Department of Mechatronics and Electronics, Faculty of Electrical Engineering, University of Zilina, Slovakia
³Automatics, Computer Science and Biomedical Engineering, Faculty of Electrical Engineering, AGH University of Science and Technology, Krakow, Poland
⁴Faculty of Electrical Engineering, Silesian University of Technology, Gliwice, Poland
E-mail: gutten@fel.uniza.sk
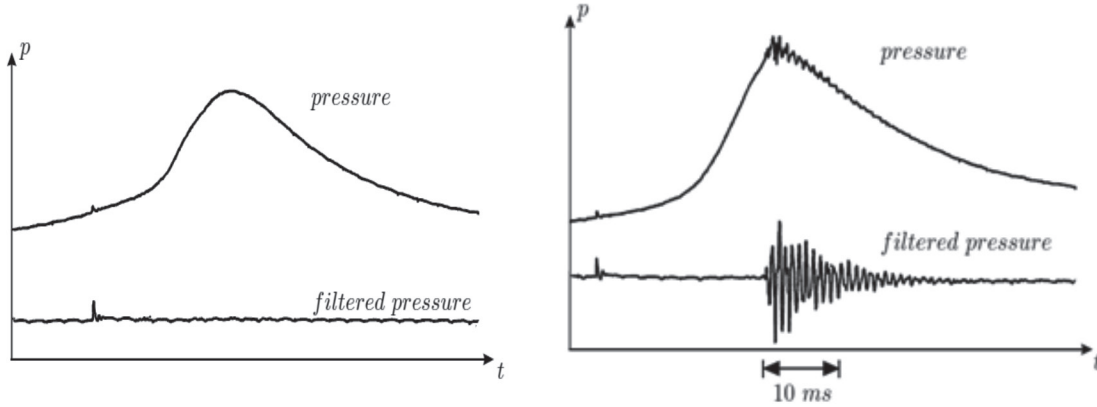
Figure 1 Bandpass output signal: a) non-knocking combustion, b) knocking combustion [1]
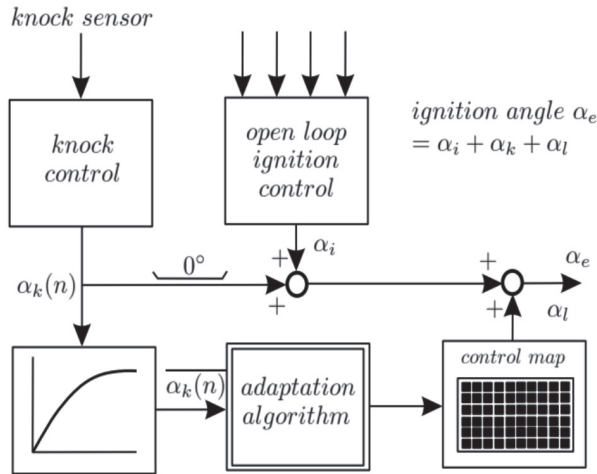
Figure 2 Knock control with feed-forward adaptive ignition angle map [5]

Figure 3 Control of knock occurrence rate by ignition angle shifting [5]

therefore be adapted in every individual engine operating point for all cylinders.

The ignition angle at one cylinder is the sum:

$$\alpha_e(n) = \alpha_i(n) + \alpha_k(n) + \alpha_l(n) \qquad (1)$$

where α_e is the effective ignition angle, α_i is the open loop ignition angle from fixed map, α_k is the knock control ignition angle, and αl is the learned ignition angle from adaptive map.

The average knock control ignition angle $\alpha_k(n)$ is the basis to teach the adaptive ignition angle map $\alpha_l(n)$ into the direction of retarding. A figed advance angle α_a is superimposed to the teaching process providing a forgetting function of the thought angles. The learned ignition angle is

$$\alpha_l(n) = (1 - k_l)\alpha_l(n-1) + k_l(\overline{\alpha}_k(n-1) + \alpha_a(n-1)) \quad (2)$$

The factor k_l determines how fast the learning process is [5]. The illustration of knock control with feed-forward adaptive ignition angle map is shown in Figure 2.

The usual actuation is a retardation of the ignition angle, shifting the energy conversion process backwards and thus reducing peak pressures and temperatures. An alternative input may be to lower the boost pressure of a turbo charger. The knock control ignition angle is calculated at discrete combustion cycles n as

$$\alpha_k(n) = \alpha_k(n-1) + \Delta\alpha_k - \beta \cdot \Delta E_y(n) \qquad (3)$$

where $\Delta\alpha_k$ is a permanent ignition angle advance, and β$\Delta E_y(n)$ the ignition angle retard at knocking. A typical control cycle is shown in Figure 3. The knock control ignition angle α_k(n) is added to the ignition angle obtained from the ignition map.
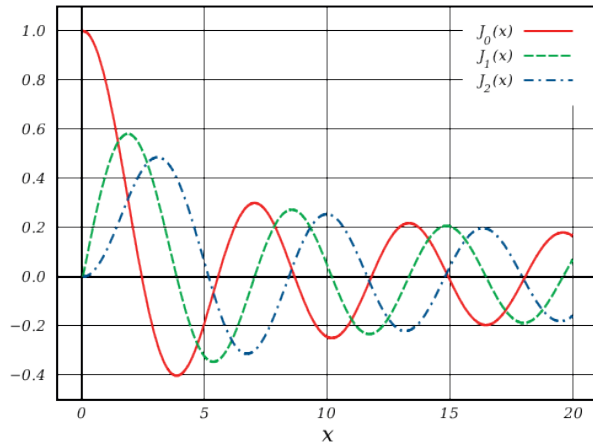
Figure 4 *Plot of Bessel function of the first kind, Jα(x) [6]*

Figure 5 *Testing device*

4. Knock sensor output signal

Sound waves generated by detonation during combustion have a frequency of between 6 to 20 kHz. Their frequency can be approximated by:

$$f_{mn} = c_0 \sqrt{v \Big/ 273} \cdot \beta_{mn} \Big/ d \tag{4}$$

where c_0 is the sound propagation velocity at 273 K, v is the temperature within combustion chamber, d is the cylinder diameter, βmn is the Bessel function (e.g. β_{10}=0.5861, β_{20}=0.9722, β_{30}=1.2197).

From the parameters c_0= 330 m/s, v= 2500 K, d= 0.089 m we can calculate the knock resonance frequencies f_{10}= 6.6 kHz, f_{20} = 10.9 kHz, f_{30}= 13.7 kHz.

Bessel functions are defined as the solutions $y(x)$ of Bessel's differential equation:

$$x^2 \frac{d^2 y}{dx^2} + x \frac{dy}{dx} + (x^2 - a^2)y = 0 \tag{5}$$

It is possible to define the function by its Taylor series expansion around x = 0:

$$J_\alpha(x) = \sum_{n=0}^{\infty} \frac{(-1)^m}{m! \Gamma(m+\alpha+1)} \left(\frac{x}{2}\right)^{2m+\alpha} \tag{6}$$

where Γ is the gamma function, a shifted generalization of the factorial function to non-integer values.

The Bessel function of the first kind is an entire function if α is an integer (Figure 4). The graphs of Bessel functions look roughly like oscillating sine or cosine functions that decay proportionally to $1/\sqrt{x}$ (see also their asymptotic forms below), although their roots are not generally periodic, except asymptotically for large x.

The Taylor series indicates that $-J_1(x)$ is the derivative of $J_0(x)$, much like $-\sin(x)$ is the derivative of $\cos(x)$; more generally, the derivative of $J_n(x)$ can be expressed in terms of $J_{n\pm1}(x)$ by the identities below [7].
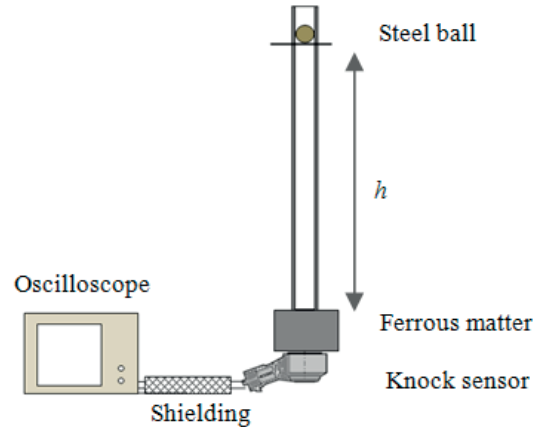
A simple but effective test knock sensor is shown in Figure 5. The sensor is attached to a metal cylindrical body. The plastic tube is adjusted so as to allow for the impact of the metal balls of different heights h.

Impact of ball on a metallic material with a height of 1.8 cm and a diameter of 3.4 cm generates sound waves. These waves are captured by a knock sensor. The output voltage signal, which is shown in Figure 6, corresponds with Bessel function.

Using a measuring apparatus consisting of an oscilloscope, metal impact surface, plastic tube with adjustable height and metal ball, we tested the response the knock sensor from Bosch which was used in VW Golf. The response was stored in oscilloscope and then the values of voltage were shown in Figure 6.

The principally schematic of sound waves spreading in metal environment created by ball impact on surface of metal material is shown in Figure 7. The knock sensor is placed on the bottom of the metal plate. In the middle of the plate is screw which is tighten to rated torque. This arrangement provides the best possible transfer of mechanical waves on the surface of the sensor [8].

The diagnostic of knock sensor is based on the response of knock sensor on the first two extremes of the measured signal. The amplitude of the signal shows level of sensor sensitive and what is the shape of the sensor response. From the measured values we could specify a "normal curve" which shows how big the voltage response should be from this kind of sensor. It replaces the mounting used by the manufacturer for this sensor [9].

The value of the generated voltage depends on the gravitational potential energy of the falling bullet [10]:

$$E_p = m \cdot g \cdot h \tag{7}$$

where m is the mass of the body (2050 mg), g is the acceleration due to gravity (9.81 m/s^2), h is the height of the body above the surface (5 cm, 10 cm, 15 cm, 20 cm, 25 cm, 30 cm, 40 cm, 50 cm).
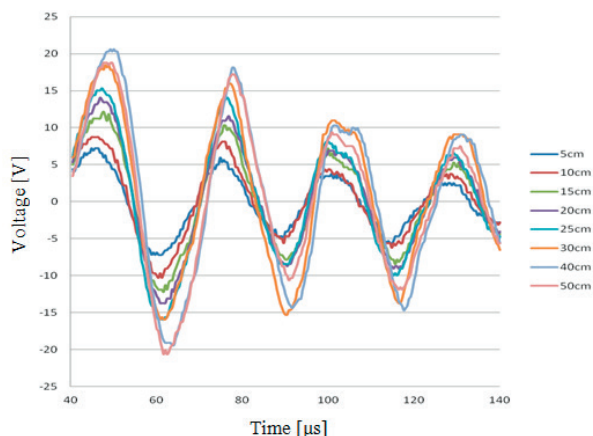
Figure 6 Output voltage of the sensor
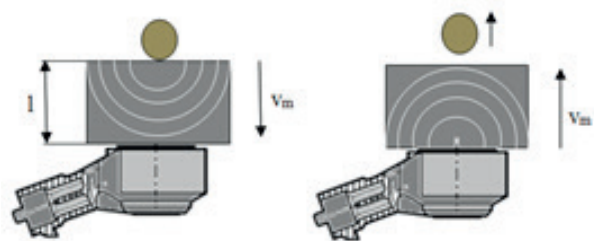
Figure 7 Sound reflection after the bullets' impact
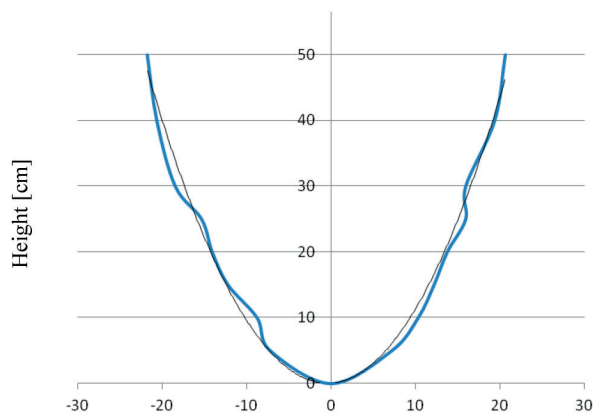
Figure 8 Output voltage depending on the amount of the impact

Calculation of the output voltage can be realized by means of the formula:

$$U = 20 \cdot \log(E_p + 1) \tag{8}$$

Restriction reflecting the sound waves can be accomplished by changing the shape of a metallic material. An experiment was conducted where a steel ball was thrown directly at the sensor. In this impact we can already consider the Bessel function [11].
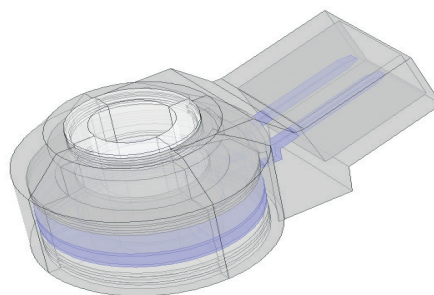
Figure 9 3D model of knock sensor
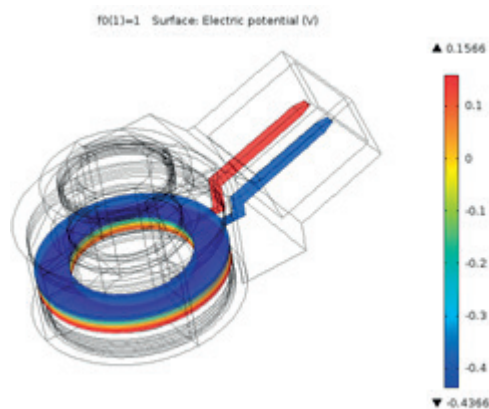
Figure 10 Output potentials of sensor with 1N of force affecting on piezoelectric element

Figure 9 shows the 3D model of the knock sensor. It is modelled on materials composition and functions like in real use. The cover of the sensor is made from plastic and electrodes are made from metal. Inner pressure sensitive layer is simulated by a crystal. On this model it is affecting outer force. The model is detailed because the response of the crystal is influenced by the sensor cover and the body of the sensor too. Figure 10 shows the knock sensor simulation in the COMSOL [12] at pressure of 1N. In Figure 10 we can see an electric potential of the sensor.

5. Conclusion

A construction of the testing device for the knock sensor suitable for diagnostics of the knock combustion in internal combustion engines has been presented.

The output signal of the presented sensor has been described by Bessel functions. Using the first voltage extremes on the characteristics from Figure 6 it is possible to create a reference for the evaluation of the polynomial residue. It should be taken into account that the velocity of sound in the air is 330 m/s. This sound impinges on the walls of the combustion chamber and is detected by the sensor. The resonant frequency of the clicking of the motor is usually in the range from 5 kHz to 15 kHz. The

sensor worked in the field to 37 kHz, which shall be taken into account on an own sensor resonance.

References

1. GUPTA, H. N.: Fundamentals of Internal Combustion Engines. PHI Learning, 169–173, 2006.
2. CLINE, A. W.: Engine Basics: Detonation and Pre-Ignition. Accessed June 2007.
3. FAYETTE TAYLOR, Ch.: Internal Combustion Engine in Theory and Practice, Second Edition, Revised, Volume 2, Chapter 2 "Detonation and Preignition". MIT Press, pp. 34–85, 1985.
4. Modeling Pressure Oscillations under Knocking Conditions: A Partial Differential Wave Equation Approach. SAE Technical Paper n. 2010-01-2185, 2010.
5. KIENCKE, U., NIELSEN, L.: Automotive Control Systems for Engine, Driveline, and Vehicle. Springer Berlin, Heidelberg, 2005.
6. GRANDSHTEYN, I. S., RYZHIK, I. M., JEFFREY, A., ZWILLINGER, D. (Eds): Table of Integrals, Series, and Products, Seventh edition. Academic Press, 2007.
7. TEMME, N. M.: Special Functions: An Introduction to the Classical Functions of Mathematical Physics, Second Edition. Wiley, New York, pp. 228–231.
8. SIMKO, M., CHUPAC, M.: Non-Destructive Method of Measurement of Radio Transmitters Antenna Systems. Elektronika ir Elektrotechnika/Electronics and Electrical Engineering, 107(1), 33-36, 2011.
9. CONGBO, Y., ZHENDONG, Z., ZHIYUAN, L.: Experimental Research and Design for Electronic Control Injector Test about Flow Characteristic. Journal of Agricultural Mechanization Research, 12, 194-196, 2007.
10. LONGFA, X., ZHENDONG, Z., HUI, G., etc: Research on the Opening and Closing Times of an Electromagnetic Injector. Journal of University of Shanghai for Science and Technology, 32, 297-301, 2010.
11. CHEN L., ZHANG, Z.: Study on the Measurement of Dynamic Characteristics for Automotive Electronic Fuel Injector. Proceeding of International Conference on Transportation, Mechanical, and Electrical Engineering (TMEE), China, 2011.
12. CONSOL [online]. Available: http://www.comsol.com.

Jan Semjon - Marek Sukop - Marek Vagas - Rudolf Janos - Peter Tuleja - Lucia Koukolova - Peter Marcinko - Ondrej Jurus - Jozef Varga*

COMPARISON OF THE DELTA ROBOT ABB IRB 360 PROPERTIES AFTER COLLISIONS

The use of robots with their partial damage is not common, and it is not used in safety terms. If the robot works in a controlled environment after partial damage, the robot can be used for a short period of time when the speed of moving and weight of the load are reduced. In the event of damage one of the arms of the parallel robot, the parallelism of the movable platform towards base is lost. This results in a loss of accuracy, which in the case of shortening one of the robots arms is reflected by a gradual change in the distance of the removal site from the storage site. This change is bigger with the greater distance of the center of gravity effector from the robot output flange. For the short--term unavailability of replacement arms, it was decided to continue the training with the robot with rebuilt and reinforced arm. This article concerned with performing a control measurement to detect the deviation value that could be compensated in the execution of the individual cycles of the robot. The measurement compared values of pose accuracy and pose repeatability of the robot after damage by using measured compensated deviations.

Keywords: delta robot, verification, precision, load, sensors

1. Introduction

The basic idea behind the delta robot ABB design is the use of parallelograms. A parallelogram allows an output link to remain at fixed orientation with respect to an input link. The use of three such parallelograms restrain completely the orientation of the mobile platform which remains only with three purely translational degrees of freedom. The input links of the three parallelograms are mounted on rotating levers via revolute joints. The revolute joints of the rotating levers are actuated in two different ways: with rotational (DC or AC servo) motors or with linear actuators. Finally, a fourth leg is used to transmit rotary motion from the base to an end-effector mounted on the mobile platform. The use of base-mounted actuators and low-mass links allows the mobile platform to achieve accelerations of up to 50 G in experimental environments and 12 G in industrial applications. This makes the delta robot ABB a perfect candidate for pick and place operations of light objects (from 10 g to 1 kg). The delta robots ABB available on the market operate typically in a cylindrical workspace which is 1 m in diameter and 0.2 m high [1, 2].

2. Basic properties of robotized workplace

The delta robot ABB is a part of a training workplace equipped with a pair of conveyors. The material flow configuration depends on the type of training that is being realized. At the workplace, it is possible to set two bases of the flow of the material to be handled. In basic training a configuration is used where the delta robot ABB picks up the manipulated objects from the pallet, which is transported on the Bosch pallet conveyor [3]. During the manipulation, the pallet is placed in a precisely defined position using programmable stops. After removing the object and moving it over the conveyor belt, the manipulated object is released and carried by the conveyor to the respective exit position. In advanced training, conveyor functions are opposite. The delta robot ABB picks up manipulated objects randomly placed on the conveyor belt. It then stores them on selected positions in the technological pallet conveyor Bosch. For manipulation used a vacuum gripper with a suction cup with diameter of 5 to 20 mm. The weight of manipulating objects ranges from 50 g to 2 kg. A view on robotized workplace equipped with delta robot ABB is shown in Figure 1.

The delta robot ABB is intended primarily for material handling, part removal, packaging operations or assembly. It is characterized by a high speed of movement, with an integrated

* [1]Jan Semjon, [1]Marek Sukop, [1]Marek Vagas, [1]Rudolf Janos, [1]Peter Tuleja, [1]Lucia Koukolova, [1]Peter Marcinko, [1]Ondrej Jurus, [2]Jozef Varga
[1]Department of Robotics, Faculty of Mechanical Engineering, Technical University of Kosice, Slovakia
[2]Prototype and Innovation Center, Faculty of Mechanical Engineering, Technical University of Kosice, Slovakia
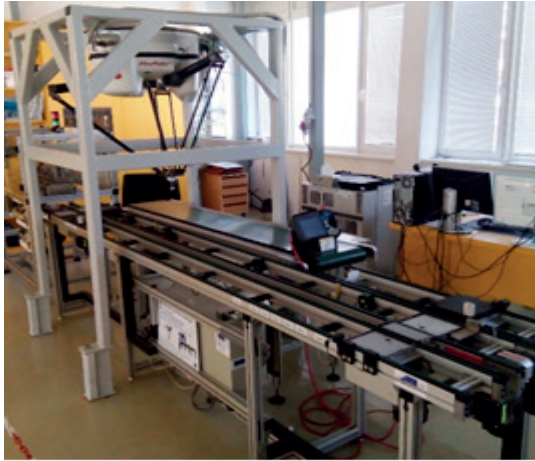Email: jan.semjon@tuke.sk

Figure 1 Robotized workplace

Figure 2 Designed measuring plane

vision software and integrated control of indexing belts. Basic parameters of delta robot ABB IRB360-3/1130: (number of degrees of freedom: 4; weight: 120 kg; load capacity: 3 kg; operating radius: R 565 mm; repeatable positions: (±) 0.1 mm; cycle time: app. 0.52-0.75 s).

During training, there was a collision between one of the robot arms and the RFID chip on the pallet of Bosch pallet conveyor. After the collision, extensive damage to one of the pair of robot arms was detected, resulting in the delta robot ABB training being stopped. After ordering spare parts, it was obvious that the delivery term for the spare arms was 10 days. Due to the necessity of completing the training according to the timetable, we proceeded to temporarily repair this arm. The damaged arm was extensively deformed, we tried to remove the deformation after dismantling. This led to further cracks in the vicinity of the deformation. In order to continue the training, the arm was cut in the crack place. A precision aluminium tube was inserted into the cavity of the carbon fiber arm and with the help of an adhesive connected to the parts of the damaged arm. The surface of the joint was covered by black insulating tape for aesthetic reasons. After the repair was completed, that the difference in length between restrained arm and undamaged arm was less than 0.1 mm. This lead to a slight shift and rotation of the centre of the delta robot ABB output flange during the work cycle. After 50 cycles end of effector towards of the programmed position and the slight deflection of the arm were visibly displaced. Another arm repair was not possible due to the use of glue. After performing further cycles, it was found that the deformation of the arm had stopped and no changes were made [4]. Because of the need to determine the shift value per work cycle, control measurements were taken. The result of the measurement was to find out the displacement value in the Cartesian coordinate system, the value being used to compensate for the inaccuracy caused by the damaged robot arm.
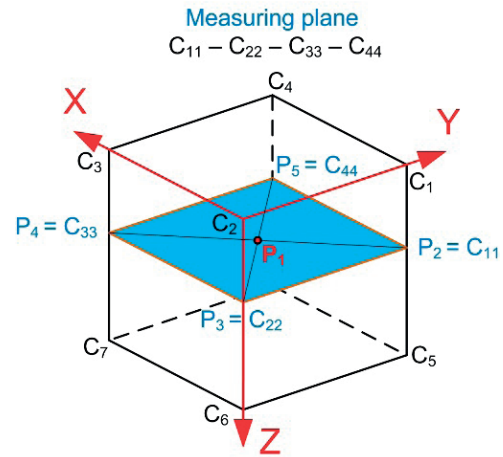
3. Selection of measurement tests and their description

After the measurement it was possible to use the measured data to create compensatory deviations. After the implementation of the compensatory deviations in the robot program, control measurements were carried out to compare the identified inaccuracy towards the manufacturer´s inaccuracies. To measure the relevance of the measurement carried out, it was based on the data and measurement methodology provided by the delta robot ABB manufacturer. In this materials the manufacturer surveyed robot parameters using ISO 9283 [5, 6], where focused overall on four types of tests (Pose accuracy *AP*, Pose repeatability *RP*). The robot manufacturer reports the measured values in Table 1, with speed 0.8 m.s^{-1} and a load of 0.1 kg.

In order to compensate for the inaccuracy caused by the damaged arms, we decided to carry out a control measurement using two tests (Pose accuracy AP, Pose repeatability RP). Before the test, the movements of the delta robot ABB must be limited as necessary to set up the measuring instruments. The test must be preceded by a specified heating operation if specified by the manufacturer. The ambient temperature in the tests should be kept within "20±2 ºC". Measured location data (coordinates x_j, y_j, z_j) must be expressed in a coordinate system whose axes are parallel to the coordinate system axis coordinates of the base of the delta robot ABB being measured. All tests must be carried out under the 100 % (10, 50 % optional) of rated load (mass, centre of gravity, moment of inertia) in accordance with the manufacturer´s specification (technical specifications). All position characteristics must be tested at the speed of 100 % (optionally 50 %, 10 %) achievable between the prescribed positions. The following requirements must be met placing the measuring cube in the robot workspace: five points (P1 to P5) are located on the diagonals of the selected plane. These five points together with manufacturer´s guideline, form the test positions must reach the centre of the mechanical test interface. The test positions must be defined by the coordinates of the base. P1 is the

Table 1 Manufacturer´s measured values according to ISO 9283

Characteristic (ISO 9283)	(mm)
Pose accuracy (AP)	0.01
Pose repeatability (RP)	0.1

Table 2 Selected test parameters

Characteristic (ISO 9283)	Load (kg)	Speed (m.s⁻¹)	Number (cycles)
Pose accuracy (AP)	0.1	0.8	30
Pose repeatability (RP)	0.1	0.8	30

diagonal intersection and is the centre of the cube. Points P2 to P5 are spaced from the diagonal ends "10±2 %" of the diagonal length. If this is not possible, the nearest diagonal point must be selected. All robots joints must be applied while moving between all test positions. Based on the experiments performed on 100 cycles it was decided that the measurement would not be carried out exactly according to ISO 9283. The robot´s workspace has a value "±X,Y= 342.5 mm" and "±Z=125 mm". The dimension of the cube according to the standard is given by the robot´s workspace, where it was limited in this case by "Z = 250 mm". For this reason, the cube would have a size of 250x250x250 mm, which would not allow a meaningful measurement to be made. The result was a design in which the measurement plane would be parallel to the plane X, Y of the delta robot ABB base, Figure 2. The distance between the extreme points of the plane (P2-P3, P3-P4, P4-P5 and P5-P2) is 685 mm. Measuring points P2, P3, P4 and P5, were selected for measurement where measurements were made to provide similar environmental conditions for all points [7].

Selected test parameters with load definitions, output speed of rotation and cycle counts are listed in Table 2.

Pose accuracy (AP) - represents a deviation between the programmed position and the average of the positions achieved when moving to the programmed position from the same direction. One way position accuracy is calculated according to:

$$AP_X = (\bar{x} - x_C), \ AP_Y = (\bar{y} - y_C), \ AP_Z = (\bar{z} - z_C) \tag{1}$$

Where, (x_c, z_c, y_c) are the programmed values and (x_j, z_j, y_j) are the actual (measured) values. While:

$$\bar{x} = \frac{1}{n}\sum_{j=1}^{n} x_j, \ \bar{y} = \frac{1}{n}\sum_{j=1}^{n} y_j, \ \bar{z} = \frac{1}{n}\sum_{j=1}^{n} z_j, \tag{2}$$

The resulting value of one-way wrist precision is based on the relationship:

$$AP = \sqrt{(\bar{x} - x_C)^2 + (\bar{y} - y_C)^2 (\bar{z} - z_C)^2} \tag{3}$$

Pose repeatability (RP) - indicates the degree of match between placements and orientation of the positions achieved after n-repetitions to the same programmed position on the same direction. For a given position, it expresses the RP value that is the radius of the sphere whose centre is the barycentre and which is calculated:

$$RP = \bar{l} + 3S_l \tag{4}$$

Table 3 Average inaccuracy values on the delta robot ABB, point P$_{1A}$

AP	Axis X	Axis Y	Axis Z
Point P$_{1A}$	0.00183	-0.00171	0.00156

where,

$$S_l = \sqrt{\frac{\sum_{j=1}^{n}(l_j - \bar{l})}{n-1}}, \ l = \frac{1}{n}\sum_{j=1}^{n} l, \tag{5}$$
$$l_j = \sqrt{(\bar{x} - x_C)^2 + (\bar{y} - y_C)^2 (\bar{z} - z_C)^2}$$

The coordinates of the barycentre of the achieved points at n-repetitions of the same position are calculated according to Equations (2).

A set of three Heidenhain MT 25 sensors was used to make the measurement (system accuracy "±2 μm"). The sensors were placed in the measuring base, which ensured their exact fitting in three perpendicular planes. Since the sensors are touching, it is necessary to carry out their admission and removal to the measuring object. This was accomplished by means of a system of three automatic triggers, the control of which was realized by means of control system delta robot ABB. The measured object was a measuring sphere with an outer diameter of 25 mm, with the center located in the axis of the outlet flange. The view of the location of the sensors and the robot is shown in Figure 3.

4. Results and discussion

To determine the degree of the accuracy of a robot caused by robot damage, a control measurement was carried out at the four P2 to P5 measurement points. At each point, 30 measurements were made. The average values of the deviation at point P1 were mathematically calculated and graphically verified in CA environments of CREO, Table 3.

The deviations in the direction of the plane XY axis are shown in Figure 4. Z-axis deviations have been neglected when creating compensation in the respective program. This is due to the use of a spring suction as the end effector that allows the delta robot ABB in the Z-axis to compensate [8].

The measured deviations were subsequently used in the robot program. On the basis of the tests carried out a method was chosen where, every 5 cycles a half value of the mean deviation was entered in the appropriate direction. After repeating 100 cycles, it was found that the resulting robot inaccuracy was within the prescribed limits.
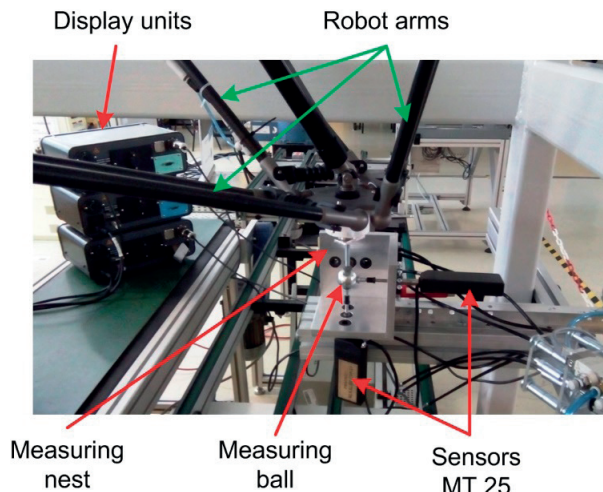
Figure 3 *Location of sensors in the robot workspace*
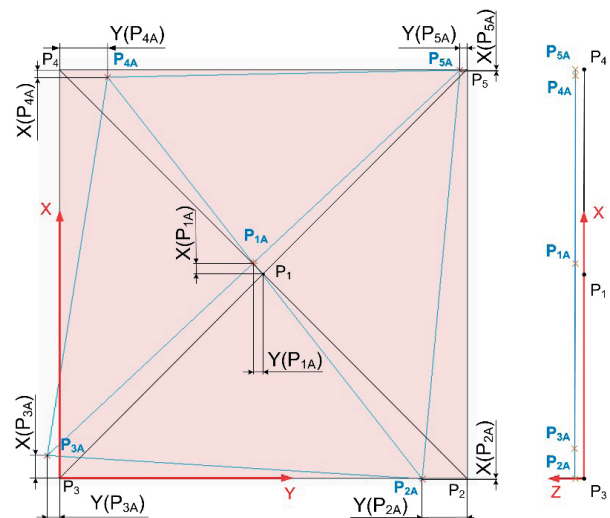
Figure 4 *Measured plane XY*
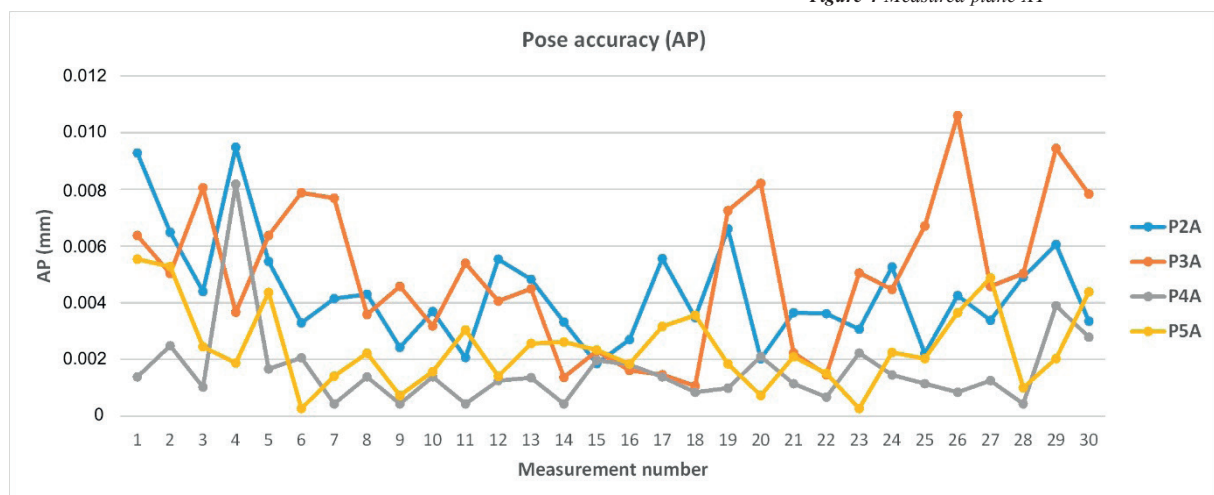
Figure 5 *Pose accuracy*

After the respective deviations were entered into the robot program a control measurement was performed. The measured values were then processed to determine one-way pose accuracy (AP) and one-way pose repeatability (RP).

Pose accuracy (AP) - Graphical representation of measured data (pose accuracy) in direction the plane XY is shown in the graph of Figure 5.

After realizing the 30 measurements at 10 % of maximal capacity of delta robot ABB "0.3 kg", we came to the following averages (pose accuracy), Table 4.

Pose repeatability (RP) - Graphical representation of measured data (pose repeatability) in direction the plane XY is shown in the graph of Figure 6.

After realizing the 30 measurements at 10 % of maximal capacity of delta robot ABB "0.3 kg", we came to the following averages (pose repeatability), Table 5.

Measurement results have shown that the use of a delta robot ABB for training purposes is also with arm damage for the

necessary time. In a controlled environment where the speed was limited to 1 m.s^{-1} and the load per 0.1 kg it was confirmed for about 500 cycles. Using a damaged robot in a normal running would not be possible in terms of security.

5. Conclusions

On the basis of the measured parameter measurements of the wrist-assembled modules with three degrees of freedom, we came to the following conclusions: The partial result of the measurement was the formation of the measured plane whose peaks P2A, P3A, P4A and P5A were obtained by determining the mean values of deviations to points P2, P3, P4 and P5. By overlapping the measured plane with the programmed plane it was possible to determine the resulting inaccuracy of the delta robot ABB at these points. Deviations could be used to create compensation values embedded in the robot´s program, so that
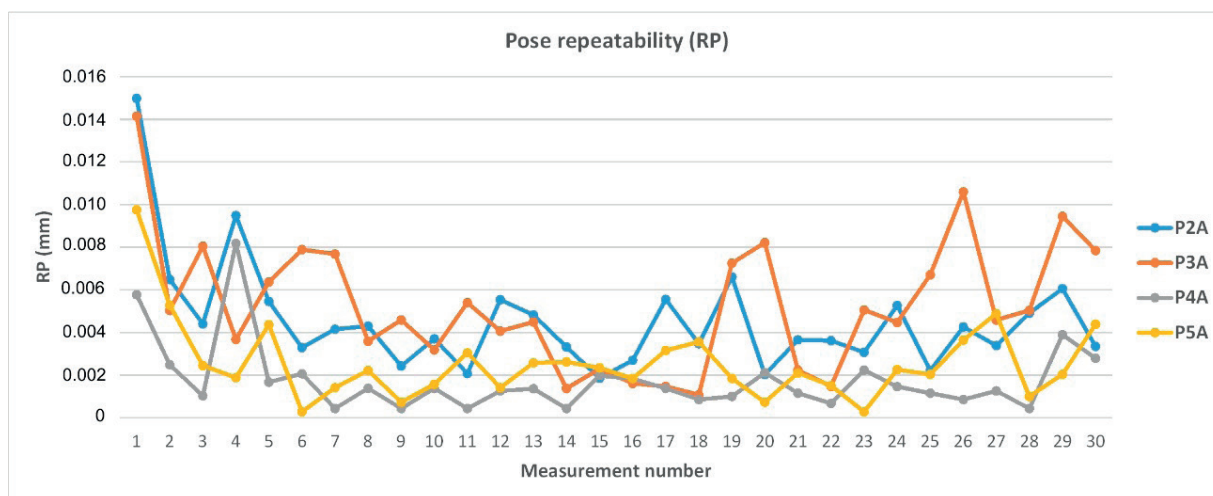
Figure 6 *Pose repeatability*

Table 4 Average-Pose accuracy (AP)

	P_2	P_3	P_4	P_5
AP	0.007679	0.004818	**0.008184**	0.001573

Table 5 Average-Pose repeatability (RP)

	P_2	P_3	P_4	P_5
RP	0.010058	**0.012820**	0.0060278	0.006652

the resulting robot motion after repeating n-cycles was within the prescribed accuracy.

Based on the delta robot ABB measurement, we have also reached the following conclusions: The manufacturer's prescribed "pose accuracy" at load 0.1 kg and movement velocity of robot 0.8 m.s^{-1} has value 0.01 mm (Table 4) and is higher than the highest average value at the point P4 (0.008154 mm). The manufacturer's prescribed "pose repeatability" at load 0.1 kg and movement velocity of robot 0.8 m.s^{-1} has value 0.1 mm (Table 5) and is higher than the highest average value at the point P3 (0.01282 mm). On the basis of realized measurements, we can conclude that of the delta robot ABB is within the desired range (that is, it meets ISO 9283).

Damaged delta robot ABB from a safety point of view can only be used at lower speeds. For this reason, it is only suitable for use in training or during exhibitions.

Acknowledgements

References

[1] Delta Robots ABB [online]. Available: http://www.parallemic.org/Reviews/Review002.html.

[2] Delta Robots ABB [online]. Available: https://library.e.abb.com/public/31305748911b4da18b1463233d91b83a/3HAC029963-en.pdf.

[3] SHETTY, D., KOLK, R. A.: Mechatronics System Design, SI Version, 2nd edition. Global Engineering, Stanford, 2011.

[4] COP, V., DUROVSKY, F.: (2013). Advanced Mechatronic Components, Driving and Positioning Modules for Intelligent Manufacturing and Robotics Systems. Internationales Forum Mechatronik, Switzerland, 2-19, 2013.

[5] STN EN ISO 9283:2001-12. Manipulating Industrial Robots-Performance Criteria and Related Test Methods. Slovak Office of Standards, Metrology and Testing (SOSMT), Bratislava.

[6] ISO 9283:1998. Manipulating Industrial Robots-Performance Criteria and Related Test Methods. International Organization for Standardization, Geneva.

[7] HOCK, O., DRGONA, P., PASKALA, M.: Simulation Model of Adjustable Arm Using Denavit-Hartenberg Parameters. Proceedings of 10th international conference ELEKTRO 2014, Slovakia, CD-ROM, 176-179, 2014.

[8] HOCK, O., DRGONA, P., FRIVALDSKY, M., HAVRILA, R.: Simulation of Manipulator Positioning Methodology Using Inverse Kinematics. Proceedings of the 16th international scientific conference Electric power engineering (EPE 2015), Czech Republic, 706-711, 2015.

KOMUNikácie
C O M M U N I C A T I O N S

Martin Sumega - Lubos Struharnansky - Lukas Gorel - Matej Pacha*

SIMULATION AND EXPERIMENTAL STUDY OF BALL POSITION CONTROL AT BIAXIAL PLATFORM USING STATE SPACE APPROACH

Ball on plate platform is a great tool for testing of various control techniques. This study provides a detailed design and comparison of three control structures for automatic stabilization of the ball´s location on plate and ball trajectory tracking. Namely PD controller, state space feedback and state space observer with state space feedback. All three methods are designed and practically compared. All structures have a common feature. It is the methodology for calculating the parameters of the controllers. Ball - on - plate mathematical model derived by Newton´s method and DC motor position loop control are also part of this article.

For the authors of this article, this study is an opportunity to create an educative setup to explain the principles of basic control system for non - technical person and offers motivation to future students.

Keywords: *ball on plate, trajectory tracking, parameter analysis, position control systems*

1. Introduction

In application practice, the properties of new control theories are often investigated at inverted pendulum. Balancing a ball of on two - axis platform is a variant of this testbed in which you can successfully find the limits and observe behavior of the control structure. Practical impact of these control structures is immense. Generally, in defense military technology such as camera stabilizations on moving vehicle or pointing camera angle control during drone flying are used. The same principle of operation like in this article is used for stabilizing platforms in sea ships and aircrafts. General idea is also used in high - end applications like vertical landing of space rockets.

Bench - marking system consists of two DC machines connected with a long stick at moving platform. DC motors are controlled via standard full bridge topology. The processing unit is Kinetis K60 which is a novel digital signal controller designed for the automotive industry. The position of subject placed at plate is obtained from the resistive touch panel in terms of voltage drop. In some articles, the camera [1, 2] is used to estimate the position of the globule. Optical detection requires heavy processing for position estimation. This method leads to huge computation power. Another approach is based on laser technology or basic sonar rangefinders. For stabilizing one degree of freedom applications gyro and accelerometers are used to measure system states [3]. Resistive touch surface excel over others due to its positive features. From the perspective of the automatic regulation conductive surface represents zero order transfer function. This means that the response will be recovered immediately without undesirable delay [4].

2. Ball on plate mathematical model

To be able to analyze the behavior of an ideal ball - and - plate balancing system it is necessary to create mathematical model and equivalent transfer function.

Our testbed is biaxial. It means that it has two degrees of freedom X and Y, and in a center is anchored on a rotating joint. The ball is stabilized and controlled to the demanded position through the movements of the plate, which are performed by two DC motors with permanent magnets. Each of the motors is responsible for the movements of the platform just in one axis. This is the reason why the same scheme is applied to both degrees of freedom Figure 1b).

* [1]**Martin Sumega,** [1]**Lubos Struharnansky,** [1]**Lukas Gorel,** [2]**Matej Pacha**
[1]Department of Power Electrical Systems, Faculty of Electrical Engineering, University of Zilina, Slovakia
[2]NXP Semiconductors, Roznov pod Radhostem, Czech Republic
E - mail: martin.sumega@fel.uniza.sk
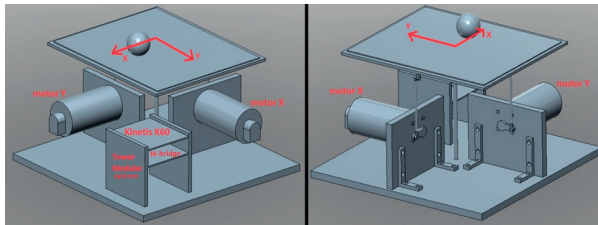
<center>a)</center>
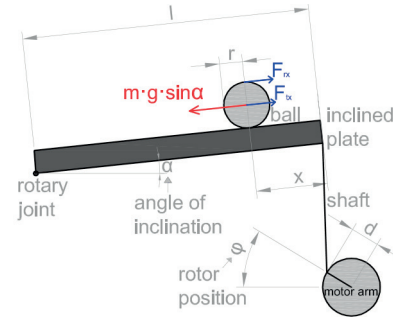
<center>b)</center>

Figure 1 a) *Platform visualization;* ***b)*** *Model for X axis*

Many authors use Lagrange equations of second kind or Euler - Lagrange equations for dynamical description of the ball on plate system [5]. It is universal method which is mostly used in mechanical engineering to derive dynamic motion equations. Number of generalized positions q_i and velocities $\dot{q}_i$ depends on degrees of freedom of the system. It is more complex method, but for this application it is sufficient to use another approach based on the Newton's second law [6, 7]. This method considers just the relation between the inclination angle of the plate and ball position, see Figure 1b). Friction is neglected.

Forces which affect the ball:

$\mathbf{F_{rx}}$ - rotational part and $\mathbf{F_{tx}}$ - translational part of the force which affect the ball.

Translational part of the force depending on the ball's acceleration:

$$F_{tx} = m \cdot \ddot{x} \tag{1}$$

Torque of rotational motion:

$$T_{rx} = F_{rx} \cdot r = J \cdot \frac{d\omega_x}{dt} = J \cdot \frac{d\left(\frac{\dot{x}}{r}\right)}{dt} = J \cdot \frac{d^2\left(\frac{\dot{x}}{r}\right)}{dt^2} = \frac{J}{r} \cdot \ddot{x} \tag{2}$$

Where ω_x is angular velocity of the ball in X axis and J is its moment of inertia. Equation (2) leads to rotational part of the force which affect the ball:

$$F_{rx} = \frac{J}{r^2} \ddot{x} \tag{3}$$

Moment of inertia of the sphere:

$$J = \frac{2}{5} m \cdot r^2 \tag{4}$$

Substituting Equation (4) into the Equation (3) we get rotational part of the force which affects the ball acceleration:

$$F_{rx} = \frac{2}{5} m \cdot \ddot{x} \tag{5}$$

For equilibrium state, the sum of the rotational and translational force component of the ball is equal to the force that moves it on the inclined plane downwards.

$$F_{tx} + F_{rx} = m \cdot g \cdot \sin\alpha \tag{6}$$

Substituting Equation (1) and Equation (5) into the Equation (6) leads to:

$$m \cdot \ddot{x} + \frac{2}{5} m \cdot \ddot{x} = m \cdot g \cdot \sin\alpha \tag{7}$$

After mathematical corrections of Equation (7) we can get the relationship between ball acceleration and sin(α). Due to sin function, nonlinear system model was created. In the area of angles up to ± 5° it is possible to neglected the influence of sin function and substitute expression sin(α) = α. By applying Laplace transformation, we can get transfer function of the ball on plate system. Relation between ball position x and inclination angle of the plate α is as follows:

$$F(s) = \frac{x(s)}{a(s)} = \frac{5}{7} \cdot \frac{g}{s^2} = \frac{g}{h} \cdot \frac{1}{s^2} \tag{8}$$

Where *g* is gravitational acceleration. Relation between motor arm angle and inclination angle of the plate:

$$\phi = \frac{l}{d} \cdot \alpha \tag{9}$$

Our main goal during stabilizing platform is to ensure a stable objective position and to achieve position reference tracking. Active force in this task is gravity. The ball is capable of rolling on the beam under the action of gravity. Combination of gravitational force and inclination of plate leads to unstable position change in an open loop system. Root locus plot Figure 2b) explains instability of derivation transfer function Equation (8). Closer look for steady state shows us the behavior of the system under the following condition s = 0. When s approaches 0, the denominator of the transfer function approaches 0, but final value of Equation (8) approaches infinity Figure 2a). A well - known principle as the final value theorem applied at Equation (8), lead us directly to the reason for instability. The same theorem offers a huge space for feedback control by algorithms ensuring stability.
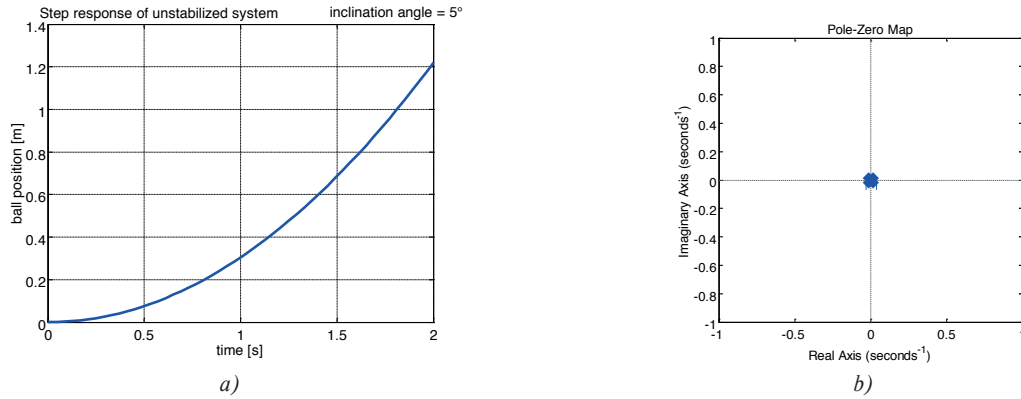
Figure 2 a) Step response of Equation (8); b) Pole placement of Equation (8)
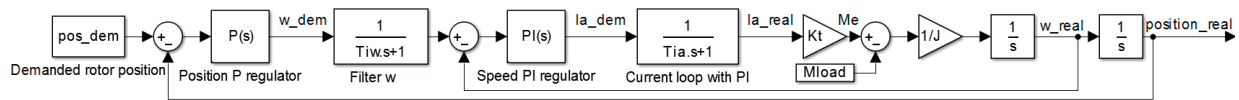
Figure 3 Axis inclination control via DC machine position loop

3. Control of DC machines

3.1 Mathematical model of DC machine with permanent magnet

Inclination of the plate, respectively the angle of platform, is controlled by standard position loop of DC machine. Permanent magnet DC machine is represented by following equations:

$$\frac{di_a}{dt} = \frac{1}{L_a}(U_a - R_a i_a - \omega \psi_{PM}), \frac{d\omega}{dt} = \frac{p}{J}(M_e - M_{load}),$$
$$M_e = p \psi_{PM} i_a \tag{10}$$

Parameters of DC machines are listed in the appendix.

3.2 Position loop design

Angular position control with PI controllers was implemented in to Kinetis K60. The most important in this step is to ensure the prescribed behavior and set up correct dynamic response. Standard Dodd's formula was applied in prescribed band width finding [8] in combination with pole placement method. The results of this approach describe comparison between simulation and real measurement Figure 4. Step response and bode plots for speed and position loop are shown below.

From a practical standpoint, knowing how the system responds to Heaviside step function is important because this concept shows us systems transient phenomenon. Fast and stable systems such as in Figure 3 and Figure 4 with settling time 0.05 sec are able to damp fast deviations. Bode plot analysis shows ability of the trajectory following. Any trajectory can be divided

into axes X, Y. The resulting curve is decomposed by offline FFT and then compared with the original position loop bode plot Figure 4b). If the resulting frequencies are part of the position loop bandwidth, then trajectory will be followed without error.

4. Master control algorithm

The proposed testbed is controlled by the Kinetis K60 digital signal controller. K60 device detects five feedbacks. Voltage drop on resistive touch screen, two currents from hall effect sensors and pulses from two encoders. Each DC machine has its own full bridge topology of power supply converter integrated in BTN8982/86TA.

5. Stabilization design

The first experimentally verified structure is standard PD controller. By adding the PD controller (the green part of Figure 6a)), a stable structure is created to provide the both objectives. The transfer function Equation (11) of the whole structure was derived from the Masson's rule formula [8]. Parameters of PD controller K_D, K_P were determined by pole placement method. Equation (11) shows experimental results of PD structure.

Closed loop transfer function of Figure 6a) PD controller:

$$F_{PD}(s) = \frac{F_{PDo}(s)}{1 + F_{PDo}(s)} = \frac{a_1 \cdot (K_P + K_D \cdot s)}{s^2 + a_1 \cdot K_D \cdot s + a_1 \cdot K_p};$$
$$K_D = \frac{2 \cdot \xi \cdot \omega_0}{a_1}, K_P = \frac{\omega_0^2}{a_1} \tag{11}$$
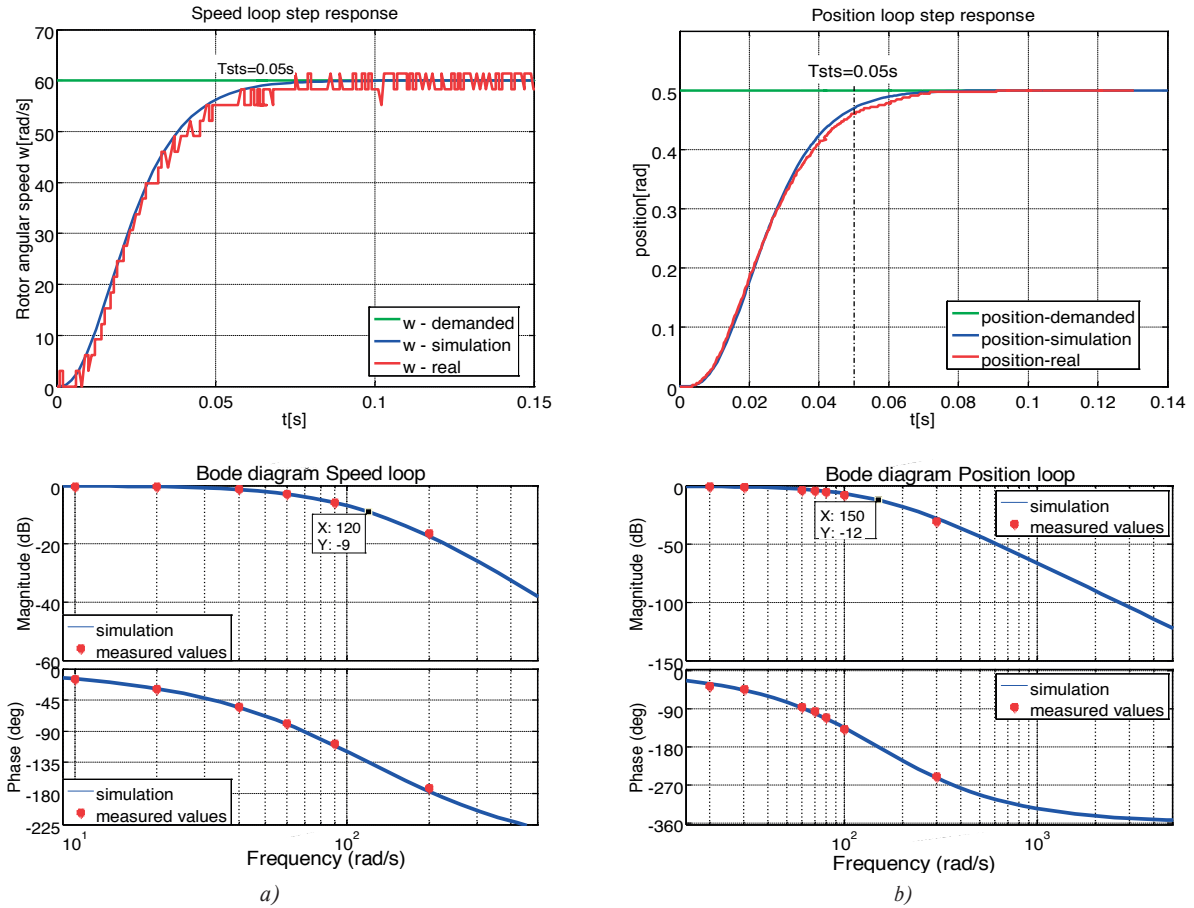
Figure 4 *Step response and Bode diagram of a) Speed loop; b) Position loop*
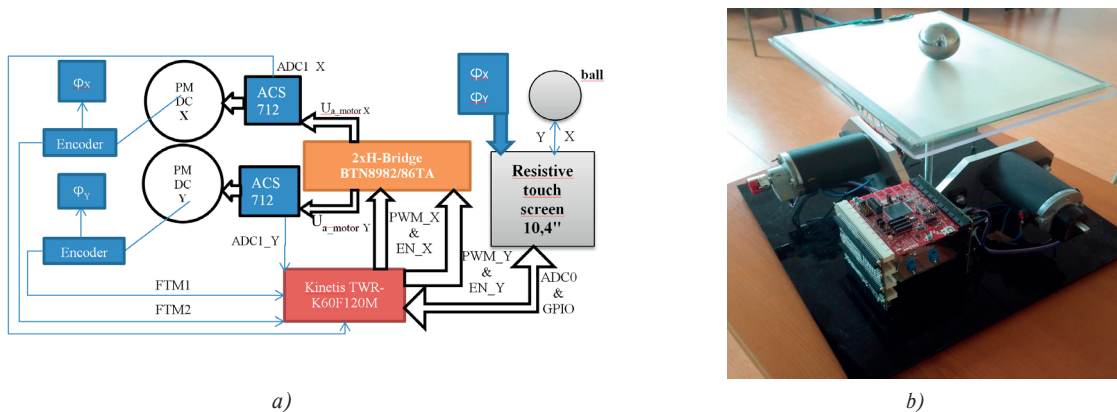
Figure 5 a) *Block diagram of proposed structure;* **b)** *Final form of investigated testbed*

The second control algorithm is based on a full state feedback. A state variable is one of the variables used to describe ability to accumulate energy which is speed and position of the ball. The general equation of the linear system with the state feedback is Equation (12). After the following adjustment occurs Equation (13).

$$\dot{X} = A \cdot X + B \cdot \left(K_z \cdot Ball\_position\_dem - K_R \cdot X \right) \qquad (12)$$

$$\dot{X} = \left(A - B \cdot K_R \right) \cdot X + B \cdot K_z \cdot Ball\_position\_dem \qquad (13)$$

Where X is a matrix of state variables (ball position, ball velocity), A is a system matrix, B is a matrix of input variables,

Figure 6 *Stabilization structures: a) PD controller; b) Full State Space Feedback, c) State Space Observer with State Space Feedback*

K_R is a feedback gain matrix, K_z is a compensatory input gain, and *Ball_position_dem* is demanded value of the ball's position at resistive surface. To determine dynamic properties of the proposed structure, eigenvalues placement of M_{CL} are important. Due to the

$$M_{CL} = [A - B \cdot K_R],$$

$$[A - B \cdot K_R] = \begin{bmatrix} 0 & 1 \\ 0 & 0 \end{bmatrix} - \begin{bmatrix} 0 \\ a_1 \end{bmatrix} \cdot [K_1 K_2] = \begin{bmatrix} 0 & 1 \\ -K_1 a_1 & -K_2 a_2 \end{bmatrix} \quad (14)$$

stability of the system, the left side of the complex plane is selected. Eigenvalues are obtained by solving characteristic equation **det** $[\lambda - A] = 0$. Subsequently, the result is compared to the polynomial with the prescribed behavior Equation (15). Searched constants K_1, K_2 Equation (16) have finally emerged.

$$\det[1 - A] = \lambda^2 + \lambda K_2 a_1 + K_1 a_1 \; ;$$
$$\lambda^2 + \lambda K_2 a_1 + K_1 a_1 = s^2 + 2\xi\omega_0 + \omega_0^2 \quad (15)$$

$$K_1 = \frac{\omega_0^2}{a_1}; K_2 = \frac{2\xi\omega_0}{a_1}; \frac{K_z a_1}{K_1 a_1} = 1 \Rightarrow K_z = K_1 \quad (16)$$

At this point, we are again using the final value theorem. There is a steady state error which will be compensated by the K_z constant Equation (16).

The last structure uses speed feedback from the state space observer. In the previous structures, the speed was obtained by differentiation of position. For the last structure, the derivation was replaced by a more complex observer. State observer reconstructs state variables by using a mathematical model of a controlled system. Observer equations are created by adding

measurable deviation $\varepsilon = x - \hat{x}$ into each system Equation (17). To determine the properties of the proposed structure, dynamic error system is important. By subtracting the observer matrix from the whole system matrix for one axis, we obtain a dynamic error system Equation (18). When time groves to infinity the errors and their derivations are equal to 0.

$$\begin{bmatrix} \dot{\hat{x}} \\ \ddot{\hat{x}} \end{bmatrix} = \begin{bmatrix} 0 & 1 \\ 0 & 0 \end{bmatrix} \begin{bmatrix} \hat{x} \\ \dot{\hat{x}} \end{bmatrix} + \begin{bmatrix} 0 \\ a_1 \end{bmatrix} \cdot \alpha_x + \begin{bmatrix} g_0 \\ g_1 \end{bmatrix} \cdot (x - \hat{x})$$
$$a_1 = \frac{5}{7} g = \frac{g}{h} \quad (17)$$

$$\begin{bmatrix} \dot{\varepsilon} \\ \ddot{\varepsilon} \end{bmatrix} = \begin{bmatrix} 0 & 1 \\ 0 & 0 \end{bmatrix} \cdot \begin{bm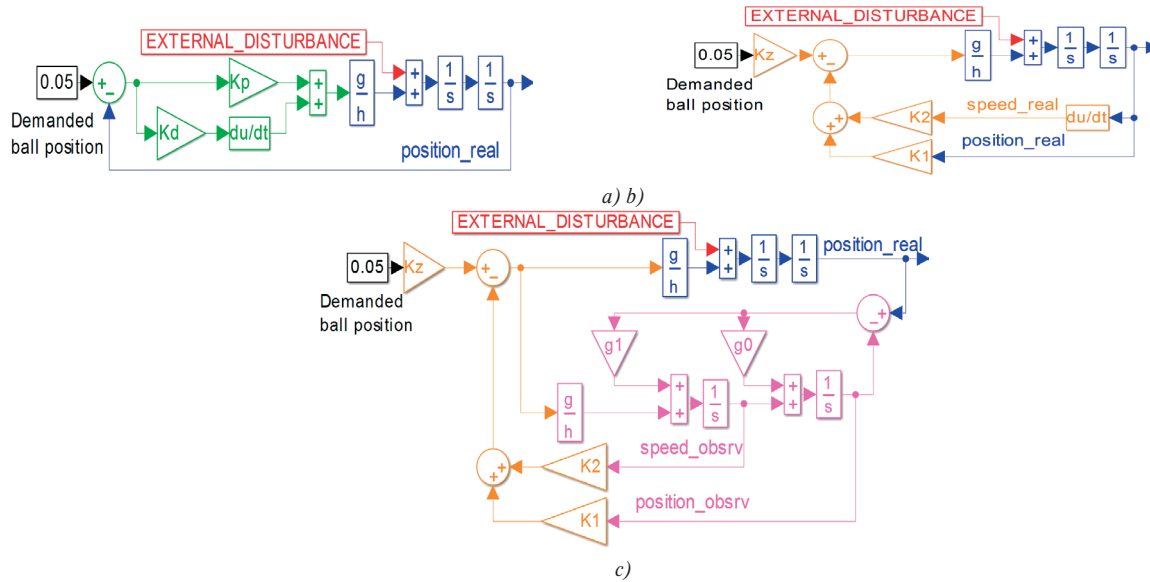atrix} \varepsilon \\ \dot{\varepsilon} \end{bmatrix} - \begin{bmatrix} g_0 \\ g_1 \end{bmatrix} \cdot \varepsilon \;\Rightarrow\; \begin{bmatrix} \dot{\varepsilon} \\ \ddot{\varepsilon} \end{bmatrix} = \begin{bmatrix} -g_0 & 1 \\ -g_1 & 0 \end{bmatrix} \cdot \begin{bmatrix} \varepsilon \\ \dot{\varepsilon} \end{bmatrix} \quad (18)$$

This stability condition is met when eigenvalues of the dynamic error system are located in the left part of the complex plane, det $[\lambda - A] = 0$. The result is compared to the second order polynomial with the prescribed behavior Equation (19). The calculated constants of the observer are according to the Equation (20).

$$\det[\lambda - A] = \begin{bmatrix} \lambda + g_0 & -1 \\ g_1 & \lambda \end{bmatrix} = \lambda^2 + \lambda g_0 + g_1 \; ,$$
$$\lambda^2 + \lambda g_0 + g_1 = s^2 + 2\xi\omega_0 + \omega_0^2 \quad (19)$$

$$g_0 = 2 \cdot \xi \cdot \omega_0 \qquad g_1 = \omega_0^2 \quad (20)$$

The same approach for designing the parameters was used in all three stabilization techniques.

All techniques were set using pole placement method. Settling time resp., the bandwidth was chosen by Dodd's formula. In the Figure 7 [9] there is a comparison of stabilization structures, which were implemented on real platform Figure 5b). All three structures have the same settling time $T_{sts} = 1 sec$. On the left side

Figure 7 Stabilization structures comparison

of Figure 7 there is stabilization on zero reference after deflection from the equilibrium position. At right side, there is stabilization from the rest position, to the new equilibrium position. Position loop of DC machine for one axis is shown below. The position of the ball is stable in all graphs at the desired value. The different situation can be seen in the position loop of DC machine for each axis. In the control structure with PD and full state feedback, there is visible noise in axis position loop. This is due to the computation method for the ball speed. The speed is here obtained by derivation of the measured ball position. This means that the noise from the touch screen sensing is also transmitted to the desired position value for the investigated axis. The position of the ball is stable, but the entire platform vibrates due to the noise amplified by derivative amplification. This negative property was removed in the third structure. A smooth change of both positions is ensured by the structure of the state observer. The observer has a smoothing effect, acting as a filter, but adds a delay to the whole control. In our case, the delay is negligible because the settling time of the observer (0.01sec) is too small in comparison to the dynamics of the entire structure (1sec).

Due to settling dynamics of the state space observer, the last structure shows the best results. The entire control diagram used for the testbed regulation is in the Figure 9b). The black part is position loop of DC machine. The blue belongs to the mathematical model of the ball at beam. The orange part represents the state space control low, and with purple color, the state space observer is highlighted. The two most important graphs are plotted for the analysis.

In step response, the initial intersection in the negative position is seen. This is mostly due to the mechanical backlash of the system. The following increase and settlement is in a very good (Figure 8) accordance with the simulations of the structure in Figure 9b). Simulated and measured frequency characteristics are just as good as shown in Figure 8. The reference trajectory tracking is shown in Figure 9a).
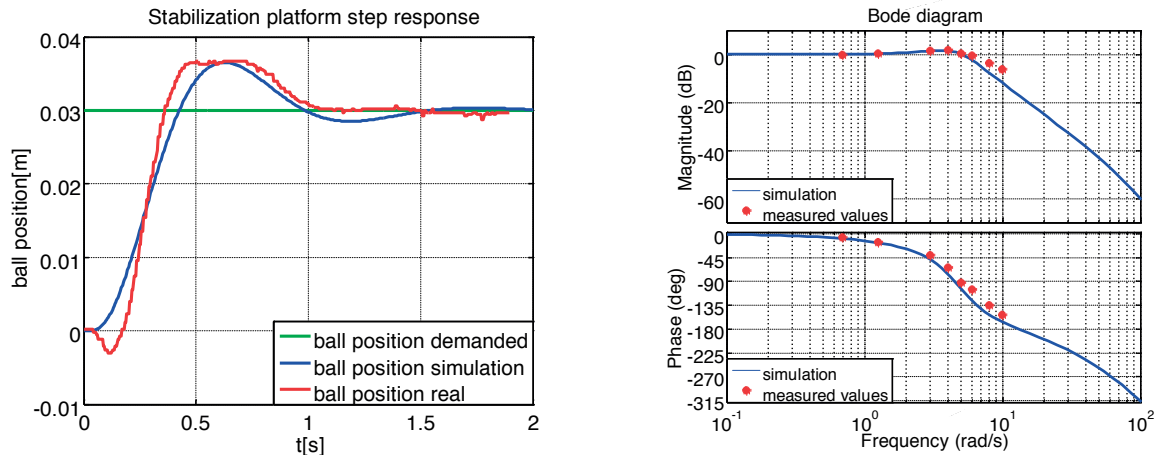
Figure 8 Final structure step response and Bode diagram

a)   *b)*
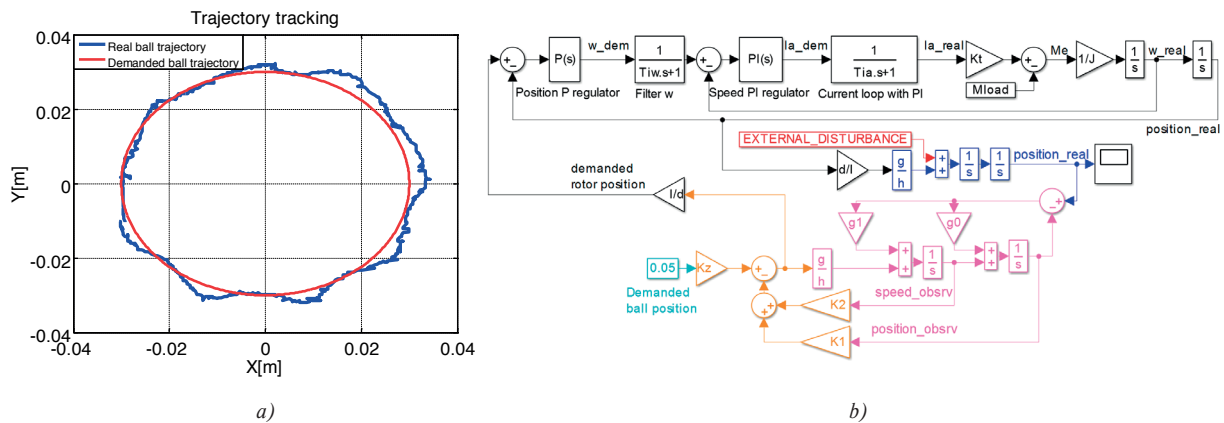
Figure 9 a) Trajectory tracking; *b)* Block diagram of control structure with PMDC position control

6. Conclusion

We have developed control strategies for stabilizing a ball on a plate. The basic system in an open loop is unstable. With minor modifications after applying linearization strategy, the system provides stable behavior. Linearization of the system is valid in very narrow operating range. The proposed system is capable of satisfying both intended goals. The controller was able to track the ball to the reference trajectory points. The presentation of the behavior of the most successful structure is on the following link: https://www.youtube.com/watch?v=Rr90hb_Rn3M.

Appendix

Table 1 Parameters of used PMDC

Sign	Definition	Value	Unit
R_a	Armature winding resistance	5.32	Ω
L_a	Armature winding inductance	0.01534	H
Ψ_{PM}	Linkage magnetic flux of PM	0.1432	Wb
J	Rotor moment of inertia	0.0000414	kg.m^2

References

[1] WETTSTEIN, N.: Balancing a Ball on a Plate Using Stereo Vision. Master Thesis. (ETH) Zurich, 2013.

[2] MING - TZU, H., YUSIE R., LI - MING CH.: Visual Servo Tracking Control of a Ball and Plate System. International Journal of Advanced Robotic Systems, 10(7), 1-16, 2013.

[3] HAIDER, A., NASIR, M., SAFIR, B., FAROOQ, F.: A Novel Ball on Beam Stabilizing Platform with Inertial Sensors, Part I: Modeling & Simulation with Detailed Geometrical Analysis. International Journal of Advanced Computer Science and Applications, 6(8), 54-61, 2015.

[4] SIMONOVA, A., DRGONA, P., FRIVALDSKY, M.: Automatic regulation (in Slovak). EDIS, Zilina, 2011.

[5] CHI - CHENG, CH., CHEN - HSUN, T.: Visual Servo Control for Balancing a Ball - Plate System. International Journal of Mechanical Engineering and Robotics Research, 5(1), 28-32, 2016.

[6] DUSEK, F., HRONC, D., SHARMA, K.: Modelling of Ball and Plate System Based on First Principle Model and Optimal Control. Proceeding of 21st International Conference on Process Control (PC), Slovakia, 216-221, 2017.

[7] VIRSEDA, M.: Modeling and Control of the Ball and Beam Process. Master Thesis. Lund Institute of Technology, 2004.

[8] VITTEK J.: Selected methods of control of electric drives in Matlab - Simulink. Trencin, 2004.

[9] SUMEGA, M.: Control of platform with two degrees of freedom (in Slovak). Master Thesis. Zilina, 2017.

Lubica Mikova - Ivan Virgala - Michal Kelemen - Tomas Liptak - Darina Hroncova*

MICROMACHINE FOR LOCOMOTION INSIDE PIPE

The paper deals with miniature machine for locomotion inside pipe. It uses impact energy as a principle of motion. Dynamics description and simulation model has been created. The deviations of the features are resulting from the fact that within the simulation model the friction between the bristle and the pipe wall is presented through the model not regarding the variability of the friction force and existing geometric deviations of the pipe inner surface.

Keywords: *mobile machine, pipelines, simulation*

1. Introduction

There are many applications where it is necessary to make inspection of pipes like steam generators, power plants, heat exchangers, chemical plants etc. Very often, the inspection is possible to be made only from the internal side of pipes. In-pipe machines are developed for this purpose. Inspection made via using of these in-pipe machines is needed as a prevention tool before dangerous accidents. This requirement was a driving impulse for the research and developing of in-pipe machines. The in-pipe machine is able to locomote inside the pipe and makes any activities like carrying of inspection tools or making repairmen of pipes [1-20].

The topic of this paper is in-pipe machine, which is designed for locomotion inside the pipe with inner diameter 11 mm (Figure 1).

2. Description of locomotion principle

For in-pipe locomotion the micromachine (Figure 1) uses the energy released during the impact of the two bodies [16-17] where one of the bodies is the drive (permanent magnet) and another one is driven (other parts of the micromachine). The driven body consists of the electromagnet and the guiding rod and the adjusting module. The drive body-permanent magnet (SmCo - Samarium Cobalt) is of a cylindrical shape with the axial hole and moves under the influence of the magnetic force and on the guiding rod between two impact surfaces of the driven body.

The active surface is one of the impact surfaces of the driven body (Figure 1). The second of the impact surfaces consists of the abutting surface of the helical spring being the part of the adjusting module. The front electromagnet position of the spring may be adjusted by the adjusting module.

The inertial stepping principle (Figure 2) rises from the impact of the drive body (permanent magnet) on the micromachine driven body.

On the perimeter of both the adjusting module and the electromagnet cover there are fixed the bristles. The bristles provide the micromachine contact with the inner pipe wall. The micromachine one-way locomotion results from the fact that the impact force on the active surface exceeds the frictional force between the bristles and the inner pipe wall and it does not apply for the impact force on the adjusting module spring. The micromachine diameter is 11 mm and its length is 35 mm.

The drive body-permanent magnet is embedded on a brass sleeve (Figure 1) with which it is moving on the guiding rod. The solenoid coil is excited by the square current pulses. A stabilized current supply maintains the constant value of the current pulse. Both the width and the frequency of the pulses may be adjusted by the single board microcomputer.

So that to take into account the essential details influencing the micromachine locomotion is an advisable micromachine operation to be divided into three tacts interlocking one another:
1. preparing tact,
2. active tact,
3. regeneration tact.

These tacts together form the micromachine motion cycle repeating during its operation with the repetitive frequency *f* resp.

---

* **Lubica Mikova, Ivan Virgala, Michal Kelemen, Tomas Liptak, Darina Hroncova**
Department of Mechatronics, Faculty of Mechanical Engineering, Technical University of Kosice, Slovakia
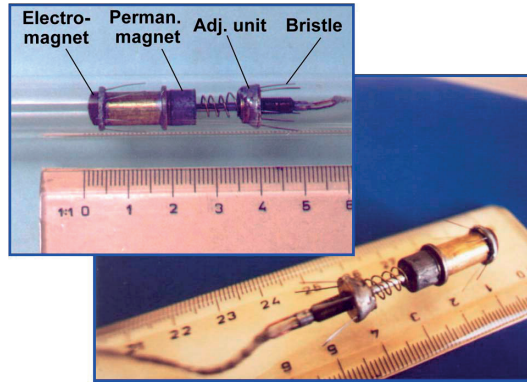E-mail: michal.kelemen@tuke.sk

Figure 1 Overall micromachine arrangement
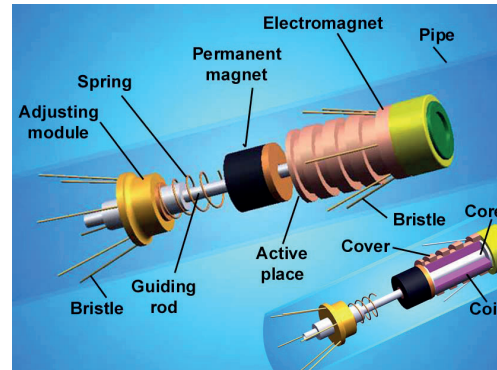
Figure 2 Simplified locomotion principle
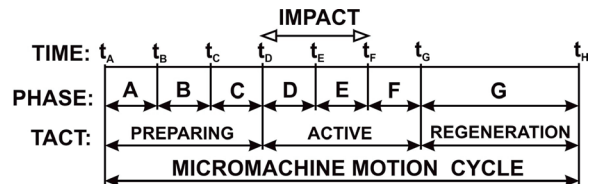
Figure 3 Time decomposition of micromachine motion cycle
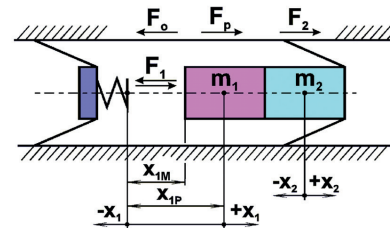
Figure 4 Simplified micromachine model
(m_1 driving body, m_2 driven body)

with the time of the cycle T. The respective tacts are divided into the phases. The diagram of the time decomposition and the initial and final phases times are shown in Figure 3. Further, there is described the operation of the micromachine during the respective phases and based on the micromachine model according to Figure 4.

The preparing tact consists of three phases: A, B, C (Figure 3 and Figure 5). During the initial part of the **phase A** the drive body (permanent magnet) contacts the active surface of the micromachine as the result of affecting attractive force F_P (Figure 4). Through the current impulse supplying into the coil of the electromagnet in the time $t = t_A$ the repulsive force F_O is activated where $|F_O| > |F_P|$ and resulting in drive body (permanent magnet) motion towards the adjusting module. The frictional force between the magnet and the guiding rod F_1 counterworks the permanent magnet motion. The time of duration of the repulsive force is adjusted experimentally and for example according to demanded micromachine motion speed and following the distance of the adjusting model spring x_{1P} from the micromachine permanent magnet. In the moment of finishing the repulsive force (time $t = t_B$) the phase A terminates and the phase B starts.

The phase B starts in the moment of termination of the repulsive force F_O in the time of $t = t_B$ and is finishing in the moment of termination of the driving body contact with the adjusting module spring in the time of $t = t_C$. During this phase the driving body is affected by the attractive force F_p. The absolute value of the damping spring deformation force resulting from the driving body impact on the adjusting module spring is lower than the absolute value of the frictional force F_2 during this phase. It means that the in-pipe machine does not change its position. The theoretical analysis [16] results in the fact that the maximum speed of the driving body impact on the active surface of the in-pipe machine occurs at the time when the repulsive force F_O works up to the moment of the maximum compression of the adjusting module spring.

The phase C starts at the moment of finishing the drive body and spring contacts during the phase B and in the time of $t = t_C$. Within this phase the drive body is accelerated by the attractive force F_P and towards the active impact surface of the in-pipe micromachine. At the moment of the contact with this surface and in the time of $t = t_D$ this phase is finished and the phase D of the active tact starts.

***Figure 5** Micromachine motion cycle*

The active tact consists of three phases: D, E, F (Figure 3 and Figure 5).

The phase D starts at the moment when the drive body contacts the driven body on the active impact surface. The phase D is an immediate continuation of the preparing tact and its duration is limited by duration of the impact of both the driven and drive bodies and in the time of $t = t_D$ and it finishes when the driving force F_h is equal to the frictional force F_2 and in the time of $t = t_E$. It means that the in-pipe machine is motionless (it does not change its position).
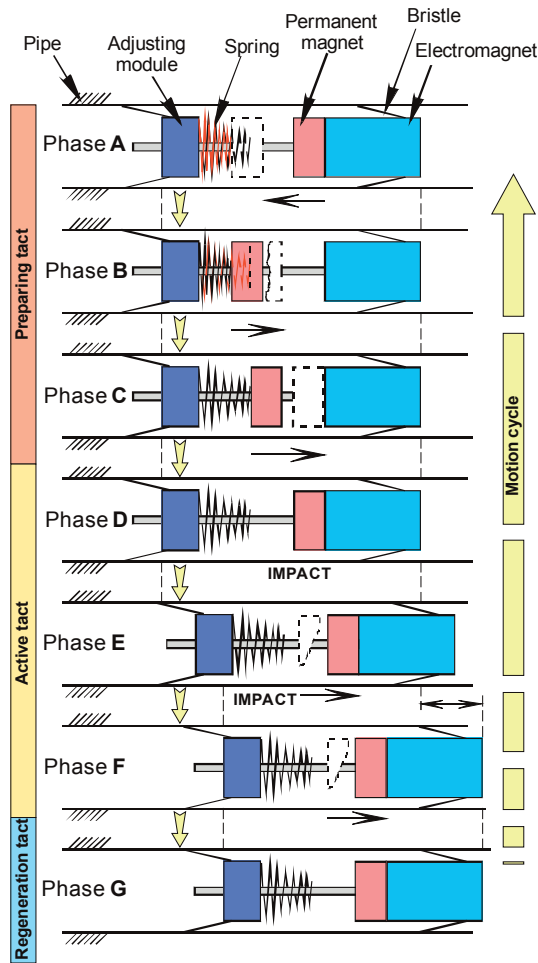
The **phase E** starts at the moment of $t = t_E$, when the driving force is equal to the frictional force $F_h = F_2$ and it is finishing in the time of $t = t_F$, when the driving force is $F_h = 0$. During the entire phase the in-pipe machine is in motion.

The phase F immediately follows the drive and driven bodies impact on the active surface and in the time of $t = t_F$ and it finishes at the moment when the micromachine stops and in the time of $t = t_G$ and when the micromachine activity turns to the regeneration tact.

The regeneration tact consists only of one **phase G** (Figure 3 and Figure 5). In the time of t_H - t_G its duration is determined by

allowed operational micromachine temperature (the heating up results from the joule loss in the coil of electromagnet). The coil is cooling down and both the in-pipe machine and the permanent magnet are motionless during this phase.

3. Dynamics of the machine

Regarding the preparation of the in-pipe machine description a simplified model is used (Figure 2 and Figure 5). The following description is prepared providing the motion within the horizontal pipe.

The beginning of the phase A falls within the time of the impact where the time in which the set mechanism initiates the repulsive force i.e. the speed of the driving body changes the positive speed sign to the negative speed of ($t = t_A$). The repulsive force lasts up to the moment when the speed drops to zero due to the deformation force of the adjusting module spring. At this moment ($t = t_B$) the phase A is finished and the phase B starts. The state space equations are responding to the phase A as follows:

a) Phase A with no adjusting module spring contact

$$\frac{dx_1(t)}{dt} = v_1(t)$$
$$\frac{dv_1(t)}{dt} = \frac{1}{m_1} \cdot [F_o(x_1) - F_1(v_1)] \tag{1}$$

b) Phase A in adjusting module spring contact

$$\frac{dx_1(t)}{dt} = v_1(t)$$
$$\frac{dv_1}{dt} = \frac{1}{m_1} \cdot [F_o(x_1) - F_1(v_1) - k_p \cdot (x_1(t) - x_2(t) - x_{1P})] \tag{2}$$

The phase B starts at the time of $t = t_B$ and finishes at the moment of termination of the adjusting module spring contact in the time of $t = t_C$. The attractive force F_p influences the driving body during this phase. The state space equations describing this phase are as follows:

$$\frac{dx_1(t)}{dt} = v_1(t)$$
$$\frac{dv_1}{dt} = \frac{1}{m_1} \cdot [F_p(x_1) - F_1(v_1) - k_p \cdot (x_1(t) - x_2(t) - x_{1P})] \tag{3}$$

The phase C starts in the time of $t = t_C$ and finishes at the moment of the contact with the active in-pipe machine impact surface in the time of $t = t_D$. The driving body is accelerated by the attractive force F_p during this phase. This phase is represented by the state space Equations (4).

$$\frac{dx_1(t)}{dt} = v_1(t)$$
$$\frac{dv_1(t)}{dt} = \frac{1}{m_1} \cdot [F_p(x_1) - F_1(v_1)] \tag{4}$$
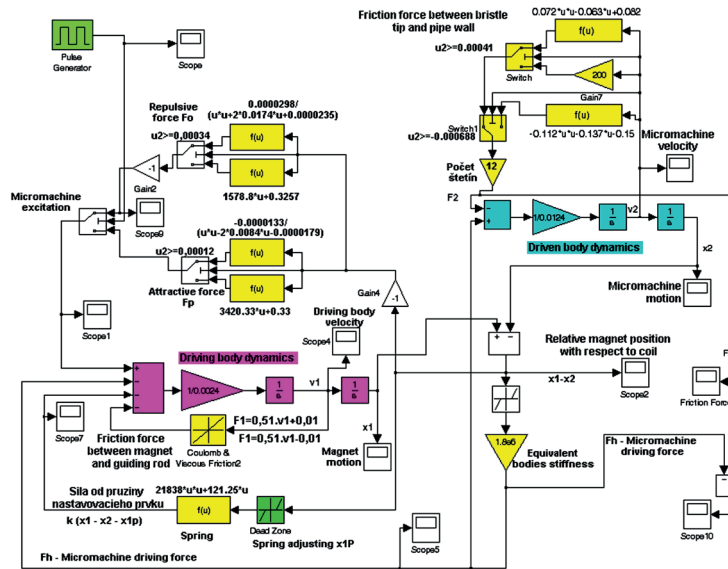
Figure 6 Simulation model of in-pipe machine

The phases D and E are connected since it may be described through the common scheme of the state space equations within the simulation experiment. The phase D starts at the moment of the driving and driven bodies contact on the active surface ($t = t_D$). The phase E finishes at the moment of $t = t_F$ when the speed v_1 changes the positive sign for the negative value. The motion dynamics is described by the equation scheme as follows:

Phase D + phase E (time of impact with $v_1 \geq 0$)

$$\frac{dx_1(t)}{dt} = v_1(t)$$
$$\frac{dv_1(t)}{dt} = \frac{1}{m_1} \cdot [F_p(x_1) - F_1(v_1) - F_h]$$
$$\frac{dx_2(t)}{dt} = v_2(t)$$
$$\frac{dv_2(t)}{dt} = \frac{1}{m_2} \cdot [F_h - F_2(v_2)]$$

(5)

where $F_h = k_e \cdot [x_1(t) - x_2(t)]$

As in any moment the value of the attractive force is lower than the frictional force between the bristles and the pipe wall then no attractive force influencing the driven body motion will be regarded.

The phase F is immediately following the drive and driven bodies impact and it finishes at the time t_G and at the moment of stopping the in-pipe machine. From the mathematical description aspect this phase is the most sophisticated. If the drive and driven bodies would not be influenced by the magnetic forces then the both bodies could move independently after the impact. As the mutual influence occurs then the entire course of this phase will be more complicated. In effort to avoid the complications it is predicted that the influence by the magnetic forces does not occurs and that the driven body is moving independently from the driving body. The state space equations of this phase are as follows:

$$\frac{dx_2(t)}{dt} = v_2(t)$$
$$\frac{dv_2(t)}{dt} = \frac{F_2(v_2)}{m_2}$$

(6)

In the work [16] is derived the steady velocity of the micromachine:

$$v_{2str} = \frac{1}{T} \cdot \int_{t_A}^{t_G} v_2(t) dt = \frac{2 \cdot m_r^2 \cdot v_{1Dd}^2}{m_2 \cdot T \cdot F_2}, m_r = \frac{m_1 \cdot m_2}{m_1 + m_2}$$

(7)

The steady velocity of the micromachine depends on the time of the micromachine cycle and on the integral of the micromachine driven body velocity.

4. Simulation model of the machine and experimental results

The simulation model which is shown in Figure 6, is assembled on the base of the previous description. The blocks, which are highlighted with yellow colour, represent the unknown parameters and dependencies:

- repulsive force between electromagnet and permanent magnet on relative distance between them,
- repulsive force between electromagnet and permanent magnet on relative distance between them,
- frictional force between the bristles and the pipe wall,
- friction force between the guiding rod and the magnet sleeve.

These parameters and dependencies have been identified experimentally.

Figure 7 Experimental examination of the traction force and velocity of in-pipe machine locomotion in horizontal steel pipe

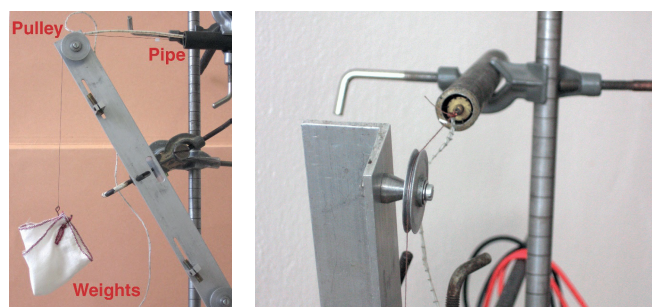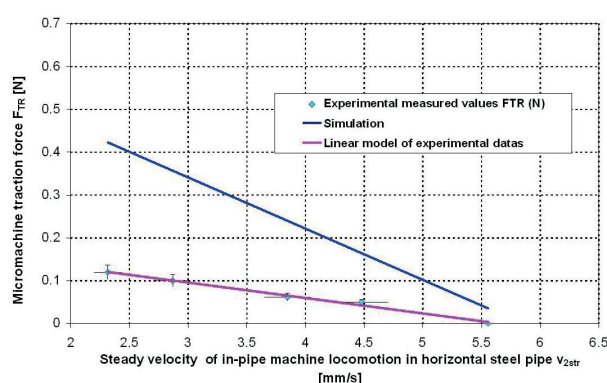*Figure 8 Traction force dependence on velocity of in-pipe machine locomotion in horizontal steel pipe*

Blocks, which are highlighted with green colour, are input variables. Figure 6 shows the simulation model of the micromachine locomotion. The model consists of two basic subsystems, i.e. a dynamic of the driving body (highlighted with magenta colour in Figure 6) and the dynamic of the driven body (highlighted with cyan colour in Figure 6).

Based on the mentioned equations (1-6) the simulation model was prepared within Matlab/Simulink and where the unknown parameters and the relations were completed (Figure 6). Regarding the verification of the results there were realized the experiments concerning the in-pipe machine in the horizontal pipe (Figure 7).

Figure 8 shows the relation of the traction force to the velocity of in-pipe machine locomotion in horizontal pipe and determined by both the experiments and the simulations.

The deviations of the features are resulting from the fact that within the simulation model the friction between the bristle and the pipe wall is presented through the model not regarding the variability of the friction force and existing geometric deviations of the pipe inner surface. In full the geometric deviations of the pipe inner surface effect the changes of the reference bristle force on the pipe wall and the same the friction force between the pipe wall and the in-pipe machine tips of the bristle.

The mathematical model of the friction force was experimentally identified by a simplified model not regarding the geometric deviations of the pipe inner surface (dimension deviation, shape deviation, surface roughness) [16].

5. Conclusion

The paper describes the in-pipe machine based on the two bodies impact principle and which is from the category of the in-pipe machines utilizing the inertial stepping principle.

One of the most important problems occurring during the in-pipe machine locomotion is its warming. The coil of the electromagnet is excited by relatively high current (1.6 A) with regard to the diameter of the wire (0.2 mm) of the coil winding. Thus for long-term operation of the in-pipe machine it is necessary to optimize the time of the regeneration tact in which the coil of the in-pipe machine cools down. The warming of the electromagnet coil represents a dangerous risk of a coil winding damage. From that reason on the case of the coil the in-pipe machine is equipped with a "cooling radiator" by which the temperature exchanges the surface of the in-pipe machine is extended. The miniature temperature sensor Ni200 for the purpose of automatic adjustment of the regeneration tact time duration is implanted in the front part of the coil. The length of the path passed during one motion cycle is 0.32 mm under the simulation. The maximum steady velocity of the in-pipe machine is 4.8 mm/s under the simulation (exciting frequency of 15 Hz). Experimentally was reached the maximum in-pipe machine locomotion velocity of 5.55 mm/s. In respect of existing geometric deviations of the pipe inner surface the unstable operation of the in-pipe machine occurs in some places of the pipe.

The presented solution of mobile robot uses un-conventional type of locomotion. Many other types of robots use only wheeled locomotion which is sensitive to dirties and wheel slipping occurs. The proposed principle is better to smaller diameter pipes, where conventional locomotion types cannot be used.

Acknowledgement

References

[1] AOSHIMA, S., TSUJIMURA, T., YABUTA, T.: A Miniature Mobile Robot Using Piezo Vibration for Mobility in a Thin Tube. Transactions of *ASME*, *Journal* of *Dynamic Systems*, *Measurements* and *Control*, 115, 270-278, 1993.

[2] IDOGAKI, T., KANAYAMA, H., OHYA, N., SUZUKI, H., HATTORI, T.: Characteristics of Piezoelectric Locomotive Mechanism for an In-Pipe Micro Inspection Machine. Proceedings of IEEE 6th International Symposium on Micro Machine and Human Science (MHS '95), Japan, 193-198, 1995.

[3] SUN, L., SUN, P., QIN, X., WANG, C.: Micro Robot in Small Pipe with Electromagnetic Actuator. Proceedings of the 1998 International Symposium on Micromechatronics and Human Science (MHS '98), Japan, 243-248, 1998.

[4] MATSUMOTO, T., OKAMOTO, H., ASANO, M., MITSUISHI, S., MATSUI, T.: A Prototype Model of Micro Mobile Machine with Piezoelectric Driving Force Actuator. Proceedings of IEEE 5th International Symposium on Micro Machine and Human Sciences (MHS '94), Japan, 47-54, 1994.

[5] FUKUDA, T., HOSOKAI, H., UEMURA, M.: Rubber Gas Actuator Driven by Hydrogen Storage Alloy for In-Pipe Inspection Mobile Robot with Flexible Structure. Proceedings of IEEE International Conference on Robotics and Automation, USA, 3, 1847-1852, 1989.

[6] IWASHITA, S., HAYASHI, I., IWATSUKI, N., NAKAMURA, K.: Development of in-pipe operation micro robots. Proceedings of IEEE 5th International Symposium on Micro Machine and Human Sciences (MHS '94), Japan, 41-45, 1994.

[7] SUZUMORI, K., MIYAGAWA, T., KIMURA, M., HASEGAWA, Y.: Micro Inspection Robot for 1-In Pipes. IEEE/ASME Transactions on Mechatronics, 4(3), 286-292, 1999.

[8] TAKAHASHI, M., HAYASHI, I., IWATSUKI, N., SUZUMORI, K., OHKI, N.: The Development of an In-Pipe Microrobot Applying the Motion of an Earthworm. Proceedings of IEEE 5th International Symposium on Micro Machine and Human Sciences (MHS '94), Japan, 35-40, 1994.

[9] SUN, L., SUN, P., QIN, X., WANG, C.: Micro Robot in Small Pipe with Electromagnetic Actuator. Proceedings of the 1998 International Symposium on Micromechatronics and Human Science (MHS '98), Japan, 243-248, 1998.

[10] HIROSE, S., OHNO, H., MITSUI, T., SUYAMA, K.: Design of In-Pipe Inspection Vehicles for -25, -50, -150 Pipes. Proceedings of IEEE International Conference on Robotics and Automation, USA, 2309-2314, 1999.

[11] DEGANI, A., FENG, S., CHOSET, H., MASON, M. T.: Minimalistic, Dynamic, Tube Climbing Robot. Proceedings of IEEE International Conference on Robotics and Automation, USA, 1100-1101, 2010.

[12] VITKO, A., JURISICA, L., KLUCIK, M., DUCHON, F.: Context Based Intelligent Behaviour of Mechatronic Systems. Acta Mechanica Slovaca, 12(3-B), 907-916, 2008.

[13] ANTAL, D.: Dynamical Modelling of a Path Controlled Vehicle. International Scientific Conference XXIV. micro CAD, Hungary, 1-6, 2010.

[14] GMITERKO, A., DOVICA, M., KELEMEN, M., FEDAK, V., MLYNKOVA, Z.: In-Pipe Bristled Micromachine. Proceedings of 7th International Workshop on Advances Motion Control, Slovenia, 467-472, 2002.

[15] GMITERKO, A., KELEMEN, M.: Bristled In-Pipe Micromachine Simulation. Mechatronika, 193-198, 2003.

[16] KELEMEN, M., MATASOVSKA, T.: Identification of the In-Pipe Machine Properties Based on Inertial Stepping Principle. AT&P Journal, 13(1), 5, 2006.

[17] GMITERKO, A., KELEMEN, M., GOTS, I.: Basic Characteristics of In-Pipe Micromachine Karolina. Mechatronika, 146-151, 2001.

[18] KELEMEN, M., MATASOVSKA, T.: Simulation of the In-Pipe Machine Locomotion Based on the Innertial Stepping Principle. Bulletin of Applied Mechanics, 1(4), 231-246, 2005.

[19] KARAVAEV, Y. L., KILIN, A. A., KLEKOVKIN, A. V.: Experimental Investigations of the Controlled Motion of a Screwless Underwater Robot. Regular and Chaotic Dynamics, 21(7-8), 918-926, 2016.

[20] HARGAS, L., KONIAR, D., SIMONOVA, A., Hrianka, M., Loncova, Z.: Novel Machine Vision Tools Applied in Biomechatronic Tasks. Proceedings of 6th Conference on Modelling of Mechanical and Mechatronic Systems (MMaMS), Slovakia, 148-156, 2014.

KOMUNIKÁCIE
COMMUNICATIONS

Tomas Kavalir - Michal Krizek - Jiri Sika - Vladimir Kindl*

UPGRADING OF THE SINGLE POINT LASER VIBROMETER INTO A LASER SCANNING VIBROMETER

The paper proposes a construction design of measuring device for fast and reliable non-contact modal analysis of object surfaces which cannot be measured using classical methods. The design combines conventional non-contact laser interferometer with an active optics module to be able to measure multiple points in a rapid sequence. The paper briefly discusses all the key constructional components and describes in detail the system functional layout. It also introduces the experimental measurement of a HV transformer under operation to demonstrate the system functionality.

Keywords: modal analysis, laser, doppler, vibrometry, measurement, prototype

1. Introduction

The method of Laser Doppler Vibrometry (LDV) has been widely used in medical [1, 2] or engineering applications involving the non-contact vibration [3-7] and can be also adopted for electrical engineering, especially when contact with the measured surface is not possible, such as measuring machines under operation, measuring of hot surfaces or surfaces which are under high voltage operation [8, 9].

However, since most single point LDV systems are only capable of sensing data for one point at a time, performing modal analysis to obtain an operational deflection shape tend to be quite long process. This problem is even more difficult for bigger structures or for structures with low natural frequencies, such as aircraft, space structures or civil structures, which would require more measurement points and excessively longer testing time if a single point LDV were used [10-12].

There are several types of laser-scanning vibrometers available on the market that can measure multiple points simultaneously, but their cost is too high. Only a few literature sources deal with its own vibrometer design whereas the most relevant work to this issue has been published in [13]. Here, the authors introduced a design of three-dimensional vibration measurement system consisting of one laser scanning vibrometer, one CCO camera and one laser scanner. Though it can measure the shape and vibration of the tested object at the same time, it is still expensive.

This paper describes the unique device developed to measure vibration for fast and reliable modal analysis of facial surfaces. Measurement of vibration via LDV has been used as the instrument of choice when contactless measurement and measurement with high spatial detail is required. The proposed vibrometer construction allows us to redirect the laser beam via computer controlled mirrors to acquire data for predefined matrix of measurement points. Moreover, it upgrades the single-point vibrometer into the fast programmable 2D fullfield vibration scanner [14, 15].

2. Construction design

The proposed measuring device, seen in Figure 1, exploits the benefits of a functional connection of the conventional non-contact laser interferometer (PDV 100) and the active optics with the fast steering mirrors. The interferometer generates laser beam which is sequentially redirected via the computer controlled mirrors in a predefined pattern. This solution enables us to perform multi-point measurements in a rapid sequence, having no back effect on the tested object. In addition, it will considerably simplify either the operational deflection shape (ODS) or the modal analysis of complicated 3D objects. The influence of the varying deflection angle of the laser beam pointing the measurement locations can be reduced using the proper software

* [1]Tomas Kavalir, [1]Michal Krizek, [1]Jiri Sika, [2]Vladimir Kindl
  [1]Regional Technological Institute, Faculty of Mechanical Engineering, University of West Bohemia, Pilsen, Czech Republic
  [2]Regional Innovation Centre for Electrical Engineering, Faculty of Electrical Engineering, University of West Bohemia, Pilsen, Czech Republic
  E-mail: vkindl@kev.zcu.cz
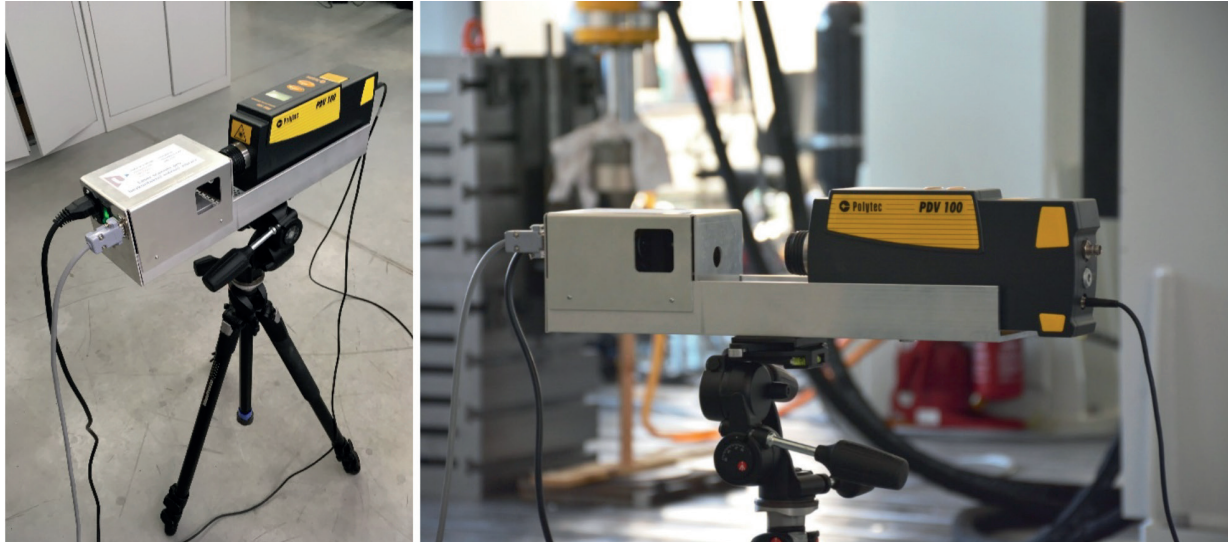
Figure 1 LDV with XY scan head
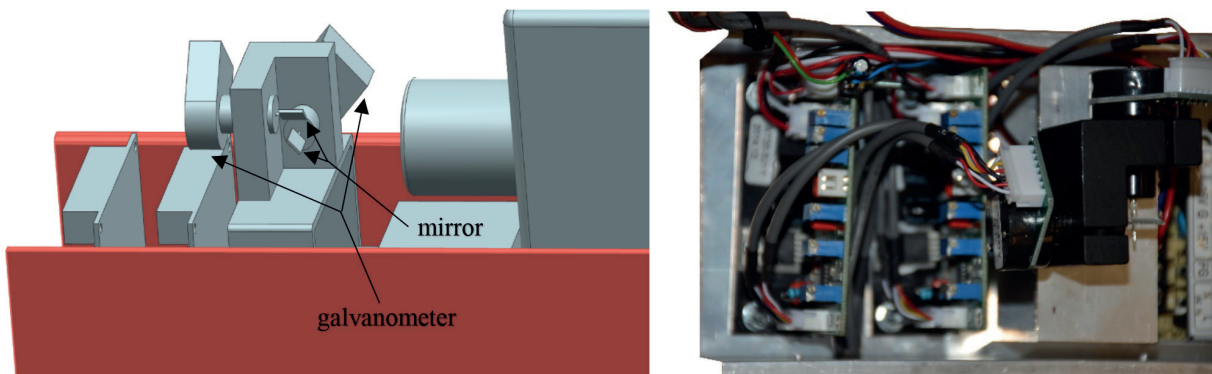
Figure 2 Detailed 3D mechanical model of the measuring system with the LDV (left), inside view of the mirrors with galvanometer and control electronics (right)

compensation, but if the testing object is far enough, it would be neglected.

The laser deflecting module (see Figure 2) is based on the principle of galvanometer with special mirrors mounted on its axes. In this case, we adapted the mechanism of the low-cost X-Y GALVO scanner, commonly used in the field of entertainment electronics for sweeping and rendering the laser beam patterns. In order to prevent any laser beam disturbance, the mirrors should provide high reflectivity and low roughness. The mechanism is driven by electronics, sometimes called DC servo, giving us very fast and accurate dynamic response of the deflection module measured in both axes. All the components are assembled together on a mutual chassis made up of structural AL profiles, forming a compact device suitable for practical application.

Figure 3 shows an input control console, based on a single-board microcomputer, using an intelligent graphical display to show either the relevant communication data or the main systems settings. The controller is based on the Arduino Esplora programmable array, including control buttons, joystick for the

laser beam control and local storage to store programmable data for further re-editing or resetting the measurement sequence. The control console is mounted into a compact plastic chassis printed by a 3D printer.

The measured data are processed using the PULSE™ analyses system developed by BK Company [16]. The system is extended with our own software routine to perform the modal analyses and includes measurement card with accessories that processes the signals from the LDV and the auxiliary reference sensor. The overall specification of developed measuring device may be listed in Table 1.

3. Experiment

For the functional demonstration, the operational deflection shape of a 22 kV transformer, with 1000 kVA of rated power, was made. The transformer was partially loaded during the test and was located in the HV transformer cell behind a barrier (see
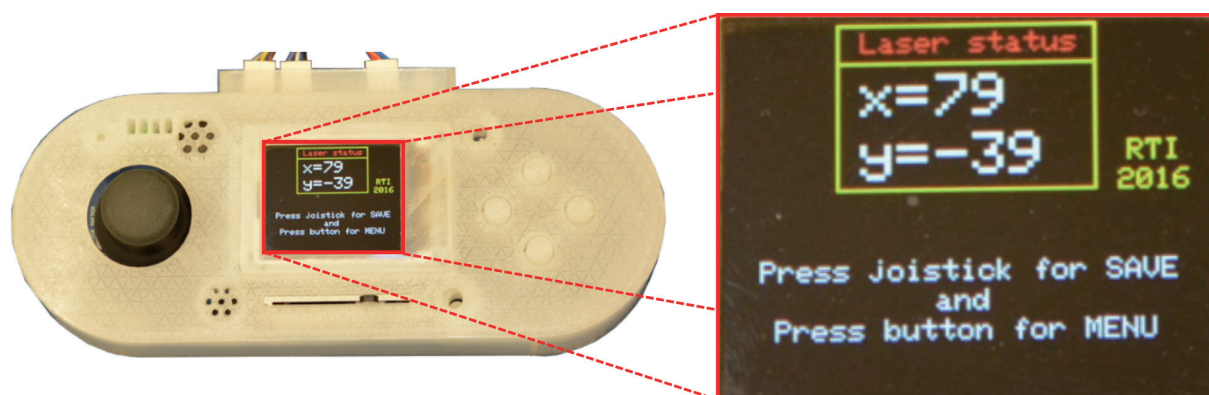
Figure 3 *The control console with Arduino Esplora for XY scan head*

Figure 4 *Tested HV transformer; without the safety barrier (left), measuring points programming (right)*

Table 1 Proposed device specification

Parameter	Values	Additional Notes
Input resistance	200 kΩ	differential
Signal input voltage	± 5 V	
Input voltage requirements	+ 15 V/1.0 A and - 15 V/0.6 A	
Operating temperature range	0 ÷ 50 °C	
Operational optical angle	± 30 degrees	max
Scanner speed	>15 kpps	30 kpps, ± 20° optical
Mirror dimensions (width, height, thickness)	7 mm, 11 mm, 0.6 mm	wide wave-length

Figure 4). Our goal was to demonstrate the strong advantage of the proposed system laying in possibility to measure under conditions when the testing operator has no direct access to the tested object. Thus, it is particularly relevant to the application where there is no possibility to measure using classical contact methods (like accelerometers) due to the high voltage, high temperature or other possible reasons.

The testing procedure may be understood from Figure 5. The required x- and y- positions of the laser beam are considered as inputs to the CPU (Arduino Esplora). This command is set using the joystick and then it is sampled by an 8-bit A/D transducer. Data are further processed by the predefined algorithm, but they could be additionally modified or manipulated. Up to 256 x 256 pixels (measuring points) can be uploaded into the internal or external storage (micro SD card). Then, the sequence of stored points can be recalled and executed by defined scanning speed. At the output of the CPU, two signals corresponding to the x- and y- positions are generated by the PWM modulation. Since the control unit for the galvanometer requires a DC signal fluctuating in the range of 0÷5 V, a low-pass filter is applied at the output of
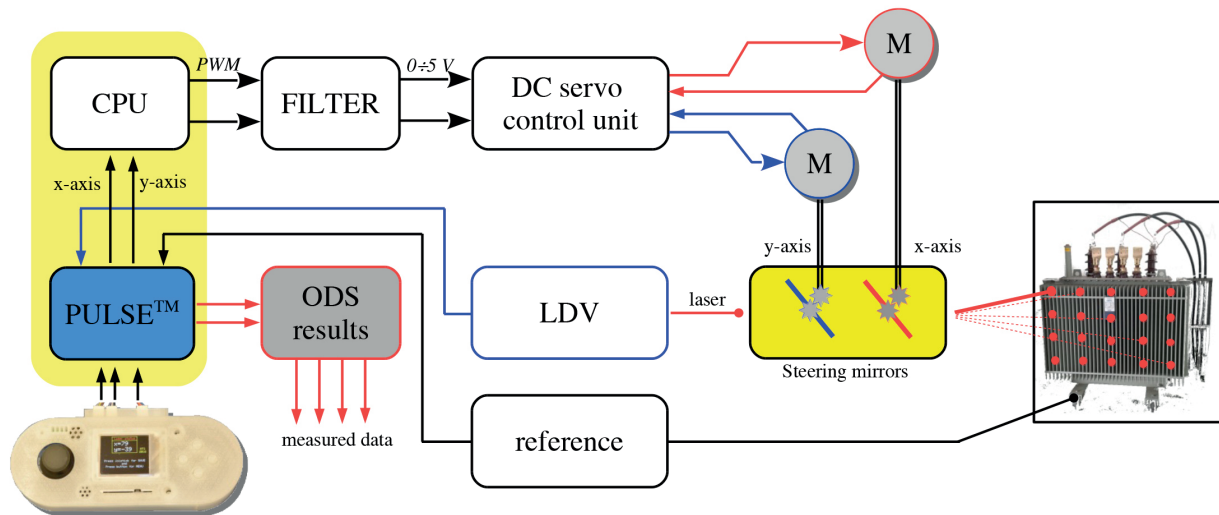
Figure 5 *Block diagram of the measuring procedure*
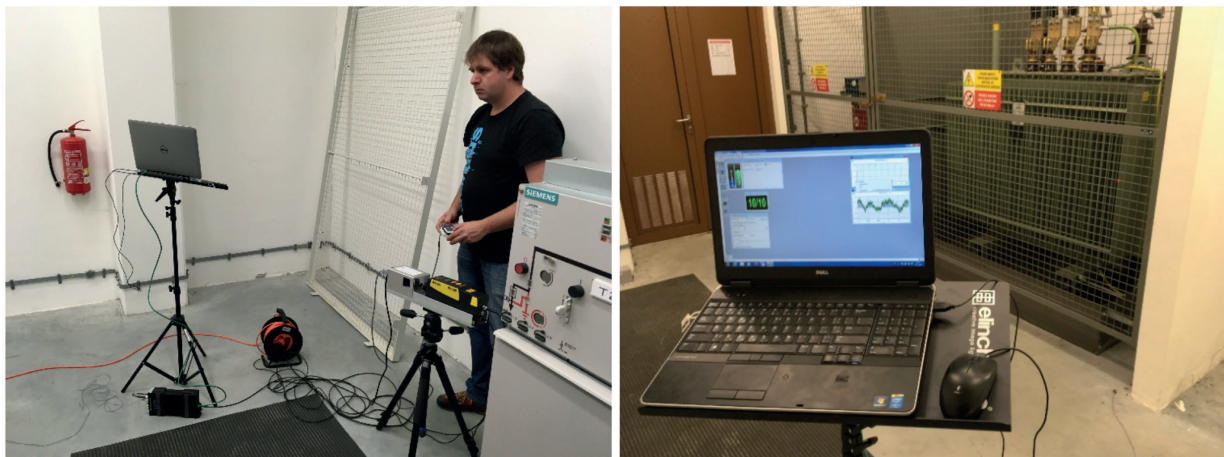
Figure 6 *Experimental setup; the programming procedure (left), calibration (right)*

the CPU. This regulation is highly accurate and quick enough to provide precise mirror adjustments according to set commands.

The measuring mechanism is driven by the PULSE™ system extended with our own SW routine for data processing. It continuously collects data from the LDV and the reference sensor, needed for the proper system synchronization. Based on these data, the operational deflection shape, corresponding to the evaluated vibration, is calculated.

Figure 6 shows the situation during the measurement. On the left-hand side, the procedure of programming is seen, the right-hand side shows the preparatory measurement and the system calibration.

The resulting vibration map measured on the transformer is seen in Figure 7. The results show that the proposed constructive solution of the testing device is fully functional and it is also suitable for the non-contact vibration sensing. As a consequence, the device upgrades a common single point vibrometer into the

full-filed vibrometer, which can visualize either the Eigen modes or the operating deflection shapes of any tested object.

4. Conclusion

The experimental measurement has proven good operability of the proposed laser-scanning vibrometer even in an industry application. Due to the fact that the design combines conventional non-contact laser interferometer with a low-cost X-Y GALVO scanner, primary designated to the field of entertainment electronics, we have achieved significant financial savings while maintaining very good operational usability. The vibrometer can measure multiple points in a rapid sequence and hence it will find its purpose especially when measuring either the Eigen modes or the operating deflection shapes. Moreover, the measurement is non-contact and therefore it has no feedback effect on
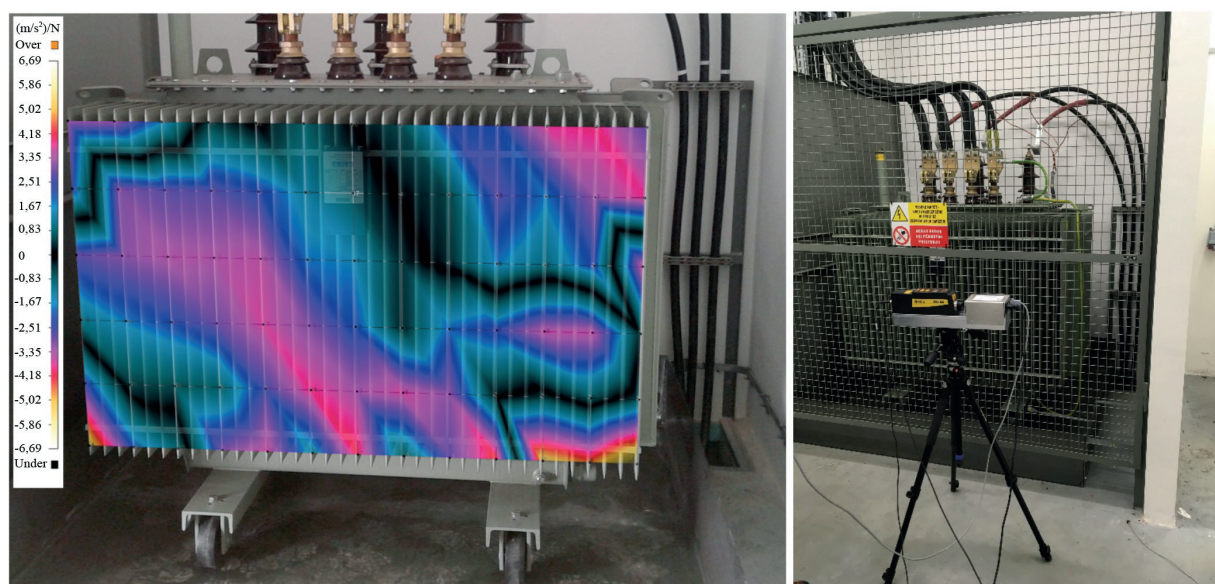
Figure 7 *Measured ODS results mapped onto the transformer*

a tested object. This may also be beneficial for testing objects operating under high voltage, high temperature or being otherwise inaccessible. The bottle neck seems to be ensuring proper surfaces reflection together with manual focusing of laser beam between measured points. There is also the need of dedicated analysis hardware and software tool to display results. For field measurement it is recommend a dust protection because dust can damage the functionality of the mirror based optical system.

Acknowledgements

References

[1] CASACCIA, S., SCALISE, L., CASACANDITELLA, L., TOMASINI, E. P., ROHRBAUGH, J. W.: Non-Contact Assessment of Muscle Contraction: Laser Doppler Myography. *Proceedings of IEEE International Symposium on Medical Measurements and Applications (MeMeA)*, Italy, 610-615, 2015.

[2] SCALISE, L., ERCOLI, I., MARCHIONNI, P., TOMASINI, E. P.: Measurement of Respiration Rate in Preterm Infants by Laser Doppler Vibrometry. *Proceedings of IEEE International Symposium on Medical Measurements and Applications*, Italy, 657-661, 2011.

[3] KANDRAC, J., FRIVALDSKY, M., PRAZENICA, M., SIMONOVA, A.: Design and Verification of Proposed Operation Modes of LLC Converter. Elektronika ir Elektrotechnika/ Electronics and Electrical Engineering, 18(8), 27-30, 2012.

[4] TORCIANTI, B., CRISTALLI, C., VASS, J.: Non-Contact Measurement for Mechanical Fault Detection in Production Line. *Proceedings of* IEEE International Symposium on Diagnostics for Electric Machines, Power Electronics and Drives, Poland, 297-301, 2007.

[5] SPANIK, P., SEDO, J., DRGONA, P., FRIVALDSKY, M.: Real Time Harmonic Analysis of Recuperative Current through Utilization of Digital Measuring Equipment. Elektronika ir Elektrotechnika/ Electronics and Electrical Engineering, 19(5), 33-38, 2013.

[6] HUANG, Y. H., MA, C. C.: Experimental Measurements and Finite Element Analysis of the Coupled Vibrational Characteristics of Piezoelectric Shells. IEEE Transactions on Ultrasonics, Ferroelectrics, and Frequency Control, 59(4), 785-798, 2012.

[7] MALLYA, A. N., RAMAMURTHY, P. C. : Mechanical Actuation of Conducting Polymer in the Presence of Organic Vapor Stimulus. IEEE Sensors Journal, 17(11), 3391-3397, 2017.

[8] SUGIMOTO, T., AKAMATSU, R., UTAGAWA, N., TSUJINO, S.: Study on Non Contact Acoustic Imaging Method for Non Destructive Inspection Using SLDV and LRAD. *Proceedings of IEEE International Ultrasonics Symposium,* USA, 744-747, 2011.

[9] KOSCELNIK, J., FRIVALDSKY, M., PRAZENICA, M., MAZGUT, R.: A Review of Multi-Elements Resonant Converters Topologies. *Proceedings of* 10th IEEE International Conference ELEKTRO 2014, Slovakia, 312-317, 2014.

[10] LAURENTIU-MARIAN, A., ALEXANDROS, R.: A Theoretical Approach Based on the Correlation of Unified Data for Different Analyzing Techniques Used in the Modern Investigation of Artworks. *Proceedings of Developments in E-systems Engineering*, England, 89-92, 2010.

[11] REITEN, M. T., WRIGHT, R. G.: Laser Doppler Vibrometry Use in Detecting Faulty Printed Circuit Boards. *Proceedings of IEEE AUTOTESTCON*, USA, 33-36, 2008.

[12] KIM, D., SONG, H., KHALIL, H., LEE, J., WANG, S., PARK, K.: Corrections to "3-D Vibration Measurement Using a Single Laser Scanning Vibrometer by Moving to Three Different Locations" [Aug 14 2028-2033]. *IEEE Transactions on Instrumentation and Measurement*, 63(10), 2504-2504, 2014.

[13] AMBROZINSKI, L., SPYTEK, J., DZIEDZIECH, K., PIECZONKA, L., STASZEWSKI, W. J.: Damage Detection in Plate-Like Structures Based on Mode-Conversion Sensing With 3D Laser Vibrometer. *Proceedings of IEEE International Ultrasonics Symposium (IUS)*, USA, 1-4, 2017.

[14] YOON, H., SONG, H., PARK, K.: A Phase-Shift Laser Scanner Based on a Time-Counting Method for High Linearity Performance. Review of Scientific Instruments, 82(7), 075108, 2011.

[15] KIM, D., PARK, K.: Development of a Three-Dimensional Vibration Measurement System Using a Single Laser Scanning Vibrometer and Laser Scanner. *Proceedings of 13th International Conference on Control, Automation and Systems (ICCAS 2013)*, South Korea, 1378-1380, 2013.

[16] BK Company: Pulse [online]. Available: https://www.bksv.com/media/doc/bu0229.pdf.

Oleg V. Chernoyarov - Yury A. Kutoyants - Mariana Marcokova*

ON FREQUENCY ESTIMATION FOR PARTIALLY OBSERVED SYSTEM WITH SMALL NOISES IN STATE AND OBSERVATION EQUATIONS

We consider the problem of frequency estimation of the periodic signal multiplied by a Gaussian process (Ornstein-Uhlenbeck) and observed in the presence of the white Gaussian noise. We demonstrate the consistency and asymptotic normality of the maximum likelihood and Bayesian estimators in the sense of the small noise asymptotics. The model of observations is a linear nonhomogeneous partially observed system and the construction of the estimators is based on the Kalman-Bucy filtration equations. For the study of the properties of the estimators, we apply the techniques introduced by Ibragimov and Has'minskii.

Keywords: *partially observed linear system, stochastic signal, frequency estimator, maximum likelihood method, Bayesian approach, characteristics of estimators, small noise asymptotic*

1. Introduction

The problem of the estimation of the frequency (Doppler shift) of the signal is of a great importance in the fields of radio-and-hydroacoustic communications and positioning, radio-and-hydrolocation, radio-and-hydroacoustic positioning, etc. [1-3]. The simplest model for the useful signal is the harmonic wave with the amplitude A and the frequency ϑ_0:

$$s(t) = A\cos(2\pi\vartheta_0 t) \tag{1}$$

While propagating, the signal $s(t)$ can be distorted by both additive $n(t)$ and multiplicative $Y(t)$ interferences [3-6]. As the model of the additive interferences, following [1-3], we choose the white Gaussian noise (WGN) with the double-sided spectral density σ_2 (correlation function $\langle n(t_1)n(t_2)\rangle = \sigma^2\delta(t_2 - t_1)$). For the statistical description of the multiplicative interferences, the stationary centered Gaussian random process can be often applied [3, 7]. As a result, the mix

$$X(t) = A\cos(2\pi\vartheta_0 t)Y(t) + n(t), \quad 0 \le t \le T \tag{2}$$

is available for an observation.

We presuppose that the process $Y(t)$ satisfies a linear stochastic equation. The simplest examples are the following.

Example 1. Ornstein-Uhlenbeck (O-U) process

$$\dot{Y}(t) + aY(t) = bN(t), \quad 0 \le t \le T \tag{3}$$

where $\dot{Y}(t) = dY(t)/dt$; $a > 0$, $b > 0$ are certain parameters; $N(t)$ is WGN with the unit double-sided spectral density, while the processes $n(t)$ and $N(t)$ are statistically independent. As it is well known [2], the correlation function $R(\tau)$ and the spectral density $G(\lambda)$ of the process $Y(t)$ are determined as

$$R(\tau) = b^2\exp(-a|\tau|)/2a \quad G(\lambda) = b^2/(a^2 + 4\pi^2\lambda^2) \tag{4}$$

Example 2. The process $Y(t)$ described by the equation

$$\ddot{Y}(t) + a\dot{Y}(t) + a_0Y(t) = bN(t), \quad 0 \le t \le T \tag{5}$$

subject to condition $a_1^2 < 4a_0$. For the correlation function and the spectral density of the process $Y(t)$ (5), we have [2]

* [1]Oleg V. Chernoyarov, [2]Yury A. Kutoyants, [2]Mariana Marcokova
  [1]Department of Electronics and Nanoelectronics, National Research University "Moscow Power Engineering Institute", Russia and International Laboratory of Statistics of Stochastic Processes and Quantitative Finance of Tomsk State University, Russia
  [2]Laboratoire Manceau de Mathématiques, Le Mans University, France and International Laboratory of Statistics of Stochastic Processes and Quantitative Finance of Tomsk State University, Russia
  [3]Department of Structural Mechanics and Applied Mathematics, University of Zilina, Slovakia
  E-mail: chernoyarovov@mpei.ru

$$R(\tau) = \frac{b^2}{2a_0 a_1} \exp(-\gamma|t|) \left[\cos(\omega\tau) + \frac{\gamma}{\omega} \sin(\omega|\tau|) \right]$$
$$G(\lambda) = \frac{b^2}{[a_0 - 4\pi^2\lambda^2]^2 + 4\pi^2 a_1^2 \lambda^2} \tag{6}$$

Here $\gamma = a_1 / 2$ and $\gamma^2 + \omega^2 = a_0$.

For simplicity of description, we presuppose that $Y(t)$ is the O-U process and we refer to the formalism of stochastic calculus. It should be noted that all the results presented below for the O-U process can be directly extended to encompass not only the model presented in Example 2, but the much more complicated linear partially observed systems as well, though in this case the calculus and the expressions involved turn to be much more cumbersome.

Thus, we have the observation model (2) and (3) presented in the form of the two-dimensional stochastic process $(X_t, Y_t, 0 \le t \le T)$ satisfying the differential equations

$$dX_t = A\cos(2\pi\vartheta_0 t)Y_t dt + \sigma dW, \quad X_0 = 0$$
$$dY_t = -aY_t dt + bdV_t, \qquad\qquad Y_0 = y_0 \tag{7}$$

Here $W_t, 0 \le t \le T$ and $V_t, 0 \le t \le T$ are two independent Wiener processes. The parameters A, σ, a, b are presupposed to be already known and positive, while the parameter $\vartheta_0 \in \Theta = (\alpha, \beta)$ is unknown and has to be estimated by the observations $X^T = X(T)$ (2). We have partially observed linear system, where the component Y_T is not observable.

In [1, 3], the estimate is considered of the band center of random process with the fractional rational spectrum observed against Gaussian white noise; in [5], the results [1, 3] are generalized for the case when the spectral density of the random process is described by Gaussian curve. At last, in [6], the characteristics are found of the estimate of the band center of random process with free-form spectral density. And it is presupposed everywhere that the analyzed random process is stationary, while the asymptotic properties of the introduced band center estimates are examined under $T \to \infty$ only. The further extension of the specified problem is the use of non-stationary model of the useful random signal of the type (7) describing a practically important wide class of stochastic information processes and obtaining the properties of the estimate of unknown frequency parameter in wider range of asymptotics. In such context, the problem of statistical analysis of the estimate of random process band center is considered for the first time.

We now study two estimators of the parameter ϑ: $\hat{\vartheta}_T$ – the maximum likelihood estimator (MLE) and $\tilde{\vartheta}_T$ – the Bayesian estimator (BE). Let us remind the definitions of these estimators. We designate the current value of the unknown parameter ϑ_0 as ϑ and introduce the conditional mathematical expectation

$$m(\vartheta, t) = E_\vartheta(Y_t | X_s, 0 \le s \le t), \quad 0 \le t \le T \tag{8}$$

Then, according to [8], the likelihood ratio function can be formulated as

$$V(\vartheta, X^T) = \exp\left[\frac{1}{\sigma^2} \int_0^T \cos(2\pi\vartheta t)m(\vartheta, t)dX_t - \right.$$
$$\left. -\frac{1}{2\sigma^2} \int_0^T \cos^2(2\pi\vartheta t)m^2(\vartheta, t)dt \right], \quad \vartheta \in \Theta \tag{9}$$

The MLE $\hat{\vartheta}_T$ is determined by the relation [1-3]

$$V(\hat{\vartheta}_T, X^T) = \sup_{\vartheta \in \Theta} V(\vartheta, X^T) \tag{10}$$

To introduce the BE $\tilde{\vartheta}_T$, we presuppose that the parameter ϑ is a random variable having the continuous positive probability density $p(\theta)$, with $\alpha < \theta < \beta$ and the quadratic loss function. Then the BE is [1-3]

$$\tilde{\vartheta}_T = \int_\alpha^\beta \theta p(\theta)V(\theta, X^T)d\theta \bigg/ \int_\alpha^\beta p(\theta)V(\theta, X^T)d\theta \tag{11}$$

In our research, we are interested in the asymptotic behavior of these estimators. The asymptotics providing the consistency of the estimators can refer to the following groups of conditions: a) $\sigma \to 0$, $b \to 0$, T is fixed; b) $\sigma \to 0$, b and T are fixed; c) $T \to \infty$, σ and b are fixed. One should remember that the asymptotics $A \to \infty$ can be reduced to the case b).

In all the three cases, the problem of the parameter estimation is a regular one, therefore, the MLE and the BE are asymptotically normal with the natural normalization by the Fisher information $I_T(\vartheta_0)$ [1-3]:

$$\sqrt{I_T(\vartheta_0)}(\hat{\vartheta}_T - \vartheta_0) \Rightarrow N(0, 1)$$
$$\sqrt{I_T(\vartheta_0)}(\tilde{\vartheta}_T - \vartheta_0) \Rightarrow N(0, 1) \tag{12}$$

According to [8], for the Fisher information in Equation (12) we can write

$$I_T(\vartheta) = \frac{A^2}{\sigma^2} \int_0^T [\cos(2\pi\vartheta t)\dot{m}(\vartheta, t) - $$
$$- 2\pi t \sin(2\pi\vartheta t)m(\vartheta, t)]^2 dt \tag{13}$$

Here and in the sequel dot means differentiation w.r.t. ϑ and prime differentiation w.r.t. t.

We suggest a slightly more general model for the observations

$$dX_t = f(\vartheta_0 t)Y_t dt + \sigma dW_t, \quad X_0 = 0, \quad 0 \le t \le T \tag{14}$$

$$dY_t = -a(t)Y_t dt + b(t)dV_t, \quad Y_0 = y_0 \tag{15}$$

where $f(t)$ is a known smooth periodic function with the period 1, and for the asymptotics we take the case a) when there is a small noise asymptotics in the state (15) and the observation (14) equations:

$$\sigma = b = \varepsilon \to 0 \tag{16}$$

The case b) is considered in the paper [9]. The statistical problems for the partially observed linear and nonlinear systems are studied in [10]. You can find there useful references to the related statistical problems. The case $T \to \infty$ can be treated following the study of similar problems in [11], where identification of the partially observed system is considered.

2. Auxiliary results

The process $m(\vartheta, t)$, $0 \le t \le T$ satisfies the following equation of Kalman-Bucy filtration [8, 12]:

$$dm(\vartheta, t) = -a(t)m(\vartheta, t)dt + \gamma(\vartheta, t)f(\vartheta, t) \cdot \\ \cdot [dX_t - f(\vartheta t)m(\vartheta, t)dt]/\sigma^2 \qquad (17)$$

where the function $\gamma(\vartheta, t) = \mathbf{E}_\vartheta (m(\vartheta, t) - Y_t)^2$ is the solution for the Ricatti equation.

$$\frac{\partial \gamma(\vartheta, t)}{\partial t} = -2a(t)\gamma(\vartheta, t) - \\ -\frac{1}{\sigma^2}\gamma^2(\vartheta, t)f^2(\vartheta t) + b^2(t), \qquad (18) \\ \gamma(\vartheta, t) = 0$$

Then, for the derivate $\dot{m}(\vartheta, t)$, we obtain

$$d\dot{m}(\vartheta, t) = -[a(t) + \gamma(\vartheta, t)f^2(\vartheta t)/\sigma^2]\dot{m}(\vartheta, t)dt + \\ + h(\vartheta, t)m(\vartheta, t)dt + g(\vartheta, t)[dX_t - f(\vartheta t)m(\vartheta, t)dt] \qquad (19)$$

where $\dot{m}(\vartheta, 0) = 0$ and

$$g(\vartheta, t) = [\dot{\gamma}(\vartheta, t)f(\vartheta t) + t\gamma(\vartheta, t)f'(\vartheta, t)]/\sigma^2 \\ h(\vartheta, t) = t\gamma(\vartheta, t)f(\vartheta t)f'(\vartheta, t)/\sigma^2 \qquad (20)$$

For the derivate $\dot{\gamma}(\vartheta, t)$, from Equation (18), we get the equation

$$\frac{\partial \dot{\gamma}(\vartheta, t)}{\partial t} = -2\Big[a(t) + \frac{1}{\sigma^2}\gamma(\vartheta, t)f^2(\vartheta t)\Big] \cdot \\ \cdot \dot{\gamma}(\vartheta, t) - \frac{2t}{\sigma^2}\gamma^2(\vartheta, t)f(\vartheta t)f'(\vartheta t), \ \dot{\gamma}(\vartheta, 0) = 0 \qquad (21)$$

These equations are obtained by the formal differentiation but this derivation can be justified by the standard methods. The both functions (the Gaussian – $m(\vartheta, t)$ and the deterministic – $g(\vartheta, t)$) are infinitely differentiable.

Equations (19) and (21) are linear and their solutions can be found explicitly. Let us denote

$$q(\vartheta, t) = a(t) + \gamma(\vartheta, t)f^2(\vartheta t)/\sigma^2 \qquad (22)$$

Then we get

$$\dot{m}(\vartheta, t) = \int_0^t \exp\Big[-\int_s^t q(\vartheta, v)dv\Big]h(\vartheta, s)m(\vartheta, s)ds + \\ + \int_0^t \exp\Big[-\int_s^t q(\vartheta, v)dv\Big]g(\vartheta, s)[dX_s - f(\vartheta s)m(\vartheta, s)ds] \qquad (23)$$

and

$$\dot{\gamma}(\vartheta, t) = \frac{1}{\sigma^2}\int_0^t s\exp\Big[-2\int_s^t q(\vartheta, v)dv\Big] \cdot \\ \cdot \gamma^2(\vartheta, s)f'(\vartheta s)ds \qquad (24)$$

3. Main result

While analyzing the specified asymptotics (16), we denote the MLE and the BE as $\hat{\vartheta}_\varepsilon$ and $\tilde{\vartheta}_\varepsilon$, correspondingly and we present the model of observations as follows

$$dX_t = f(\vartheta_0 t)Y_t dt + \varepsilon dW_t, \quad X_0 = 0, \quad 0 \le t \le T \qquad (25)$$

$$dY_t = -a(t)Y_t dt + b(t)\psi(\varepsilon)dV_t, \quad Y_0 = y_0 \ne 0 \qquad (26)$$

Our goal is to estimate the parameter ϑ_0 and to describe the properties of the estimators for the case when $\varepsilon \to 0$, $\psi(\varepsilon) \to 0$. We presuppose that the functions $a(t)$, $b(t)$ are bounded and positive. In this study we also assume that

$$\psi(\varepsilon) = \mu\varepsilon \qquad (27)$$

The case $\psi(\varepsilon) \to 0$, $\psi(\varepsilon)/\varepsilon \to \infty$ and the case $\psi(\varepsilon) \to 0$, $\psi(\varepsilon)/\varepsilon \to 0$ will be considered later, using the same method applied.

We introduce the function $\gamma_*(\vartheta, t) = \varepsilon^{-2}\gamma(\vartheta, t)$ and point out that

$$dm(\vartheta, t) = -a(t)m(\vartheta, t)dt + \gamma_*(\vartheta, t)f(\vartheta t) \cdot \\ \cdot [dX_t - f(\vartheta t)m(\vartheta, t)dt] \qquad (28)$$

If the Equation (27) holds, then the function $\gamma_*(\vartheta, t)$ satisfies the Riccati equation

$$\frac{\partial \gamma_*(\vartheta, t)}{\partial t} = -2a(t)\gamma_*(\vartheta, t) - \gamma_*^2(\vartheta, t)f^2(\vartheta t) + \\ + \mu^2 b^2(t), \quad \gamma_*(\vartheta, t) = 0 \qquad (29)$$

and the solution $\gamma_*(\vartheta, t)$ does not depend on ε.

We can show now that the Fisher information in this problem is

$$I_\varepsilon(\vartheta) = \varepsilon^{-2} I_0(\vartheta)(1 + o(1)) \tag{30}$$

where

$$I_0(\vartheta) = \int_0^T \left[f(\vartheta t)\dot{m}_0(\vartheta,t) + tf'(\vartheta t)m_0(\vartheta,t) \right]^2 dt \tag{31}$$

and $m_0(\vartheta,t)$, $\dot{m}_0(\vartheta,t)$ are the limits of the processes $m(\vartheta,t)$, $\dot{m}(\vartheta,t)$, correspondingly, when $\varepsilon \to 0$. It is easy to see that

$$m_0(\vartheta,t) = y_0 \exp\left[-\int_0^t a(s)ds \right]$$
$$\dot{m}(\vartheta,t) = \int_0^t \exp\left[-\int_s^t q(\vartheta,v)dv \right] h(\vartheta,s)ds \tag{32}$$

where

$$h(\vartheta,t) = \gamma_*(\vartheta,t) f(\vartheta t) \tag{33}$$

It is shown below (Lemma 1) that the corresponding family of measurers is locally asymptotically normal (LAN), and, therefore, we can define the lower bound (Hajek-Le Cam) for the mean square risk of any estimator $\overline{\vartheta}_\varepsilon$:

$$\lim_{\delta \to 0} \lim_{\varepsilon \to 0} \sup_{|\vartheta - \vartheta_0| < \delta} \varepsilon^{-2} \mathbf{E}_\vartheta |\overline{\vartheta}_\varepsilon - \vartheta| \geq I^{-1}(\vartheta_0) \tag{34}$$

We call an estimator ϑ_ε^* the asymptotically efficient, if for all $\vartheta_0 \in \Theta$ we have the equality in Equation (34).

Theorem 1. Referring to the compact $K \in \Theta$, the MLE and the BE are uniformly consistent and asymptotically normal:

$$(\hat{\vartheta}_\varepsilon - \vartheta_0)/\varepsilon \Rightarrow N(0, I_0^{-1}(\vartheta_0))$$
$$(\tilde{\vartheta}_\varepsilon - \vartheta_0)/\varepsilon \Rightarrow N(0, I_0^{-1}(\vartheta_0)) \tag{35}$$

and we have the convergence of all the polynomial moments ($p > 0$):

$$\varepsilon^{-p} I_0^{p/2}(\vartheta_0) \mathbf{E}_{\vartheta_0} |\hat{\vartheta}_\varepsilon - \vartheta_0|^p \to \mathbf{E}|\zeta|^p,$$
$$\varepsilon^{-p} I_0^{p/2}(\vartheta_0) \mathbf{E}_{\vartheta_0} |\tilde{\vartheta}_\varepsilon - \vartheta_0|^p \to \mathbf{E}|\zeta|^p, \zeta \sim N(0,1) \tag{36}$$

and thus both estimators are asymptotically efficient.

Proof. The proof of this theorem follows from the general results of the Theorems 3.2.1 and 3.2.2 in [13]. The conditions for these theorems are fulfilled, if we prove the following three lemmas.

Lemma 1. The normalized likelihood ratio

$$Z_\varepsilon(u) = V(\vartheta_0 + \varepsilon u, X^T)$$
$$u \in U_\varepsilon = ((\alpha - \vartheta_0)/\varepsilon, (\beta - \vartheta_0)/\varepsilon) \tag{37}$$

allows the representation

$$Z_\varepsilon(u) = \exp\left[u\Delta_\varepsilon(\vartheta_0, X^T) - u^2 I_0(\vartheta_0)/2 + r_\varepsilon \right] \tag{38}$$

where $r_\varepsilon \to 0$ and

$$\Delta_\varepsilon(\vartheta_0, X^T) = \int_0^T \left[f(\vartheta t)\dot{m}_0(\vartheta,t) + tf'(\vartheta t)m_0(\vartheta,t) \right] \cdot$$
$$\cdot dW \sim N(0, I_0(\vartheta_0)) \tag{39}$$

Proof. Let us put that $M(\vartheta,t) = f(\vartheta t)m(\vartheta,t)$ and hence

$$\dot{M}_0(\vartheta,t) = f(\vartheta t)\dot{m}(\vartheta,t) + tf'(\vartheta t)m_0(\vartheta,t) \tag{40}$$

As it is easy to see, we have: $M(\vartheta_0 + \varepsilon u, t) - M(\vartheta_0, t) = \varepsilon u \dot{M}_0(\vartheta_0, t)(1 + o(1))$. Therefore,

$$\ln Z_\varepsilon(u) = \frac{1}{\varepsilon} \int_0^T [M(\vartheta_0 + \varepsilon u, t) - M(\vartheta_0, t)] dW_t -$$
$$- \frac{1}{2\varepsilon^2} \int_0^T [M(\vartheta_0 + \varepsilon u, t) - M(\vartheta_0, t)]^2 dt = \tag{41}$$
$$= u\Delta_\varepsilon(\vartheta_0, X^T) - u^2 I_0(\vartheta_0)/2 + r$$

where $r_\varepsilon \to 0$.

Lemma 2. There exists a constant $C > 0$, such as this

$$\mathbf{E}_{\vartheta_0} |Z_\varepsilon^{1/2}(u_2) - Z_\varepsilon^{1/2}(u_1)|^2 \leq C|u_2 - u_1|^2 \tag{42}$$

Proof. Let us put

$$Q_{t,\varepsilon} = \left[\frac{V(\vartheta_0 + \varepsilon u_2, X^t)}{V(\vartheta_0 + \varepsilon u_1, X^t)} \right]^{1/2},$$
$$\delta_t = M(\vartheta_0 + \varepsilon u_2, t) - M(\vartheta_0 + \varepsilon u_1, t) \tag{43}$$

Then, by applying the Ito formula, we come to the following relation

$$dQ_{t,\varepsilon} = -\frac{1}{8\varepsilon^2} Q_{t,\varepsilon} \delta_t^2 dt + \frac{1}{2\varepsilon} Q_{t,\varepsilon} \delta_t dW_T, \ Q_{0,\varepsilon} = 1 \tag{44}$$

and we can write

$$\mathbf{E}_{\vartheta_0} |Z_\varepsilon^{1/2}(u_2) - Z_\varepsilon^{1/2}(u_1)|^2 = \mathbf{E}_{\vartheta_1}(Q_{T,\varepsilon} - 1)^2 =$$
$$= 2 - 2\mathbf{E}_{\vartheta_1} Q_{T,\varepsilon} = \frac{1}{4\varepsilon^2} \int_0^T \mathbf{E}_{\vartheta_1} Q_{t,\varepsilon} \delta_1^2 dt \leq \tag{45}$$
$$\leq \frac{1}{8\varepsilon^2} \int_0^T \mathbf{E}_{\vartheta_1} \delta_1^2 dt + \frac{1}{8\varepsilon^2} \int_0^T \mathbf{E}_{\vartheta_2} \delta_1^2 dt \leq C|u_2 - u_1|^2$$

Here we have changed the measures: $\mathbf{E}_{\vartheta_1} Q_{t,\varepsilon} \delta_1^2 = \mathbf{E}_{\vartheta_2} \delta_1^2$, where $\vartheta_i = \vartheta_0 + \varepsilon u_i, i = 1, 2$, and the relations used are: $\mathbf{E}_{\vartheta_1} Q_{T,\varepsilon} = 1$ and $2ab \leq a^2 + b^2$.

Lemma 3. There exists a constant $\kappa > 0$, such as this

$$\mathbf{E}_{\vartheta_1} Z_\varepsilon^{1/2}(u) \leq \exp(-\kappa u^2) \tag{46}$$

Proof. The proof of this lemma is omitted because it is cumbersome but it follows the same steps as the proof of the Lemma 2.4 in [10].

The properties of the normalized likelihood ratio $Z_\varepsilon(u)$ established in these three lemmas allows us to cite the Theorem 1.3.1 and 1.3.2 from [13] and, therefore, obtain the properties of MLE and BE, announced in the Theorem 1. Particularly, the convergence of the random process $Z_\varepsilon(u) \Rightarrow Z(u)$, where

$$Z(u) = \exp\left[u\Delta - u^2 I_0(\vartheta_0)/2 \right], \Delta \sim N(0, I_0(\vartheta_0)) \qquad (47)$$

allows one to obtain the asymptotic normality of the MLE in the following way:

$$\begin{aligned} P_{\vartheta_0}\left(\frac{\hat{\vartheta}_\varepsilon - \vartheta_0}{\varepsilon} < x \right) &= P_{\vartheta_0}(\hat{\vartheta}_\varepsilon < \vartheta_0 + \varepsilon x) = \\ &= P_{\vartheta_0}\left[\sup_{\vartheta < \vartheta_0 + \varepsilon x} V(\vartheta, X^T) > \sup_{\vartheta \geq \vartheta_0 + \varepsilon x} V(\vartheta, X^T) \right] = \\ &= P_{\vartheta_0}\left[\sup_{\vartheta < \vartheta_0 + \varepsilon x} \frac{V(\vartheta, X^T)}{V(\vartheta_0, X^T)} > \sup_{\vartheta \geq \vartheta_0 + \varepsilon x} \frac{V(\vartheta, X^T)}{V(\vartheta_0, X^T)} \right] = \\ &= P_{\vartheta_0}\left[\sup_{u < x, u \in U_\varepsilon} Z_\varepsilon(u) > \sup_{u \geq x, u \in U_\varepsilon} Z_\varepsilon(u) \right] \to \\ &\to P_{\vartheta_0}\left[\sup_{u < x} Z(u) > \sup_{u \geq x} Z(u) \right] = P_{\vartheta_0}(\hat{u} < x) \end{aligned} \qquad (48)$$

Here we have changed the variable $\vartheta = \vartheta_0 + \varepsilon u$. It is easy to see that

$$\hat{u} = I_0^{-1}(\vartheta_0)\Delta \sim N(0, I_0^{-1}(\vartheta_0)) \qquad (49)$$

Thus, the asymptotic normality of the MLE is obtained. For the BE, the corresponding limits provide us the relation

$$\frac{\tilde{\vartheta}_\varepsilon - \vartheta_0}{\varepsilon} \Rightarrow \frac{\int_{-\infty}^{\infty} u Z(u) du}{\int_{-\infty}^{\infty} Z(u) du} = \frac{\Delta}{I_0(\vartheta_0)} \sim N(0, I_0^{-1}(\vartheta_0)) \qquad (50)$$

For the details see [13].

4. Discussion

It is of interest to see what would happen, if the rates $\varepsilon \to 0$, $\psi(\varepsilon) \to 0$ are different. Let us suppose that $\phi_\varepsilon = \varepsilon/\psi(\varepsilon) \to 0$. Then, this case would correspond to the situation when the noise in the state equation is essentially bigger than in the observation one. We are specifically concerned with the rate of the MLE convergence to the true value.

Let us consider the Riccati equation

$$\left[\frac{\partial \gamma_*(\vartheta, t)}{\partial t} + 2a(t)\gamma_*(\vartheta, t) \right]\phi_\varepsilon = \\ = -\gamma_*^2(\vartheta, t)f^2(\vartheta t) + b^2(t), \qquad \gamma_*(\vartheta, t) = 0 \qquad (51)$$

where we have $\gamma_*(\vartheta, t) = \varepsilon^{-1}\psi^{-1}(\varepsilon)\gamma(\vartheta, t)$. Our supposition is that the functions $a(t)$, $b(t)$ and $f(t)$ are strictly positive and bounded. It can be shown that, for any $t_0 > 0$, we have uniform convergence over $t \in [t_0, T]$

$$\gamma_*^2(\vartheta, t) = f^{-2}(\vartheta t)b^2(t)[1 + o(1)] \qquad (52)$$

This convergence allows us to study the asymptotics of $\dot{m}(\vartheta, t)$ and $\gamma_*(\vartheta, t)$, and, therefore, to describe the mean square error $\mathbf{E}_\vartheta(\hat{\vartheta}_\varepsilon - \vartheta)^2$. For example, if $\psi(\varepsilon) = c > 0$, then $\mathbf{E}_\vartheta(\hat{\vartheta}_\varepsilon - \vartheta)^2 = \varepsilon I_0^{-1}(\vartheta)[1 + o(1)]$, with a different Fisher information $I_0(\vartheta)$ [9]. Particularly, we show that $\varepsilon^{1/2}(\hat{\vartheta}_\varepsilon - \vartheta_0) \Rightarrow N(0, I_0^{-1}(\vartheta_0))$. The general case when $\psi(\varepsilon) \to 0$ and $\phi_\varepsilon \to 0$ is to be treated later.

5. Conclusion

Thus, maximum likelihood and Bayesian estimators of the frequency of the regular periodic signal in the presence of a multiplicative interference described by the Gaussian Markov random process and the additive distortions, like the white Gaussian noise, are asymptotically normal, consistent, effective, and have the rate of convergence inversely proportional to the voltage signal-to-noise ratio. The limiting variance of the estimators is determined by the Fisher information for which the expression in explicit form can be found analytically.

The domain of applicability of the obtained theoretical results (their satisfactory concordance with the corresponding experimental data) can be evaluated on the basis of the studies presented in [1].

Acknowledgement

References

[1] KULIKOV, E. I., TRIFONOV A. P.: Estimation of the Signal Parameters against an Interference Background [in Russian]. Sovetskoe Radio, Moscow, 1978.
[2] PEROV, A. I.: Statistical Radio System Theory [in Russian]. Radiotekhnika, Moscow, 2003.
[3] VAN TREES, H. L.: Detection, Estimation, and Modulation Theory, Part III: Radar-Sonar Signal Processing and Gaussian Signals in Noise. Wiley, New York, 2001.

[4] SOBOLEV, V. S., FESHENKO, A. A.: Accuracy Cramer-Rao Bounds for a Laser Doppler Velocimeter. IEEE Transactions on Instrumentation and Measurement, 55(2), 659-665, 2006.

[5] SOBOLEV, V. S., ZHURAVEL F.A.: Quasioptimal Estimates of the Center Frequency of a Narrow-Band Normal Random Process with a Gaussian Spectrum. Optoelectronics, Instrumentation and Data Processing, 46(6), 565-570, 2010.

[6] TRIFONOV, A. P., ZAKHAROV, A. V.: Joint Estimator Characteristics of Random Radiopulse Arrival Time and Frequency. Izvestiya Vysshikh Uchebnykh Zavedenij, Radioelektronika, 45(5), 3-12, 1999.

[7] CHERNOYAROV, O. V., VACULIK, M., SHIRIKYAN, A., SALNIKOVA, A. V.: Statistical Analysis of Fast Fluctuating Random Signals with Arbitrary-Function Envelope and Unknown Parameters. Communications – Scientific Letters of the University of Zilina, 17(1A), 35-43, 2015.

[8] LIPTSER, R. S., SHIRYAYEV, A. N.: Statistics of Random Processes, I, II. (2nd edition). Springer, New York, 2001.

[9] CHERNOYAROV, O. V., KUTOYANTS, Y. A.: On Frequency Estimation for Partially Observed System with Small Noise in Observations. Submitted, 2017.

[10] KUTOYANTS, Y. A.: Identification of Dynamical Systems with Small Noise. Kluwer Academic Publisher, Dordrecht, 1994.

[11] KUTOYANTS, Y. A.: Statistical Inference for Ergodic Diffusion Processes. Springer, London, 2004.

[12] KALMAN, R. E., BUCY, R. S.: New Results in Linear Filtering and Prediction Theory. Transactions of ASME, Series D, Journal of Basic Engineering, 83(1), 95-108, 1961.

[13] IBRAGIMOV, I. A., HAS'MINSKII, R. Z.: Statistical Estimation – Asymptotic Theory. Springer, New York, 1981.

Evgeny Pchelintsev - Valeriy Pchelintsev - Serguei Pergamenshchikov*

NON ASYMPTOTIC SHARP ORACLE INEQUALITIES FOR THE IMPROVED MODEL SELECTION PROCEDURES FOR THE ADAPTIVE NONPARAMETRIC SIGNAL ESTIMATION PROBLEM

In this paper, we consider the robust adaptive non parametric estimation problem for the periodic function observed with the Levy noises in continuous time. An adaptive model selection procedure, based on the improved weighted least square estimates, is proposed. Sharp oracle inequalities for the robust risks have been obtained.

Keywords: improved non-asymptotic estimation, weighted least squares estimates, robust quadratic risk, non-parametric regression, Levy process, model selection, sharp oracle inequality, asymptotic efficiency

1. Introduction

In this paper, we consider a signal statistical treatment problem in the framework of a nonparametric regression model in continuous time, i.e.

$$dy_t = S(t)dt + d\xi_t, \quad 0 \leq t \leq n \tag{1}$$

where $S(\cdot)$ is an unknown 1-periodic signal, $(\xi_t)_{0 \leq t \leq n}$ is an unobserved noise and n is the duration of observation. The problem is to estimate the function S on the observations $(y_t)_{0 \leq t \leq n}$. Note that if $(\xi_t)_{0 \leq t \leq n}$ is a Brownian motion, then we obtain the well-known "signal + white noise" model which is very popular in statistical radio-physics (see, for example, [1-3] and etc.). In this paper, we assume that in addition to the intrinsic noise in the radio-electronic system, approximated usually by the Gaussian white or color noise, the useful signal S is distorted by the impulse flow described by the Levy process, i.e. we assume that the noise process $(\xi_t)_{0 \leq t \leq n}$ is defined as

$$\xi_t = \rho_1 w_t + \rho_2 z_t \quad \text{and} \quad z_t = x^*(\mu - \bar{\mu})_t \tag{2}$$

where ρ_1 and ρ_2 are some unknown constants, $(w_t)_{t \geq 0}$ is a standard Brownian motion, $\mu(ds\,dx)$ is a jump measure with

deterministic compensator $\bar{\mu}(ds\,dx) = ds\Pi(dx), \Pi(\cdot)$ is a Levy measure, i.e. some positive measure on $\mathbb{R}_* = \mathbb{R}\backslash\{0\}$, such that

$$\Pi(x^2) = 1 \quad \text{and} \quad \Pi(x^6) < \infty \tag{3}$$

Here we use the notation $\Pi(|x|^m) = \int_{\mathbb{R}_*} |y|^m \Pi(dy)$. Note that the Levy measure $\Pi(\mathbb{R}_*)$ could be equal to $+\infty$. We use * for the stochastic integrals with respect to random measures (see [4], Chs. 2 and 3), i.e.

$$x*(\mu - \bar{\mu})_t = \int_0^t \int_{\mathbb{R}_*} y(\mu - \bar{\mu})(ds, dy) \tag{4}$$

In the sequel we will denote by Q the distribution of the process $(\xi_t)_{0 \leq t \leq n}$ and by Q_n^* we denote all these distributions for which the parameters $\rho_1 \geq \varsigma_*$ and $\rho_1^2 + \rho_2^2 \leq \varsigma^*$ where ς_* and ς^* are some fixed positive bounds. The cause of the appearance of a pulse stream in the radio-electronic systems can be, for example, either external unintended (atmospheric) or intentional impulse noise and the errors in the demodulation and the channel decoding for the binary information symbols. Note that, for the first time the impulse noises for detection signal problems have been introduced on the basis of compound Poisson processes was

* [1]Evgeny Pchelintsev, [2]Valeriy Pchelintsev, [3]Serguei Pergamenshchikov
[1]Department of Information Technologies and Business Analytics, Tomsk State University, Russia
[2]Department of Mathematics and Informatics, Tomsk Polytechnic University, Russia
[3]Laboratoire de Mathematiques Raphael Salem, Universite de Rouen, Saint Etienne du Rouvray, France and International Laboratory of Statistics of Stochastic Processes and Quantitative Finance of Tomsk State University, Russia
E-mail: evgen-pch@yandex.ru

by Kassam in [2]. However, the compound Poisson process can describe only the large impulses influence of fixed single frequency. There should be taking into account that in telecommunication systems, impulses are without limitations on frequencies. So, one needs to extend the framework of the observation model by making use of the Levy processes as in Equations (2). In this paper, we consider the estimation problem in the adaptive setting, i.e. when the regularity of S is unknown. Since the distribution Q of the noise process $(\xi_t)_{0 \le t \le n}$ is unknown we use the robust estimation approach developed for nonparametric problems in [5]. We define the robust risk as

$$\mathcal{R}^*(\hat{S}_n, S) = \sup_{Q \in \mathcal{Q}_n^*} \mathcal{R}_Q(\hat{S}_n, S) \qquad (5)$$

where $\hat{s}_n$ is an estimation of the unknown signal S, i.e. some function of $(y_t)_{0 \le t \le n}$, $\mathcal{R}_Q(\cdot, \cdot)$ is the usual quadratic risk defined as

$$\mathcal{R}^*(\hat{S}_n, S) := \mathbf{E}_{Q,S} \|\hat{S}_n - S\|^2 \text{ and } \|S\|^2 = \int_0^1 S^2(t)dt \qquad (6)$$

Here $\mathbf{E}_{Q,S}$ stands for the expectation with respect to the distribution $\mathbf{P}_{Q,S}$ of the process in the Equation (1) with a fixed distribution Q of the noise $(\xi_t)_{0 \le t \le n}$ and a given function S.

In this paper, we consider minimax optimization criteria which aim to minimize the robust risk which is defined in the Equation (5) (see, for example, in [6]). To do this we use the model selection methods. The interest to such statistical procedures is explained by the fact that they provide adaptive solutions for a nonparametric estimation through oracle inequalities which give a non-asymptotic upper bound for a quadratic risk including a minimal risk over chosen family of estimators. It should be noted that the model selection methods for parametric models were proposed, for the first time, by Akaike [7]. Then, these methods had been developed by Barron, Birge and Massart [8] and Fourdrinier and Pergamenshchikov [9] for the nonparametric estimation and oracle inequalities for the quadratic risks. Unfortunately, the oracle inequalities obtained in these papers cannot provide the efficient estimation in the adaptive setting, since the upper bounds in these inequalities have some fixed coefficients in the main terms which are more than one. In order to obtain the efficiency property for estimation procedures, one has to obtain the sharp oracle inequalities, i.e. in which the factor at the principal term on the right-hand side of the inequality is close to unity. For this reason, one needs to use the general semimartingale approach for the robust adaptive efficient estimation of the nonparametric signals in continuous time proposed by Konev and Pergamenshchikov [5]. The goal of this paper is to develop a new sharp model selection method for estimating the unknown signal S using the improved estimation approach. Usually, the model selection procedures are based on the least square estimators. However, in this paper, we propose to use the improved least square estimators which enable us to

considerably improve the non-asymptotic estimation accuracy. Such idea was proposed, for the first time, in [9]. Our goal is to develop these methods for non-Gaussian regression models in continuous time and to obtain the sharp oracle inequalities. It should be noted that to apply the improved estimation methods to the non-Gaussian regression models in continuous time one needs to modify the well-known James-Stein procedure introduced in [10] in the way proposed in [11, 12]. So, by using these estimators we construct the improved model selection procedure and we show that the constructed estimation procedure is optimal in the sense of the sharp non-asymptotic oracle inequalities for the robust risks which are defined in the Equation (5).

2. Improved estimation

Let $(\phi_j)_{j \ge 1}$ be an orthonormal basis in $\mathbf{L}_2[0, 1]$. We extend these functions by the periodic way on $\mathbb{R}$, i.e. $\phi_j(t) = \phi_j(t + 1)$ for any $t \in \mathbb{R}$. For estimating the unknown function S in the Equation (1) we consider it's Fourier expansion (see, for example, [13])

$$S(t) = \sum_{j=1}^{\infty} \theta_j \phi_j(t) \text{ and } \theta_j = (S, \phi_j) = \int_0^1 S(t)\phi_j(t)dt \quad (7)$$

The corresponding Fourier coefficients can be estimated as

$$\hat{\theta}_{j,n} = \frac{1}{n} \int_0^n \phi(t)dy_t \qquad (8)$$

We define a class of weighted least squares estimates for $S(t)$ as

$$\hat{S}_\lambda = \sum_{j=1}^n \lambda(j)\hat{\theta}_{j,n}\phi_j \qquad (9)$$

where the weights $\lambda \in \mathbb{R}^n$ belong to some finite set Λ from $[0, 1]^n$.

Now, for the first d Fourier coefficients in Equations (7) we use the improved estimation method proposed for parametric models in [12]. To this end we set $\tilde{\theta}_n = (\hat{\theta}_{j,n})_{1 \le j \le d}$. In the sequel we will use the norm $|x|_d^2 = \sum_{j=1}^d x_j^2$ for any vector $x = (x_j)_{1 \le j \le d}$ from $\mathbb{R}^n$. Now we define the shrinkage estimators as

$$\theta_{j,n}^* = (1 - g(j))\hat{\theta}_{j,n} \qquad (10)$$

where $g(j) = \frac{\mathbf{c}_n}{|\tilde{\theta}_n|_d} \mathbf{1}_{\{1 \le j \le d\}}$, $\mathbf{1}_A$ is the indicator of the set A and $\mathbf{c}_n$ is some known parameter such that $\mathbf{c}_n \approx \frac{d}{n}$ as $n \to \infty$. Now we introduce a class of shrinkage weighted least squares estimates for S as

$$S_\lambda^* = \sum_{j=1}^n \lambda(j)\theta_{j,n}^*\phi_j \qquad (11)$$

We denote the difference of quadratic risks of the estimates in Equation (11) and Equation (9) as $\Delta_Q(S) := \mathcal{R}_Q(S_\lambda^*, S) - \mathcal{R}_Q(\hat{S}_\lambda, S)$. Now for this deviation we obtain the following result.

Theorem 1. *Assume that for any vector $\lambda \in \Lambda$ there exists some fixed integer $d = d(\lambda)$ such that their first d components equal to one, i.e. $\lambda(j) = 1$ for $1 \leq j \leq d$ for any $\lambda \in \Lambda$. Then for any $n \geq 1$ and $r > 0$*

$$\sup_{Q \in Q_4} \sup_{\|S\| \leq r} \Delta_Q(S) < -\mathbf{c}_n^2 \qquad (12)$$

The inequality (12) means that non-asymptotically, i.e. for any $n \geq 1$ the estimate in the Equation (11) outperforms in mean square accuracy the estimate in the Equation (9). Moreover, as we will see below, $n\mathbf{c}_n \to \infty$ as $d \to \infty$. This means that improvement is considerable may be better than for the parametric regression [11].

3. Model selection

This Section gives the construction of a model selection procedure for estimating a function S in the Equation (1) on the basis of improved weighted least square estimates and states the sharp oracle inequality for the robust risk of proposed procedure.

The model selection procedure for the unknown function S in the Equation (1) will be constructed on the basis of a family of estimates $(S_\lambda^*)_{\lambda \in \Lambda}$.

The performance of any estimate S_λ^* will be measured by the empirical squared error

$$\text{Err}_n(\lambda) = \|S_\lambda^* - S\|^2 \qquad (13)$$

In order to obtain a good estimate, we have to write a rule to choose a weight vector $\lambda \in \Lambda$ in the Equation (6). It is obvious, that the best way is to minimize the empirical squared error with respect to λ. Making use the estimate definition in the Equation (6) and the Fourier transformation of S implies

$$\text{Err}_n(\lambda) = \sum_{j=1}^n \lambda^2(j)(\theta_{j,n}^*)^2 - 2\sum_{j=1}^n \lambda(j)\theta_{j,n}^*\theta_j + \sum_{j=1}^n \theta_j^2 \qquad (14)$$

Since the Fourier coefficients $(\theta_j)_{j \geq 1}$ are unknown, the weight coefficients $(\lambda_j)_{j \geq 1}$ cannot be found by minimizing this quantity. To circumvent this difficulty one needs to replace the terms $\theta_{j,n}^*\theta_j$ by their estimators $\tilde{\theta}_{j,n}$. We set

$$\tilde{\theta}_{j,n} = \theta_{j,n}^*\hat{\theta}_{j,n} - \frac{\hat{\sigma}_n}{n} \qquad (15)$$

where $\hat{\sigma}_n$ is the estimate for the noise variance of $\sigma_Q = \mathbf{E}_Q\xi_{j,n}^2 = \rho_1^2 + \rho_2^2$ which we choose in the following form

$$\hat{\sigma}_n = \sum_{j=[\sqrt{n}]+1}^n \hat{t}_{j,n}^2 \quad \text{and} \quad \hat{t}_{j,n} = \frac{1}{n}\int_0^n \text{Tr}_j(t)dy_t \qquad (16)$$

Here we denoted by $(\text{Tr}_j)_{j \geq 1}$ the trigonometric basis in $\mathbf{L}_2[0, 1]$. For this change in the empirical squared error, one has to pay some penalty. Thus, one comes to the cost function of the form

$$J_n(\lambda) = \sum_{j=1}^n \lambda^2(j)(\theta_{j,n}^*)^2 - 2\sum_{j=1}^n \lambda(j)\tilde{\theta}_{j,n} + \delta\hat{P}_n(\lambda) \qquad (17)$$

where δ is some positive constant, $\hat{P}_n(\lambda)$ is the penalty term defined as

$$\hat{P}_n(\lambda) = \frac{\hat{\sigma}_n|\lambda|_n^2}{n} \qquad (18)$$

Substituting the weight coefficients, minimizing the cost function

$$\lambda^* = \text{agr min}_{\lambda \in \Lambda}J_n(\lambda) \qquad (19)$$

in the Equation (11) leads to the improved model selection procedure

$$S^* = S_{\lambda^*}^* \qquad (20)$$

It will be noted that λ^* exists because Λ is a finite set. If the minimizing sequence in the Equation (19) λ^* is not unique, one can take any minimizer. In the case, when the value of σ_Q is known, one can take $\hat{\sigma}_n = \sigma_Q$ and $P_n(\lambda) = \sigma_Q|\lambda|_n^2 n^{-1}$.

Theorem 2. *For any $n \geq 2$ and $0 < \delta < 1/3$, the robust risks defined in the Equation* (5) *of estimate in the Equation* (20) *for continuously differentiable function S satisfies the oracle inequality*

$$\mathcal{R}^*(S_{\lambda^*}^*, S) \leq \frac{1+3\delta}{1-3\delta}\min_{\lambda \in \Lambda}\mathcal{R}^*(S_\lambda^*, S) + \frac{B_n^*}{n\delta} \qquad (21)$$

where the rest term is such that $B_n^* n^{-\varepsilon} \to 0$ as $n \to \infty$ for any $\varepsilon > 0$.

The inequality (21) means that the procedure in the Equation (20) is optimal in the oracle inequalities sense. This property enables to provide asymptotic efficiency in the adaptive setting, i.e. when information about the signal regularity is unknown.

4. Monte Carlo simulations

In this section we report the results of a Monte Carlo experiment to assess the performance of the proposed model selection procedure in the Equation (20). In the Equation (1) we choose 1-periodic function S which, for $0 \leq t \leq 1$, is defined as $S(t) = |t - \frac{1}{2}|$, if $\frac{1}{4} \leq t \leq \frac{3}{4}$ and $S(t) = \frac{1}{4}$ elsewhere. We simulate the Equation (1) with the noise process defined as

$$\xi_t = 0.5w_t + 0.5z_t \qquad (22)$$

Table 1 Empirical risks

n	$\overline{R}(\hat{S},S)$	$\overline{R}(S^*,S)$	$\overline{R}(\hat{S},S)/\overline{R}(S^*,S)$
20	0.0462	0.0331	1.40
100	0.0262	0.0133	1.97
200	0.0126	0.00824	1.53
1000	0.00129	0.00094	1.37

where $z_t = \sum_{j=1}^{N_t} Y_j$, N_t is a Poisson process with the intensity $\lambda=1$ and $(Y_j)_{j\geq1}$ is i.i.d. Gaussian (0,1). We use the model selection procedure defined in the Equation (20) with the weights proposed in [5]: $k^* = 100 + \sqrt{\ln n}$, $\varepsilon = 1/\ln n$ and $m = [1/\varepsilon^2]$. We used the cost function with $\delta = (3 + \ln n)^{-2}$. We define the empirical risk as $\overline{R}(\tilde{S},S) = \frac{1}{p}\sum_{j=1}^{p}\hat{E}(\tilde{S}_n(t_j) - S(t_j))^2$ and $\hat{E}(\tilde{S}_n(\cdot) - S(\cdot))^2 = \frac{1}{N}\sum_{l=1}^{N}(\tilde{S}_n^l(\cdot) - S(\cdot))^2$ with the frequency of observations p=100001 and numbers of replications N=10000.

Table 1 give the values for the sample risks for different numbers of observation period n.

5. Conclusion

In conclusion, we would like to emphasize that in this paper we developed new model selection procedures based on the improved versions of the least square estimators. It turns out that the improvement effect in the nonparametric estimation is more important than for the parameter estimation problems since the accuracy improvement is proportional to the parameter dimension. We remember that for the nonparametric estimation this dimension tends to infinity, but in the parametric case it is always fixed. Therefore, the gain in the non-asymptotic quadratic accuracy from the application of the improved estimation methods is much more significant in statistical treatment problems of nonparametric signals. Moreover, as shown by the results of numerical simulation, the improved estimate for non-asymptotic accuracy exceeds the usual least squares estimators approximately in 1.5-2 times for the chosen experimental model.

References

[1] CHERNOYAROV, O. V., VACULIK, M., SHIRIKYAN, A., SALNIKOVA, A. V.: Statistical Analysis of Fast Fluctuating Random Signals with Arbitrary - Function Envelope and Unknown Parameters. Communications - Scientific Letters of the University of Zilina, 17(1a), 35-43, 2015.
[2] KASSAM, S. A.: Signal Detection in Non-Gaussian Noise. Springer, New York, 1988.
[3] IBRAGIMOV, I. A., KHASMINSKII, R. Z.: Statistical Estimation: Asymptotic Theory. Springer, New York, 1981.
[4] CONT, R., TANKOV, P.: Financial Modelling with Jump Processes. Chapman & Hall, London, 2004.
[5] KONEV, V. V., PERGAMENSHCHIKOV, S.: Robust Model Selection for a Semimartingale Continuous Time Regression from Discrete Data. Stochastic Processes and their Applications, 125, 294-326, 2015.
[6] JANACEK, J., KVET, M.: Min-Max Optimization of Emergency Service System by Exposing Constraints. Communications - Scientific Letters of the University of Zilina, 17(2), 15-22, 2015.
[7] AKAIKE, H.: A New Look at the Statistical Model Identification. IEEE Transactions on Automatic Control, 19(7), 716 – 723, 1974.
[8] BARRON, A., BIRGE, L., MASSART, P.: Risk Bounds for Model Selection via Penalization. Probability Theory and Related Fields, 113, 301-415, 1999.
[9] FOURDRINIER, D., PERGAMENSHCHIKOV, S.: Improved Selection Model Method for the Regression with Dependent Noise. Annals of the Institute of Statistical Mathematics, 59(3), 435-464. 2007.

[10] JAMES, W., STEIN, C.: Estimation with Quadratic Loss. Proceedings of the Fourth Berkeley Symposium Mathematics, Statistics and Probability, California, USA, 1, 361-380, 1966.

[11] KONEV, V., PERGAMENSHCHIKOV, S., PCHELINTSEV, E.: Estimation of a Regression with the Pulse Type Noise from Discrete Data. Theory of Probability and Its Applications, 58(3), 442-457, 2014.

[12] PCHELINTSEV, E.: Improved Estimation in a Non-Gaussian Parametric Regression. Statistical Inference for Stochastic Processes, 16(1), 15-28, 2013.

[13] MARCOKOVA, M.: Equiconvergence of Two Fourier series. Journal of Approximation Theory, 80(2), 151-163, 1995.

kaMuNikacie
COMMUNICATIONS

Michal Frivaldsky - Pavol Spanik - Jan Morgos - Norbert Glapa*

OPTIMIZED THERMAL SIMULATION MODEL OF MULTILAYER PRINTED CIRCUIT BOARD

Very thin multi-layers of Cu and epoxy compound in PCB (printed circuit board) make difficult to design computational meshes in finite element method simulation programs. Number of degrees of freedom in simulated system rapidly increases – it significantly extends simulation computational time. In this paper we propose substitution of the PCB in axial and radial direction with the composite structure with equivalent physical parameters of multilayer PCB.

Keywords: *multilayer printed circuit board, thermal modeling, approximation, simulation*

1. Introduction

Considering high degree of geometrical complexity of electronic products which are being developed, it is quite important to focus on the preconstruction phases within the development process. It is well known, that efficiency is the main indicator that defines the qualities of any electronic system. Efficiency is directly dependent on the temperature, because any unwanted temperature rise in electronic systems is related to the existance of undesirable power losses. When complex systems, like integrated circuits, i.e. switched mode power supplies SMPS are considered the efficiency is the most important parameter [1-3].

Nowadays, the market offers various rapid prototyping software, thus enabling the researchers fast identification of unwanted processes and consequent system optimization. When talking about SMPS it is valuable to perform identification of the thermal performance. The simulation model is very valuable because fast and very accurate results can be achieved [4-6]. Consequently, optimization processes are much more effective to be done with the use of good thermal simulation model [7, 8]. On the other side, there are some challenges which are related to the complexity of such systems. It is well known that any SMPS consists of huge number of active and passive components, which might be modeled in order to have very good simulation results. At the same time, printed circuit board PCB has to be modeled too, because it is a part of each SMPS. It is known, that multilayer PCB are being used in almost every hi-tec SMPS

design. Multilayer PCBs are composed of several interleaved layers of copper, FR4 material and other mask materials. These layers represent a very thin structure and again, when precise simulation model is required, then each layer must be considered.

In this paper the optimized thermal simulation model of multilayer PCB is shown, whereby we have focused on factors, which are affecting thermal conductivity of multilayer PCB. Modeling of the PCB in the way that FR4 material for whole subdomain of PCB is assigned is not correct. Thin copper layers which are placed on the TOP and BOTTOM side of PCB, and even inside of PCB subdomain, have high impact on thermal distribution on the surface of PCB as well as inside of this subdomain.

The main problem of multilayer PCB is thin copper layer (35um – 100um) in combination with epoxy layers. This thin geometry of copper in combination with the other neighboring epoxy layers produces a high number of mesh elements what in final makes the simulation model more complex. Then the simulation time of solution is much longer. We propose to replace physical properties of multilayer PCB by thermal conductivity tensor in radial and axial part, which will have the same properties as the mentioned multilayer PCB structure.

2. Principle of PCB thermal model optimization

In this paper, the basic study of the behavior of multilayer PCB and consequently possibilities how to simplify such geometry

* ¹Michal Frivaldsky, ¹Pavol Spanik, ¹Jan Morgos, ²Norbert Glapa
¹Department of Mechatronics and Electronics, Faculty of Electrical Engineering, University of Zilina, Slovakia
²Panasonic Industrial Devices, GmbH, Luneburg, Germany
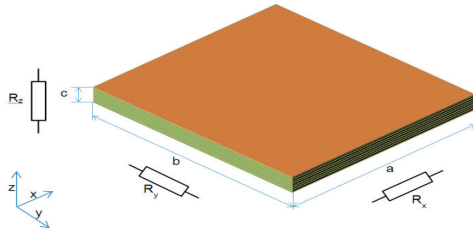 E-mail: michal.frivaldsky@ef.uniza.sk
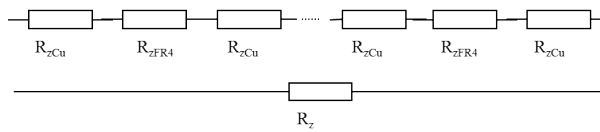
Figure 1 Simple model of multilayer PCB board

Figure 2 Thermal resistance of PCB in z-direction

Figure 3 Thermal resistance of PCB in x, y direction

are given. Multilayer PCB is replaced by geometrically and physically similar composite whose physical properties will be accurate and sufficient for thermal simulations in COMSOL environment.

Considering axial and radial direction of PCB structure, it has different conditions for heat transfer within its volume. The fact is given by the structural compound of the PCB, while most used materials are FR4 and Cu mutually interleaved. These processes can be related to the different values of the thermal resistances in *x, y, z* directions in 3D space according to Figure 1.

In Figure 1 it is seen, that interleaved copper layers and epoxy compound layers form sandwich structure of the PCB. Thermal resistances of the entire board in x and y directions differ from thermal resistance in z direction.

Cross-sectional thermal resistance in z axis is derived and based on the sandwich structure in Figure 2 as follows: it consists of separate layer thermal resistances connected in series, whereby the number of FR4 material and Cu material is based on the number of layers of PCB.

According to Figure 2 the thermal resistance of PCB structure in z-axis direction is given by the Equation (1) as follows:

$$R_z = \sum_{k=1}^{n} R_{zCu}(n) + \sum_{k=1}^{n} R_{zFR4}(m) = n \cdot R_{zCu} + m \cdot R_{zFR4} \qquad (1)$$

where:
R_{zCu} - thermal resistance of copper
R_{zFR4} - epoxy compound FR4 type,
n - number of copper layers,
m - number of epoxy layers.

Thermal resistance (and therefore thermal conductivity) in „x" and „y" directions are representing parallel connection of resistances of several PCB layers.
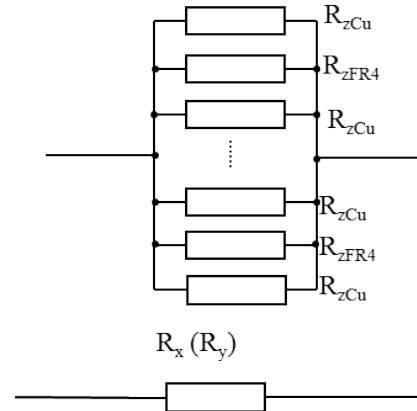
According to Figure 3 the thermal resistance of PCB structure in *x, y* – axes is inverse to the Equation (1) and thus based on the Equation (2) it is possible to determine its values as follows:

$$R_x(R_y) = \frac{1}{R_z} = \sum_{k=1}^{n} \frac{1}{R_{zCu}(n)} + \sum_{k=1}^{m} \frac{1}{R_{zFR4}(m)_z} =$$
$$= n \cdot \frac{1}{R_{zCu}} + m \cdot \frac{1}{R_{zFR4}} \qquad (2)$$

Small layers of PCB (Figure 1) represent interconnected system of very thin blocks with the same surface and different thickness of copper or epoxy compound. Thermal resistance of block in 3D space for *x, y, z* directions can then be simplified into the next Equation (3):

$$R_x = \frac{\Delta x}{k_x \cdot A_{yz}}$$
$$R_y = \frac{\Delta y}{k_y \cdot A_{xz}} \qquad (3)$$
$$R_z = \frac{\Delta z}{k_z \cdot A_{xy}}$$

where:
Δx - thickness of block in x direction,
A_{yz} - area which thermal flow runs through in perpendicular direction,
Δy - thickness of block in y direction,
A_{xz} - area which thermal flow runs through in perpendicular direction,
Δz - thickness of block in z direction,
A_{xy} - area which thermal flow runs through in perpendicular direction,
k_x, k_y, k_z - thermal conductivity of material in the given direction.

For thermal simulation model of the PCB it is necessary to derive thermal conductivities in each direction. In principle the thermal conductivity is the inverse value of the thermal resistance, thus based on the Equation (3) it is possible to derive equations
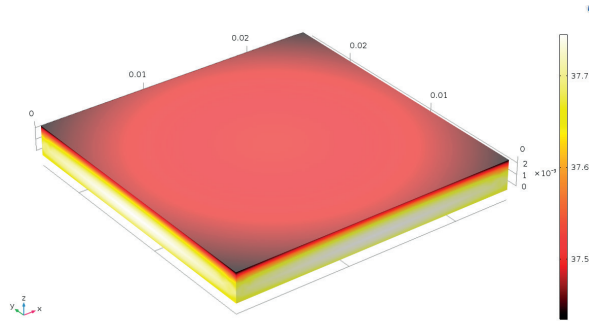
Figure 4 Surface temperature distribution in simulated model of PCB 8xCu+7xFR4
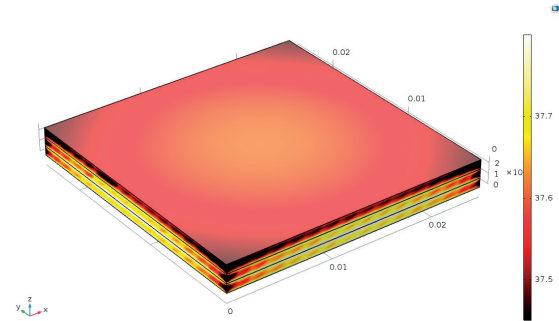

Figure 5 Surface temperature distribution in simulated composite model of PCB

for the computation of thermal conductivities of multilayer PCB in the following Equation (4):

$$k_z = \frac{n \cdot w_{Cu} + m \cdot w_{FR4}}{\frac{n \cdot w_{Cu}}{k_{cu}} + \frac{m \cdot w_{FR4}}{k_{FR4}}} = \frac{w}{\frac{n \cdot w_{Cu}}{k_{Cu}} + \frac{m \cdot w_{FR4}}{k_{FR4}}}$$

$$k_x = \frac{n \cdot k_{Cu} \cdot w_{Cu} + m \cdot k_{FR4} \cdot w_{FR4}}{n \cdot w_{Cu} + m \cdot w_{FR4}} =$$

$$= \frac{n \cdot k_{Cu} \cdot w_{Cu} + m \cdot k_{FR4} \cdot w_{FR4}}{w} \qquad (3)$$

$$k_y = \frac{n \cdot k_{Cu} \cdot w_{Cu} + m \cdot k_{FR4} \cdot w_{FR4}}{n \cdot w_{Cu} + m \cdot w_{FR4}} =$$

$$= \frac{n \cdot k_{Cu} \cdot w_{Cu} + m \cdot k_{FR4} \cdot w_{FR4}}{w}$$

where:

w_{Cu} – thickness of copper layer

w_{FR4} – thickness of epoxy layer

w – total thickness of PCB

k_{Cu} – copper thermal conductivity

k_{FR4} – epoxy layers thermal conductivity

The previous simple analysis allows using Equations (1) – (4) for derivation of the required values of thermal conductivities for any multilayer PCB. These values together with material properties are then necessary for the development of optimized thermal simulation model.

3. Simulation results

For the implementation purposes, we have selected geometrical dimensions of PCB of brick DC-DC converter sample [9, 10]. Independent simulations in COMSOL environment with thermal module were accomplished with two samples of PCB with the same dimensions 24.4 mm x 27.9 mm. The same value of power dissipation 0.2 W was applied within the volume of the PCB sample. The boundary conditions for both of samples were set to the same conditions (external temperature 20 ˚C, natural laminar flow - COMSOL setting of boundary condition when radiation is considered and natural external convection).

The first model is the structured detailed sample, which contains 8 copper layers with thickness w_{Cu}= 0.035 mm, thermal conductivity k_{Cu}=400 W/m.K and 7 epoxy compound layers with thickness w_{FR4}=0.3 mm, k_{FR4}=0.3 W/m.K. The mesh size for this model is pretty complex, because the model consist of several thick layers. Complete mesh consists of 307632 domain elements, 113304 boundary elements and 3900 edge elements.

The second sample contained one block of composite material with thickness 2.38 mm and thermal conductivity as tensor with components calculated from Equation (4), k_x= 47.3235 W/m.K, k_y= 47.3235 W/m.K, k_z= 0.3399 W/m.K. For this case the mesh consists of 92227 domain elements, 23542 boundary elements and 708 edge elements.

The graphic representation of temperature field distribution on PCB board surface is shown in Figure 4 and Figure 5. Figure 4 shows 3D graphical results of 8-layer PCB board while Figure 5 shows 3D graphical results of composite PCB board. It is seen that results of temperature distribution within the volume/area are almost identical when both models are compared. Instead of that, computation time for composite model has decreased compared to structural model from 42 seconds to 4 seconds. This result is valuable, because the decrease factor is 10. For more complex simulation models, the save of time might be beneficial.

Figure 6 gives the detailed comparison of the internal temperature of 8-layer PCB board and composite PCB board in the z-axis cross-section of PCB in its middle point. Based on this results it is seen, that the temperature difference inside the PCB board is almost negligible, while just value of 0.02 ˚C is overreached. Figure 7 shows the percentage representation of relative temperature difference.

4. Conclusion

Contemporary construction of electronic power equipment utilizes as a mechanical and electrical base a multilayer PCB board. Single semiconductor elements and integrated circuits are built-in the board. It is suitable to reduce the number of thin and large planes by creation of geometric model of electronic
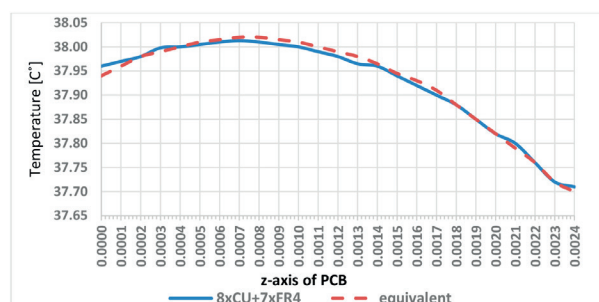
Figure 6 *Comparison of internal temperatures in the middle of PCB board 8xCu+7xFR4 and in composite model*
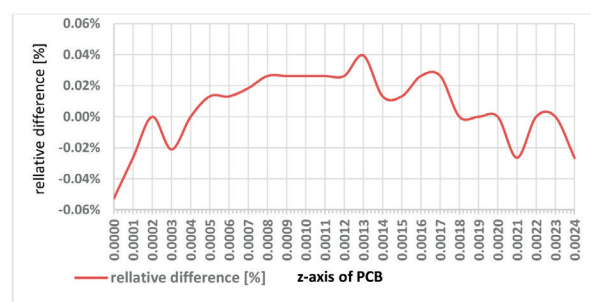

Figure 7 *Relative temperature difference cross-line section plots of the 8xCu+7xFR4 and equivalent PCBs*

equipment. This is the case of multilayer PCB board. Authors used a composite physical model applicable for the temperature simulation needs. The equivalent model unlike a multilayer geometry significantly decreases the number of elements of computational mesh. The results of simulation confirm that the temperature fields in 8-layer PCB board and in composite PCB board differ very little. The results of simulation of PCB board samples for DC-DC converter with dimensions 24.4 mm x 27.9 mm show that relative temperature deviation is 0.04 % in the worst case.

Acknowledgements

References

[1] HARGAS, L., HRIANKA, M., LAKATOS, J., KONIAR, D.: Heat Fields Modelling and Verification of Electronic Parts of Mechatronics Systems. Metalurgija (Metalurgy), 49(2), 2010.

[2] HRIANKA, M., CUNTALA, J., LAKATOS, J., HARGAS, L., KONIAR, D.: Thermal field modeling of the power electronic systems (in Slovak). Acta Mechanica Slovaca 12(3-B), 281-284, 2008.

[3] COMSOL: Multiphysics user guide.

[4] SPANIK, P., CUNTALA, J., FRIVALDSKY, M., GLAPA, N., MADLENAK, D.: Thermal Simulation of Electrochemical Double Layer Capacitor. Proceedings of the 8th International Conference ELEKTRO 2010, Slovak Republic, 62-66, 2010.

[5] SHAHIN, A., PAYMAN, A., MARTIN, J. P., PIERFEDERICI, S., MEIBODY-TABAR, F.: Approximate Novel Loss Formulae Estimation for Optimization of Power Controller of DC/DC Converter. Proceedings of 36th Annual Conference on IEEE Industrial Electronics Society (IECON 2010), USA, 373-378, 2010.

[6] SARAJCEV, I., MAJSTROVIC, M., MEDIC, I.: Calculation of Losses in Electric Power Cables as the Base for Cable Temperature Analysis. Advanced Computational Methodes in Heat Transfer VI, 27, 529 – 537, 2000.

[7] GAMIL, A., GUELDNER, H., BOEHME, F., WOLF, H.: Determine the efficiency of any power electronic device using heat transfer theory. Proceedings of the Fifth International Conference on Electrical Machines and Systems (ICEMS 2001), China, 1, 488-491, 2001.

[8] BOREKCI, S., ACAR, N. C..: An Accurate Way of Determining BJT's Switching Loss in Medium and High Voltage Applications. Proceeding of IEEE International Conference on Electronics Design, Systems and Applications (ICEDSA 2012), Malaysia, 183-187, 2012.

[9] APSE-APSITIS, P., AVOTINS, A., RIBICKIS, L.: Self-Tuning Core-Less Serial Resonant DC/DC Converter for Powering Loads on Rotating Shafts. Electronics and Electrical Engineering, 19(2), 41 - 44, 2013.

[10] DOBRUCKY, B., PRAZENICA, M., KASCAK, S., KASSA, J.: HF Link LCTLC Resonant Converter with LF AC Output. Proceedings of 38th Annual Conference on IEEE Industrial Electronics Society (IECON 2012), 447-452, 2012.

KOMUNIKÁCIE
COMMUNICATIONS

Andrea Strakova Fedorkova - Katarina Gavalierova - Dominika Capkova - Tomas Kazda*

ELECTROCHEMICAL CHARACTERIZATION OF HIGH-PERFORMANCE SULFUR COMPOSITES AS CATHODES FOR Li-S BATTERIES WITH APPLICATION IN AUTOMOTIVE INDUSTRY

Lithium-sulfur batteries are based on principle of conversion and their properties are very promising for their high theoretical energy density and low cost. However, current electrodes and materials used in Li-S batteries suffer from irreversible electrochemical reaction of polysulfides, low conductivity and stability. Here we summarize preparation and characterization of sulfur samples with polymer additive polypyrrole/polyethylene glycol to improve conductivity and stability of Li-S batteries. We also discuss very simple preparation technique of polypyrrole suitable also for industrial production. The electrochemical properties of sulfur-carbon-polypyrrole (S-C-PPy) composites were investigated by cyclic voltammetry (CV), electrochemical impedance spectroscopy (EIS) and galvanostatic charge/discharge measurements. Properties of resulting composite samples (especially conductivity) are strongly affected by the preparation technique and conditions. Insulating polymer PEG was used to improve the polymeric structure and mechanical robustness of PPy chain. Porosity of composite sample increase with increasing amount of PPy. On the other hand conductivity is reduced with increased porosity. Electrochemical measurements confirmed that addition of PEG can improve conductivity also in the presence of higher amounts of PPy in the sample. PPy-PEG composite polymer decrease particle to particle contact resistance. Co-polymer coating consisting of PPy-PEG significantly decreases the charge transfer resistance of prepared samples what was confirmed by impedance measurements.

Keywords: *lithium, sulfur, batteries, polypyrrole, conductivity*

1. Introduction

Lithium-ion batteries (LIBs) are very important power sources since 1991. They can be used in many portable small electronic devices and electric vehicles due to the high capacity, long cycling and high energy density [1, 2]. New cathode materials need to be developed and improved for high energy applications as electric vehicles. Sulfur is considered to be one of the most promising cathode for next-generation LIBs due to the high theoretical capacity (1672 mAh/g) [3], abundant reserves and nontoxic nature. However, a few drawbacks are related to Li-S battery practical application as low conductivity, volumetric changes, polysulfide shuttle mechanism or short life time. The theoretical capacity of sulfur coupled with the average operating voltage of a Li-S cell (2.15 V vs Li^+/Li^0) and the theoretical capacity of a pure lithium anode (3862 mAh/g) gives the energy density as high as ˜2500 Wh/kg. Although Li-S batteries possess many advantages, low active material utilization, capacity degradation, self-discharge, poor Coulombic efficiency, poor cycle life, and electrode volume expansion are still the challenges remaining with the Li-S cells [4].

Electroactive conducting polymers (ECPs) are conjugated polymers that exhibit electronic conduction when partially oxidized or reduced and are capable of undergoing oxidation/reduction reactions [5, 6]. Examples of ECPs include polypyrrole (PPy), polyaniline, polythiophene and polyphenylene vinylene. Several of these polymers have been tested as cathode materials for lithium batteries. Polypyrrole, for instance, can act as a host material for Li^+-ion insertion/extraction in the voltage range of 2.0-4.5 V versus Li/Li^+, with a theoretical capacity of 72 mAh/g [7]. Therefore, PPy is a possible additive which can be used both as a conductive agent as well as a polymeric cathode material.

Herein, we report a simple preparation technique of sulfur-PPy/PEG composites with improved conductivity and stability.

* [1]Andrea Strakova Fedorkova, [1]Katarina Gavalierova, [1]Dominika Capkova, [2]Tomas Kazda
[1]Institute of Chemistry, Faculty of Science, P.J. Safarik University, Kosice, Slovakia
[2]Department of Electrical and Electronic Technology, Faculty of Electrical Engineering and Communication,
Brno University of Technology, Czech Republic
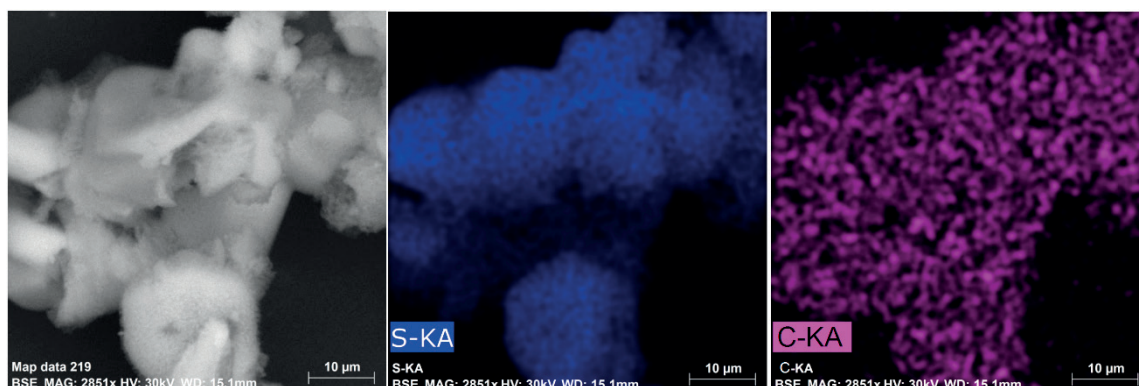E-mail: andrea.fedorkova@upjs.sk

Figure 1 SEM image of S-C-PPy13% composite sample and corresponding elemental maps for sulfur and carbon

Our aim is to produce composite samples with conductive polymer polypyrole to improve the conductivity and with higher porosity to accommodate insoluble polysulfides. Our results presents an effective approach to stabilize sulfur cathodes and obtain higher stability, efficiency and rate performance.

2. Experimental

2.1 Preparation of polypyrrole and sulfur composites

Polypyrrole was prepared by simple chemical oxidative polymerization in acid solution. $FeCl_3$ was used as an oxidative agent. Temperature of polymerization was kept by the ice bath at a value 4 °C. Sulfur-carbon-PPy composites were synthesized by heating the mixture of sulfur (Sigma-Aldrich), carbon Super P and PPy at 150 °C for 15 minutes. Sulfur at this temperature has low viscosity and can penetrate into the pores of polypyrrole and carbon. The weight ratio of PPy in composite sample was 5, 10, 13 and 15 wt. %. Polyethylene glycol (PEG 600) (0.5 wt. %) was added to sample with 13 wt. % of PPy to improve the mechanical properties of the prepared composite.

2.2 Preparation of cathodes and test cells

Electrode slurries were made by mixing the sulfur composite as the active material with polyvinylidene fluorid (PVdF) in N-methyl-2-pyrrolidone (NMP) with a weight ratio of 80:20. The slurry was then coated onto aluminium foil as current collector using the doctor-blade technique and subsequently dried in a vacuum oven at 60 °C for 18 h. Circular electrodes with 18 mm diameter were cut out of the coated foil, with an area of 2.54 cm^2 and total mass of 1.5-2 mg on a substrate of Al foil. Three electrode test cells (ECC-STD El-Cell©) were assembled using these cathodes with lithium metal foil as counter and reference electrode and a fiber glass separator. All handling was done in an argon filled dry glove box (Jacomex, France). The electrolyte
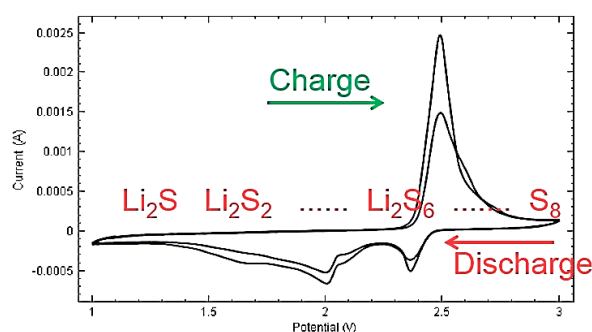

Figure 2 The cyclic voltammogram of S-C-PPy13% composite sample at scan rate 0.1 mV/s

used for all measurements consisted of 0.25 M $LiNO_3$ and 0.7 M LiTFSI dissolved in DME-DIOX (2:1).

2.3 Sample characterization

Galvanostatic charge/discharge measurements were performed within a potential window from 1.0 to 3.0 $V_{vs.\ Li}$ at different C-rates. CV curves were recorded in the potential window from 1.0 to 3.0 $V_{vs.\ Li}$, and the scan rate was set to 0.1 mV/s. All electrochemical measurements were performed with Autolab potentiostat at room temperature. A typical sulfur mass loading on the electrode was 0.8-0.9 mg/cm^2. Scanning electron microscope JEOL JSM-7000F + EDX INCA were used to observe the structure, morfology and composition of samples.

3. Results and discussion

Figure 1 shows the SEM image of S-C-PPy13% composite cathode materials. We can see the porous agglomerated particles after polymerization of PPy. EDX elemental mapping confirmed homogeneous distribution of carbon, PPy and sulfur. Carbon and polymer composite created a continuous coating and sulfur
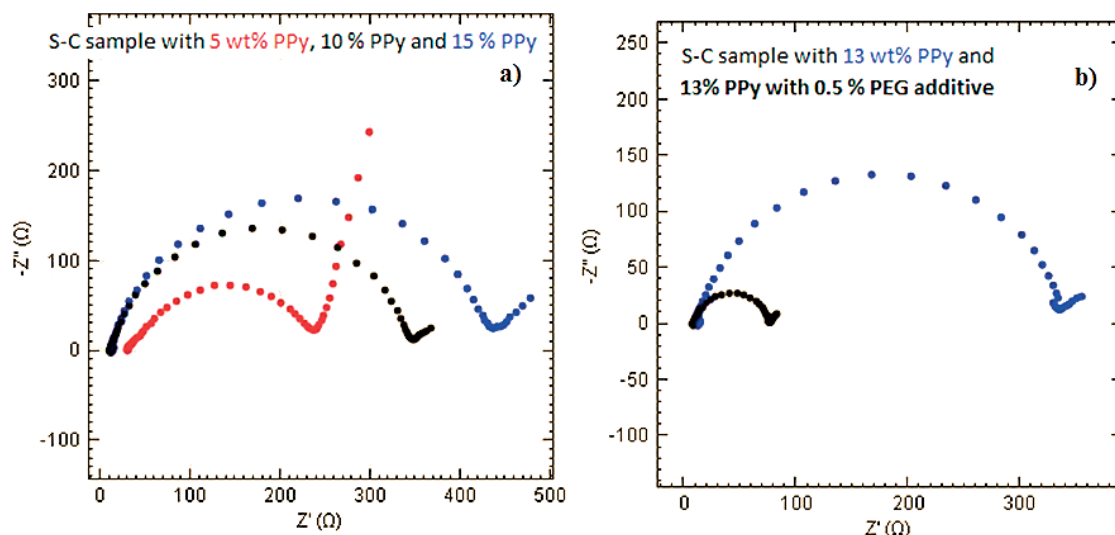
Figure 3 Nyquist plots of the **a)** S-C sample with 5 wt. % PPy (red), 10 wt. % PPy (black), 15 wt. % (blue) and **b)** S-C samples withMCWCS-S electrodes recorded at room temperature
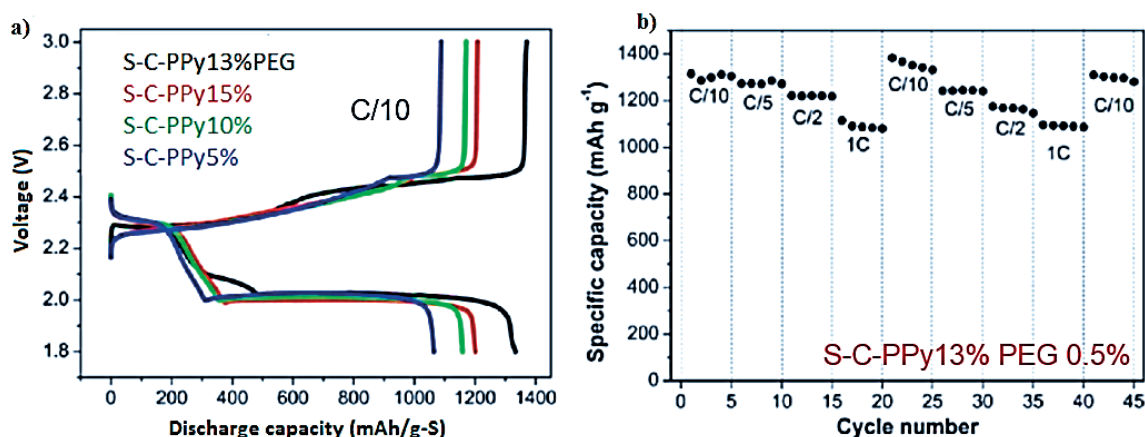

Figure 4 **a)** Galvanostatic charge-discharge profiles of the S-C samples with different amount of PPy at a C-rate of 0.1 C and **b)** rate performance of the S-C-PPy13%PEG0.5% cathode at different C-rates

was accommodated in pores of carbon and polypyrrole. Smooth conductive layer can enhance the electron transfer and improve the total efficiency of Li-S battery.

Figure 2 shows the cyclic voltammograms (CV) of the composite electrode (S-C sample with 13 wt. % of PPy and 0.5 wt. % of PEG) for the 1st and 2nd cycle. During the first reduction process (discharging), two typical peaks at 2.38 and 2.1 V are observed, corresponding to the reduction of elemental sulfur and to long-chain polysulfide (Li_2S_n, n ≥ 8) and further to short-chain polysulfide (such as Li_2S_6, Li_2S_4) [8, 9]. In the subsequent anodic scan (charging), an intense, broader characteristic peak was observed at 2.5-2.6 V, reporting oxidation of sulfides to elemental sulfur. Anodic and cathodic current for the second cycle was decreased due to the partially irreversible reaction and formation of insoluble polysulfides.

The electrochemical impedance spectra (EIS) of different S-C-PPy samples at open circuit potential are shown in Figure 3 a, b. The charge-transfer resistance (Rct) of the S-C sample with 13 wt. % of PPy and 0.5 wt. % of PEG additive (75 Ω) is much smaller than that of the S-C-PPy sample without PEG additive (330 Ω). This result supports the hypothesis that the insulating polymer PEG improves electron and ion transport in the cathode and charge-transfer resistance of Li⁺ ion is improved due to improved mechanical properties of PPy-PEG composite.

Galvanostatic charge/discharge measurements are shown in Figure 4 a, b. The S-C sample with 13 wt. % of PPy and 0.5 wt. % of PEG shows the faster electrochemical reaction with a smallest polarization compared with other samples. This result is in agreement with our previous EIS measurements. The highest discharge capacity observed for sample with PEG additive was 1325 mAh/g-sulfur at a current density of 0.1 C. The discharge

capacities of other samples are 1200, 1179 and 1068 mAh/g-sulfur, respectively. These values can be compared with recently reported results for Li-S batteries [10-12].

The rate capability of the S-C sample with 13 wt. % of PPy and 0.5 wt. % of PEG electrode was investigated using a different C-rates. The discharge capacities of this electrode at 0.1C, 0.2C, 0.5C, and 1C after several cycles correspond to value of 1300, 1250, 1160 and 1100 mAh/g-sulfur, respectively. Even at a higher C-rate, the S-C-PPy-PEG sample still presents a high specific capacity of 1100 mAh/g-sulfur. When the rate returns back to 0.1C, a specific capacity of 1300 mAh/g-sulfur can still be obtained. This results indicates the excellent stability of S-C-PPy-PEG composite sample. Improved PPy-PEG structure and increased porosity of resulting samples with sulfur can overcome polysulfides shuttling effect.

4. Conclusions

In conclusion, the S-C-PPy-PEG composites have been prepared by a simple oxidation polymerization reaction of Py monomere in acid solution and by evaporation of sulfur into the pores of carbon-polyppyrole composite matrix. To explore the effect of PPy-PEG additive, a series of samples with various content of PPy were investigated to optimize the electrode conductivity, porosity and performance. With increasing amount of PPy porosity was increasing but conductivity was decreasing. After optimization of composition between the sulfur, PPy and PEG a series of electrochemical measurements was performed. As the result, S-C sample with 13 wt. % of PPy and 0.5 wt. % of PEG delivers an optimal discharge capacity of 1300 mAh/g-sulfur at 0.1C after 45 cycles, which owns to improved balance between two components. This material will indicate a new route to rationally design cathode materials for Li-S batteries with superior stability and performance.

Acknowledgement

References

[1] SAGAR, R. U. R., MAHMOOD, N., STADLER, F. J., ANWAR, T., NAVALE, S.T., SHEHZAD, K., DU, B.: High Capacity Retention Anode Material for Lithium Ion Battery. Electrochimica Acta, 211, 156-163, 2016.

[2] HU, J. T., JIANG, Y., CUI, S. H., DUAN, Y. D., LIU, T. C., GUO, H., LIN, L. P., LIN, Y., ZHENG, J. X., AMINE, K., et al.: 3D-Printed Cathodes of LiMn1-xFexPO4 Nanocrystals Achieve Both Ultrahigh Rate and High Capacity for Advanced Lithium-Ion Battery. Advanced Energy Materials, 6(18), 1600856-1600868, 2016.

[3] Manthiram, A., Chung, S. H., Zu, C.: Lithium-Sulfur Batteries: Progress and Prospects. Advanced Materials, 25;27(12), 1980-2006, 2015.

[4] FEDORKOVA, A., ORINAKOVA, R., CECH, O., SEDLARIKOVA, M.: New Composite Cathode Materials for Li/S Batteries: A Review. International Journal of Electrochemical Science, 8, 10308-10319, 2013.

[5] TALLMAN, D. E., VANG, C., WALLACE, G. G., BIERWAGEN, G. P.: Direct Electrodeposition of Polypyrrole on Aluminum and Aluminum Alloy by Electron Transfer Mediation. Journal of the Electrochemical Society, 149(3), C173-C179, 2002.

[6] OSAKA, T., MOMMA, T., NISHIMURA, K., KAKUDA, S., ISHII, T.: Application of Solid Polymer Electrolyte to Lithium/Polypyrrole Secondary Battery System. Journal of the Electrochemical Society, 141(8), 1994-1998, 1994.

[7] BRUCE, P. G., FREUNBERGER, S. A., HARDWICK, L. J., TARASCON, J.-M.: Li-O2 and Li-S Batteries with High Energy Storage. Nature Materials, 11(1), 19-29, 2012.

[8] FANG, X., LIU, S., ZANG, J., XU, C., ZHENG, M., DONG, Q., SUN, D., ZHENG, N.: Precisely Controlled Resorcinol-Formaldehyde Resin Coating for Fabricating Core-Shell, Hollow, and Yolk-Shell Carbon Nanostructures. Nanoscale, 5, 6908-6916, 2013.

[9] DU, X., ZHANG, X., GUO, J., ZHAO, S., ZHANG, F.: Hierarchical Sulfur Confinement by Graphene Oxide Wrapped, Walnut-Like Carbon Spheres for Cathode of Li-S Battery. Journal of Alloys and Compounds, 714, 311-317, 2017.

[10] CHEN, H., WANG, CH., DONG, W., LU, W., DU, Z., CHEN, L.: Monodispersed sulfur nanoparticles for lithium-sulfur batteries with theoretical performance. Nano Letters, 14;15(1):798-802, 2015.

[11] KAZDA, T., KRBAL, M., POUZAR, M., VONDRAK, J., STRAKOVA FEDORKOVA, A., SLAVIK, M., WAGNER, T., MACAK, J.: Highly Efficient and Stable Cryo-Ground Sulphur Cathode for Li-S batteries. Journal of Power Sources, 331, 293-298, 2016.

[12] KAZDA, T., CUDEK, P., VONDRAK, J., SEDLARIKOVA, M., TICHY, J., SLAVIK, M., FAFILEK, G., CECH, O.: Lithium-Sulphur Batteries Based on Biological 3D Structures. Journal of Solid State Electrochemistry, 1-10, 2017. https://doi.org/10.1007/s10008-017-3791-0.

kaMUNikacie
C O M M U N I C A T I O N S

Giuseppe Aiello - Mario Cacciato - Sebastiano Messina - Marco Torrisi*

A HIGH EFFICIENCY INTERLEAVED PFC FRONT – END CONVERTER FOR EV BATTERY CHARGER

Nowadays, an increasingly present application in the automotive field is the battery charger that usually consists of two high efficiency parts: an AC/DC converter with power factor correction (PFC) capability and a DC/DC converter. In this paper, a three-channel interleaved Power Factor Correction (PFC) based on a new digital controller STNRGPF01 operating in Continuous Conduction Mode (CCM) is presented addressing high efficiency. In the considered applications, the most challenging control issues are the input current control and the fast overcurrent protections. Exploiting mixed signal control approach some benefits have been obtained and confirmed by experimental results on a 3 kW prototype.

***Keywords:** active front-end, interleaved converters, battery charger, power factor correction, digital control*

1. Introduction

For electric vehicle manufacturers (EVs) and for the consumer market it is important to have high efficiency and high power chargers to optimize charging times. The charger consists of an AC/DC used as power factor correction (PFC), and a DC/DC to adapt the voltage levels to the battery type. If the efficiency of each part is greater than 97 %, the overall efficiency of the battery charger will be 94 % higher, unlike most of the chargers on the market [1].

In many high power applications active Power Factor Corrector (PFC) converters are widely used as the first stage in AC/DC conversion in order to meet the IEC 61000-3-2 standard for electrical equipment [2].

In order to charge the battery pack of Electrical Vehicles (EVs) from the grid, a battery charger with unity power factor correction (PFC) capacity is required. For the on-board charger (OBC) with two-stage structure [3], the front-end PFC AC/DC converter is used to rectify the input supply from AC form to DC form while controlling the input current of converter to be in phase with the input voltage, therefore, high power factor control is achieved to minimize the negative effect of OBC on the power quality of the grid. The result consists in an electrical appliance that work virtually as a pure resistive load thus the overall grid efficiency can be improved.

The conventional boost topology is the most popular topology used to realize PFC and ac/dc conversion in the power range of a few kilowatts. Generally, the converter is controlled based on the conventional dual closed-loop PI control, among which an external voltage loop regulates the output voltage and generates the reference current and an internal current loop shapes the input current to achieve the unity power factor correction [4].

In applications of power greater than 1 kW, interleaved converters are often used. Interleaving of PFCs consists of paralleling two or more active stages (Figure 1), each rated for a fractional power, instead of a bigger one rated for the full power. During normal operation the PWM driving signals are out of phase of a proper value according to sequent equation:

$$phase\ shift = \frac{360°}{number\ of\ channels} \qquad (1)$$

The benefits of the interleaved topology [5], compared to traditional single-stage PFC, are measured in terms of:
- Input current ripple reduction
- EMI filter volume reduction
- Inductor volume reduction
- Output capacitor RMS current value reduction
- Better power management for the switches
- higher efficiency thanks to channels power management

* [1]Giuseppe Aiello, [1]Mario Cacciato, [2]Sebastiano Messina, [2]Marco Torrisi
[1]Department of Electrical, Electronics Engineering and Computer Science, University of Catania, Italy
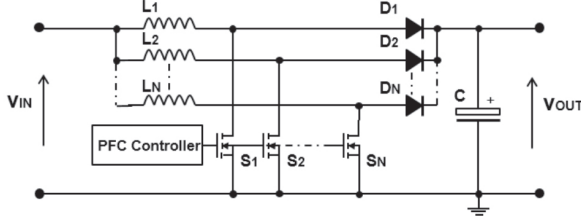[2]STMicroelectronics, Catania, Italy
E-mail: mario.cacciato@unict.it

Figure 1 Interleaved boost PFC with N active channels
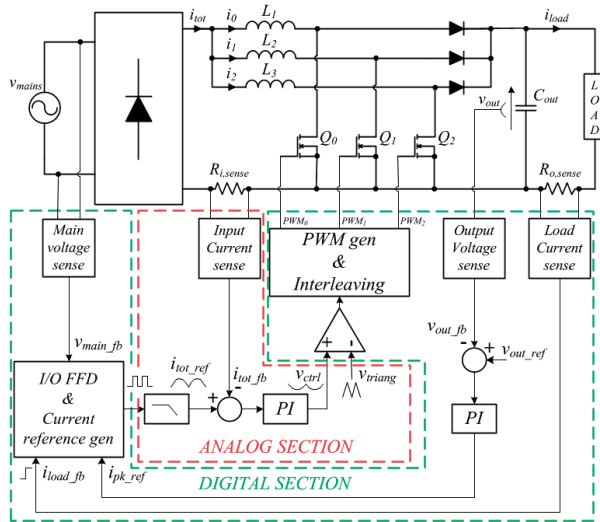

Figure 2 IPFC mixed signal control scheme

2. Mixed signal concept

If only Analog ICs are used, generally it not allows to totally fulfill the multi specification of power converter. For such a reason, full digital solutions are often preferred to analog ones for their flexibility and programmability. Consequently, costly microcontrollers with high computational power are needed to meet the high bandwidth requested by the current control loops. Moreover, full digital control has bandwidth limitations compared to analog implementation [6 - 8].

As a consequence, the mixed-signal control represents a good compromise because it provides at the same time the flexibility of digital solution and the dynamics of analog controllers. For the addressed application, the proposed control scheme is shown in Figure 2 [9].

An outer voltage control loop is used to set the PFC bus voltage to a reference value while an inner current loop regulates the value of the total average inductor current. A digital PI regulator calculates the peak of total input average current ipk_ref by considering the difference between the output voltage feedback Vout_fb and the reference Vout_ref. In this scheme, the PFC current reference is obtained from the I/O Feed Forward (I/O FFD) block exploiting a PWM waveform filtered using a low pass analog filter to achieve the pre-modulation reference waveform. Then, the difference between the current reference itot_ref and
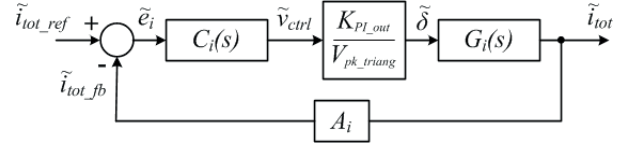

Figure 3 PFC current control loop block diagram

the input current feedback itot_fb is processed by an analog PI controller whose output vctrl is compared with a triangular wave Vtriang at the switching frequency to generate the master signal PWM0. In Figure 2, the digital and analog sections are highlighted by the green and red dashed line respectively. Input and load feed-forward control are used to ensure fast dynamic response when main voltage changes suddenly or a load current step occurs. Moreover, in order to obtain an almost flat figure of merit a phase shedding function is implemented in order to enable/disable the slave channels according to the load.

3. Theoretical analysis of control loops

3.1 Current control loop design

The small-signal transfer functions of the interleaved boost converter are obtained using the State-Space Averaging (SSA) method and a linearization operation (Taylor's series around an operating point) [10, 11]. In order to simplify the problem, the following assumption has been considered:
- Converter CCM operation
- Ideal active and passive components
- The three boost inductors show identical parameters and the total power is equally split among the channels
- The grid voltage is assumed to be stable during several switching cycles.

In the following equations the notation '~' specifies small-signal variables while the uppercase letter indicates quantities operating in steady-state. The control-to-input current transfer function is shown in Equation 2.

$$G_i(s) = \frac{\tilde{i}_{tot}}{\tilde{\delta}} = \frac{C_{OUT}V_{OUT}^3 s + P_{OUT}\left(1 + \frac{1}{\eta}\right)V_{OUT}}{C_{OUT}L_{PFC}V_{OUT}^2 + L_{PFC}P_{OUT}s + N_{ch}V_{IN}^2} \quad (2)$$

The current control loop block diagram is shown in Figure 3.

Where Vpk_triang is the peak to peak voltage of the triangular carrier and KPI_out is a scaling factor that allow to match the PI regulator maximum output voltage value with that of the triangular carrier peak.

Ai is the input current sensing gain and Ci(s) is the compensator transfer function. The open loop compensated transfer function is then given by:

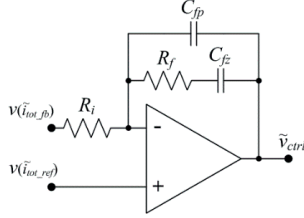$$T_i(s) = C_i(s)\frac{K_{PI\_out}}{V_{pk\_tirang}}A_i G_i(s) \quad (3)$$

Figure 4 Type II compensation amplifier

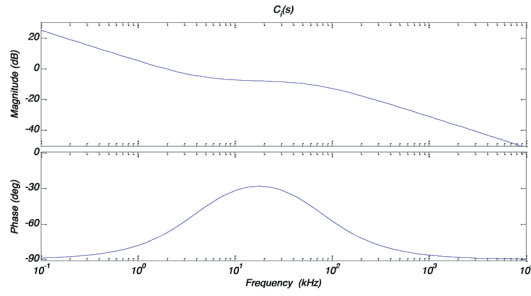Figure 5 Complete cascaded control loop block diagram

Figure 6 Bode diagrams of current compensator $C_i(s)$ and current open loop $T_i(s)$ transfer functions

where the typical PI controller transfer function is $C_i(s) = (K_{P\_Itot}s + K_{I\_Itot})/s$. Based on general Bode criteria equation - Equation (4) ensure system stability for a desired bandwidth ω_{Ti_des} (crossover pulsation) and phase margin PM_{i_des} and the PI controller parameters can be calculated from Equation (5)

$$\begin{cases} |T_i(j\omega_{Ti\_des})| = 1 \\ \angle T_i(j\omega_{Ti\_des}) = -180° + PM_{i\_des} \end{cases} \qquad (4)$$

$$\begin{cases} K_{I\_Itot} = \dfrac{\omega_{Ti\_des}}{|L_i(j\omega_{Ti\_des})|\sqrt{1 + \tan^2(PM_{i\_des} - 90° - \angle L_i(j\omega_{Ti\_des}))}} \\ K_{P\_Itot} = \dfrac{K_{I\_Itot}\tan(PM_{i\_des} - 90° - \angle L_i(j\omega_{Ti\_des}))}{\omega_{Ti\_des}} \end{cases} \qquad (5)$$

Typically, the crossover frequency is selected within the range 2 - 10 kHz [12], while phase margin 45 - 60 degrees.

Since the current controller is implemented with analog type - II compensation amplifier (Figure 4) the transfer function of this compensator is given by Equation (5).

$$C_i(s) = \frac{1}{(C_{fz} + C_{fp})R_i} \frac{C_{fz}R_f s + 1}{s\left(\dfrac{C_{fz}C_{fp}R_f}{C_{fz} + C_{fp}}s + 1\right)} \qquad (6)$$

3.2 Voltage loop design

The input current-to-output voltage transfer function is specified in Equation (7):

$$G_v(s) = \frac{\tilde{v}_{out}}{\tilde{i}_{tot}} = \frac{2\left(N_{ch}V_{IN} - \dfrac{P_{OUT}}{\eta V_{IN}}L_{PFC}s\right)V_{OUT}^2}{C_{OUT}V_{OUT}^3 s + P_{OUT}\left(1 + \dfrac{1}{\eta}\right)V_{OUT}} \qquad (7)$$
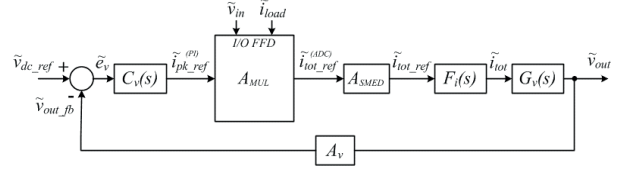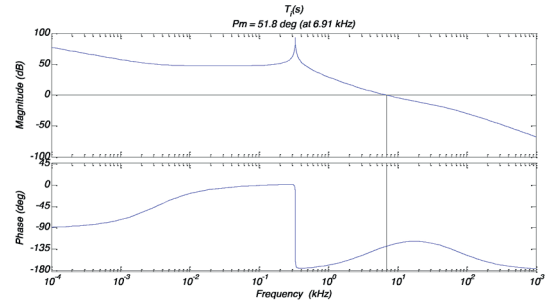
voltage loop crossover frequency is generally selected in the range 5 - 15 Hz [12], thus the right half plane zero (higher frequency) can be neglected. The cascaded control block diagram is shown in Figure 5.

where:

$F_i(s)$ = Input current closed-loop transfer function

$C_v(s)$ = Output voltage compensator transfer function

A_{MUL} = Digital multiplier gain for digital current reference generation

A_{SMED} = Digital to analog gain for analog current reference generation

A_v = Output voltage sensing gain

The I/O FFD block can be simply considered as a constant gain block A_{MUL}. The output voltage loop regulation is done with a digital PI controller:

$$C_v(s) = \frac{K_{P\_Vdc}s + K_{I\_Vdc}}{s} \qquad (8)$$

Considering the open loop compensated transfer function shown in Equation (9):

$$T_v(s) = C_v(s)A_{MUL}A_{SMED}F_iG_v(s)A_v \qquad (9)$$

and that stable system is obtained if the two following conditions are verified:

$$\begin{cases} |T_v(j\omega_{Tv\_des})| = 1 \\ \angle T_v(j\omega_{Tv\_des}) = -180° + PM_{v\_des} \end{cases} \qquad (10)$$
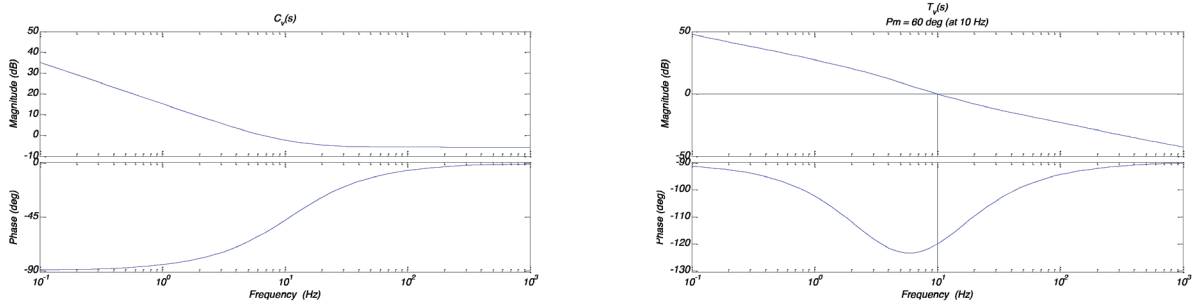
Figure 7 Bode diagrams of voltage compensator $C_v(s)$ and voltage open loop $T_v(s)$ transfer functions

Table 1 3 kW three-channel IPFC prototype specifications

Design parameter	Description	Value
P_{OUT}	output power	3 kW@230 Vac
N_{ch}	Number of channels	3
V_{IN}	rms nominal input voltage	230 V
V_{OUT}	rms nominal output voltage	400 V
f	line frequency	50 - 60 Hz
η	estimated efficiency	98 %
L_{PFC}	single channel boost inductor	120 µH
C_{OUT}	output capacitor	4x470 µF
V_{pk_triang}	peak-to-peak voltage of triangular wave	2 V
K_{PI_out}	PI out scale factor	0.5909
A_i	Input current sensing gain	0.0927
A_v	Output voltage sensing gain	1.9128
A_{MUL}	Digital multiplier gain	3.3086
A_{SMED}	Digital to analog gain	0.00068
f_{sw}	Switching frequency	111 kHz
f_{Ti_des}	Current loop crossover frequency	7.5 kHz
f_{Tv_des}	Voltage loop crossover frequency	10 Hz
PM_{i_des}	Current loop phase margin	60°
PM_{v_des}	Voltage loop phase margin	60°

The compensator parameters can be obtained by solving the following system:

$$\begin{cases} K_{I\_Vdc} = \dfrac{\omega_{Tv\_des}}{|L_i(j\omega_{Tv\_des})|\sqrt{1+\tan^2(PM_{v\_des}-90°-\angle L_v(j\omega_{Tv\_des}))}} \\ K_{P\_Vtot} = \dfrac{K_{I\_Vdc}\tan(PM_{v\_des}-90°-\angle L_v(j\omega_{Tv\_des}))}{\omega_{Tv\_des}} \end{cases}$$

(11)

Finally, according to Table 1 specifications, Figure 6 and Figure 7 show respectively the Bode diagrams for current and voltage loops. Because of the high-frequency pole and standard passive components values the actual phase margin and crossover frequency of Ci(s) are lower than the target values (60°, 7.5 kHz), therefore it has to be compensated by imposing a slightly larger value as specific.

4. Experimental results

A 3 kW three-channel IPFC prototype, showed in Figure 8, has been designed and realized in order to test the proposed control scheme, according to the following specifications - see Table 1.

The power density of 52 W/inch^3 is achieved exploiting a compact layout and the small size of magnetic components related with the benefits of interleaving and high switching frequency.

Figure 9 shows the inductor currents waveforms in small time scale. The interleaving operation is properly set with 120 degrees of phase shift.
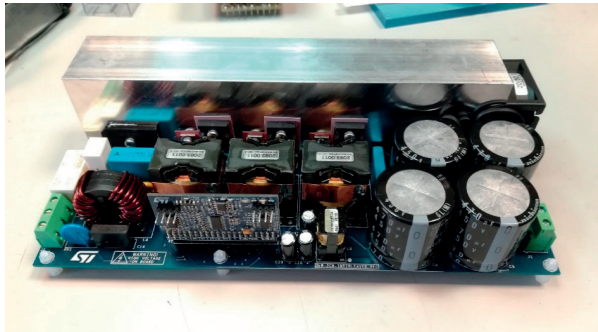
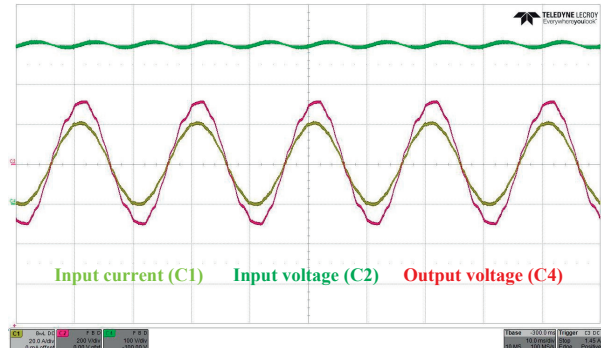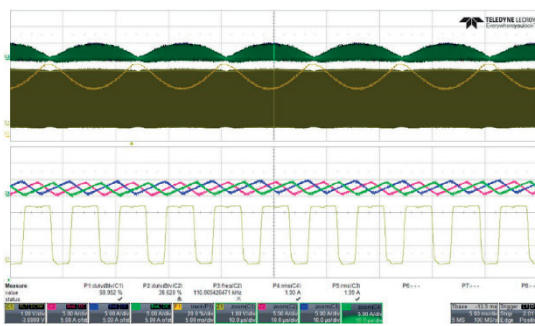*Figure 8 3 kW 3-channel interleaved PFC prototype*

Figure 9 Inductor current waveforms at switching frequency

Figure 10 IPFC at 1.5 kW (115 Vac, 60 Hz)

Input current (C1)   Input voltage (C2)   Output voltage (C4)

Figure 11 IPFC at 3 kW (230 Vac, 50 Hz)

Load current (C3)

Input current (C1)

Output voltage (C4)

Figure 12 10 % - 100 % - 10 % load transition
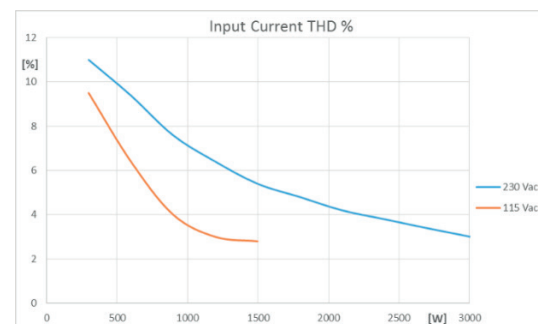
Figure 13 Input Current THD %

The waveform in steady state at line frequency are shown in Figure 10 and Figure 11. The board is supplied by a power AC source at 115 Vac and the power is de-rated for thermal reasons down to 1.5 kW while it is 3 kW when connected to the 230 Vac grid. The input current faithfully follows the reference thus an almost sinusoidal shaped waveform with near unity power factor is obtained even in case of line voltage distortion.

The control fast dynamic response is clearly stated in Figure 12 where a load step from 10 % to 100 % and again to 10 % is considered. Thanks to the load feed-forward the output voltage fluctuations during load transitions have been reduced.

In steady state condition THD, PF and efficiency performance are evaluated. Figure 13 shows a THD lower than 10 % at loads higher than 20 %. It decreases down to 3 % at full load for 230 Vac

and below 3 % for 115 Vac. High power factor (> 0.99) is achieved from 20 % load.

Finally, a high and nearly flat efficiency has been obtained and showed in Figure 14 thanks to the phase shedding operation. Its value is about 97.6 % from 50 % to 100 % load.

5. Conclusion

For automotive application of PFC AC/DC converter to be used as front-end stage in battery charger, a new approach is presented combining mixed signal control and phases interleaving that allows to match at the same time the advantages of analog
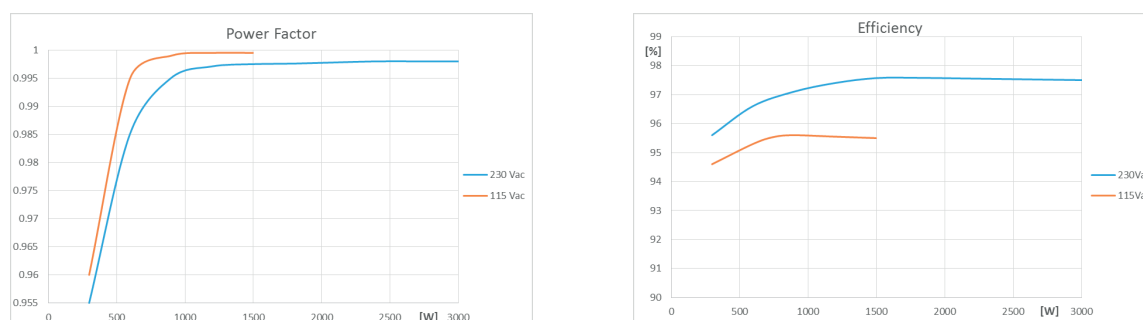
Figure 14 *Power factor vs output PFC power (left) and converter efficiency (right)*

cycle by cycle regulation and the flexibility of a digital system still performing high effiency.

In the paper, theoretical aspects have been considered, the design of both the analog and the digital control loops is introduced and the procedure for the control implementation has been provided.

A prototype has been realized in order to test the proposed control scheme. THD of 3 % and PF well above 0.99 are achieved for the rated power, the measured efficiency at 230 Vac is just below 98 % and shows a nearly flat behavior. Moreover, input current waveform is not affected from grid voltage distortion and test results show very good performances for both steady-state and dynamic conditions.

References

[1] Develops Prototype Medium-Voltage Utility Direct Fast Charger. Epri Journal, Spring, 2012.

[2] CONSOLI, A., CACCIATO, M., TESTA, A., GENNARO, F.: Single Chip Integration for Motor Drive Converters with Power Factor Capability. IEEE Transactions on Power Electronics, 19(6), 1372-1379, 2004.

[3] YOUNG-JOO LEE, KHALIGH, A., EMADI, A.: Advanced Integrated Bidirectional AC/DC and DC/DC Converter for Plug-In Hybrid Electric Vehicles. IEEE Transactions on Vehicular Technology, 58(8), 3970-3980, 2009.

[4] LU, Y. W., ZHANG, W., LIU, Y.: A Large Signal Dynamic Model for Single Phase AC-To-DC Converters with Power Factor Correction. Proceedings of 35th Annual IEEE Power Electronics Specialists Conference, Germany, 2, 1057-1063, 2004.

[5] Power Factor Correction (PFC) Handbook: Choosing the Right Power Factor Controller Solution [online], 2014, SCILLC, USA, rev. 5, 2014.

[6] ZHANG, W., FENG, G., LIU, Y., WU, B.: A Digital Power Factor Correction (PFC) Control Strategy Optimized for DSP. IEEE Transactions on Power Electronics, 19(6), 1474-1485, 2004.

[7] CACCIATO, M., SCARCELLA, G., SCELBA, G., FINOCCHIARO, L.: Multi-Reference Frame Based PLL for Single Phase Systems in Voltage Distorted Grids. Proceedings of 16th European Conference on Power Electronics and Applications, Finland, 1-8, 2014.

[8] CACCIATO, M., CONSOLI, A., AIELLO, N., ATTANASIO, R., GENNARO, F., MACINA, G.: A Digitally Controlled Double Stage Soft-Switching Converter for Grid-Connected Photovoltaic Applications. Proceedings of 23rd Annual IEEE Applied Power Electronics Conference and Exposition, USA, 141-147, 2008.

[9] STNRGPF01 Three-channel interleaved CCM PFC digital controller, Data Sheet DS10246 [online]. STMicroelectronics, 2017.

[10] NAGULAPATI, K., RANGAVALLI, V., VANAJAKSHI, B.: Modeling, Analysis and Simulation of 4-Phase Boost Converter. International Journal of Electrical, Computer, Electronics and Communication Engineering, 8(9), 1452-1462, 2014.

[11] BRYANT, B., KAZIMIERCZUK, M. K.: Open-Loop Power-Stage Transfer Functions Relevant to Current-Mode Control of Boost PWM Converter Operating in CCM. IEEE Transactions on Circuits and Systems-I: regular papers, 52(10), 2158–2164, 2005.

[12] MORICONI, U.: Designing a High Power Factor Switching Pre-Regulator with the L4981 Continuous Mode, Application Note AN628 [online]. STMicroelectronics, 2004.

kəMUNikácie
C O M M U N I C A T I O N S

Patrik Varecha - Vladimir Vavrus - Bretislav Zuczek*

ISSUES IN DESIGNS OF HIGH CURRENT APPLICATIONS

This paper deals with design high current printed circuit boards (PCB), with the issues of implementation the power layer into standard PCB and influence of parasitic parameters of conductive traces of PCB. The parasitic parameters of conductive traces play a significant role in design of high current PCB, and therefore must be minimized. The technology of manufacturing PCB for high current designs as a compact device is mentioned in the paper. The quality of MOSFET switching power in high current design was compared in two ways of proposed leading power lines in order to demonstrate the influence of parasitic inductances of conductive traces.

Keywords: *automotive, high current, printed circuit board*

1. Introduction

Automotive industry is one of the fastest developing kind of industry. It is characterized by high requirements on reliability and safety of all devices. The important sign of automotive industry is voltage power supply, 12 volts for personal cars and 24 volts for trucks.

Modern trend of automotive area is set on the replacement of less reliable, usually mechanical systems by more reliable and smarter electrical systems. The electric turbocharger, power steering or electric assisted parking brake are modern electrical systems based on principle, as were the previous mechanical systems [1 - 3]. These electrical systems are usually driven by 3-phase PMSM motors and they are supplied by high performance inverter.

There are many important factors in development of high current application. Three key factors of high current applications development will be mentioned, which are needed to be solved. First factor relates minimizing of parasitic inductances of design, due to influence on quality of switching, and total electromagnetic interference of design. Second factor relates to thermal performance of the design. That means, minimizing of generated heat, dissipation of heat and cooling. Third factor relates to feasibility of manufacturing of the design, in terms of dimensions limitations.

The geometry and the material of the PCB have impact on the thermal performance of the high current design. This influence of material and geometry of PCB on thermal performance of design is mentioned in [4].

In order to minimize parasitic inductances and reaching good thermal performance, the optimization of layout is mentioned in [5]. The authors have developed high current power converter design for three-phase motors and investigate the influence of parasitic inductances on the quality of switching and thermal performance.

In the end, it is necessary to mention, that the automotive industry is targeting low cost and high efficiency designs. With the growing market of electrical vehicles, the efficiency of the devices will play the key role of the development.

2. Topology of the printed circuit boards for high current applications

Function of printed circuit board (PCB) in electronics is physical and electrical connection of the components, forming an electronic device. The main challenge of high current PCB, is necessity to withstand flow of current and to ensure that the device would work in standard and safe operation. The design approach of PCB for high current application is mentioned in [6]. The authors propose making multilayer power board with stack of power layers. Advanced method of manufacturing the PCB for high current applications is called Iceberg. This technology was patented by KSG Leterplatten GmbH company. Iceberg technology allows to design the conductive layer with different thickness. This technology is suitable for compact devices to source high current loads. The mechanical and electrical

* ¹Patrik Varecha, ¹Vladimir Vavrus, ²Bretislav Zuczek
¹Department of Power Electrical Systems, Faculty of Electrical Engineering, University of Zilina, Slovakia,
²NXP Semiconductors, Roznov pod Radhostem, Czech Republic
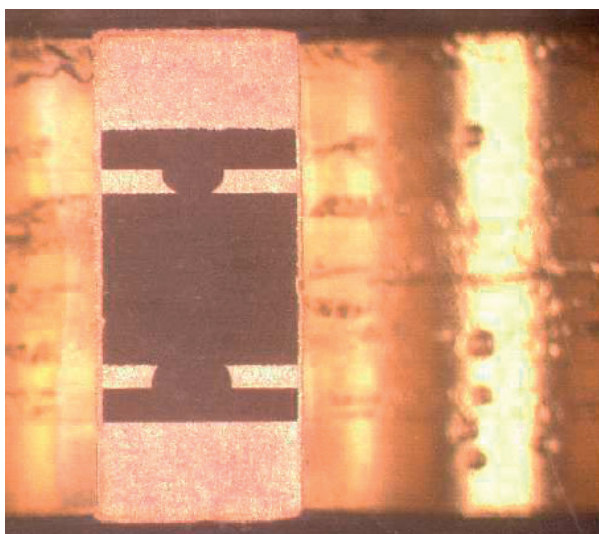 E-mail: vladimir.vavrus@kves.uniza.sk

Figure 1 *Cross section of four layers PCB made by Iceberg technology with power layers on outer side*

Figure 2 *Cross section of four layers PCB made by Iceberg technology with one layer of power line on outer side*
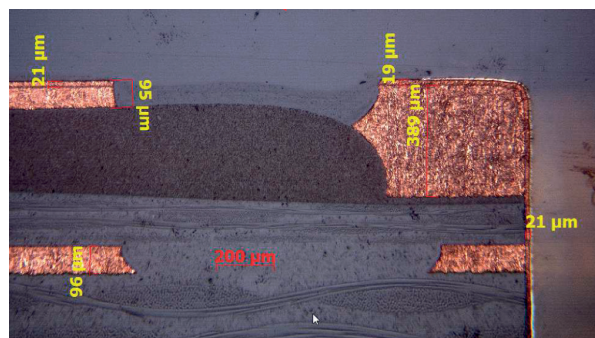

Figure 3 *Cross section of PCB made by Iceberg technology with different thickness of conductive layer on outer side*
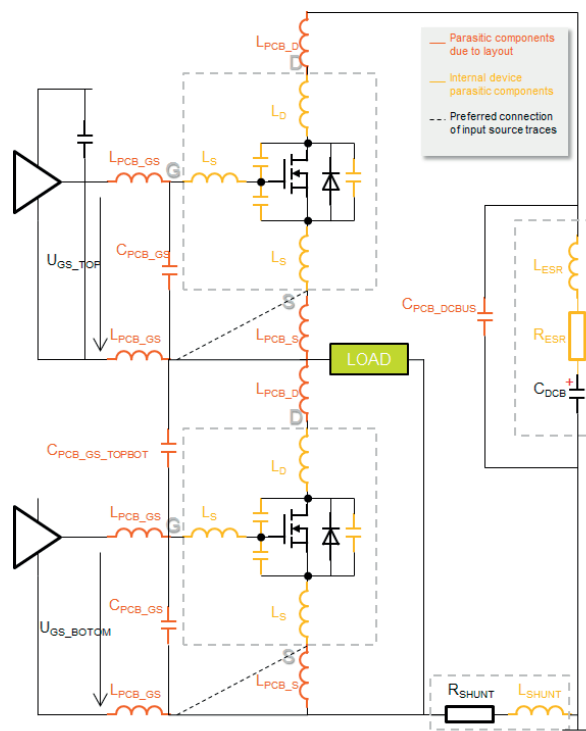

Figure 4 *One branch of power inverter with parasitic components*

components signal or power circuits are integrated on the same side of PCB [7].

The designer has two possibilities of designing the PCB with Iceberg technology. The first design defines the thickness of conductive material for one layer of PCB. The thickness of conductive layer can be determined for leading of high density of current, or can be determined for conductive connection of signal circuits.

Figure 1 shows a cross section of 4 layers PCB with implementation 400 μm thickness of conductive layer on both outer layers of PCB. This power conductive layer can be also implemented on one outer layer of PCB only, while the thickness of other layers can be different. The cross section of this PCB type is shown in Figure 2. This design of thick outer layers is not suitable for combination of signal and power circuits together on the same side of PCB. The issues have occurred in the etching. The minimum distance of two conductive lines must be greater as for standard 70 μm thickness of conductive layer.

Figure 3 partially shows the cross section of four layers PCB with implementation of two conductive layers with different thickness on the same outer layer of PCB. This way of integration of conductive layers makes possible to implement signal and power circuits on the same side of PCB. It is suitable design for compact devices.

Iceberg technology has also some disadvantages in real application. If the power layers of PCB are disproportionately overloaded and the conductive layers are suffering from high temperature, the PCB can be more susceptible to delamination.
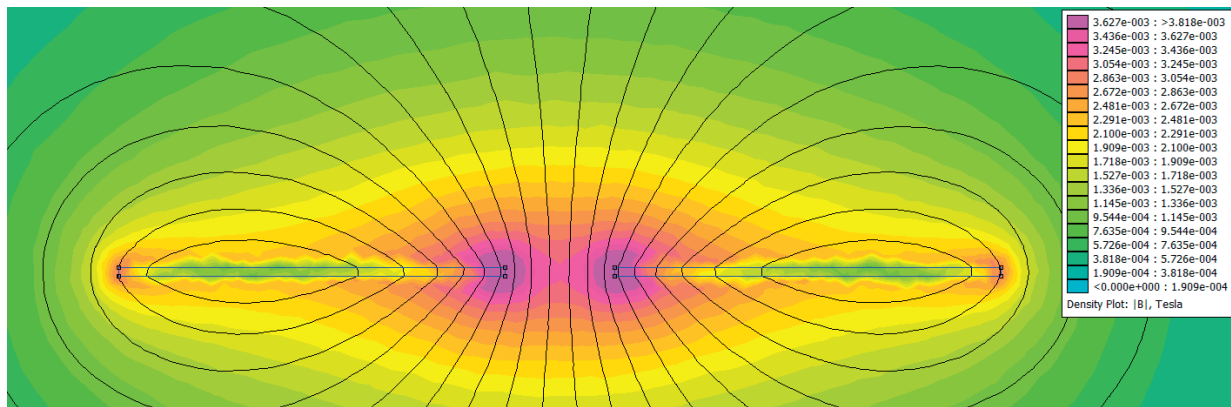
Figure 5 *FEM analysis of coplanar leading of conductive lines PCB*

The disadvantage of this technology is also in soldering of components on the thick layer. The heat is greatly depleted and soldering is complicated.

3. Influence of parasitic inductance in high current applications

The influence of parasitic parameters of the PCB in high current applications is more significant than standard low current applications. Combination of fast dynamic of switching and high value of controlled current can bring complications in the form of high voltage peaks, increased intensity of radiation and the decreasing of the efficiency.

Figure 4 shows one branch of 3-phase inverter with respecting parasitic components of the circuit. The aim of this chapter is to show and describe parasitic parameters of the power circuit and to find the solution for reducing these parameters.

Parasitic parameters of the components, MOSFETs, shunt resistor and DC link capacitors, are shown by yellow colour. There are parasitic inductances and capacitances of the power MOSFETs, parasitic inductance and equivalent serial resistance of the DC buss capacitor, and parasitic inductance of the shunt resistor. These parasitic parameters are affected by the manufacturer. Other parasitic parameters are affected by the layout. These parasitic inductances and capacitances are shown by red colour.

The inductance of the electric wire is defined as energy stored in the field and the value is determined by the current. It is necessary to reduce the trace inductance of PCB, due to the generating of high voltage peaks. This inductance can be directly reduced by increasing cross section area of the trace or decreasing the length of the trace. The thickness of the trace is limited by standards, therefore the cross section can be increased by the width of the trace.

The parasitic inductance of the source trace L_{PCB_S} and parasitic inductance of the drain trace L_{PCB_D} are affected by the trace of power line and parasitic inductances of the gate-source

loop L_{PCB_GS} are affected by routing the gate and source traces to MOSFETs. The parasitic inductance of gate traces is mitigated by minimizing of vias in gate-source loop, minimizing of length of this loop and making gate source traces wider. In case of insufficient mitigating of parasitic inductance of gate-source loop, the capacitor C_{PCB_GS} is added.

Figure 5 shows FEM analysis of two standard leading conductive lines. This arrangement of conductive lines is usually used in low current design of PCB. Due to the influence of magnetic flux, this layout of power lines is not suitable for high current applications. The total parasitic inductance of power lines is 23 nH, and these two conductive layers are coupled by inductive linkage with coincident direction. The magnetic flux density in the coplanar arrangement has maximum value in the place of the minimum distance of two power lines, see in Figure 5. In this case, emissions of magnetic flux to surroundings increases parasitic inductance. The magnetic flux density value is determined by current and distance of these two layers.

The following arrangement of conductive traces allows reducing the influence of parasitic inductance in the design. Figure 6 shows analysis of parallel leading of conductive traces. In this case, total parasitic inductance of power lines is 2.4 nH. Inductance of this arrangement is much smaller than in coplanar arrangement of power lines. Maximum value of magnetic flux density is generated between power lines and the value is determined by current and distance of two layers. The emission of magnetic flux to surrounding is lower in comparison with coplanar arrangement so parasitic inductance is lower too. Main benefit of parallel arrangement is compensation transient state by opposite layer.

All conductive traces of the design, gate-source loops and power loop, should be routed in recommended arrangement. The conductive lines of the routed circuits, where the current loop is closed from source to the load and back to the source, are proposed to lead opposite each other. That means that the magnetic field generated by the current with the positive direction of flow in one conductive line will be suppressed by the magnetic field generated by current with the negative direction of flow.
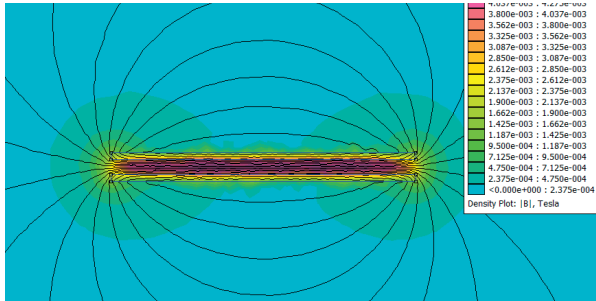
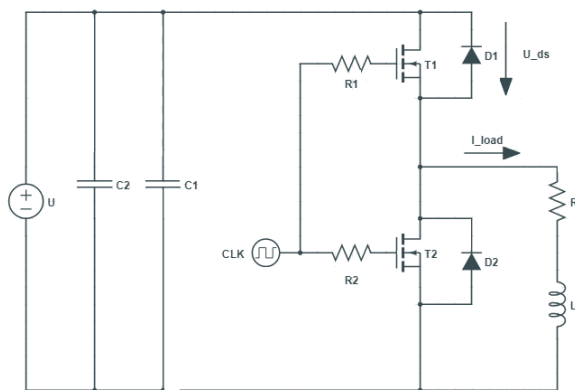*Figure 6 FEM analysis of parallel leading conductive lines of PCB*

Figure 7 Schematic of half bridge power inverter for testing purpose

These two conductive layers are coupled by inductive linkage with anti-coincident direction.

4. Quality comparision of switching for parallel and coplanar leading power lines

This chapter deals with comparison of switching quality for parallel and coplanar leading of power conductive traces. The testing of the switching was realized in one leg of 3 - phase power inverter, also known as a half bridge converter, shown in the Figure 7. The switching of power MOSFETs was realized in complementary mode. The voltage of top MOSFET transistor UDS was measured by differential probe and load current was measured by current probe.

The load was created by stator coils in the star connection, without neutral point, where the resistance of two coils is $R = 0.014\ \Omega$ and inductance of two coils is $L = 20\ \mu H$.

The waveforms of drain-source voltage and load current are shown in the Figure 8. It is necessary to mention, that both of MOSFETs are switching, the snubbers are not realized in design, and therefore the voltage U_{DS} is oscillating. The aim of this chapter is to compare the influence of coplanar and parallel leading of power traces on the quality of MOSFET switching power, without
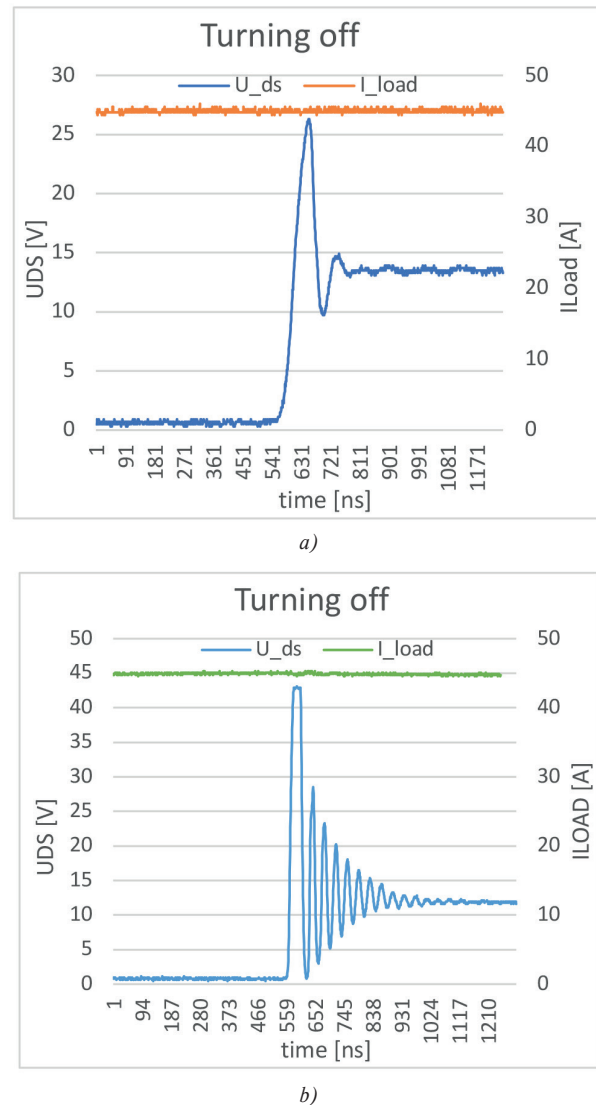

a)

b)

*Figure 8 Waveforms of the U_{DS} of top transistor and load current for turn-off sequence **a)** parallel leading of power lines; **b)** coplanar leading of power lines*

additional snubbers. Half-bridge converter is regulated to constant current of RL load.

Experimental results show different quality of switching the power MOSFET for coplanar and parallel leading of power traces. The influence of voltage U_{DS} oscillation is mitigated by parallel leading of power traces. The waveforms of voltage U_{DS} and load current are shown in Figure 8a). In the coplanar leading of power traces, the oscillation of voltage U_{DS} is considerable. In this case, the oscillation of voltage U_{DS} may be mitigated by the design of suitable snubbers [8]. In both case, the load current is the same and the axis of load current is on the opposite side as axis of voltage U_{DS}.

5. Conclusion

This paper presents two possible ways of high current PCB designs and their influence on the switching quality. The suitable technique for manufacturing high current PCB with signal and power layer on the same side of PCB was described. The power line of high current board is possible to lead by coplanar or parallel way. The experimental results show better quality of switching for parallel leading of power trace. In this case the electromagnetic interference will be lower in comparison with coplanar leading power trace. The following steps will be related to the efficiency analysis of losses, and it will be published later.

References

[1] LIM, M., B., KIM, J., HWANG, Y., HONG, J.: Design of an Ultra-High-Speed Permanent-Magnet Motor for an Electric Turbocharger Considering Speed Response Characteristics. IEEE/ASME Transactions on Mechatronics, 22 (2), 774-784, 2016.

[2] ABE, T., FUJIMURA, Y., HIROSE, T., HASHIMOTO, S., KAJITANI, M., SATO, K., GONPEI, K.: Linear Quadratic Control Design in Electric Power Steering System. International Conference on Advanced Mechatronic Systems (ICAMechS), Australia, 73-78, 2016.

[3] PARK, J., JEON, K., CHOI, S.: Design of Fail-Safe Controller for Brake-by-Wire Systems Using Optimal Braking Force Distribution. World Electric Vehicle Symposium and Exhibition (EVS27), Spain, 1-7, 2013.

[4] MROSSKO, R., NEEB, CH., HOFMANN, T.: Thermal Design of a High Current Circuit Board for Automotive Applications. Thermal Investigations of ICs and Systems (THERMINIC), Germany, 206-209, 2013.

[5] YAZDI, B., M., WU, X., HAAF, P., NEUMAIER, K.: A Study of the Thermal and Parasitic Optimization of a Large Current Density Highly Parallelized Three-Phase Reference Board for Motor Drive. International Exhibition and Conference for Power Electronics, Intelligent Motion, Renewable Energy and Energy Management, Germany, 1-8, 2016.

[6] BAI, H. - CH., CHEN, Y.-W.: Improvement of High-Current Density PCB Design with PSU Load Balance and Redundancy on a High End Server System. IEEE Transactions on Power Electronics, 2004.

[7] BECHTLOFF, U., FIEHLER, R., SCHAUER, J., SCHMIEDER, K.: Describtion of "Iceberg" Technology/Leiterplattenfertigung in der „Iceberg"-Technologie (in German) [online]. Available: http://www.all-electronics.de/wp-content/uploads/migrated/article-pdf/98431/pr07-07-051.pdf (accessed 17.07.2012).

[8] Designing RC snubbers, Application note [online]. Available: https://assets.nexperia.com/documents/application-note/AN11160.pdf (accessed 25.04.2012).

R E V I E W

Giovanni Nobile - Mario Cacciato - Giuseppe Scarcella - Giacomo Scelba*

MULTI-CRITERIA EXPERIMENTAL COMPARISON OF BATTERIES CIRCUITAL MODELS FOR AUTOMOTIVE APPLICATIONS

Electrochemical batteries used in energy storage systems provide a significant contribution to the development of smart grids and green transportation. In recent years, intensive research activities have been oriented to the optimal management of energy storage systems for power electronics applications in fast growing industrial sectors as EVs and HEVs. The accurate modeling of electrochemical batteries is fundamental in the design of control algorithms applied to energy storage systems. Focusing on automotive applications, in this paper a comprehensive analysis of ESS models based on equivalent electric circuits using a multi-criteria approach is presented. An extensive experimental validation has been carried out to evaluate the performance of battery models in automotive applications.

Keywords: battery modeling, SOC estimation, SOH estimation, energy storage systems, automotive

1. Introduction

The energy management of storage systems based on electrochemical batteries is one of the most investigated topics in smart grid and transportation issues [1]. In particular, in EV and HEV applications the battery pack requires a Battery Management System BMS to optimize the control strategies in terms of safety and performance. Such control strategies are usually implemented on Energy Storage System (ESS) exploiting a suitable model of the battery pack that ensure an appropriate accuracy in the estimation of State of Charge (SOC) and State of Health (SOH) while avoiding too large computational complexity. In the field of power electronics for automotive applications, the trade-off between the response accuracy and the computational effort is obtained by using models based on equivalent electric circuits [2].

In BMS applications, a significant example about the influence of the ESS circuit model can be reported by considering SOC estimation methods based on observers [3, 4]. This category includes sliding mode, Luenberger, PI-based and other similar observers. Their implementation always leads to the use of parameter-varying circuit models. In Figure 1, the schematic representation of a generic PI-based observer is shown [5]. In such a case, the correctness of SOC and SOH estimations is strongly related to the accuracy of the circuit model response. In

particular, considering demanding application that shows huge current range, the circuit model can provide a wrong voltage estimation that implies large errors in the ESS state evaluation.

In recent years, several authors have carried out some reviews about models for ESS. Significant examples are in [6-8]. From a review of the existing literature, it can be stated that a comprehensive analysis on battery circuit models cannot be conducted by considering a single comparison criterion. In this paper, a comparison of different equivalent circuits used to model battery packs in the automotive field has been reported on the basis of a multi-criteria analysis, also considering large experimental data.

2. Energy storage systems modeling

It is possible to sort the main circuit models for ESS used in the automotive field in a few main categories, as listed in the following.

- *Basic Models*

The basic circuit used to model a battery is the series connection of a voltage generator E_0 and a resistor R_i [8]. This equivalent circuit is shown in Table 3 - model A. E_0 is the no-load voltage at full charge state while R_i models the internal and

* **Giovanni Nobile, Mario Cacciato, Giuseppe Scarcella, Giacomo Scelba**
  Department of Electrical, Electronics Engineering and Computer Science, University of Catania, Italy
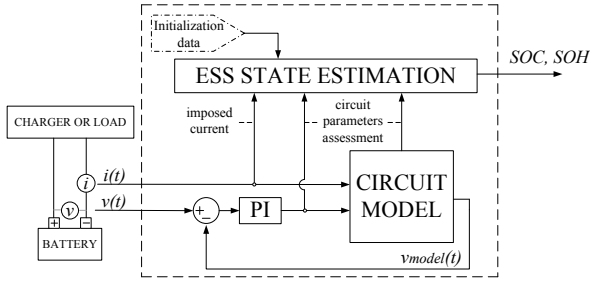 E-mail: giovanni.nobile@dieei.unict.it

Figure 1 *PI-based observer scheme including the battery circuit model*

terminal resistances. Higher accuracy can be obtained by taking into account the function R_i(SOC) [8].

- *Sheperd, Unnewehr and Nernst models*

These models are obtained starting from stoichiometric electrochemical formulations. Different models belong to this category and have been proposed by Sheperd, Unnewehr and Nernst [7]. The basic Sheperd formulation is in stoichiometric form, anyway a transition to a simpler equivalent electric circuit model can be obtained by considering acceptable approximations. A popular simplified version, cited in [7], is displayed in Table 3 - model C:

$$v_{model}(t) = E_0 - R_i \cdot i(t) - \frac{\mu}{SOC} \qquad (1)$$

where μ_s is a constant term which models the variation of the voltage waveform v_{model} as a function of the actual SOC. A similar formulation can be reported for the Unnewehr and Nernst models represented in Table 3 – model D and E, respectively.

- *RC linear models*

The basic RC linear model is shown in Table 3 - model F. The RC network R_d-C_d is used to plot the transient behavior of ESS during current steps [7, 8]. In some applications extra RC networks are included to increase accuracy in voltage estimation during transients. A modified version of the previous model is the Thevenin model [8], represented in Table 3 - model G. A functional relation is introduced between the no-load voltage E_0 and the actual SOC. An additional resistor R_{sd} is often included to take into account the self-discharge phenomena, [9].

- *Runtime models*

In the "runtime models" the electric circuit is split in two or three sections [6] as shown in Table 3 - model H. The first section models the voltage response during a charge or a discharge. A secondary section provides an estimation of the actual SOC estimation from the voltage on a capacitor $C_{capacity}$ whose capacitance value depends on SOH. An advanced runtime model capable of model runtime and current-voltage (IV) waveforms, while reducing the complexity is reported in [10]. Such model is represented in Table 3 - model I.

- *Tremblay and Jackey models*

The main software houses in the field of power electronics for automotive applications have developed specific battery models to be integrated into their simulations platforms. An overview of these models is in [8]. In [11] Tremblay et al. have proposed an equivalent circuit model derived from Sheperd formulation. This model can be used for Lead Acid batteries, Nickel Cadmium and Ni-MH technologies. Another ESS model has been proposed by Jackey, considering the target of a fast implementation in electronic circuit simulations by performing some approximations [12].

- *Randles models*

In this equivalent circuit models category some of the circuit elements are time-varying parameters. Their value depends on the actual SOC and SOH as well as on external conditions (e.g. current rate and temperature). Randles model is often used in combination with Kalman Filter (KF). A significant example is in [13]. The typical configuration of the Randles circuit is shown in Table 3 - model L. The capacitance C_{bulk} models the main charge store, its voltage is an indicator of SOC, its capacitance is related to actual SOH.

- *Other circuit models*

Many other circuit models can be found in literature. Some of them are obtained from the numerical elaboration of a significant amount of experimental data collected for a given application. Unfortunately, in these cases, it is usually impossible to re-use the same model for different operating scenarios. Two significant examples, presented in [14], are the CIEMAT model and the Monegon model. In [15] an impedance modeling for lead acid batteries is presented by Salkind et al. Experimental data from the Electrochemical Impedance Spectroscopy (EIS) lead to a series impedance model, as described in [16]. Another circuit which is fairly widespread is usually named as "third order model" [17]. Basic concept is related to parasitic effects during charge operation. A parasitic branch is added to a basic Thevenin topology.

3. Comparative evaluation of ESS circuit models

Features and performance comparison

In Table 1, the information collected from a comprehensive literature review about the battery circuit models in the automotive field are summarized. It can be easily observed that none of the models can totally fulfill all the requirements. Besides, the inclusion of additional parameters in the equivalent circuits and/ or the exploitation of parameter-varying models can satisfy many requirements e.g. memory effect, temperature influence and so on. In parameter-varying models, the parameters have to be continuously tuned by using real-time estimation algorithms.

In terms of applications and technologies that can be associated to each model category, Figure 2 shows that almost all the battery models fit different battery technologies. On
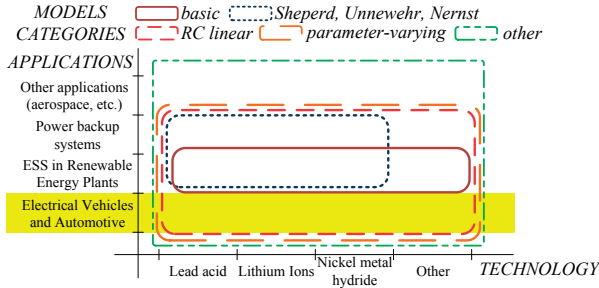
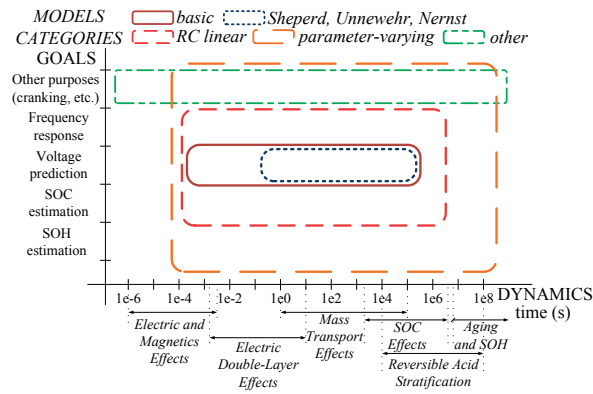Figure 2 Comparison based on applications and technologies

Figure 3 Comparison based on goals and dynamics

Figure 4 Schematical representation of the experimental setup

Figure 5 DC/AC power converter

the contrary, referring to automotive applications, the simplest models are usually not suitable to be used in this challenging field. In Figure 3 the models are classified on the basis of the frequency range related to the main goals in ESS modeling. From this chart, it is quite evident that only more complex models can be used in a large frequency range to fulfill several modeling goals. On the contrary, the simpler models are usually devoted to the voltage estimation only while the estimation of SOC and SOH requires additional algorithms and/or more complicated models. Moreover, the bandwidth for the simpler models can be sometimes too narrow for an effective implementation in the automotive field.

Experimental comparison

A large amount of experimental tests has been done using the test bench shown in Figure 4, technical data of the main components are in Table 2. The power converter used to supply AC loads is displayed in Figure 5. The first stage is a 50 kHz push-pull DC/DC converter connected to the 24 V_{DC} VRLA battery pack and controlled in order to obtain a stable 430 V DC bus. The second stage is a 17 kHz PWM VSI sine wave inverter connected to the DC bus and controlled to ensure a stable 230 V_{AC} 50 Hz output [18, 19]. The overall efficiency of the converter at rated load is 95 %. The control firmware has been developed in a 32 bit 72 MHz Micro Controller Unit (MCU).

The performance of each model is evaluated by comparing the waveform of the measured battery voltage with the voltage
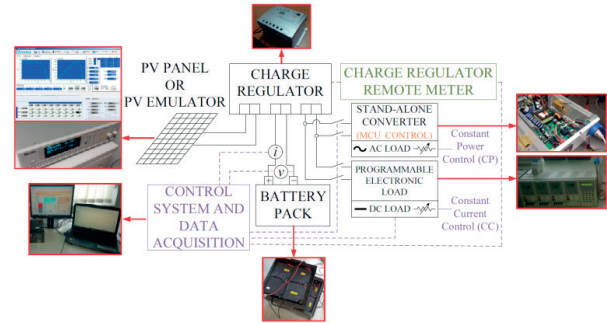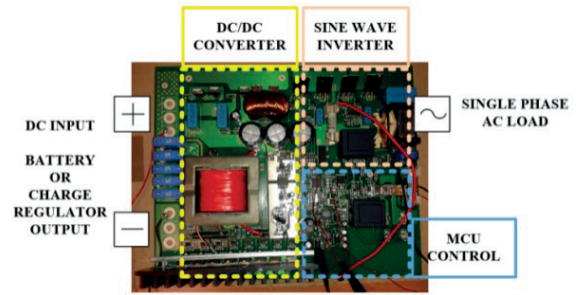
waveform provided by the equivalent circuits. In order to assign an analytical evaluation of the accuracy, some numerical indexes have been introduced.

For each model, the identification of parameters is not trivial. In order to perform an appropriate comparison between the models, a constrained minimums formulation has been implemented for the identification of parameters in every models. Input data is the forced current $i(t)$ and the corresponding voltage $v(t)$ measured at battery terminals. The experimental tests are carried out at different current rates C_R, the environmental temperature ranges between 20°C and 40°C. Referring to a generic equivalent circuit, the Kirchhoff's Voltage Law is:

$$v_{model,k} = h_{k1} \cdot x_1 + h_{k2} \cdot x_2 + \ldots + h_{kn} \cdot x_n \qquad (2)$$

hence, for N tests:

$$\begin{bmatrix} v_{model,1} \\ v_{model,2} \\ \ldots \\ v_{model,k} \\ \ldots \\ v_{model,N} \end{bmatrix} = \begin{bmatrix} h_{11} & h_{12} & \ldots & h_{1n} \\ h_{21} & h_{22} & \ldots & h_{2n} \\ \ldots & \ldots & \ldots & \ldots \\ h_{k1} & h_{k2} & \ldots & h_{kn} \\ \ldots & \ldots & \ldots & \ldots \\ h_{N1} & h_{N2} & \ldots & h_{Nn} \end{bmatrix} \cdot \begin{bmatrix} x_1 \\ x_2 \\ \ldots \\ x_n \end{bmatrix} \qquad (3)$$

$$[V_{model}] = [H] \cdot [X] \qquad (4)$$

k is a time index and h_{ki} is a term about the relation between $v_{model,k}$ and parameter x_i. Thanks to the implementation of the

Table 1 Models comparison based on main requirements

Models (*)		Requirements or performance (**)												
Category	ID	1	2	3	4	5	6	7	8	9	10	11	12	13
Basic models	A	X	O	O	O	O	O	O	O	O	O	O	O	O
	B	X	O	O	O	O	O	O	O	O	O	O	O	O
Sheperd, Unnewehr and Nernst	C	X	O	O	O	O	O	O	O	O	O	O	O	O
	D	X	O	O	O	O	O	O	O	O	O	O	O	O
	E	X	O	O	O	O	O	O	O	O	O	O	O	O
RC linear models	F	X	X	O	O	O	O	O	O	O	O	O	O	O
	G	X	X	O	X	X	O	O	O	O	O	O	O	O
Parameter-varying models	H	X	X	O	X	X	O	X	O	O	X	O	O	O
	I	X	X	X	X	X	X	X	X	O	X	O	O	O
	J	X	X	O	O	X	O	X	X	X	O	O	O	O
	K	X	O	O	X	X	O	O	O	O	X	O	O	O
	L	X	X	O	O	X	X	X	X	O	O	X	X	O
Other models	M	X	X	O	O	X	O	X	X	X	X	O	O	X
	N	X	X	O	O	X	O	X	X	X	X	O	O	X
	O	X	X	X	O	X	X	O	O	O	X	O	X	X
	P	X	X	X	O	X	O	O	O	O	X	O	X	X

(*) *Model ID*

A = Basic [6],[8],[14]

B = Basic RSOC [6]

C = Sheperd [7]

D = Unnewehr [7]

E = Nernst [7]

F = RC [8]

G = Thevenin [9]

H = Runtime [8]

I = Runtime IV [8],[10]

J = Tremblay et al. [8],[11]

K= Jackey [8],[12]

L = Randles [13]

M= CIEMAT [14]

N = Monegon [14]

O = Impedance [15],[16]

P = Third order [17]

(**) *Requirements and performance in modeling physical phenomena*

1 = Voltage estimation during continuous current discharge [7]

2 = Transient behavior, large period pulse current [9]

3 = Transient behavior, short period pulse current [9]

4 = Self discharge [9], 5 = Charge operation modeling [11]

6 = SOC estimation provided by adaptive parameters [13]

7 = Real-time parameters estimation [8],[10]

8 = Real-time and IV curve prediction [8],[10]

9 = Exponential operation area [11],[14], 10 = Peukert effect [10]

11 = Memory effect

12 = SOH estimation provided by adaptive parameters [13]

13 = Temperature effect [14]

X = Requirement fulfilled O = Requirement not fulfilled

constrained minimums formulation, a set of parameters can be assigned to each model in order to reduce the deviation among real and model voltage:

$$[X] \cong (H^T \cdot H)^{-1} \cdot H^T \cdot [V_{measured}] \qquad (5)$$

Even in case of experimental data acquired at different temperatures, this identification method allows to obtain a good accuracy in the estimation of parameters. Anyway, since in the automotive applications the temperature fluctuations can be usually very large, it is often required the implementation of an estimation algorithms to continuously tune the parameters of the

Table 2 Technical specifications of the main components in the test bench

V panel		Charge regulator		Battery pack		Stand-alone DC/AC converter (AC loads)	
rated power	250 W	system voltage	24 V_{DC}	technology	VRLA (x 8)	rated power	2 kW
V_{OC}	37.0 V_{DC}	rated PV current	20 A	rated voltage	24 V_{DC}	rated input	24 V_{DC}
I_{SC}	8.26 A	rated load	20 A				
V_{MPP}	29.8 V_{DC}	max PV power	520 W	rated capacity	108 Ah	rated output	230 V_{AC}
I_{MPP}	7.72 A	max PV voltage	100 V_{DC}				50 Hz

circuit model especially for the simplest models listed in Table 1 [3]. The analysis of the sensitivity to temperature variations in parameters identification and the review of the methods to mitigate such effect is out of the scope of this work.

Considering the VRLA battery pack of Table 2, Table 3 lists the parameters identified for each model. The input experimental data have been acquired at various initial SOC values (from 10 to 100 %, steps of 10 %) and for different currents (from -5 to 20 A, steps of 1 A). The current counting formula [6] is applied for those models that require a continuous evaluation of SOC as input data. The relation $E_0(SOC)$ is a quasi-straight line between the extreme points (22.8 V; 2 %) and (26.4 V; 100 %) in the plane (E_0; SOC), as provided by the manufacturer.

Over 200 experimental tests at different current and SOC values have been scheduled. During the tests, the battery, having an initial SOC, is discharged (or charged) at a given current in a time period from a minimum of 2 hours to a maximum of 10 hours. For each couple of values $i(t)$ and SOC, the mean relative error and the error standard deviation have been calculated for each model:

$$error_{mean} = \frac{\sum_{k=1}^{N} error_k}{k} \tag{6}$$

$$std = \sqrt{\frac{\sum_{k=1}^{N} (error_k - error_{mean})^2}{N}} \tag{7}$$

obtaining the 3D plots shown in Figure 6 and Figure 7. The standard deviation has been introduced because, in some cases, even if the mean error is close to zero, a significant deviation in most part of the waveform can be detected. Starting from data displayed in Figure 6, Figure 8 and Figure 9, there are shown the mean error values for different SOC values at a fixed current, while Figure 10 and Figure 11 show the mean error values for different current rates at a fixed SOC value.

Examining the experimental results, the first evidence is that the mean error in voltage estimation is strongly affected by the actual ESS state. In particular, a significant dependence on the SOC actual value can be observed: large deviations can be detected at low SOC values for almost all the models, Figure 8 and Figure 9. On the contrary, looking at Figure 10 and Figure 11 the influence of current variations on voltage estimation is quite
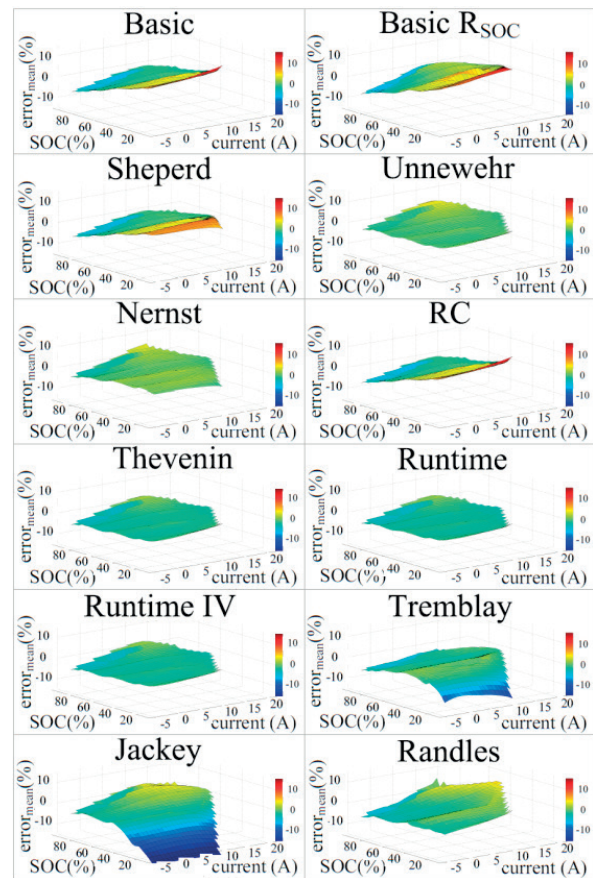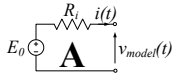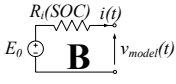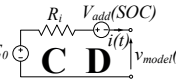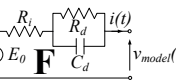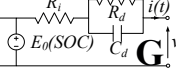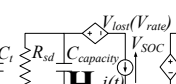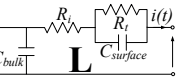

Figure 6 *3D plots - Mean relative error related to the voltage estimation provided by each equivalent circuit model for different currents and SOC values*

limited. Charge operation modeling typically implies a strong degradation in accuracy level due to complicated phenomena to be modeled, Figure 6 and Figure7. From Figure 7, there is no large difference between models in terms of standard deviations related to the error values. For each model, larger values of standard deviation can be identified at low or high SOC values.

Table 3 Circuit models and parameters

	Parameters	Equivalent circuit
A	E_0=25.355 V R_i=0.191 Ω	
B	E_0=25.274 V $R_{i,SOC100}=$ =0.0165 Ω k=1.05	
C	E_0=25.517 V R_i=0.193 Ω μ_s=4.806	
D	E_0=22.955 V R_i=0.215 Ω μ_u=0.041	
E	E_0=25.832 V R_i=0.213 Ω μ_1=1.176 μ_2=0.281	
F	E_0=25.355 V R_i=0.181 Ω R_d= 0.009 Ω C_d=5247 F	
G	$E_0(SOC)$ datasheet R_i=0.187 Ω R_d=0.010 Ω C_d=5071 F R_{sd}=100000 Ω	
H	$E_0(V_{SOC})$ datasheet R_i=0.197 Ω R_t=0.018 Ω C_t=951 F R_{sd}=100000 Ω $C_{capacity}$=388kF	
I	$E_0(V_{SOC})$ datasheet R_i=0.1973 Ω R_{ts}=0.018 Ω C_{ts}=5555 F R_{tl}=0.005 Ω C_{tl}=20000 F R_{sd}=100000 Ω $C_{capacity}$=388kF	
J	See [8],[11]	See [8],[11]
K	See [8],[12]	See [8],[12]
L	R_i=0.187 Ω R_t=0.010 Ω $C_{surface}$=5071 F R_{sd}=100000 Ω C_{bulk}=388kF	
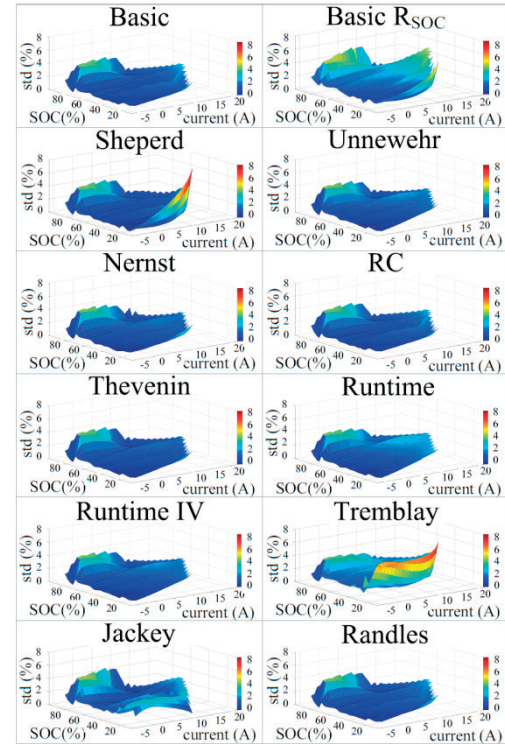
Figure 7 3D plots - Standard deviation related to error values in voltage estimation provided by each equivalent circuit for different currents and SOC
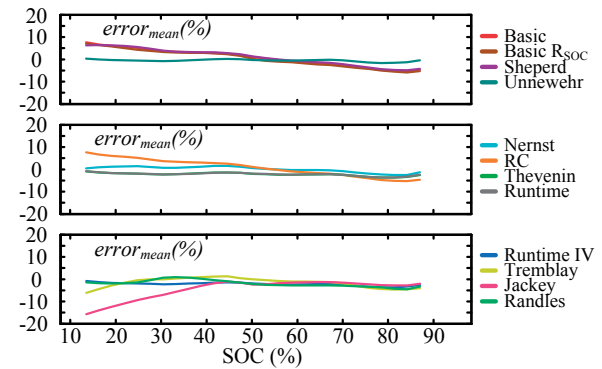

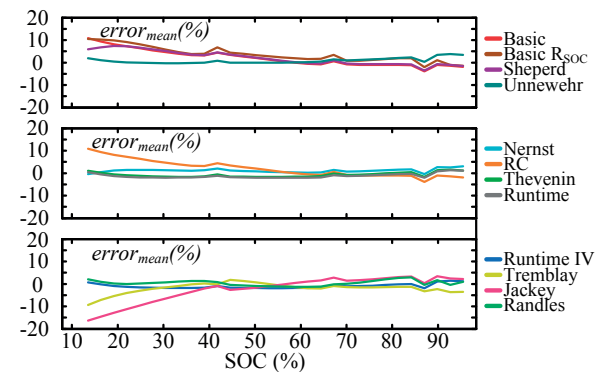*Figure 8 Mean error vs SOC, current is fixed -2 A*
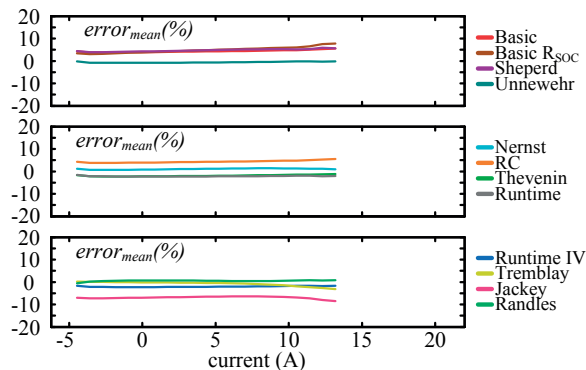

Figure 9 Mean error vs SOC, current is fixed 10 A
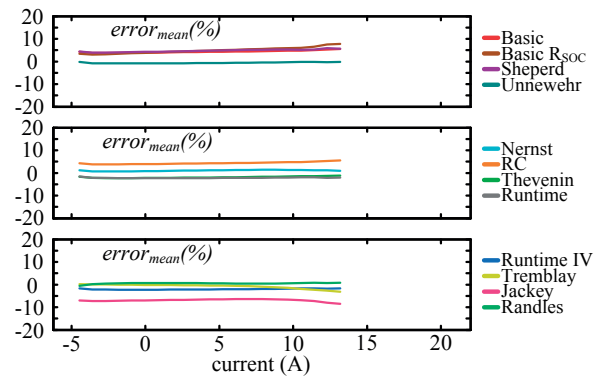
Figure 10 *Mean error vs SOC, SOC is fixed 30 %*

Figure 11 *Mean error vs SOC, SOC is fixed 80 %*

4. Conclusions

This paper deals with a study on the main equivalent electric circuits used in ESS modeling for automotive applications. The characteristics of each model have been studied and compared by means of a multi-criteria approach using both the data gathered by an in-depth literature review and those collected by performing several experimental tests. Using such a method, features and performance associated to each equivalent circuit have been highlighted. The results of the comparative multi-criteria analysis show that Thevenin, Runtime and Runtime IV models can be considered as the best compromise between performance and complexity in standard automotive applications. Nevertheless, to reach a satisfactory accuracy in automotive applications, it is usually necessary to use an estimation algorithm capable to continuously tune the parameters of the circuit model in order to compensate their variation related to large temperature fluctuations, SOH degradation and so on.

References

[1] TUMMURU, N. R., MISHRA, M. K., SRINIVAS, S.: Dynamic Energy Management of Hybrid Energy Storage System with High-Gain PV Converter. IEEE Transactions on Energy Conversion, 30(1), 150-160, 2015.

[2] CUGNET, M., DUBARRY, M., LYAW, B.: Secondary Batteries – Lead-Acid Systems – Modeling. Reference Module in Chemistry, Molecular Sciences and Chemical Engineering Encyclopedia of Electrochemical Power Sources, Elsevier, 816–828, 2009.

[3] CACCIATO, M., NOBILE, G., SCARCELLA, G., SCELBA, G.: Real-Time Model-Based Estimation of SOC and SOH for Energy Storage Systems. IEEE Transactions on Power Electronics, 32(1), 794-803, 2016.

[4] CACCIATO, M., NOBILE, G., PULVIRENTI, M., RACITI, A., SCARCELLA, G., SCELBA, G.: Energy Management in Parallel Hybrid Electric Vehicles Exploiting an Integrated Multi-Drives Topology. Proceedings of International Conference of Electrical and Electronic Technologies for Automotive, Italy, 2017.

[5] CACCIATO, M., NOBILE, G., SCARCELLA, G., SCELBA, G., SCIACCA, A. G.: Energy Management Optimization in Stand-Alone Power Supplies Using Online Estimation of Battery SOC. Proceedings of IEEE 18th European Conference on Power Electronics and Applications (EPE), Germany, 2016.

[6] SEAMAN, A., DAO, T., MCPHEE, J.: A Survey of Mathematical-Based Equivalent-Circuit and Electrochemical Battery Models for Hybrid and Electric Vehicle Simulation. Journal of Power Sources, 256, 410-423, 2014.

[7] HUSSEIN, A., BATARSEH, I.: An Overview of Generic Battery Models. Proceedings of IEEE Power and Energy Society General Meeting, USA, 1-6, 2011.

[8] MOUSAVI, S. M., NIKDEL, M: Various Battery Models for Various Simulation Studies and Applications. Renewable and Sustainable Energy Reviews, 32, 477-485, 2014.

[9] LI, J., MAZZOLA, M.: Accurate Battery Pack Modeling for Automotive Applications. Journal of Power Sources, 237, 215-228, 2013.

[10] CHEN, M., RINCON-MORA, A.: Accurate Electrical Battery Model Capable of Predicting Runtime and I-V Performance. IEEE Transactions on Energy Conversion, 21(2), 504-511, 2006.

[11] TREMBLAY, O., DESSAINT, L.: Experimental Validation of a Battery Dynamic Model for EV Applications. World Electric Vehicle Journal, 3, 1-10, 2009.

[12] JACKEY, R. A.: A Simple, Effective Lead-Acid Battery Modeling Process for Electrical System Component Selection. Proceedings SAE World Congress and Exhibition, USA, paper 2007-01-0778, 2007.

[13] BHANGU, B. S., BINGHAM, C. M., STONE, D. A., BENTLEY, P.: Nonlinear Observer techniques for Prediction State-of-Charge and State-of-Health of Lead-Acid Batteries for Hybrid-Electric Vehicles. IEEE Transactions on Vehicular Technology, 54(3), 783-794, 2005.

[14] ACHAIBOU, N., HADDADI, M., MALEK, A.: Lead Acid Batteries Simulation Including Experimental Validation. Journal of Power Sources, 185(2), 1484-1491, 2008.

[15] SALKIND, A., SINGH, P., CANNONE, A., ATWATER, T., WANG, X., REISNER, D.: Impedance Modeling of Intermediate Size Lead-Acid Batteries. Journal of Power Sources, 116, 174-184, 2003.

[16] STROE, D. I., SWIERCZYNSKI, M., STROE, A. I., KNAP, V., TEODORESCU, R., ANDREASEN, S. J.: Evaluation of Different Methods for Measuring the Impedance of Lithium-Ion Batteries during Ageing. Proceedings of Tenth International Conference on Ecological Vehicles and Renewable Energies (EVER), Monaco, 1-8, 2015.

[17] WANG, H., LI, G., LI, M., JIANG, Z., WANG, X., ZHAO, Q.: Third-Order Dynamic Model of a Lead Acid Battery for Use in Fuel Cell Vehicle Simulation. Proceedings of IEEE Mechatronic Science, Electric Engineering and Computer Conference (MEC), China, 715-720, 2011.

[18] ATTANASIO, R., CACCIATO M., CONSOLI A., SCARCELLA G., TESTA A., GENNARO F.: A Novel Converter System for Fuel Cell Distributed Energy Generation. Proceedings of IEEE Annual Power Electronics Specialists Conference (PESC ´05), Brazil, 1621-1627, 2005.

[19] CACCIATO M., CONSOLI A., SCARCELLA G., SCELBA G., TESTA A.: Modified Space-Vector-Modulation Technique for Common Mode Currents Reduction and Full Utilization of the DC bus. Proceedings of 24th Annual IEEE Applied Power Electronics Conference and Exposition (APEC 2009), USA, 109-115, 2009.

COMMUNICATIONS – Scientific Letters of the University of Zilina
Author guidelines

l. Submitted papers must be unpublished and must not be currently under review for any other publication.

2. Submitted manuscripts should not exceed 8 pages including figures and graphs (in Microsoft WORD – format A4, Times Roman size 12, page margins 2.5 cm).

3. Manuscripts written in good English must include abstract and keywords also written in English. The abstract should not exceed 10 lines.

4. Submission should be sent by e-mail – as an attachment – to the following address: komunikacie@uniza.sk.

5. Uncommon abbreviations must be defined the first time they are used in the text.

6. Figures, graphs and diagrams, if not processed in Microsoft WORD, must be sent in electronic form (as JPG, GIF, TIF, TTF or BMP files) or drawn in high contrast on white paper. Photographs for publication must be either contrastive or on a slide.

7. The numbered reference citation within text should be enclosed in square brackets - in numerical order. The reference list should appear at the end of the article (in compliance with ISO 690).

8. The numbered figures and tables must be also included in the text.

9. The author's exact mailing address, full names, E-mail address, telephone or fax number, the name and address of the organization and workplace (also written in English) must be enclosed.

10. The editorial board will assess the submitted paper in its following session. If the manuscript is accepted for publication, it will be sent to peer review and language correction. After reviewing and incorporating the editor's comments, the final draft (before printing) will be sent to authors for final review and minor adjustments.